The Hashemite Kingdom of Jordan
Scientific Research Support Fund
The Hashemite University

JJEES

Jordan Journal of Earth and Environmental Sciences

Indexed by Scopus
ELSEVIER

Volume (16) Number (1)

Cover photo © Khaled Moumani

JJEES is an International Peer-Reviewed Research Journal

ISSN 1995-6681 jjees.hu.edu.jo March 2025

Jordan Journal of Earth and Environmental Sciences (JJEES)

JJEES is an International Peer-Reviewed Research Journal, Issued by Deanship of Scientific Research, The Hashemite University, in corporation with, the Jordanian Scientific Research Support Fund, the Ministry of Higher Education and Scientific Research.

Editorial Board:

Associate Editorial Board: (Arranged Alphabetically)

International Advisory Board: (Arranged Alphabetically)

Editorial Board Support Team:

Submission address:

Manuscripts should be submitted electronically to the following e-mail:

jjees@hu.edu.jo

For more information and previous issues:

www.jjees.hu.edu.jo

Hashemite Kingdom of Jordan

Scientific Research Support Fund

Hashemite University

Jordan Journal of Earth and Environmental Sciences

JJEES

An International Peer-Reviewed Scientific Journal

Financed by the Scientific Research Support Fund

Volume 16 Number (1)

http:// jjees.hu.edu.jo/

ISSN 1995-6681

A landmark of sandstone mushrooms on tilted block of Abu Khushayba Sandstone Formation (Middle Cambrian), Wadi Araba Jordan.
Photo by Khaled Moumani

JJEES
Jordan Journal of Earth and Environmental Sciences

JJEES

JJEES (2025) 16 (1): 1-10
ISSN 1995-6681

Jordan Journal of Earth and Environmental Sciences

Examining Land Use/Land Cover Dynamics in Zarqa Governorate Major Districts: Implications for Urban and Environmental Sustainability

Shereen A. Abusmier and Salman D. Al-Kofahi*

Department of Land Management and Environment, Prince El Hassan Bin Talal Faculty of Natural Resources and Environment, The Hashemite University, P.O. Box 150459, Zarqa 13115, Jordan

Received on 13 June 2023; Accepted on 21 June 2023

Abstract

Rapid urbanization has become a serious issue, particularly in developing countries, where cities generally lack adequate planning. Nowadays, the majority of Jordan's population lives in cities. Zarqa governorate is among the most populated governorates in Jordan and is located within the boundaries of a major hydrological basin. Therefore, the objectives of this study were to explore the spatial and temporal varying dynamics in the urban area and agricultural areas over the past two decades (2001-2021) in Zarqa governorate major districts (Zarqa-Qasabah, Russeifa, and Hashemiyah) and map the changes in the land use/land cover (LULC) using remote sensing and GIS techniques. Remotely sensed surface reflectance data derived from Landsat Thematic Mapper (Landsat-5, TM) and Operational Land Imager (Landsat-8, OLI) of the study area dated 2001 and 2021 were downloaded. PCI Geomatics and GIS were used for image preparation and processing. A supervised classification technique was used to classify the images into urban, agricultural and undeveloped land categories. The LULC classification maps showed that rapid urbanization and expansion occur in all directions of existing urban areas. The urban lands increased from around 70 km² in 2001 to 109 km² in 2021, representing a change from 16% to 25% of the total study area land. The overall undeveloped area declined from 354 km² (81%) in 2001 to 317 km² (73%) by 2021 with a small change in the limited agricultural area from 14 km² (3.29%) in 2001 to 11 km² (2.63%) in 2021. Zarqa-Qasabah District showed the biggest urban area change which is 22.4 Km² (9% of the District's total area), while Russeifa showed the highest proportion (15%) of land conversion to urban land, compared to other districts. Hashemiyah occupied the largest agricultural land and the maximum agricultural land recession rate among other districts. Such changes in LULC in the study area are expected to lead to adverse impacts on the natural resources' sustainability if not monitored closely and oriented towards less fragile lands. Management of LULC changes and enhanced greenery can support groundwater recharge quality and quantity and help avoid runoff risks and other potential consequences.

Keywords: *Urban Expansion; Remote Sensing; Zarqa City; Amman Zarqa Basin*

1. Introduction

The natural lands including rangelands (Sawalhah et al., 2021), agricultural lands (Al-Kofahi et al., 2018a), their productivity (Al Qudah et al., 2021), and their intrinsic role (Arora, 2019; Abd-Elmabod et al., 2020) are continuously changing due to anthropogenic effects. There are massive fluctuations in food production at the global level (Arora 2019; Tol 2013). The world's climate is changing and threatening human life, natural resources, and ecosystems (Holechek et al., 2020; Malhi et al., 2021). These impacts have become disastrous due to the rapid increase in industrial activities, rapid population growth and urban sprawl at the expense of agricultural lands (Rimal et al., 2018). Nowadays, agricultural vulnerability due to climate change is one of the greatest challenges facing the sustainability of the global food system (Malhi et al., 2021). According to the Food and Agriculture Organization (FAO 2015), an increase of 60 percent in food production by the year 2050 is needed to satisfy the growing demand, driven by population growth. Developing countries are not an exception where they are more fragile due to climate change impacts, the reduction in food production, and limited availability of productive lands especially in arid lands (Al-Kofahi et al., 2018a).

The unplanned and uncontrolled growth of cities towards their borders might lead to multiple negative consequences on the surrounding environment (Al-Kofahi et al., 2018a; Rosni & Noor 2016; Banai & DePriest 2014), the ecological services (Li et al., 2016; Wang et al., 2017), and the overall quality of life. (Al Tarawneh 2014) reported the adverse effects of urban sprawl on agricultural land, land productivity, microclimate temperatures, pollution levels, and green spaces. (Rosni & Noor 2016) demonstrated that urbanization greatly disrupts the landscape context and has impacts on the built environment sustainability, including the environment's degradation and the community's economic and social well-being. (Tiwari et al., 2018) concluded that rapid urban development has disrupted hydrological systems, diminished groundwater recharge, lowered water supply, and raised the likelihood of natural disasters and dangers. (Fetus et al., 2020) reported that the destruction of rural residents'

* Corresponding author e-mail: salman@hu.edu.jo

livelihoods in the urban fringe area, land fragmentation, food scarcity, ecological changes, environmental pollution, biodiversity loss, and loss of wildlife habitat are some of the adverse impacts of urban expansion. Overall, unplanned and arbitrary urban development negatively impacts the total environment including plant and animal cycles (Dadashpoor & Salarian 2020), urban living conditions (Wang et al., 2017), groundwater storage, food security (Tiwari et al., 2018; Safa 2020), and population social and economic status (Rosni & Noor 2016).

Throughout the world, rapid urbanization has become a serious issue, particularly in developing countries, where cities are typically defined by the absence of adequate planning and infrastructure, excessive immigration rates, and inappropriate settlements pattern (Olajide 2010; Yiran 2020). The buffer zones among cities and natural habitats are fragmented and shrank risking the natural biodiversity and indigenous species (Al-Kofahi et al., 2019; Concepción et al., 2016; Jimenez et al., 2022). Cities are major contributors to the rising amounts of air pollution due to escalating energy use, high rates of waste disposal (Pereira 2014; Zou et al., 2016), and high total carbon emissions from construction, transportation, and industry which are key contributors to pollution (Cheng & Hu 2023).

The unstudied conversion of natural or agricultural land to urban settlements results in irreversible damage (Liu 2018) to forests and open lands and risks food security (Hu et al., 2021). (Al-Amoush et al., 2017) demonstrated that the majority of urban regions are covered with impervious concrete surfaces rather than greenery lands. Thus, the urban land is unable to soak up rain, and this result leads to extra runoff from rain over the surface. Nowadays, urbanization has frequently been reported as a main reason for flooding and poor water quality by moving a lot of sediment and pollutants during floods (Abass et al., 2020). As a result, maintaining groundwater recharge and purity becomes difficult, particularly when aquifer rechange area is the area where new developments are taking place and becomes a source of a variety of surface pollutants (Vahid 2013; Rai et al., 2015; Safa 2020).

Different land cover/land use classification approaches were used to study and monitor the advancement of urban areas towards the surrounding lands and to warn against possible environmental and health impacts (Ghurah et al., 2018; Obeidat et al., 2019; Steurer & Bayr, 2020). Change detection techniques support studying land use/land cover studies (Alqurashi & Kumar, 2013) which can help land use planners and environmentalists observe differences in a phenomenon of interest to support sustainable development while mitigating the possible adverse impacts. Remote sensing and GIS-derived land use/cover maps can be a helpful tool for sustainable land monitoring and management (Gómez al., 2016; Mashagbah, et al., 2022). The use of remote sensing, coupled with GIS, is demonstrated as an efficient effective technique for studying urban areas (Olteanu-Raimond et al., 2020; Goswami et al., 2022) with acceptable accuracy and low cost (Ahmed & Shariff 2016).

Different techniques, procedures, and data types can be employed to investigate and observe changes in cities where the specificity of the land and the availability of data sources might affect researchers' type of data or procedures used. For example, (Alqurashi et al., 2016) used Landsat images to examine the expansion of urban development and changes in land cover in Saudi Arabian cities. The generated land cover maps were classified using an object-oriented approach, Markov chain, and Cellular Automata modeling techniques. (Al-Husban 2019) studied the spatiotemporal dynamics of urban and vegetation areas in Al-Balqa Governorate, Jordan, using Landsat 5 and 8 OLI images using supervised classification and identical technique. (Al-Kofahi et al., 2018a) used Landsat 7 and 8 images along with high-resolution true color orthorectified images to run supervised classification, change detection, and accuracy assessment to investigate the major Jordanian sprawl on agricultural lands. They reported alarming recession rates of agricultural land and conversion into urban and commercial uses in major cities in Jordan.

The impacts of high recession rates in agriculture become more serious in arid and semi-arid lands due to the increasing temperatures, limited water resources, and fluctuation of precipitation rates. Jordan is a typical example where the country is classified as arid to semi-arid region with high vulnerability to climate change impacts and reduction in agricultural lands and land productivity (Al-Kofahi et al., 2018a). According to the World Food Programme (WFP), 53% of Jordanians are food insecure (Anera 2021). So, it's now considered one of the food-deficit countries and a country with limited available agricultural lands. The situation becomes alarming when food insecurity is coupled with the escalating demand for water along with growing population, inflow of refugees and increased industrial activities. Recently, Jordan has been ranked as the second poorest country in the world in terms of water scarcity, with an annual water supply of less than 100 m^3 per person (MWI 2020), which is below the threshold of the international water poverty line of 500 m^3 per year (MWI 2009). This puts more pressure on the limited land resources and calls for implementing sustainable development approaches on a country level and in all sectors (Al-Bakri et al., 2013).

Jordanian cities experienced rapid urbanization, resulting in a loss of balance between the built-up area, green spaces, and open lands (Al-Kofahi et al., 2018b). Nowadays, Jordan is considered one of the most urbanized countries where in 2020, more than 91% of the country's population lives in cities compared to 78% in 2000 (DOS 2023). As a result, urban sprawl and land use/land cover (LULC) changes have been noticed in different governorates, especially in Amman (Al-Mahasneh et al., 2012; Albattah 2015; Khawaldah 2016; Abdeljawad & Nagy 2021), Mafraq (Al Mashagbah et al., 2012; Sqour et al., 2016; Alhusban et al., 2019), Irbid (Al-Kofahi et al., 2018, Jawarneh 2021; Mashagbah, et al., (2022), and Zarqa (Al Mashagbah 2016; Othman et al., 2020; Jamhawi et al., 2020).

Zarqa governorate is currently ranked as the third most populous metropolis in Jordan (DOS 2023) where the city's population has risen quickly because of multiple factors including natural population growth, rural-urban migration,

the influx of migrant workers, Palestinian settlement, and the recent refugees' flux from Iraq and Syria due to political turbulences. Zarqa is known as a major industrial area where Al Hussein Thermal Power Plant, oil refinery, mining activities, petrochemical industries, and many other industries exist. Surface and groundwater pollution is thought to be primarily caused by these activities. Zarqa governorate land is situated within the Amman-Zarqa Basin (AZB) boundaries, the most significant hydrologic region in Jordan (Kuisi & Abdel-Fattah 2010). Zarqa City planners and officials must comprehend, monitor, and foresee future development because urban sprawl and extension have a variety of effects on the city's ecological, economic, and aesthetic components. Therefore, the objectives of this study were to explore the spatial and temporal changes in the urban area and agricultural areas during the past two decades (2001-2021) in Zarqa Governorate and map the changes in the land use/land cover to delineate the rate of urban area growth using remote sensing and GIS techniques.

2. Methodology

2.1 Study area

Zarqa Governorate is located at 32-32.15º N and 35.5-36.2º E. It connects all Jordan governorates together due to its central position among governorates. It is located around 25 kilometers northeast of Amman, the capital city of Jordan. Zarqa Governorate is the third most populated (14.3% of Jordan's total population), (DOS 2023) and the second largest governorate in terms of economic activities (Jamhawi et al., 2020). The governorate consists of six districts, the most populated districts were Zarqa-Qasabah, Russeifa, and Hashemiyah (Figure 1). These three areas occupy 89% of Zarqa governorate's population (DOS 2023). The governorate includes numerous industries and serves as the country's industrial hub and connects neighboring countries through international roads for commercial and noncommercial purposes.

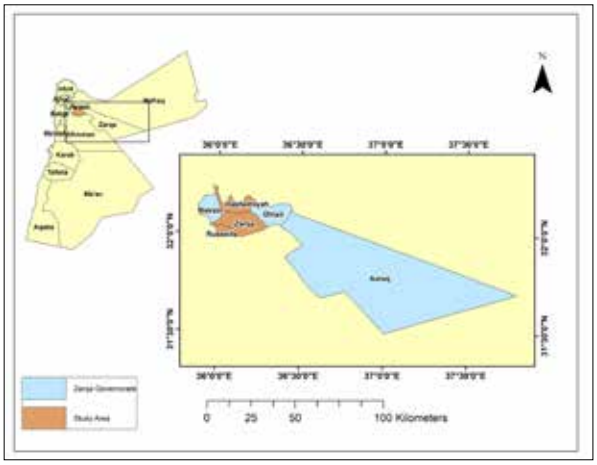

Figure 1. Study location map, Zarqa Governorate and districts, Jordan.

2.2 Images acquisition and preprocessing

Two landsat images that cover the study area were downloaded from USGS website: Landsat-8 (OLI) and Landsat-5 (TM). The images' acquired dates were 29th May, 2021 (LC08L1TP174038202105232021052901T1.tar) and 26th Jul, 2001 (LT05L1TP174038200107192018072601T1). Images preparation for classification was done using Geomatica tools. The images were clipped/subset to ensure their coverage of the study area (Figure 1). The "Dark-Pixel Substation" function was used to remove the atmospheric effects present in both images; the resulting images were exported as TIFF format images for classification using GIS.

Image Processing and Classification

The supervised image classification technique/GIS was applied (Figure 2) to both images. The maximum likelihood classification algorithm was used to classify the study area into three classes (undeveloped areas, agricultural areas, and urban areas). The classes were defined according to Al-Kofahi et al. (2018a) where urban areas represent any built-up structure for domestic, economic, or industrial uses, while agricultural lands were defined as any cultivated, planted, orchards, or forest lands. The undeveloped areas represent uncultivated, non-built-up, abandoned mountainous, or rugged lands.

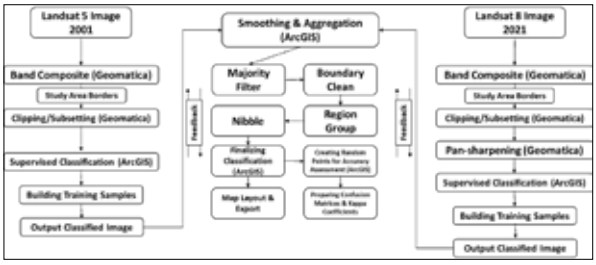

Figure 2. Workflow for image processing and classification using PCI Geomatica and ArcGIS software.

The classification training samples were built up for each of the classification categories. Training samples depended on the spatial matching of well-known identified objects for each category with the help of ArcGIS base-maps and Google Earth images and the available true color aerial images. The output classified images were then compared to the existing cover as seen in Google Earth images, true color images and GIS base-maps to visually assess the classification accuracy. The points, used to test the classification accuracy, are new points other than those used for classification training samples. The feedback process was applied when necessary (when there is a noticeable difference between the actual category and the classified category) till an acceptable result was observed. Smoothing and aggregation processes were employed including Majority Filter, Boundary Clean, Region Group, and Nibble tools (Figure 2). The areas of the classified categories were calculated based on the number of pixels in each category and pixel size and recorded separately. The output files of the classification process were used to assess the accuracy assessment.

2.3 Accuracy Assessment

The classification accuracy was determined by comparing the classified images with another confident data source that was thought to be accurate, such as field-collected ground truth point, and high-resolution and historical Google Earth images. A randomly chosen ground truth points were gathered. Following Jensen's (2005) rule of thumb, 210 points were utilized to evaluate the classification accuracy. A total of 70 points per class were used. The results were used to build a confusion matrix for each classified

image where accuracy assessment components, included the Kappa coefficient, overall accuracy, and user's and producer's accuracy.

3. Results and Discussion

3.1 Accuracy Assessment

A confusion matrix for each classified image was developed, overall classification accuracy of the classified images was between 89-92%, while users' accuracy was varying from 79% to 96%. The producer's accuracy ranged from 83-93% (Table 1). The lowest user's and producer's accuracies were in the 2001 image (Landsat 5 TM) classified image due to confusion between the undeveloped lands and each of agricultural and urban areas. Landsat 5 TM images were expected to yield lower classification accuracy compared to Landsat 8 OLI images because of the limited number of spectral bands in TM, which leads to spectral mixing and, thus, some confusion among classes. These findings were also reported by Poursanidis et al. (2015) who compared the performance of both TM and OLI images in classification of urban and peri-urban land cover. However, using TM images given the classification accuracy limitation is tolerable due to the unavailability freely downloadable historical images other than TM images serving the purpose of this study.

Table 1. Confusion matrix for the land use classification results of the study area images for the period 2001 and 2021.

Reference Data						
2001 Image						
Classified data	Class	Undeveloped	Agriculture	Urban	Totals	Users' accuracy
	Undeveloped Agriculture Urban area	68	9	9	86	0.79
		2	58	0	60	0.96
		0	3	61	64	0.95
Totals		70	70	70	210	
Producers' accuracy		0.97	0.83	0.87		
Overall accuracy						0.89
2021 Image						
Classified data	Undeveloped Agriculture Urban	65	2	2	30	0.93
		2	63	2	29	0.94
		2	5	65	31	0.90
Totals		70	70	70	210	
Producers' accuracy		0.93	0.90	0.93		
Overall accuracy						0.92

3.2 Spatio-temporal urban and undeveloped lands' change

The LULC classification maps showed that rapid urbanization had taken place over the last two decades in all directions mainly towards southwestern parts of the study area (Figure 3). It can be observed that urban and built environment had increased from around 70 km² (16%) in 2001 to 109 km² (25%) of total study area land by 2021, while undeveloped area was declined from 354 km² (81%) in 2001 to 317 km² (73%) by 2021 (Figure 4). Zarqa, as the second-largest industrial city in Jordan next to the capital Amman (Yousef 2012; Jamhawi et al., 2020) has experienced increased urbanization causing a change in the city's LULC. The newly constructed areas for residential or commercial purposes are increasing, which is expected to lead to negative impacts on environmental services. The special location of Zarqa governorate among other governorates, the international road network, industrial activities, the increase in population, and the influx of refugees and migration of people from surrounding countries of political conflicts specifically the Syrian crisis (Sawalhah et al., 2021; Al-Kofahi et al., 2018a) are the main potential causes of these changes in a metropolitan area. The Department of Statistics in Jordan reported that over the last two decades, Zarqa governorate's population increased from 0.8 million (DOS 2001) to 1.6 million per capita (DOS 2023).

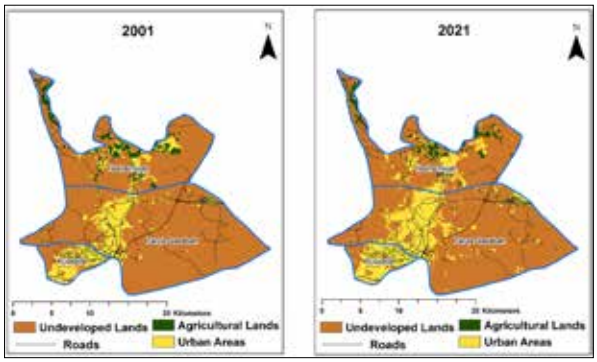

Figure 3. The spatial distribution of different LULC categories of Zarqa Governorate major districts (2001-2021)

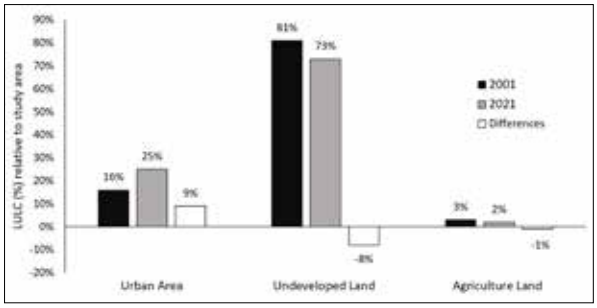

Figure 4. The relative proportion of LULC changes of Zarqa governorate's study area (2001-2021)

Among the driving factors that made Zarqa Governorate a population-attracting center is the high possibility of people recruitment. The Ministry of Planning and International Cooperation reported the presence of 23856 economical facilities in Zarqa Governorate that represent around 15% of all economic facilities in the country, therefore this governorate is considered as Jordan's industrial hub. Zarqa Governorate is a home for 52% of the country's industries, including plastic, rubber, leather, chemical, food, agricultural, information technology, packaging, and paper cardboard industries (Ministry of Planning 2017). The availability of such industries leads to adverse pollution impacts on surrounding environment (Yousef, 2012) besides the expected anthropogenic sources of pollution in the Governorate. The major industrial and commercial activities are Petroleum Refinery Company, Al-Hussein Thermal Station, iron industries, animal farms, quarries, etc. Nowadays, Zarqa Governorate, especially Hashemiyah District is considered a pollution hotspot (MOI 2022). However, the limited freshwater resources (Al-Qinna et al., 2011; Hadadin 2015), low and irregular rainfall, high evaporation rate (Al-Kilani et al., 2021), and over pumping of groundwater (Al-Qinna et al., 2011; Bajjali et al., 2017) further complicate the environmental quality sustainability in this governorate.

The whole studied area showed changes in LULC categories from low to high with respect to other categories in the studied districts. The LULC maps of Hashemiyah District, for example, showed that new urban developments are directed towards the Eastern part of the district, where numerous new avenues were observed in the direction of urban growth. These avenues are connecting the Hashemiyah District with the Hashemite University, Zarqa-Mafraq highway and Zarqa Free Zone. The urban growth is usually driven by accessibility to transportation and road networks which is widely recognized as one of the key factors influencing urban architecture (Kasraian et al., 2019; Pratama et al., 2022). Similarly, Rai and Saha (2015) reported that changes in land use around cities follow highways. This type of expansion is known as edge expansion where the new developments go radially from the urban edge outward (Forman 1995). Therefore, a sizable residential urban expansion and newly established bodies such as Steel factories and the National Electricity Company followed the recently constructed avenues. The proximity of Zarqa-Mafraq highway road, low land prices and tribal zone lands in that direction contributed to such a change. This also contributed to outlying expansion to the east of Hashemiyah districts where the Army Condominium Complexes were established western the Hashemite University and Zarqa-Mafraq highway.

The Hashemiyah District witnessed extension towards the Western side of the District. The infilling expansion was also observed and prevailed in the center of Hashemiyah Village. New outlaying developments and edge expansion in the Western parts of the district towards Jerash Governorate were noticed along with northward and eastward extensions to the Zarqa River and the southward movement to Masoum area (the boundary of the Zarqa-Qasabah District). Migration from the villages to the city center for economic and job opportunities, together with the City's natural population growth, has caused a fast increase in residential and commercial areas as well as the development of essential infrastructural networks. Similar reasons were reported to explain the urban expansion in Irbid City (Mashagbah et al., 2022) and Amman (Al-Kofahi et al., 2018a), Jordan. The settlement of Palestinian refugees in the Sukhnah Refugee Camp, the proximity of roads connecting the Governorate with Mafraq, Jerash, and Zarqa-Qasabah District, tribal zone and the lower lands prices in these areas compared with that within and surrounding the city center are possible causes for these multi directional expansion.

Zarqa-Qasabah is the most populated district of the governorate and represented around 50% of the governorate population with a population density of around 3000 capita/km^2 (MOI 2022). Younes et al. (2013) stated that the city's expansion has accelerated in recent years because of a significant change in population, commercial centers, and industrial activities. Al-Mashaqbeh et al. (2014) reported that the development of public infrastructure, such as roads, water facilities, housing, and industrial and commercial activities are among the elements leading to the emergence of urbanized regions. The presence of Hashemite University, Zarqa University, and other colleges and educational centers also contribute to the urban expansion of this district towards the east direction of the city. The observable urban change in Zarqa-Qasabah was concentric, infilling around the city center. A similar type of expansion was observed in other Jordanian cities such as Irbid and Amman (Al-Kofahi et al., 2018a). Edge-type expansion is observed in the eastern portions of Zarqa where various military camps are spread and the establishment of King Abdullah bin Abdulaziz City as a new residential development with an area of 250 hectares, benefiting from multiple regional highways (Amman-Zarqa Highway, Zarqa-Mafraq Road, and Zarqa Road), connecting the Kingdom to Saudi Arabia, Iraqi, and Syrian borders and other mega industrial and governmental bodies such as Al-Musfah and Zarqa Free Zones. However, outlying types of sprawls exist in several locations to the eastern portion of the district such as Princess Salma Suburb, New Zarqa Governmental Hospital, Princess Iman Residence Suburb, and Military Centers. These findings are consistent with Al Mashagbah (2016), who reported that the development of the urban area is a result of the city's infrastructure upgrades and population growth. Thus, municipalities and city planners, to a certain extent, can control or govern the new urban developments by establishment of governmental bodies or mega projects towards allocating more green spaces that would yield less environmental or ecological impacts.

The Russeifa District is 15 kilometers northeast of Amman. The District stretches from the western boundaries of the capital city, Amman, to the eastern boundaries of Zarqa-Qasabah District, and from the southern boundaries of Amman Zarqa highway to the northern boundaries of Zarqa-Qasabah District. This district serves as a transit point between the capital city, Amman, and Mafraq and northern cities. According to the DOS data, Russeifa population was duplicated in the last two decades (DOS 2004; DOS 2023). The district witnessed rapid natural population growth with

a recorded population density of 6792 per capita/km^2 (MOI 2022). An infilling type of sprawl in the center of the district is observed with remarkable expansion to the west direction towards Amman, where a newly developed residential area called Al-Karamah neighborhood was established.

3.3 Spatio-Temporal Changes on Agricultural Lands

The LULC maps showed that the identified agricultural areas in 2001 and 2021 are concentrated around the north border of the Hashemiyah District. The temporal changes in the agricultural land proportion (-1%) between the studied years were very low in the study area, while the spatial changes in the agricultural areas' locations are observable (Figure 3). Considerable portions of the identified agricultural lands were on both sides of the Zarqa River (not identified on the maps as no flow exists at the images' dates), as well as in the nearby regions around the As-Samra Wastewater Treatment Plant (WWTP). As-Samra WWTP is located at the northeastern parts of the Hashemiyah Village. Zarqa River floodplain is irrigated using the wastewater from WWTP (Al-Bakri et al., 2013). However, the study's findings revealed that the overall agricultural lands of the study area slightly declined from 14.4 km^2 (3.29%) in 2001 to 11.5 km^2 (2.63%) in 2021 (Figure 4). The possible reasons behind the spatial and temporal changes in agricultural land are the fluctuation in rainfall amount and distribution in the last two decades. Additionally, the projects of upgrading As-Samra WWTP, meant to handle the rising volumes of wastewater from the growing population in the source governorates (Amman and Zarqa) (Al Omari et al., 2013) during the study period, exploited the surrounding lands of WWTP where some of them were agricultural lands in 2001. The expansion plans for As-Samra WWTP have resulted in a reduction of agricultural farms in the southeast and southwest direction of the WWTP, with observable changes in land use in these spots from agricultural to urban areas. The project of As-Samra upgrades is expected to continue to 2025 and may possibly lead to further reduction in the agricultural lands there until project completion (SPC 2012). The northeastern area of As-Samra WWTP showed large agricultural areas in 2021 that were not observed in 2001, while there was a kind of shift or change in exploitation of different lands depending on the availability of lands and water sources. The field visits of these farms upstream area cultivated with annual and forage crops and irrigated from wells.

3.4 Spatio-Temporal LULC Changes among Districts

The three districts showed major changes in the urban areas. Zarqa-Qasabah District showed a fundamental change in terms of urbanized area where the overall urban area increased 22.4 Km^2 (9% of the District's total area) in 20 years; this represents a net annual increase in the urban area of around 1.2 Km^2 and an equivalent reduction in the undeveloped lands (Figure 5). Such new urban areas in Zarqa-Qasabah District, compared to the other districts, is due to its industrial position among other districts and cities. It has a major role in the country's industrial sector (Yousef 2012; Jamhawi et al., 2020; Ministry of Planning 2017). The urban area of the Hashemiyah District, similarly, showed an increment of 6.45 Km^2 (5% of district's total area) and reduction in the overall district agricultural area of around 2 Km^2. The major recession area in agricultural land among the studied districts was observed for the Hashemiyah District. This is because it originally had the largest overall agricultural area due to the presence of WWTP within the district borders. The presence of WWTP contributed to the development of agricultural lands in Hashemiyah (Al-Bakri et al., 2013). Russeifa District showed the smallest increment in urban area, relative to other districts while representing the largest proportion (15%). It is also relative to the district total area which is the smallest size district of the three. It can be observed that the net agricultural area reduction in Zarqa-Qasabah and Russeifa Districts was negligible (≤0.5 Km^2).

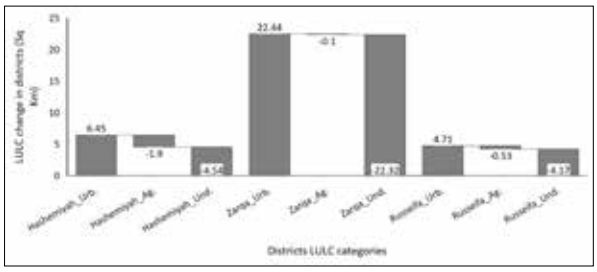

Figure 5. LULC dynamics (Km^2) in different Zarqa Governorate districts between 2001 and 2021.

4. Implications

Such large spatial changes and new urban developments in the three districts are expected to lead to adverse impacts, attained from the needed infrastructure, mobility, waste disposal, air pollution and water resources. One of the major concerns in this governorate is the management of sustainable water resources. It is important to monitor the LULC changes as they affect groundwater recharge and surface runoff (Owuor et al., 2016). Surface runoff, resulting from changes in LULC, were raised by several researchers (Eshtawi et al., 2016; Al-Amoush et al., 2017). In urban catchments, the change in LULC, when combined with climate change, may increase the danger of flooding (Shammout et al., 2021). Alananzah (2022) warned from the expected and observed higher frequency of sudden surface runoff events in Russifa District and recommended removing built-up structures from stream banks to avoid the possible risk of flooding on these structures. Alananzah study suggested installing drainage networks for running water in main and secondary roads. Furthermore, urban runoff is widely regarded as a major transporter of contaminants from and to urban environments and consequently represents a significant contributor to the deterioration of the quality of urban water resources (Björklund et al., 2018; Astuti et al., 2019). These impacts are not restricted to Russifa as it is the District with the largest proportion of land conversion to urban area but also Zarqa-Qasabah District that showed the largest area of changed to urban area.

The growing industry, rapid urbanization, regular population growth, and the rise of civilization are rapidly driving today's freshwater demand. As a result, wastewater is increasingly being used to irrigate agricultural land to attain food security (Mizyed 2013), especially in arid and semi-arid countries where freshwater resources are scarce. Jordan is a country that suffers from scarce water resources, frequent droughts episodes, uneven rainfall distribution, a high rate

of evaporation, and a decline in groundwater recharge (Hadadin 2015). As a result, treated wastewater is used as an alternative and an unconventional source of water (Alfarra et al., 2011), and Jordan supports recharging of ground water (Bajjali et al., 2017). Wastewater consists of mainly municipal wastewater, industrial effluents, and storm water runoff. It can transport dangerous substances which affect crops, soil, and groundwater quality. It also contains some pathogens that can harm people (Ashraf et al., 2018). According to (Owuor et al., 2016), improper planning of urban growth will accelerate the runoff which will affect surface water bodies and groundwater quality. Studies on runoff quality improvements are needed to help policy makers implement strategies and plans that could lower pollutant levels in urban runoff. The involvement of effective water harvesting plans potentially will reduce adverse effects on recipient water bodies and better water quality to enrich groundwater.

5. Conclusion

In recent decades, most Jordanian cities have witnessed substantial urban growth. Between 2001 and 2021, the urbanization rate in the Zarqa Governorate increased quickly. The study area witnessed significant changes and advancements in its transportation system, roads, residential complexes, industrial activities, and numerous educational institutions. These are among the factors that are observed to drive the expansion of urban areas. These changes in the natural environment have exacerbated problems associated with natural resources sustainability such as flash floods, environmental pollution, loss of agricultural lands, land degradation and desertification. The study area showed urban advancement in all districts with recession of the limited agricultural lands in Hashemiyah area that depend on wells and treated wastewater. The urban growth is anticipated to continue, which might put further stress on the surrounding environment. Satellite images, remote sensing, GIS, and other software can serve to monitor and direct urban development frequently. Additionally, such tools could help show the future trajectory of urbanization and other land uses which are expected to aid in the development of sustainable environmental policies through cooperative work of decision-makers, environmentalists, and urban planners.

References

Abass, K., Buor, D., Afriyie, K., Dumedah, G., Segbefi, A. Y., Guodaar, L., ... & Gyasi, R. M. (2020). Urban sprawl and green space depletion: Implications for flood incidence in Kumasi, Ghana. International Journal of Disaster Risk Reduction, 51, 101915. https://doi.org/10.1016/j.ijdrr.2020.101915.

Abdeljawad, N., & Nagy, I. (2021). Urban Environmental Challenges and Management Facing Amman Growing City. Review of International Geographical Education Online, 11(5). https://doi.org/10.48047/rigeo.11.05.192

Abd-Elmabod, S. K., Muñoz-Rojas, M., Jordán, A., Anaya-Romero, M., Phillips, J. D., Jones, L., ... & de la Rosa, D. (2020). Climate change impacts on agricultural suitability and yield reduction in a Mediterranean region. Geoderma, 374, 114453. https://doi.org/10.1016/j.geoderma.2020.114453

Ahmed, G. B., & Shariff, A. R. M. (2016). Predicting the Vegetation Expansion in Selangor, Malaysia using the NDVI and Cellular Automata Markov Chain. Proceedings of the World Congress on Civil, Structural, and Environmental Engineering. Prague, Czech Republic – March 30 – 31, Paper No. ICGRE 115. https://doi.org/10.11159/icgre16.115

Al Mashagbah, A. F. (2016). The use of GIS, remote sensing and Shannon's entropy statistical techniques to analyze and monitor the spatial and temporal patterns of urbanization and sprawl in Zarqa City, Jordan. Journal of Geographic Information System, 8(2), 293-300. https://doi.org/10.4236/jgis.2016.82025

Al Mashagbah, A., Al-Adamat, R., & Al-Amoush, H. (2012). GIS and remote sensing to investigate urban growth in Mafraq City/Jordan between 1987 and 2010. https://doi.org/10.4236/jgis.2012.44043

Al Qudah, A., Rusan, M. J., Al-Qinna, M. I., & Abdulla, F. A. (2021). Climate change vulnerability assessment for selected agricultural responses at Yarmouk River Basin Area, Jordan. Mitigation and Adaptation Strategies for Global Change, 26, 1-21. https://doi.org/10.1007/s11027-021-09944-7

Al Tarawneh, W. M. (2014). Urban Sprawl on Agricultural Land (Literature Survey of Causes, Effects, Relationship with Land Use Planning and Environment): A Case Study from Jordan (Shihan Municipality Areas). Journal of Environment and Earth Science, 4(20), 97-124.

Al-Amoush, H., Al-Shabeeb, A., Al-Adamat, R., Al-Fugara, A., Al Ayyash,S, Shdeifat, A., Al-Tarazi, E. & Abu Rajab, R. (2017). The Use of GIS Techniques and Geophysical Investigation for Flood Management at Wadi Al-Mafraq Catchment Area. Jordan Journal of Earth and Environmental Sciences, 8(2), 97-103.

Alananzeh, A. (2022). Assessment of the Geomorphological Effects of Human Activity in Russeifa District, Jordan. Dirasat: Human and Social Sciences, 49(4), 443-458. https://doi.org/10.35516/hum.v49i4.2099.

Al-Bakri, J. T., Duqqah, M., & Brewer, T. (2013). Application of remote sensing and GIS for modeling and assessment of land use/cover change in Amman/Jordan. Journal of Geographic Information System. https://doi.org/10.4236/jgis.2013.55048.

Albattah, M. M. (2015). Remote Sensing and Topographic Information in a GIS environment for Urban Growth and Change: Case Study Amman the Capital of Jordan. International Journal for Innovation Education and Research, 3, 126-142.

Alfarra, A., Kemp-Benedict, E., Hötzl, H., Sader, N., & Sonneveld, B. (2011). A framework for wastewater reuse in Jordan: utilizing a modified wastewater reuse index. Water Resources Management, 25, 1153-1167.

Alhusban, A. A., Alhusban, S. A., & Al-Betawi, Y. N. (2019). Assessing the impact of urban Syrian refugees on the urban fabric of Al Mafraq city architecturally and socially. International Journal of Disaster Resilience in the Built Environment, 10(2/3), 99-129. https://doi.org/10.1108/IJDRBE-09-2018-0039

Al-Husban, Y. (2019). Urban expansion and shrinkage of vegetation cover in Al-Balqa Governorate, the Hashemite Kingdom of Jordan. Environmental Earth Sciences, 78, 1-10. https://doi.org/10.1007/s12665-019-8635-z

Al-Kilani, M. R., Rahbeh, M., Al-Bakri, J., Tadesse, T., & Knutson, C. (2021). Evaluation of remotely sensed precipitation estimates from the NASA POWER project for drought detection over Jordan. Earth Systems and Environment, 5(3), 561-573. https://doi.org/10.1007/s41748-021-00245-2

Al-Kofahi, S. D., Gharaibeh, A. A., Bsoul, E. Y., Othman, Y. A., & St. Hilaire, R. (2019). Investigating domestic gardens' densities, spatial distribution and types among city districts. Urban Ecosystems, 22, 567-581.https://doi.org/10.1007/s11252-019-0833-7

Al-Kofahi, S. D., Hammouri, N., Sawalhah, M. N., Al-Hammouri, A. A., & Aukour, F. J. (2018a). Assessment of the urban sprawl on agriculture lands of two major municipalities in Jordan using supervised classification techniques. Arabian Journal of Geosciences 11, 1-12. https://doi.org/10.1007/s12517-018-3398-5

Al-Kofahi, S. D., Jamhawi, M. M. & Hajahjah, Z.A. (2018b) Investigating the current status of geospatial data and urban growth indicators in Jordan and Irbid municipality: implications for urban and environmental planning. Environment,

Development and Sustainability 20, 1067–1083. https://doi.org/10.1007/s10668-017-9923-y

AL-Mahasneh, E., Al-Habees, M. A., & Al-Khaddam, H. K. (2012). Urban population growth trends in Jordan (2014-2044). International Journal of Scientific and Engineering Research, 3(10), 1-25.

Al-Mashaqbeh, O., Jiries, A., & El-HajAli, Z. (2014). Storm-water run-off quality generated from an urban and a rural area in the Amman-zarqa basin. Water Pollut, 12, 379-390.

Al-Qinna, M. I., Hammouri, N. A., Obeidat, M. M., & Ahmad, F. Y. (2011). Drought analysis in Jordan under current and future climates. Climatic Change 106(3), 421-440. https://doi.org/10.1007/s10584-010-9954-y

Alqurashi, A. F., Kumar, L., & Sinha, P. (2016). Urban land cover change modelling using time-series satellite images: A case study of urban growth in five cities of Saudi Arabia. Remote Sensing, 8(10), 838. https://doi.org/10.3390/rs8100838

Alqurashi, A., & Kumar, L. (2013). Investigating the use of remote sensing and GIS techniques to detect land use and land cover change: A review. Advances in Remote Sensing. https://doi.org/10.4236/ars.2013.22022

Ashraf, M., Safdar, M. E., Shahzad, S. M., Aziz, A., Piracaha, M. A., Suleman, M., & Ahmad, M. B. (2018). Challenges and opportunities for using wastewater in agriculture: a review. Journal of Applied Agriculture and Biotechnology, 2(2), 1-20.

Anera (2021). Jordan situation report. Available at: https://www.anera.org/wp-content/uploads/2021/10/2021.10.13-Jordan-Situation-Report.pdf . Accessed in April 14, 2023.

Arora, N. K. (2019). Impact of climate change on agriculture production and its sustainable solutions. Environmental Sustainability, 2(2), 95-96. https://doi.org/10.1007/s42398-019-00078-w

Astuti, I. S., Sahoo, K., Milewski, A., & Mishra, D. R. (2019). Impact of land use land cover (LULC) change on surface runoff in an increasingly urbanized tropical watershed. Water Resources Management 33, 4087-4103.https://doi.org/10.1007/s11269-019- 02320-w

Bajjali, W., Al-Hadidi, K., & Ismail, M. M. (2017). Water quality and geochemistry evaluation of groundwater upstream and downstream of the Khirbet Al-Samra wastewater treatment plant/Jordan. Applied Water Science 7, 53-69. https://doi.org/10.1007/s13201-014-0263-x

Banai, R., & DePriest, T. (2014). Urban sprawl: Definitions, data, methods of measurement, and environmental consequences. Journal of Sustainability Education, 7(2), 1-15.

Björklund, K., Bondelind, M., Karlsson, A., Karlsson, D., & Sokolova, E. (2018). Hydrodynamic modelling of the influence of stormwater and combined sewer overflows on receiving water quality: Benzo (a) pyrene and copper risks to recreational water. Journal of environmental management, 207, 32-42. https://doi.org/10.1016/j.jenvman.2017.11.014

Cheng, Z., & Hu, X. (2023). The effects of urbanization and urban sprawl on CO2 emissions in China. Environment, Development and Sustainability, 25(2), 1792-1808. https://doi.org/10.1007/s10668-022-02123-x

Concepción, E. D., Obrist, M. K., Moretti, M., Altermatt, F., Baur, B., & Nobis, M. P. (2016). Impacts of urban sprawl on species richness of plants, butterflies, gastropods and birds: not only built-up area matters. Urban Ecosystems, 19, 225-242. https://doi.org /10.1007/s11252-015-0474-4

Dadashpoor, H., & Salarian, F. (2020). Urban sprawl on natural lands: Analyzing and predicting the trend of land use changes and sprawl in Mazandaran city region, Iran. Environment, Development and Sustainability, 22, 593-614.https://doi.org/10.1007/s10668-018-0211-2

DOS (2001). Department of statistics. Hashemite Kingdom of Jordan. Population Density and Area by Governorate and region, 2001. Available at: http://www.dos.gov.jo/dos_home_e/main/jorfig/1/jor_f_e.htm. Accessed May 24, 2023

DOS (2004). Department of statistics. Hashemite Kingdom of Jordan. Population Estimates for The End of 2004. Available at: http://www.dos.gov.jo/dos_home_e/main/population/census2004/group3/table_31.pdf. Accessed on May 19, 2023

DOS (2023). Department of statistics. Hashemite Kingdom of Jordan. Population Estimates for The End of 2022. Available at:

https://dosweb.dos.gov.jo/DataBank/Population/Population_Estimares/PopulationEstimates.pdf. Accessed on April 10, 2023.

Eshtawi, T., Evers, M., & Tischbein, B. (2016). Quantifying the impact of urban area expansion on groundwater recharge and surface runoff. Hydrological Sciences Journal 61(5), 826-843. http://doi.org/10.1080/02626667.2014.1000916

FAO (Food and Agriculture Organization), Climate change and food security: risks and responses. 2015, FAO Rome, Italy. p. 110 p. https://www.fao.org/3/i5188e/I5188E.pdf. Accessed on April 10, 2023.

Festus, I. A., Omoboye, I. F., & Andrew, O. B. (2020). Urban sprawl: environmental consequence of rapid urban expansion. Malaysian Journal of Social Sciences and Humanities 5(6), 110-118. https://doi.org/10.47405/mjssh.v5i6.411

Forman, R. (1995) Land mosaics: the ecology of landscapes and regions. Cambridge: Cambridge University Press.

Ghurah, M. A., Kamarudin, M. K. A., Wahab, N. A., Umar, R., Wan, N. N., Juahir, H., ... & Hidayat, Y. (2018). Temporal change detection of land use/land cover using GIS and remote sensing techniques in South Ghor Regions, Al-Karak, Jordan. Journal of Fundamental and Applied Sciences, 10(1S), 95-111. Available online at http://www.jfas.info

Gómez, C., White, J. C., & Wulder, M. A. (2016). Optical remotely sensed time series data for land cover classification: A review. ISPRS Journal of photogrammetry and Remote Sensing, 116, 55-72. https://doi.org/10.1016/j.isprsjprs.2016.03.008

Goswami, A., Sharma, D., Mathuku, H., Gangadharan, S. M. P., Yadav, C. S., Sahu, S. K., ... & Imran, H. (2022). Change detection in remote sensing image data comparing algebraic and machine learning methods. Electronics 11(3), 431. https://doi.org/10.3390/electronics11030431.

Hadadin, N. (2015). Dams in Jordan current and future perspective. Canadian Journal of Pure and Applied Sciences 9(1), 3279-3290.

Holechek, J. L., Geli, H. M., Cibils, A. F., & Sawalhah, M. N. (2020). Climate change, rangelands, and sustainability of ranching in the Western United States. Sustainability 12(12), 4942. https://doi.org/10.3390/su12124942

Hu, X., Huang, B., Verones, F., Cavalett, O., & Cherubini, F. (2021). Overview of recent land-cover changes in biodiversity hotspots. Frontiers in Ecology and the Environment 19(2), 91-97.

Jamhawi, M., Alshawabkeh, R., & Alobaidat, E. (2020). Spatial Modelling of Transformation of Public Open Spaces in Zarqa, Jordan. Int. J. Sustain. Dev. Plan 15, 685-703. https://doi.org/10.18280/ijsdp.150511

Jawarneh, R. N. (2021). Modeling past, present, and future urban growth impacts on primary agricultural land in Greater Irbid Municipality, Jordan using SLEUTH (1972–2050). ISPRS International Journal of Geo-Information, 10(4), 212. https://doi.org/10.3390/ijgi10040212

Jensen, J. R. (2005). Introductory Digital Image Processing: a Remote Sensing Perspective, third ed. Prentice-Hall, Upper Saddle River, NJ

Jimenez, M. F., Pejchar, L., Reed, S. E., & McHale, M. R. (2022). The efficacy of urban habitat enhancement programs for conserving native plants and human-sensitive animals. Landscape and Urban Planning, 220, 104356. https://

doi.org/10.1016/j.landurbplan.2022.104356

Kasraian, D., Maat, K., & van Wee, B. (2019). The impact of urban proximity, transport accessibility and policy on urban growth: A longitudinal analysis over five decades. Environment and Planning B: Urban Analytics and City Science 46(6), 1000-1017. https://doi.org/10.1177/2399808317740355

Khawaldah, H. A. (2016). A prediction of future land use/land cover in Amman area using GIS-based Markov Model and remote sensing. Journal of Geographic Information System, 8(3), 412-427. https://doi.org/10.4236/jgis.2016.83035

Kuisi, M. A., & Abdel-Fattah, A. (2010). Groundwater vulnerability to selenium in semi-arid environments: Amman Zarqa Basin, Jordan. Environmental geochemistry and health, 32, 107-128. 2:107–128.https://doi.org/10.1007/s10653-009-9269-y

Li, B., Chen, D., Wu, S., Zhou, S., Wang, T., & Chen, H. (2016). Spatio-temporal assessment of urbanization impacts on ecosystem services: Case study of Nanjing City, China. Ecological Indicators, 71, 416-427. https://doi.org/10.1016/j.ecolind.2016.07.017

Liu, Y. (2018). Introduction to land use and rural sustainability in China. Land Use Policy, 74, 1-4. https://doi.org/10.1016/j.landusepol.2018.01.032

Malhi, G. S., Kaur, M., & Kaushik, P. (2021). Impact of climate change on agriculture and its mitigation strategies: A review. Sustainability, 13(3), 1318. https://doi.org/10.3390/su13031318

Mashagbah, A. F., Ibrahim, M., Al-Fugara, A., & Alzaben, H. (2022). Spatial and temporal modeling of the urban growth and land cover changes using remote sensing, spatial indexes and GIS techniques in Irbid city, Jordan. Applied Ecology and Environmental Research, 20(3), 2769-2781. http://doi.org/10.15666/aeer/2003_27692781.

Ministry of Interior (MOI) (2022). Governorates and sectors-Zarqa Governorate. Available at: moi.gov.jo/EN/ListDetails/Governorates_and_Sectors/57/6. Accessed on June 9, 2023.

Ministry of Planning (2017). Zarqa Governorate's Development program 2017-2019. Available at: https://shorturl.at/JTY79. Accessed on May 24, 2023.

Mizyed, N. R. (2013). Challenges to treated wastewater reuse in arid and semi-arid areas. Environmental Science & Policy, 25, 186-195. https://doi.org/10.1016/j.envsci.2012.10.016

MWI (2009) Ministry of Water and Irrigation, Jordan. "Water for Life: Jordan's Water Strategy 2008-2022," Amman, Jordan. Available at: https://jordankmportal.com/resources/water-for-life-jordans-water-strategy-2008-2022. Accessed on April 14, 2023

MWI (2020) Ministry of Water and Irrigation, Jordan. Jordan Water Sector Facts and Figures. Ministry of Water and Irrigation, Amman, Jordan. http://www.mwi.gov.jo/ebv4.0/root_storage/ar/eb_list_page/facts_and_figures_english_2020.pdf. Accessed on April 10, 2023.

Noor, N. M., & Rosni, N. A. (2013). Determination of spatial factors in measuring urban sprawl in Kuantan using remote sensing and GIS. Procedia-Social and Behavioral Sciences, 85, 502-512. https://doi.org/10.1016/j.sbspro.2013.08.379.

Obeidat, M., Awawdeh, M., & Lababneh, A. (2019). Assessment of land use/land cover change and its environmental impacts using remote sensing and GIS techniques, Yarmouk River Basin, north Jordan. Arabian Journal of Geosciences, 12, 1-15. https://doi.org/10.1007/s12517-019-4905-z

Olajide, O. (2010). Urban poverty and environmental conditions in informal settlements of Ajegunle. Proceeding of the 28th International Conference on Urban Planning and Regional Development in the Information Society, Lagos Nigeria.18-20 May 2010. Available at: https://corp.at/archive/CORP2010_148.pdf. Accessed on April 18, 2023.

Olteanu-Raimond, A. M., See, L., Schultz, M., Foody, G., Riffler, M., Gasber, T., ... & Gombert, M. (2020). Use of automated change detection and VGI sources for identifying and validating urban land use change. Remote Sensing, 12(7), 1186. https://doi.org/10.3390/rs12071186

Othman, H. A. S., & Alshboul, A. A. (2020). The role of urban morphology on outdoor thermal comfort: The case of Al-Sharq City–Az Zarqa. Urban Climate, 34, 100706. https://doi.org/10.1016/j.uclim.2020.100706

Owuor, S. O., Butterbach-Bahl, K., Guzha, A. C., Rufino, M. C., Pelster, D. E., Díaz-Pinés, E., & Breuer, L. (2016). Groundwater recharge rates and surface runoff response to land use and land cover changes in semi-arid environments. Ecological Processes, 5(1), 1-21.

Pereira, P. (2014). Public perception of environmental, social and economic impacts of urban sprawl in Vilnius. Socialinių Mokslų Studijos, 6(2).

Poursanidis, D., Chrysoulakis, N., Mitrakaa, Z. (2015). Landsat 8 vs. Landsat 5: A comparison based on urban and peri-urban land cover mapping. International Journal of Applied Earth Observation and Geoinformation, 35, 259-269.

Pratama, A. P., Yudhistira, M. H., & Koomen, E. (2022). Highway expansion and urban sprawl in the Jakarta Metropolitan Area. Land Use Policy, 112, 105856. https://doi.org/10.1016/j.landusepol.2021.105856

Rai, S. C., & Saha, A. K. (2015). Impact of urban sprawl on groundwater quality: a case study of Faridabad city, National Capital Region of Delhi. Arabian Journal of Geosciences, 8, 8039-8045.

Rimal, B., Zhang, L., Stork, N., Sloan, S., & Rijal, S. (2018). Urban expansion occurred at the expense of agricultural lands in the Tarai region of Nepal from 1989 to 2016. Sustainability, 10(5), 1341. https://doi.org/10.3390/su10051341

Rosni, N. A., & Noor, N. M. (2016). A review of literature on urban sprawl: Assessment of factors and causes. Journal of Architecture, Planning and Construction Management, 6(1).

Safa, G., Najiba, C., El Houda, B. N., Monji, H., Soumaya, A., & Kamel, Z. (2020). Assessment of urban groundwater vulnerability in arid areas: Case of Sidi Bouzid aquifer (central Tunisia). Journal of African Earth Sciences, 168, 103849. https://doi.org/10.1016/j.jafrearsci.2020.103849

Sawalhah, M. N., Othman, Y. A., Abu Yahya, A., Al-Kofahi, S. D., Al-Lataifeh, F. A., & Cibils, A. F. (2021). Evaluating the influence of COVID-19 pandemic lockdown on Jordan Badia rangelands. Arid Land Research and Management, 35(4), 483-495. https://doi.org/10.1080/15324982.2021.1921071

Shammout, M. A. W., Shatanawi, K., Al-Bakri, J., & Abualhaija, M. M. (2021). Impact of Land Use/Cover Changes on the Flow of the Zarqa River in Jordan. Journal of Ecological Engineering, 22(10), 40-50.https://doi.org/10.12911/22998993/142184

SPC, 2012. Samra wastewater treatment plant company. Environmental & social impact study for the expansion of As-Samra wastewater treatment plant. Available at: http://www.mca-jordan.gov.jo/SystemFiles/Pages/file_635053196963205703.pdf. Accessed on May 14, 2023

Sqour, S. M., Rjoub, A., & Tarrad, M. (2016). Development and trends of urban growth in Mafraq City, Jordan. Architecture Research, 6(5), 116-122.

Steurer, M., & Bayr, C. (2020). Measuring urban sprawl using land use data. Land Use Policy, 97, 104799. https://doi.org/10.1016/j.landusepol.2020.104799

Tiwari, P. C., Tiwari, A., & Joshi, B. (2018). Urban growth in Himalaya: understanding the process and options for sustainable development. Journal of Urban and Regional Studies on Contemporary India, 4(2), 15-27.

Tol, R. S. (2013). The economic impact of climate change in the 20th and 21st centuries. Climatic Change, 117, 795-808. https://doi.org/10.1007/s10584-012-0613-3

Vahid, G. (2013). Modeling of ground water level using

statistical method and GIS. A Case Study: Amol-Babol Plain, Iran, 2(3), 53-59.

Wang, X., Dong, X., Liu, H., Wei, H., Fan, W., Lu, N., ... & Xing, K. (2017). Linking land use change, ecosystem services and human well-being: A case study of the Manas River Basin of Xinjiang, China. Ecosystem Services, 27, 113-123. https://doi.org/10.1016/j.ecoser.2017.08.013

Yiran, G. A. B., Ablo, A. D., Asem, F. E., & Owusu, G. (2020). Urban sprawl in sub-Saharan Africa: A review of the literature in selected countries. Ghana Journal of Geography, 12(1), 1-28. https://doi.org/10.4314/gjg.v12i1.1

Younes, M. K., Nopiah, Z. M., Nadi, B., Basri, N. A., Basri, H., Mohammed, F. M., & Shatanawi, K. (2013). Investigation of solid waste characterization, composition and generation using management of environmental systems in Zarqa, Jordan. Asian Journal of Chemistry, 25(17), 9523.

Yousef, Y. (2012). Identification of polycyclic aromatic hydrocarbons in air samples from Zarqa City, Jordan, using high resolution laser excited luminescence spectroscopy combined with Shpolskii matrix technique. Jordan Journal of Chemistry (JJC), 7(3), 311-328.

Zou, B., Xu, S., Sternberg, T., & Fang, X. (2016). Effect of land use and cover change on air quality in urban sprawl. Sustainability, 8(7), 677. https://doi.org/10.3390/su8070677

JJEES

JJEES (2025) 16 (1): 11-16
ISSN 1995-6681

Jordan Journal of Earth and Environmental Sciences

Geographic Distribution of the b-value in north Morocco and its Surrounding for Seismic Zones Identification

Abderrahim Boulanouar[1*], Amin Khalil[2],
Jamal Sebbani[3], Anas El Ouali[4], Abdelaali Rahmouni[5]

[1]*Laboratory of Applied Sciences, National School of Applied Sciences of Al-Hoceima, Abdelmalek Essaadi University, P.O Box 03 Ajdir, Al-Hoceima, Morocco*
[2]*Geology Department, Faculty of Science, Helwan University, Egypt*
[3]*Faculty of Science, Mohammed V University, Rabat, Morocco*
[4]*Department of Geomorphology and Geomatics, Scientific Institute, Mohammed V University in Rabat, Avenue Ibn Batouta, BP 703, Agdal, Rabat, Morocco*
[5]*Laboratory of Solid State Physics, Department of Physics, Faculty of Science Dhar El Mahraz, Sidi Mohamed Ben Abdellah University, Fez, Morocco*

Received on 8 August 2023; Accepted on 21 October 2023

Abstract

Earthquakes are one of the deadliest hazards. To reduce their effects, seismic hazard assessments are applied to predict the levels of ground motion during future possible large earthquakes. The assessments depend on the so-called recurrence relationship. The recurrence relationship is based on the average or mean earthquake (denoted by the a-value) and the tectonic activity (denoted by the b-value). The seismotectonic activity in the study area has not been well studied. Hence, seismic hazard assessments may not provide adequate information for earthquake mitigation and preparedness strategies. An important step for seismic hazard assessments is the determination of the homogeneous seismic zones or sources. The present work aims to define seismic zones using the spatial records of past earthquake activities. The methodology adopted begins with building a complete catalog based on local catalogs and international data center products. Besides, the magnitudes are homogenized to the moment magnitude scale. The area is subdivided into several blocks. For each block, the Gutenberg-Richter formula is fitted to get the b-value. The parameters are then mapped to define seismic sources in the study area. The results show high b-value in the north of the study area. This area witnessed two moderate earthquakes near Al Hoceima City. To the south, b-value determined was low between 0.6 to 0.8. Low b-value may indicate high shear stress. This manuscript was prepared before Al Haouz earthquake with magnitude Mw=6.8. This event occurred in a region with low seismicity which may indicate a seismic gap.

Keywords: Seismic b Value Anomalies, Spatial and Temporal Distribution, Gutenberg-Richter Frequency Formula, North Morocco, Southern Spain.

1. Introduction

The investigation of the Gutenberg-Richter parameters, a and b values, has been used to analyze seismic activity in different areas of the world. Several authors have used the b-value computation successfully (Husein et al., 1995; Xie et al., 2019; Enescu and Ito, 2003; Chen et al., 2022). One of the most well-known empirical relationships in seismology between the number of earthquakes N in a given area and the magnitude M is the Gutenberg-Richter equation (Gutenberg and Richter, 1944; Nekrasova and Kosobokov, 2006). This equation can be expressed as:

$$\log_{10} N = a - b.M \quad (1)$$

where 'N' indicates the global number of earthquakes. The constant 'a' indicates the level of seismic activity of a region, whereas the slope 'b' represents the size distribution of its earthquakes, and it's called seismic b value (Kijko and Smit, 2012).

Within the last few decades, parameter b has received significant attention and has been treated in numerous statistical, analytical, and evaluation techniques (Xie et al., 2019; Enescu and Ito, 2003; Alvarado-Corona et al., 2014; Chen et al., 2022). It has been reported that the b-value fluctuates either spatially and/or temporally (Huang and Beroza, 2015). Several mechanisms can cause the change in the seismic b value (Maden and Öztürk, 2015): the presence of heterogeneity, the anomaly in the thermal gradient, the temperature gradient, the fracturing degree, and the shear stress concentration. According to several authors (Main et al., 1989; Botvina et al., 2012; Singh, 2016), it is discovered that stress remains the principal component, affecting the b-value and its changes.

In the literature, various approaches have been used to estimate the seismic b value. The most popular method for estimating the seismic b value is the maximum likelihood (Aki, 1965; Utsu, 1965). The equation for calculating the b-value in the Aki-Utsu formulation is the following (Kijko and Smit, 2012):

$$b = \frac{\log_{10} e}{M - M_c} \quad (2)$$

* Corresponding author e-mail: aboulanouar@uae.ac.ma

where e represents the natural logarithms, M denotes the average magnitude, and M_c is the magnitude of completeness.

The determination of the seismic b values needs to recognize the completeness magnitude of the earthquake catalog (Vorobieva et al., 2013). Estimating the seismic b value is considered an important issue for analyzing and evaluating the probability of occurrence of an earthquake. Most of the time, the seismic b value is very close to 1 and can change depending on many factors: the estimating method choice, the variation of the magnitude range, and the earthquake catalog. Many authors have investigated the spatial variability of b. There have been many studies in different parts of the world about the spatial and temporal variation of the seismic b value. El-Sayed and Wahlström (1996) studied the spatio-temporal distribution of the b value in different areas of Egypt to investigate the state of rock stress. Using the maximum likelihood approach, Lombardi et al. (2005) estimated some hazard assessment parameters, especially the b value in Central and Northern Italy. Khan et al. (2011) has estimated the spatial characterization of the b value for Northeast India. Through the medium of an earthquake catalog in the period between January 1984 and March 2002 in the NE of Japan island arc, a map of b value distribution has been created and discussed (Cao and Gao, 2002).

This study focuses on spatial-temporal variations of the seismic b-values of the Instituto Geográfico Nacional IGN catalog for Northern Morocco. In this paper, a map of the distribution of the seismic b value in this area was estimated using the maximum likelihood method. The results of this study were compared and correlated with the seismicity and tectonics of the study area. This study will help us understand the processes that control large earthquakes and their spatial variations (Naghoj et al., 2010; Al-Tarazi and Qadan 1997; Nicholas et al., 2022). Also, it can help us comprehend plate dynamics and practical applications like improving the quality of the seismic of building codes and Moroccan seismic code, PRPS2011 of Morocco (RPS 2000 (2011)). To the best of our knowledge, this is the first attempt to analyze the geographic distribution of the b-value in Morocco and its surrounding.

2. Data

This study uses a database of earthquakes obtained from IGN in Northern Morocco for the period between January 1980 and September 2022. It is limited by latitudes 31°S–36°N and longitudes -9E–-1E. This seismicity database consists of 16170 events with a magnitude less than 6.3 that occurred at depths less than 185.3 km. The website of the National Geographic Institute (IGN) from which we obtained the earthquake catalog is https://www.ign.es/web/ign/portal/sis-catalogo-terremotos (IGN).

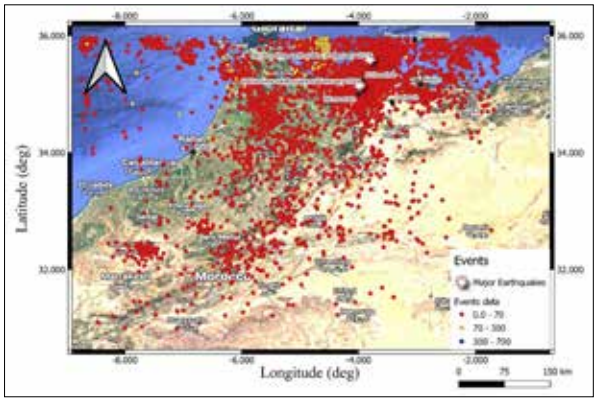

Figure 1. Distribution of earthquakes analyzed. The depth range of these earthquakes is displayed in color

Figure (1) shows the distribution of all earthquakes used in this study between January 1980 and September 2022. Stars represent the principal main shocks within this period. The first one happened on 24 February 2004 and the second on 25 January 2016. Both shocks are located around Al Hoceima City (Boulanouar et al., 2013; Kariche et al., 2018). The declustering found 357 clusters of earthquakes, a total of 7928 events (out of 16170).

Figure (1) displays the declustered catalog containing 16170 events. The declustering events are plotted in blue, red, and green colors to show the depth variations of these events. It is clearly observed that most events are recorded in the area of Rif Mountain, especially the belt between Al Hoceima and the Nador cities. This belt is present in the convergence zone between the two large continental plates: Africa and Eurasia. Furthermore, there exists an active series of faults in this area.

Before calculating the seismic b-values, a magnitude frequency distribution plot is carried out to see the completeness of the data, so that the completeness of magnitude (M_c) is obtained. Earthquakes with magnitudes smaller than M_c are discarded (Aki, 1965). The histogram of the number of earthquakes per unit of time is shown in Figure (2).

In order to study the spatial distribution of the b value, a grid system was applied. Using 50 events per node and a maximum likelihood in each grid space of 0.25°×0.25°, the b value was determined.

The histogram shows that the recorded earthquakes increase with time. This increase is most likely due to the increase of seismological stations in the region. To overcome this problem, the minimum magnitude of completeness is adopted to include only data that is completely recorded throughout the time span considered in the present study.

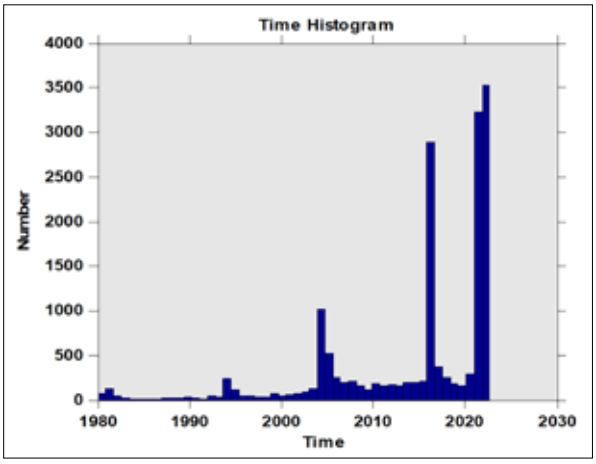

Figure 2. Histogram of the number of earthquakes depending on time

3. Results and Discussion

Figure (3) illustrates the magnitude frequency distribution, which shows the magnitude relationship with the number of earthquakes that have occurred in the period study. The red color in Figure (3) shows the curve produced by magnitude completeness (M_c).

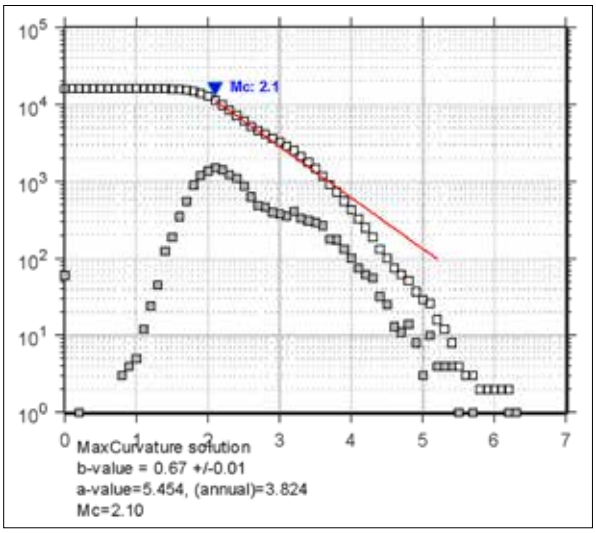

Figure 3. The plot shows the variation of cumulative number with the magnitude in Northern Morocco for the period between January 1980 and September 2022. From the figure, b=0.67+/-0.01, and $M_c = 2$

Based on the frequency magnitude variation (Figure 3), the b value of Northern Morocco is 0.67. This value seems to be lower than many other areas, like: b=1.3 for the Zinkgruvan mine in Sweden (Nuannin et al., 2002) and b=1.1 for the eastern Anatolia region in Turkey (Maden and Öztürk 2015). This low value of the b value may be due to the existence of a highly stable space in the study area. Also, it may be explained by the low number of events of high magnitude. Jafari (2008) found that for the different zone in Iran, the values of the parameter are under one. These low values of b indicate the relative abundance of larger earthquakes versus smaller earthquakes. Figure (4) shows the histogram of magnitude (M). The maximum peak magnitude observed during the period of this investigation was recorded as 2.2, with about 1500 events. The majority of the magnitudes ranges from 1.5 to 4.5.

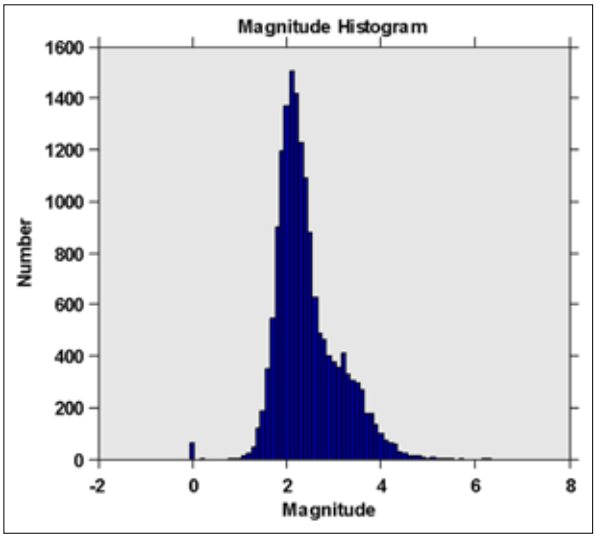

Figure 4. Histogram for the earthquake magnitude used in this study

3.1. Spatial variation of the seismic b value

Figure (5) shows the spatial distribution of the seismic b value in the Northern Morocco region as estimated using the IGN catalog for the period between 1980 and 2022. The magnitude of completeness is 2.1, and the area, limited by latitudes 30°S- 36°N and longitude -9°E -1°E was divided into 1015 grids of 0.25°×0.25° (with 50 events or more). The classic approach of Gutenberg-Richter is frequently employed for the estimation of the Frequency–Magnitude, especially for probabilistic earthquake precursors and seismic hazards. The number of earthquakes N that happen in a particular area as a function of their magnitude M is described by the Gutenberg-Richter law. The parameter 'a' is strongly related to the level of seismicity. The increase in parameter 'a' reflects higher seismicity, whereas parameter 'b' is affected by the tectonics of the area and their stress regime. As the area is subjected to shear stress the b value decreases, a lower b-value indicates that the area under study is probably under high stress.

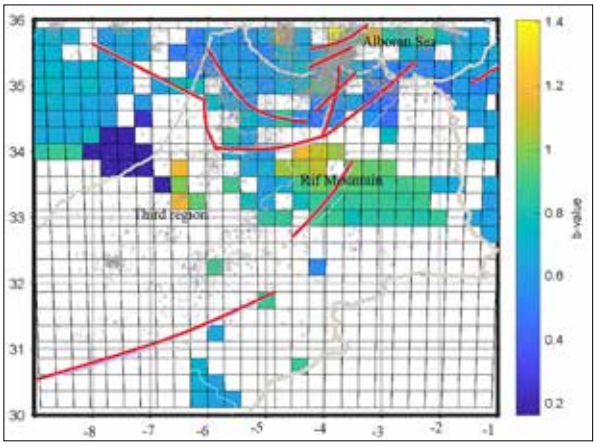

Figure 5. Map of spatial variation of the seismic b-value in Northern Morocco from the IGN catalog between 1980 and 2022. The red thick lines represent the main faults across the study region.

he spatial distribution of the seismic b value in Northern Morocco is studied in this study. Figure (5) shows the spatial distribution of this parameter with a palette of colors, which indicates a low b value by blue color and a high one by yellow. The b-value map indicates that the range of the

b-value is between 0.2 and 1.4. because of the adoption of the declustering procedure and the low number of events recorded in the precise grid. A significant portion of the grid cells is missing and is producing no results (i.e. white grids). Kulhanek (2005) found that the spatial variation around the Matano fault, Indonesia, of the b value varies between 0.3 and 1.8. The map (Figure 5) shows that the high value of the b parameter is indicated in about three regions. The first region, in the Alboran Sea, points out three parts: near Al Hoceima City, where b is around 1.4, a few kilometers at sea from the city of Dariouch with about b=1.2 and in the Alboran Sea near Tetouan City, especially in the region where the depth of the seismic events exceed 110 km (see Figure 1). The second region corresponds to the intersection zone between the external zone of the Rif Mountain and the Neogene basins. This is the area below the large fault that limits the Rif in gray color where the b value varies between 1 and 1.2. This is due to the high seismotectonic zone and the very seismic activity. This area is where the two strong earthquakes happened, one on 24 February 2004 and the other on 25 January 2016. The area around Al Hoceima City has a high-stress accumulation due to the tectonic movement and the presence of high seismic activity. Region three in the west of the study area and below the Rif Mountain has three to four cells, two in green, two in orange, and one in blue. In this region, the value of b fluctuates between 0.2 and 1.2. It is a clear anomaly of the b value that needs to be looked at separately by adding other catalogs. Average values of parameter b (between 0.6 and 0.8) were observed in most of the other regions. A low value of b value of about 0.2 is observed surrounding Rabat City. This may be due to the lack in number of earthquakes in this region.

3.2. Temporal Variations of B-value

Many research studies have been conducted to investigate temporal changes in the b value (Aitouche and Djeddi, 2018; Huang and Beroza, 2015). According to this research, strong earthquakes are generally accompanied by a decrease in the b value and an increase comes before (Sammonds et al., 1992). Monterroso (2003) supports this idea by using data from Central America. According to Molchan and Dmitrieve (1990), the b value drops by half during the hours preceding the mainshock. Figure (6) shows the temporal variation of the b-value in the Northern Morocco region during the period between January 1980 and September 2022. It is clear from Figure (6) that the b value does not constantly fluctuate during the period of the catalog. The fast increase and decrease are observed about three times. These peaks correspond clearly to the two main shocks, especially the two main earthquakes, cited in the map of the b value.

Three jumps in the b-value and cumulative number of earthquakes are observed from figures (6) and (7). The first jump is observed due to the activities accompanied Al Hoceima earthquake on May 26th, 1994. However, this jump was small possibly due to the lack of seismologic stations at that time. The other two jumps occurred following two moderate earthquakes that shocked the area. However, an interesting feature is observed that the b-value decreases after the occurrence of the mainshock. Before the next mainshock, b-value increases to a peak then decreases again. A remarkable feature is the increase again in 2023 that preceded the event of Al Haouz (Mw=6.9) that occurred after the submission of this manuscript. This observation might be useful for predicting future large events in the study area.

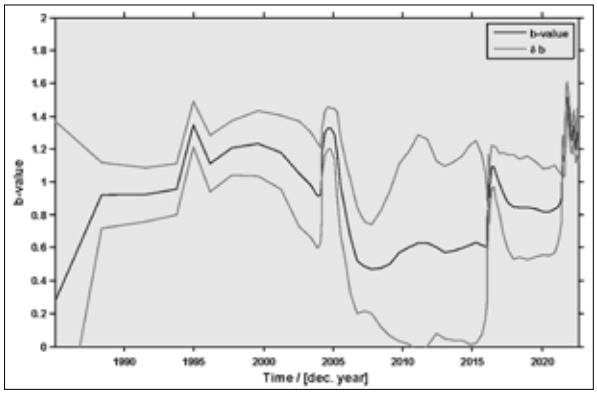

Figure 6. The seismic b-value variation accompanied by their standard error curves versus the time in Northern Morocco, using IGN the catalog for earthquakes that occurred in this region in the range of 1980 to 2022.

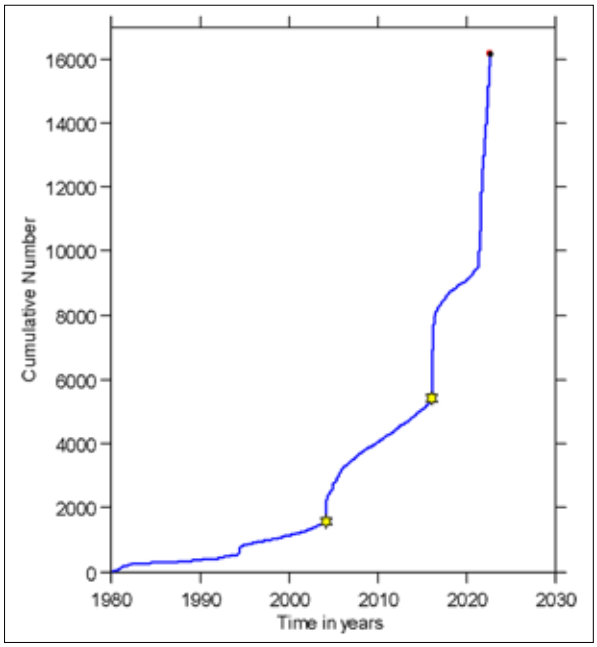

Figure 7. The Cumulative number of events vs time in years. The two gold stars represent the main shocks in the study area

4. Conclusions

The spatial variations of b values in Northern Morocco were examined, using 16170 events selected from the IGN catalog with magnitude completeness of 2.1 between January 1980 and September 2022. The declustering found 357 clusters of earthquakes, a total of 7928 events (out of 16170). This study revealed significant three anomalies of the seismic b values.

The first one exists in the region of the Alboran Sea, especially between AL Hoceima and Nador cities, where b is around 1.4, around Al Hoceima city about b=1.2, a few kilometers at sea from the city of Dariouch. The second region corresponds to the intersection zone between the external zone of the Rif Mountain and the Neogene basins where the b value varies between 1 and 1.2. Region three in the east of the study area and below the Rif Mountain has

three to four cells, two in green, two in orange, and one in blue. In this region, the value of b fluctuates between 0.2 and 1.2. These anomalies are related to the high value of the b parameter. We observed a high value of b value in the Alboran Sea which is related to a high-stress pressure indicator and a high seismic b value in the other region which indicated the presence of high crustal heterogeneity. Regarding the two main shocks that happened at Al Hoceima City, one in January 2016 and the other in February 2004. We discovered a good correlation of b-value change. At the moment of triggering of these earthquakes, the value b begins to increase to a maximum value in almost a year. This shows that the change of the value b can be used as a precursor in this region. This phenomenon is consistent with several studies. The results of this study can be used in other fields, such as civil engineering, especially for seismic design.

Acknowledgments

All data used in this study are collected from the IGN catalog https://www.ign.es/web/ign/portal/sis-catalogo-terremotos (24 September 2022)

All figures used in this paper were made using the program Zmap 7 software. This software was run with Matlab R2010a software.

Author's Contributions

Conceptualization, methodology, software, validation, formal analysis, investigation, resources, data collection, writing – original draft preparation, writing – review and editing, visualization, supervision, A. Boulanouar; methodology, software, investigation, writing, A. Khalil; analysis, interpretation, writing – review, and editing, J. Sebbani; analysis, interpretation, writing – review, and editing, A. El Ouali; methodology, software, analysis, data collection, writing, A. Rahmouni.

References

Aitouche, M. A., and Djeddi, M. (2018) Conventional and Fractal Variogram Based on Time—Space Analysis of Seismicity Distribution—Case Study: Algeria Seismicity (1673-2010). Journal of Geoscience and Environment Protection 6, p.147.

Aki, K. (1965). Maximum likelihood estimate of b in the formula logN= a-bM and its confidence limits. Bull. Earthquake Res. Inst. Univ. Tokyo 43: 237-239.

Al-Tarazi, E., & Qadan, H. (1997). Seismic hazard potential expected for dams in Jordan. DIRASAT NATURAL AND ENGINEERING SCIENCES, 24, 313-325.

Alvarado-Corona, R., Mota-Hernández, C., Félix-Hernández, J. L., Santos-Reyes, J. (2014). What Can Be Learnt from Past Disasters? Analysis of the Mw 8.8 Mega Earthquake of Central Chile with MORT. Jordan Journal of Earth and Environmental Sciences, 6 (1), 1-7.

Botvina, L. R., Soldatenkov, A. P., Tyutin, M. R. (2012). Relationship between the b^ sub AE^-value and stress under mixed mode loading conditions. In Doklady Earth Sciences 446, p. 1127.

Boulanouar, A., El Moudnib, L., Harnafi, M., Cherkaoui, T. E., Rahmouni, A., Boukalouch, M., Sebbani, J. (2013). Spatial variation of coda wave attenuation using aftershocks of the Al Hoceima earthquake of 24 February, 2004, Morocco. Natural Science 5, p. 72.

Cao, A., Gao, S. S. (2002). Temporal variation of seismic b-values beneath northeastern Japan island arc. Geophysical research letters 29: 48-1.

Chen X., Li Y., Chen L. (2022). The characteristics of the b-value anomalies preceding the 2004 M w9. 0 Sumatra earthquake. Geomatics, Natural Hazards and Risk 13: 390-399.

El-Sayed, A., Wahlström, R. (1996). Distribution of the energy release, b-values and seismic hazard in Egypt. Natural Hazards 13: 133-150.

Enescu, B., and Ito, K. (2003). Values of b and p: their Variations and Relation to Physical Processes for Earthquakes in Japan. Disaster Prevention Research Institute, Kyoto University 46: 709-719.

Gutenberg, B., Richter, C. F. (1944). Frequency of earthquakes in California. Bulletin of the Seismological society of America 34: 185-188.

Huang, Y., and Beroza, G. C. (2015). Temporal variation in the magnitude-frequency distribution during the Guy-Greenbrier earthquake sequence. Geophysical Research Letters 42: 6639-6646.

Husein, A. I., AL-HOMOUD, A. S., AL-TARAZI, E. I. D., & NUSIER, O. K. (1995). Probabilistic seismogenic ground motion hazard assessment of Karak city in Jordan. Environmental and Engineering Geoscience, 1(2), 207-218.

IGN – Instituto Geografico Nacional https://www.ign.es/web/ign/portal/sis-catalogo-terremotos (24 September 2022)

Jafari, M. A. (2008). The distribution of b-value in different seismic provinces of Iran. In 14th word conference on earthquake engineering:12-17.

Kariche, J., Meghraoui; M., Timoulali, Y., Cetin, E., Toussaint, R. (2018). The Al Hoceima earthquake sequence of 1994, 2004 and 2016: Stress transfer and poroelasticity in the Rif and Alboran Sea region. Geophysical Journal International 212: 42-53.

Khan, P. K., Ghosh, M., Chakraborty, P. P., Mukherjee, D. (2011). Seismic b-value and the assessment of ambient stress in Northeast India. Pure and applied geophysics 168: 1693-1706.

Kijko, A., Smit, A. (2012). Extension of the Aki-Utsu b-value estimator for incomplete catalogs. Bulletin of the Seismological Society of America 102: 1283-1287.

Kulhanek, O. (2005). Seminar on b-value. Dept. of Geophysics, Charles University, Prague, pp. 10-19.

Lombardi, A. M., Akinci, A., Malagnini, L., Mueller, C. S. (2005). Uncertainty analysis for seismic hazard in Northern and Central Italy. Annals of Geophysics 48: 853-865.

Maden, N., Öztürk, S. (2015). Seismic b-values, bouguer gravity and heat flow data beneath Eastern Anatolia, Turkey: Tectonic implications. Surveys in Geophysics 36: 549-570.

Main, I. G., Meredith, P. G., Jones, C. (1989). A reinterpretation of the precursory seismic b-value anomaly from fracture mechanics. Geophysical Journal International 96: 131-138.

Molchan, G. M., and Dmitriev O. E. (1990) Dynamics of the magnitude—frequency relation for foreshocks. Physics of the Earth and Planetary Interiors 61: 99-112.

Monterroso, Juárez, D. A. (2003) Statistical Seismology Studies in Central America: b-value, seismic hazard and seismic quiescence. Doctoral dissertation, Acta Universitatis Upsaliensis.

Naghoj, N. M., Youssef, N. A. R., Maaitah, O. N. (2010). Mechanical properties of natural building stone: jordanian building limestone as an example. Jordan Journal of Earth and Environmental Sciences, 3 (1), 37-48.

Nekrasova, A. K., Kosobokov, V. G. (2006). Temporal variations in the parameters of the Unified Scaling Law for Earthquakes

in the eastern part of Honshu Island (Japan). Doklady Earth Sciences 5, p. 1352.

Nicholas, O., M Dickson, N., Okeke, F. O. (2022). Building Collapse in Nigeria and its Consequences on the Architect's Role as the Leader of The Building Team. Jordan Journal of Earth and Environmental Sciences, 13(1), 16-25

Nuannin, P., Kulhane, k O., Persson, L., Tillman, K. (2002). Forecasting of increased induced seismicity in the Zinkgruvan mine, Sweden, by using temporal variation of b-values. Acta Montana, Ser. A, 21: 13-25.

RPS 2000 (2011) RPS 2000—version 2011. Ministère de l'Habitat et de La Politique de La Ville. Rabat, Morocco

Sammonds, P. R., Meredith, P. G., Main I. G. (1992) Role of pore fluids in the generation of seismic precursors to shear fracture. Nature 359: 228-230.

Singh, C. (2016). Spatial variation of seismic b-values across the NW Himalaya. Geomatics, Natural Hazards and Risk 7: 522-530.

Utsu, T. (1965). A method for determining the value of" b" in a formula log n= a-bM showing the magnitude-frequency relation for earthquakes. Geophys. Bull. Hokkaido Univ 13: 99-103.

Vorobieva, I., Narteau, C., Shebalin, P., Beauducel, F., Nercessian, A., Clouard, V. (2013). Multiscale Mapping of Completeness Magnitude of Earthquake Catalogs. Bull. Seismol. Soc. Am., 103: 2188–2202.

Xie, W., Hattori, K. Han, P. (2019). Statistical Test of Spatio-Temporal Variation of b Value in Japan. AGU Fall Meeting Abstracts, NH31D-2019, p. 0874.

JJEES

JJEES (2025) 16 (1): 17-27
ISSN 1995-6681

Jordan Journal of Earth and Environmental Sciences

Reservoir Evaluation and Improving Zonation into Flow Units Using the GHE Method, Abu El Gharadig Field, North Western Desert, Egypt

Osama M. Elnaggar[1*], Tamer E. Hamed[2]

[1]Egyptian Petroleum Research Institute, Production Department, Nasr City, Cairo, Egypt
[2]Egyptian Petroleum Research Institute, Exploration Department, Nasr City, Cairo, Egypt

Received on 13 July 2023, Accepted on 23 October 2023

Abstract

A group of sandstone core samples, representing Abu Roash ″E″ Member, was selected from AG-3 well (Abu El Gharadig field) to be evaluated in terms of petrophysics, petrography, XRD, and SEM. Enhancing the reservoir classification into hydraulic units, using (the GHEs) method, was done by creating sub-flow units within the main unit. The limits of different GHEs were determined using the experimental equations of the GHE method. In terms of flow characteristics, the examined samples were differentiated into four main GHEs which are GHE-3, GHE-4, GHE-5, and GHE-6, divided into two sub-units for each. GHE-6B and GHE-3 are the best and worst attributes respectively in terms of flow properties. The new novelty is the differentiation of the samples inside the main unit into sub-units by making new lines (using the equation of this method by adding new different FZI values) that are parallel to the limits of the main flow unit, where samples lie very closely on these lines. Hence sub-units within the main unit could be produced using this new processing, and this leads to a more accurate reservoir description. Petrographically, five microfacies were identified: Calcareous argillaceous quartz arenite, Argillaceous ferruginous quartz arenite, Argillaceous quartz arenite, Glauconitic quartz arenite, and Evaporitic ferruginous quartz arenite. These microfacies involve the main and the branched six GHEs. Diagenetic processes that affected the examined samples are compaction, cementation, replacement, glauconitization, ferrugination, leaching, and dissolution. The X-ray revealed quartz is the main component, in addition to evaporite, iron oxides, iron sulfide and clay minerals in variable amounts. SEM distinguished different pore systems that affect permeability values.

Keywords: *Abu El Gharadig Field; Reservoir Zonation; Petrography, XRD; GHE; North Western Desert*

1. Introduction

Dividing the reservoir into different hydraulic elements or flow units is very important for its assessment in terms of flow properties. The concept of reservoir flow units was examined by many researchers as (Abd El Rahman et al., 2023; Harishidayat et al., 2022; Khalid et al., 2020; Al-Jawad and Saleh, 2020; El Sharawy and Nabawy, 2019; Mohebian et al., 2017; Bear, 2013; Porras and Campos, 2001). Reservoir classification into flow units could be done using different methods as (Martin et al., 1997; Amaefule et al., 1993). Global Hydraulic Elements (GHEs) are another technique (Corbett et al., 2003) to differentiate the hydrocarbon reservoir into a number of GHEs having different relations between porosity and permeability. Even within the same GHE, the capabilities may be varied for the samples of interest, and handling them as a homogenous population is not accurate. So, it is very important to separate the samples within the main GHE into sub-units of different qualities where that will help describe the reservoir more precisely. The study area is located at Abu El Gharadig Basin (Figure 1), which represents one of the main Cretaceous reservoirs in the North Western Desert (Abuseda and El_Sayed, 2022; Farouk et al., 2022a, 2022b, 2022c). The General stratigraphic column of the area of interest is displayed (Fig. 2). Generally, the Cretaceous age was examined by many researchers in Egypt (Sharaka, et al., 2022; El-Desoky et al., 2019; Shalaby et al., 2013; Obaidalla, 2005).

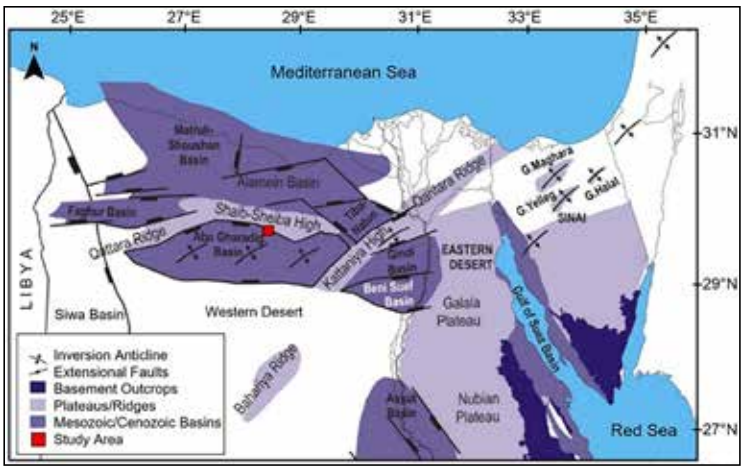

Figure 1. Location map of the study area (Abu El Gharadig field)

* Corresponding author e-mail: osama_221@yahoo.com

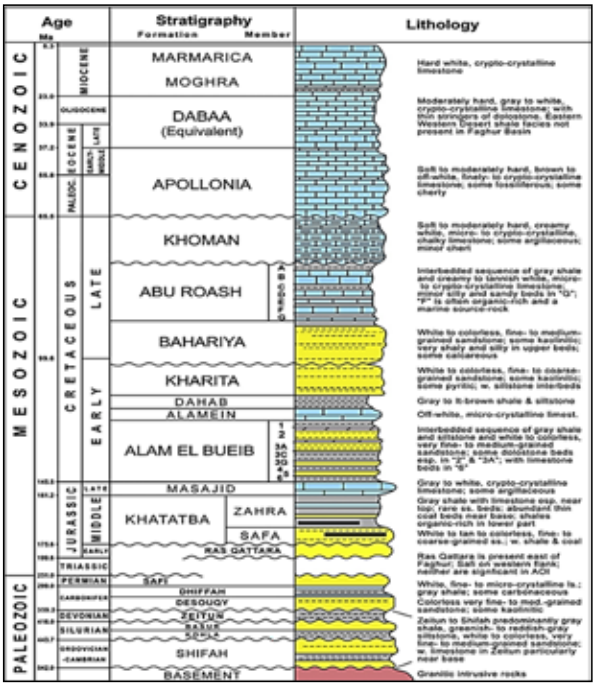

Figure 2. General stratigraphic column of North Western Desert, Egypt (Michael et al. 2016).

Concerning Global Hydraulic elements (GHEs) and for any porosity value, the corresponding permeability could be determined by the next formula:

$$K = \Phi * (((FZI) * (\Phi/1\text{-}\Phi)) / 0.0314)^2 \quad (1)$$

where:

K, permeability in mD

φ, porosity in fraction

FZI = flow zone indicator, mm.

There are 10 values of FZI that are already determined by the method of Global Hydraulic Elements (GHEs) which are 0.0938, 0.1875, 0.375, 0.75, 1.5, 3, 6, 12, 24, and 48 for (GHEs) and 1, 2, 3, 4, 5, 6, 7, 8, 9, and 10 respectively. The previous FZI values allow the determination of boundary lines of flow units to cover a wide range of permeability-porosity combination within (GHEs).

2. Study Objectives

The aim of this work is the reservoir evaluation of Abu Roash ″E″ Member, AG-3 well in Abu El Gharadig field in terms of petrophysics, petrography, XRD, and scanning electron microscope. It aims to enhance reservoir zonation into hydraulic units using GHEs method through dividing the main GHE into sub-GHEs of different flow properties. This means more accuracy in deeply investigating the hydrocarbon reservoir in terms of flow units of various capabilities.

The idea of classifying the main GHE into sub-GHE units is done by making new lines (using the equation of this method by adding new different FZI values) that pass through the data points, existing at different levels within the main GHE unit, where these lines/levels are parallel to the main limits or borders of the main GHE unit. Each line represents a subunit within the main GHE.

3. Materials and Methods

In this study, twenty-four available sandstone core samples, representing Abu Roash ″E″ Member, were selected from AG-3 well (Abu El Gharadig field) to be evaluated in terms of petrophysics, petrographic description, X-ray diffraction (XRD), and scanning electron microscope (SEM).

For petrophysical measurements, eighteen-core samples were suitable to be drilled into plugs of diameter 2.5 cm and length 5 cm. Porosity and permeability were measured at the American University of Cairo (soil Lab.), using the methods introduced by (Dakhanova, 1977; Anderson, 1975; Rzhevsky, and Novik, 1971; Kobranova, 1962). Other parameters were calculated from the measured data. We hope that other parameters will be available for deep reservoir investigation in terms of capillary pressure, electrical properties, and pore pressure (Abbey, 2020).

Twenty-four samples were thin-sectioned for petrographic examination. These thin sections were examined under an Olympus microscope in Sedimentary Lab., Egyptian Petroleum Research Institute (EPRI) which is attached to a digital camera to determine the petrographical characteristics and microfacies associations.

Twenty samples are subjected to X-ray diffraction (XRD) to recognize their mineralogy. The analysis was done at the Egyptian Petroleum Research Institute (EPRI) in Central laboratories. Automated powder diffractometer system of Philips type Pan Alytica X- pert- pro was used with Ni- filter, Cu- radiation (1.542= ƛA°) at normal scanning speed 0.02°/S and 40 K.V., 30 m. A. The reflection peaks between 2Θ = 4° and 70° were gained for the un-oriented analysis. The identification of the powder samples is determined in semi-quantitative and qualitative analysis. The corresponding relative intensities (I/I°) and d-spacing were gained and correlated with the standard data of ICDD/2010 files using the APD program. The interpretation was done using APD and PDF programs which include powder diffraction and PDf-2 Database sets 1-45.

Three samples of the different lithofacies are micro-photographed, and SEM scanned to realize the microstructure and diagenetic relations in the pore system—main contents and matrix of the examined sediments. Distinguishing the mineral contents, using SEM, is simplified by comparing their morphologic attributes with those displayed in the SEM petrology Atlas (Welton, 1984). SEM was done at the Egyptian Petroleum Research Institute (Central lab.), using a SEM of Philips X L-30 Model that was attached with EDX units, with magnification 10 X up to 400.000 X, resolution for W. (3.5nm) and accelerating voltage 30 K.V. The examined samples were gold coated.

4. Results

4.1 Petrophysics

The petrophysical reservoir properties of the samples of Abu Roash ″E″ Member from AG-3 well are displayed (Table 1). The porosity ranges from 10.9 to 28.3%, where permeability ranges from 1.8 to 90.3 MD. Reservoir quality index (RQI) ranges from 0.1 to 0.73 mm and r35 ranges from 0.65 to 7.37 mm.

Table 1. Petrophysics of the examined samples of Abu Roash ″E″ Member, AG-3 well

S#	Depth, ft	Porosity, %	Permeability, md	RQI, mm	r35, mm
1	9631	28.3	53.2	0.430	3.11
2	9637	21.4	22.4	0.322	2.38
3	9640	19.3	65.2	0.578	4.88
4	9642	25.1	76.3	0.548	4.27
5	9647	14.4	60.3	0.643	6.01
6	9649	10.9	56.9	0.717	7.37
7	9650	13.3	41.3	0.554	5.16
8	9651	26.4	90.3	0.581	4.50
9	9666	16.3	40.2	0.493	4.24
11	9670	15.2	49.4	0.565	5.08
12	9671	22.4	55.3	0.494	3.90
13	9675	16.5	49.9	0.546	4.77
14	9676	19.8	89.3	0.667	5.75
15	9678	14.3	56.4	0.625	5.82
16	9687	17.2	1.8	0.101	0.65
17	9695	14.4	43.3	0.545	4.95
23	9725	16.3	34.7	0.458	3.89
24	9727	11.9	64.6	0.731	7.35

Four main GHEs representing the measured samples are displayed (Figure 3). They are GHE-3, GHE-4, GHE-5, and finally GHE-6. The boundaries of each hydraulic element was constructed according to the equation (1).

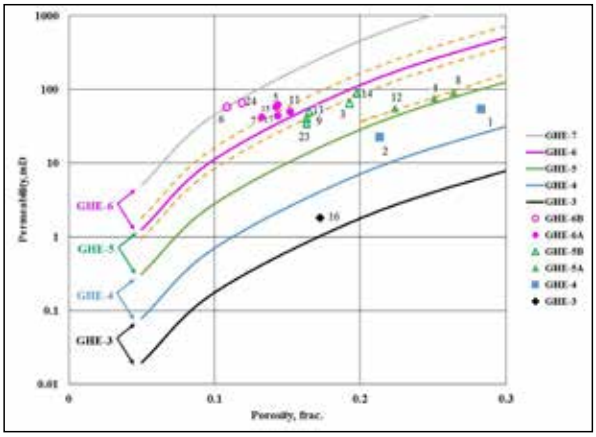

Figure 3. GHEs (main and sub) distribution of the examined samples of Abu Roash ″E″ Member, AG-3 well in the Abu El Gharadig field, (Corbett et al., 2003).

A relation between the Reservoir Quality Index (RQI) and permeability (Figure 4) affirmed the previous results, where the examined samples were distributed in a way similar entirely to that of Figure 3 through parallel trend lines.

Another relation was constructed (Figure 5), using the calculated r35 to display the hydraulic capabilities of the examined samples. The examined samples were distinguished into two groups, the mesoport flow unit, where r35 ranges from 0.5 to 2.0 mm, and the macroport unit, where r35 ranges from 2.0 to 10.0 mm (Martin et al., 1997).

The calculated pore size distribution (Figure 6) was constructed, using empirical calculations (Pittman, 1992) to define the available pore throat radii (μm) within the samples of interest that agree with different saturation percent of mercury (10-75%).

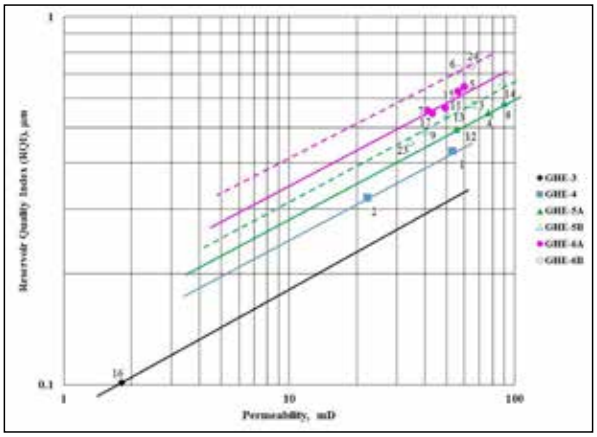

Figure 4. Reservoir quality index (RQI) versus permeability of the examined samples of Abu Roash ″E″ Member, AG-3 well in Abu El Gharadig field.

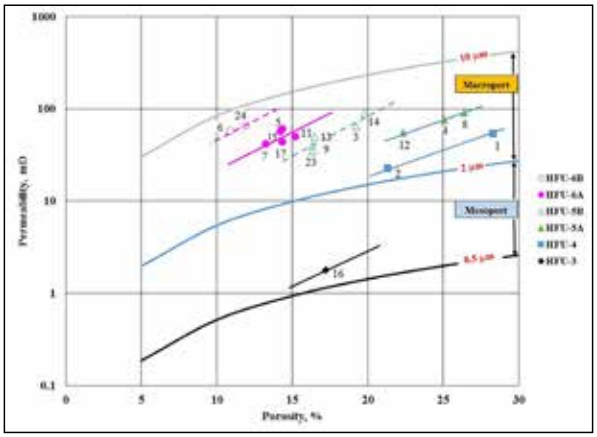

Figure 5. Flow unit distribution of the examined samples using r35 of the examined samples of Abu Roash ″E″ Member, AG-3 well in Abu El Gharadig field.

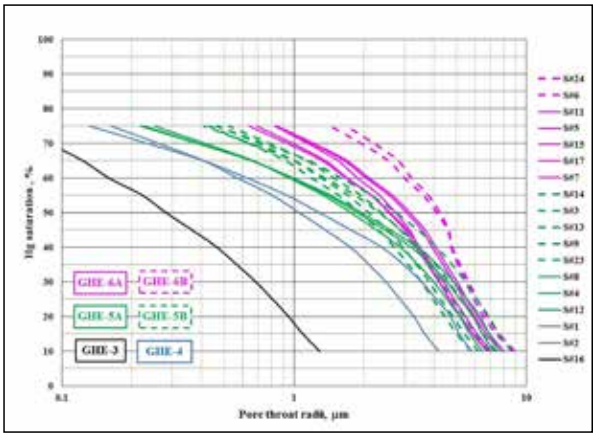

Figure 6. Calculated pore size distribution of the examined samples of Abu Roash ″E″ Member, AG-3 well in Abu El Gharadig field.

4.2 Petrography

The classification of microfacies is used for their simplicity, and they are based on characteristics that are easily determined under the microscope. The study was carried out on twenty-four prepared thin sections representing all the study samples of ″E″ Member in AG-3 well to illustrate their constituents. The petrographic description of the clastic rocks showed the next microfacies types (Plate 1). The depositional environment of clastic samples is determined here according to (Scholle and Spearing, 1982).

4.2.1. Calcareous Argillaceous Quartz Arenite

It is recorded in Abu Roash ″E″ Member from the depth of 9631 to 9647 ft, (S#1-5). This microfacies type, plate 1(B&C), is medium to coarse, sub-angular to sub-rounded detrital quartz grains (92%) and nearly (5%) clay matrix, carbonate, and cement (3%). Quartz grains are moderately to well sorted and most grains are of monocrystalline type with some polycrystalline grains, where they range from sub-mature to mature.

4.2.2. Argillaceous Ferruginous Quartz Arenite

This microfacies type exists in middle part of ″E″ Member from the depth of 9671 to 9676 ft, (S#12-14). It is medium to coarse sand size, moderately to well sorted, sub-angular to sub-rounded detrital quartz grains (about 87%) with some iron oxide fundamentally hematite nearly (7%) and about (5%) clay matrix (Plate1-D). Some of these quartz grains are mostly monocrystalline, where few are polycrystalline. Quartz grains are cemented by carbonate mainly (sparry calcite crystals) about (1%).

4.2.3. Argillaceous Quartz Arenite

This microfacies is recorded in Abu Roash ″E″ Member from the depth of 9678 to 9706 ft, (S#15-19). This microfacies is medium to coarse, sub-angular to sub-rounded detrital quartz grains (95%) and nearly (5%) clay matrix, evaporites, carbonate, and iron oxide cement (Plate1-A). Texturally, quartz grains are moderately to well sorted, and most grains of monocrystalline with some polycrystalline grains. They range from sub-mature to mature.

4.2.4. Glauconitic Quartz Arenite

This sandstone microfacies exists in Abu Roash ″E″ Member from 9710 to 9727 ft, (S#20-24). It is coarse to medium, sub-rounded to sub-angular, monocrystalline, moderately sorted, detrital quartz grains of sub-mature nature forming about (89%) of the rock and iron oxide (1%) cemented by argillaceous matrix. Glaucontization is shown as scattered grains about (7%) forming or peloids, rounded to sub-rounded, green-colored, may be formed from pre-existing clay minerals and/or by the presence of decaying matter (Plate1-F).

4.2.5. Evaporitic Ferruginous Quartz Arenite

This microfacies is recorded in Abu Roash ″E″ Member at depth from 9649 to 9670 ft, (S#6-11). It is medium to fine, sub-rounded to sub-angular, moderately sorted, sub-mature detrital quartz grains (86%), and iron oxide mainly Hematite (8%). A little amount of evaporites mainly halite (4%) and argillaceous matrix can be shown (2%). The intergranular porosity is filled mostly with iron oxide cement mainly hematite and goethite (Plate1-E). Microfacies of the examined samples and equivalent GHEs/Sub-GHEs is displayed (Table 2), where sample distribution within these microfacies is shown (Table 3). The distribution of microfacies along the depth of the examined samples is displayed (Figure 7).

Table 2. Microfacies of the examined samples and equivalent GHEs/Sub-GHEs

Microfacies	Involved samples	Representative plate	Equivalent GHEs (main/sub)
Calcareous argillaceous quartz arenite	S#1-5	Plate1 (B&C)	GHE-4, S#1,2 GHE-5B, S#3 GHE-5A, S#4 GHE-6A, S#5 GHE-6A, s#5
Argillaceous ferruginous quartz arenite	S#12-14	Plate1-D	GHE-5A, S#12 GHE-5B, S#13,14
Argillaceous quartz arenite	S#15-19	Plate1-A	GHE-6A, S#15,17 GHE-3, S#16
Glauconitic quartz arenite	S#20-24	Plate1-F	GHE-5B, S#23 GHE-6B, S#24
Evaporitic ferruginous quartz arenite	S#6-11	Plate1-E	GHE-6A, S#7&11 GHE-6B, S#6

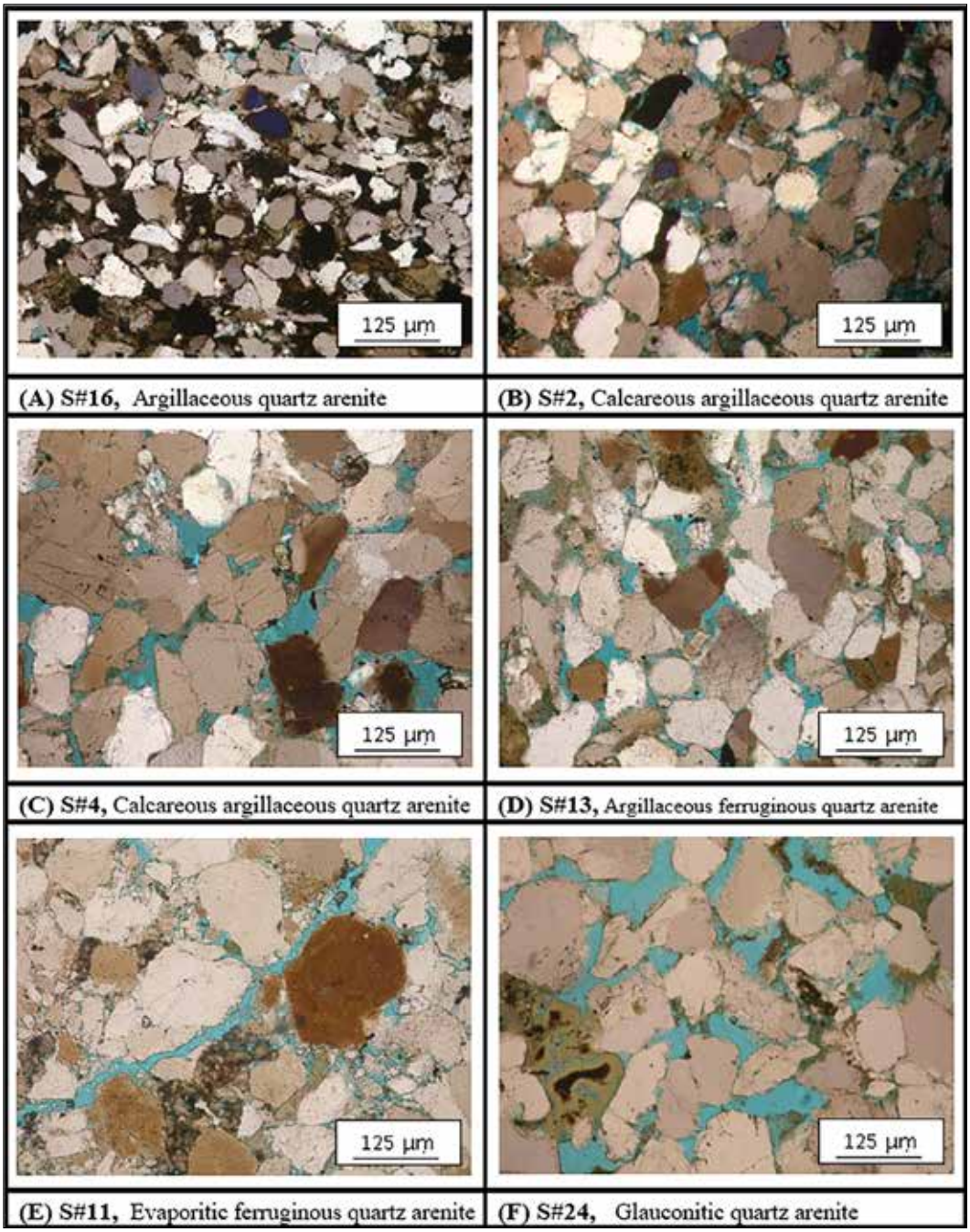

Plate 1. Microfacies of the examined samples of Abu Roash ″E″ Member, AG-3 well in Abu El Gharadig field.

Table 3. Main/sub GHEs and equivalent microfacies of the examined samples

Main GHE	Involved samples	Sub-GHE with samples	Microfacies	Plate
GHE-3	16	None	Argillaceous quartz arenite	Plate1-A
GHE-4	1, 2	None	Calcareous argillaceous quartz arenite	Plate1 (B&C)
GHE-5	8, 4, 12, 14, 3, 13, 9, 23	GHE-5A: 4, 8, 12	Calcareous argillaceous quartz arenite, S#4	Plate1-(B&C)
			Argillaceous ferruginous quartz arenite, S#12	Plate1-D
		GHE-5B: 3, 9, 13, 14, 23	Calcareous argillaceous quartz arenite, S#3	Plate1 (B&C)
			Argillaceous ferruginous quartz arenite, S#13	Plate1-D
			Glauconitic quartz arenite, S#23	Plate1-F
GHE-6	11, 5, 15, 17, 7, 24, 6	GHE-6A: 5, 7, 11, 15, 17	Calcareous argillaceous quartz arenite, S#5	Plate1 (B&C)
			Evaporitic ferruginous quartz arenite, S#7,11	Plate1-E
			Argillaceous quartz arenite, S#15,17	Plate1-A
		GHE-6B: 6, 24	Evaporitic ferruginous quartz arenite, S#6 Glauconitic quartz arenite, S#24	Plate1-E Plate1-F

4.3 Diagenetic Processes of Sandstones

The effects of diagenetic processes occurred in sandstones have been reported and classified by many researchers from different parts of the world, such as (Qian et al., 2022; Qian et al., 2020a & 2020b; Wang et al., 2020; Biorlykke and Ehrenberg, 1993; Moraes and De Ros, 1992). The petrographic investigation of thin sections displays the following main diagenetic features identified from the examined sandstone microfacies:

4.3.1. Compaction (Pressure Solution)

Mechanical compaction including dewatering, deformation, and re-orientation of grains. Chemical compaction is dissolution mainly along surfaces such as stylolite or solution seams. Compaction can lower porosity up to 40% or more and in some cases does an important function in porosity reduction than cementation (McBride et al., 1996).

4.3.2. Cementation

Cementation in clastic sediments is an essential diagenetic operation leading to solidification of the loose detrital sediments into rocks by deposition of minerals from the interstitial fluids and/or forming minerals in authigenic forms. It depends on temperature, pressure, framework assemblage composition, solute composition, pore water composition, and time (Wood, 1989). Cementation is one of the most porosity-reducing operations (Hayes, 1979).

4.3.3. Replacement

This operation includes the decay of the original minerals and the evolution of replacing minerals crystals as cement in both pre-existing and formed void space (Blatt et al., 1972). Generally, ferruginous cemented sandstone may be formed through siderite oxidation (Pettijohn, 1975). Most of the hematite and its precursor oxides (goethite) in sandstones were formed in situ after precipitation through the intrastratal alteration of iron-bearing minerals in hot arid or semi-arid climates or desert basins (Turner, 1980; Walker et al., 1978). The forming of iron oxides (goethite and hematite) is brought about by the development of well-drained oxygenated conditions and the seasonal lowering of water tables, allowing the organic matter oxidation (Selley, 1996; Besly and Turner, 1983). Iron oxides formation as cement or matrix in intergranular pore system of the study samples does an important role in porosity reduction.

4.3.4. Glauconitization

Glauconitization is noticed as peloids or scattered grains, sub-rounded to rounded, green in color, perhaps formed in warm water (15-200 Co) from pre-existing clay minerals at depth ranges from 400 up to 3000 m at pH 7-8, (Plate1-F).

4.3.5. Ferrugination

Pettijohn (1975) proposed that ferruginous cemented sandstones at most may be originated through the siderite oxidation. Selley (1996) and Besly and Turner (1983) considered that the iron oxides formation (hematite and goethite) beds happened through the development of well-drained oxygenated conditions and seasonal lowering of water tables, allowing the organic matter oxidation (Plate-1-B). Turner (1980) and Walker et al. (1978) proposed that hematite and its precursor oxides (mainly goethite) in sandstones at most, were originated in situ after deposition by the interstratal alteration of iron bearing minerals in semi-arid or hot arid climates or desert basin.

4.3.6. Leaching

The leaching diagenetic process in the examined sandstone rock samples is presented in (Plate1-A).

4.3.7. Dissolution

The early diagenetic operation of examined sandstones involves the dissolution of certain frameworks of specific minerals such as quartz. Dissolution in clastic rocks was recorded as a significant diagenetic appearance for boosting secondary porosity (Lundegard et al., 1984) and increment mineral maturity (Abd El-Wahab and McBride, 1991), in addition to texture maturity (Walker et al., 1978). The dissolution process is a very significant diagenetic agent for characterizing the reservoir rock, which improves the porosity and permeability (Selley, 1998). Displaying authigenic mineral or grain dissolution can improve the porosity as a secondary type (Ehrenberg, 1990). The acidic solution may affect quartz grains during the late stage to be etched and corroded to produce grains of irregular shapes, Plate1 (E&F).

4.4 Mineralogy (XRD)

The mineralogical bulk analysis of the examined samples was completed by the X-ray diffraction analysis (XRD) alongside the Scanning Electron Microscopy (SEM). They were used for detection of the main and minor minerals. Recognizing the mineralogical content of the examined samples can be easily detected through using the X-ray diffraction technique (XRD). The X-ray diffraction analysis is an important technique due to its active function in the field of petrography and mineralogy. Chilingar et al. (1967) pointed out that usage of X-ray diffraction analysis would make it possible to distinguish between formations having the same age as well as between different rock units of different ages.

The aim of this study also determines the mineralogical composition varieties of the rocks in the examined well, hence defining the environmental condition. The mineralogy of the twenty-four examined samples were determined by the use of X-ray diffractometer (XRD). Each sample was ground to powder, and 0.5 g. portion of the ground material was pressed into a coveter 10 mm in diameter. This pressed material was analyzed to determine the whole bulk rock mineralogical composition.

4.4.1. Mineralogical Composition of the Bulk Samples

The identification of mineralogy from bulk composition of the ″E″ Member samples was obtained from X-ray results and was explained using cards of American Society for Testing Materials (ASTM) with published data by Deer et al. (1963)and Brown (1961). The results of X-ray diffraction revealed presence of quartz as the main component, in addition to evaporate, iron sulfide, iron oxides and clay minerals in variable amounts and minor calcite.

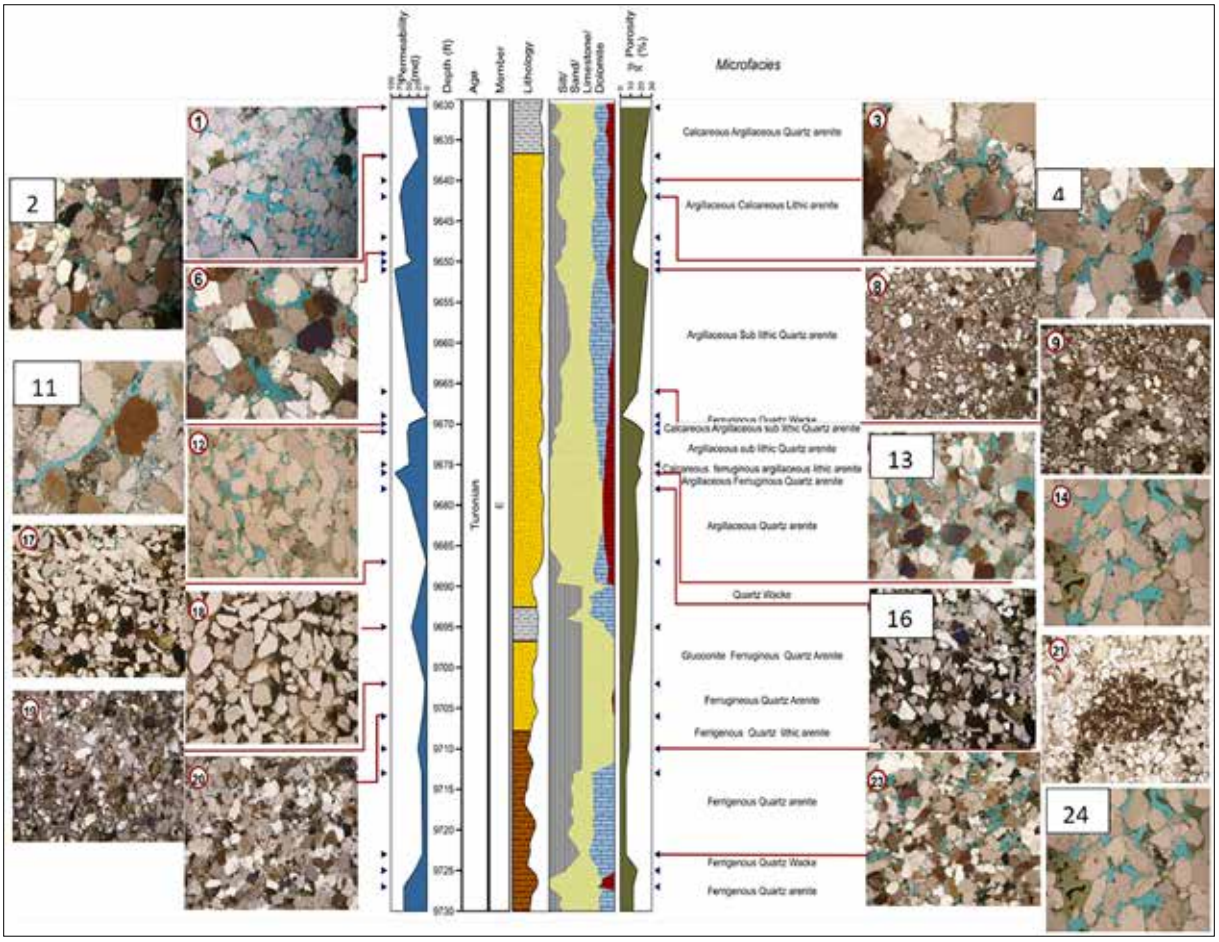

Figure 7. The distribution of microfacies of the examined samples of Abu Roash ″E″ Member, AG-3 well in Abu El Gharadig field.

4.4.2. Quartz

Quartz is the most abundant clastic mineral in the bulk samples. It can be identified at X-ray reflections 4.24 A0, 3.34 A0, and 1.82 A0 that coincide with the ASTM card No. 5-0490. The microscopic check of non-carbonate samples detected the presence of quartz as detrital grains, Plate (2).

4.4.3. Halite

Halite is recorded as a minor mineral in these samples such as S#4 (Plate2-C). Halite can be identified at reflection 2.82 A°, 1.99 A° and 1.62 A° coincide with ASTM card No. 5-0628.

4.4.4. Iron Sulfide (Pyrite)

Pyrite was discovered in the Abu Roash ″E″ Member in most samples. It was recognized in the diffractograms by its characteristic lines at 1.63 A°, 2.71 A°, and 2.42 A° that coincide with ASTM card No. 04-008-7762. The existing of pyrite in ″E″ Member indicates the spread of a reducing environment during its deposition. Pyrite is formed in sediments as a consequence of the bacterial reduction of seawater sulfate (Berner, 1982). The pyrite is also recorded in some samples, Plate2 (A-F) exist in vast quantities in numerous states of crystallization such as rhombs, framboids and specks.

4.4.5. Iron Oxides (Hematite)

The deposition of Fe2O3 in marine environments requires a lower Eh & pH, and being favorable in an oxidizing carbonic acid zone. Hematite is identified using X-ray reflections 3.69 A°, 2.69 A° and 2.51 A°, which coincide with ASTM card No. 33-664, plate2 (A&D). Generally, iron oxides occur in many different phases authigenic iron oxide in the form of hematite and detrital iron oxide as grain coating and scattered interstitial matrix, in clay structure and as iron oxide film on clay surface. The soluble of iron in hydrothermal solutions began precipitate due to change in their pH and Eh and also due to decrease in the temperature of the solution. Oxidizing Fe++ is more complete at relatively high pH solutions.

4.4.6. Clay Minerals (Montmorillonite)

Montmorillonite is identified by basal reflection 15.01A°, 5.01A°, and 3.56A° using ASTM card No. 14-164, Plate2 (A, C, D&E). Krauskopf (1979 documented that the montmorillonite formed from the weathering of intermediate to calc-mafic rocks including volcanic ash. Montmorillonite is originated from soil with relatively high pH, rich in Ca+2, and Mg+2 and under impeded drainage (Mohr et al., 1971). It can also be formed as post-depositional diagenesis of degraded micas by water of low ionic strength running through porous rocks (Velde and Nicot, 1985).

4.4.7. Carbonate Minerals

Calcite is the minor carbonate minerals in bulk sandstone samples, plate2 (C&D). Calcite can be identified at reflections 3.85 A0, 3.03 A0 and 2.09 A0 that coincide with ASTM card No. 5-0586.

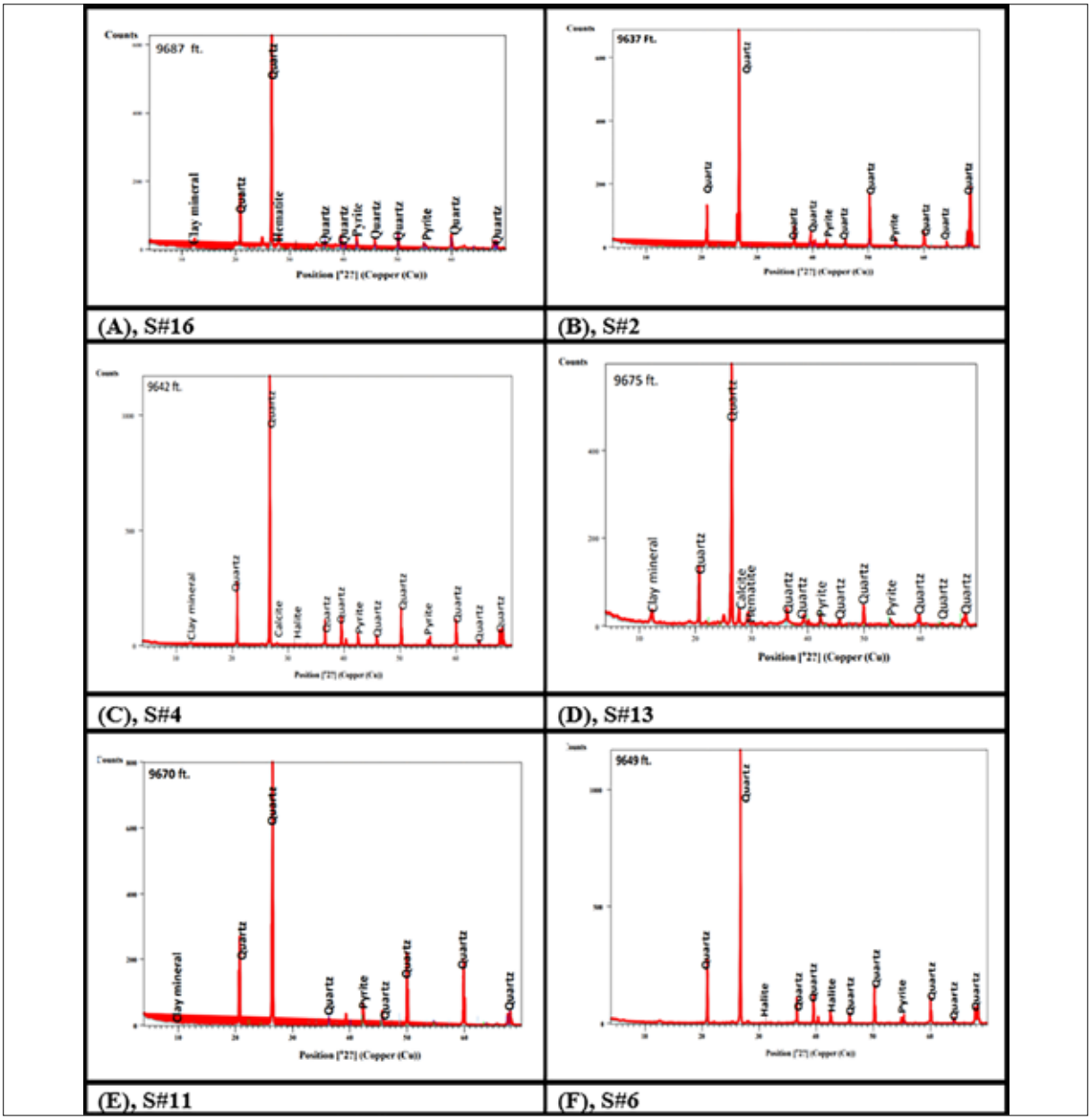

Plate 2. Bulk X- ray diffraction charts of some representative samples of Abu Roash ″E″ Member, AG-3 well in Abu El Gharadig field.

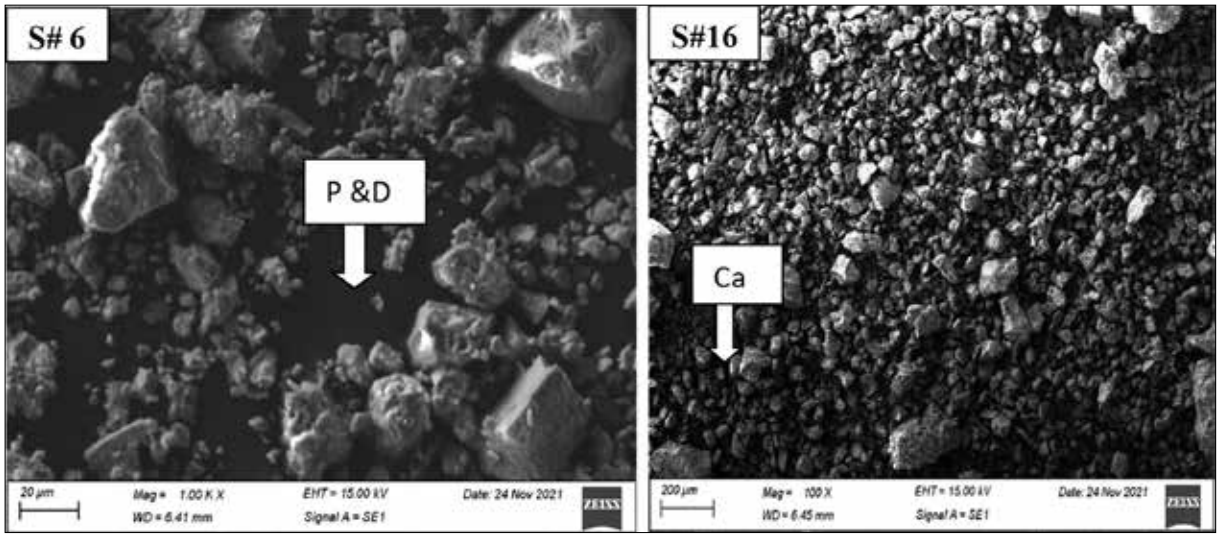

Figure 8. SEM showing quartz arenite of samples (6&16) with pore geometry, dissolution diagenetically and calcite cement, Abu Roash ″E″ Member, AG-3 well in Abu El Gharadig field.

P: Pore geometry. D: Dissolution. Ca: Cementation with calcite.

4.5. Scanning Electron Microscope (SEM) and (EDX).

The petrographic study, when integrated with SEM investigations, supplies a good way to identify the mineralogical features and the diagenetic processes that affect the rock forming minerals (Mousa et al., 2009; Khalil et al., 1999). The next SEM and EDX study was used to clarify and recognize the authigenic minerals, pore geometry (Figure 8), and diagenetic events which are produced by various environments for the examined quartz at Abu Roash ″E″ Member in Cretaceous rock units. The identified microfacies association was deposited in moderately agitated districted from tidal flat beach environments to bank margins (Flugel, 2010 and 2004).

5. Discussion

The new addition of this study as we mentioned previously is making new sub-units within the main GHE. The new sub-units (Figure 3) were found in GHE-5 and GHE-6 with different symbols for each new sub-GHE. GHE-5 involves (GHE-5A & GHE-5B), whereas GHE-6 involves (GHE-6A & GHE-6B). The differentiation of the whole samples within the main GHE into a number of sub-GHEs makes the reservoir description more accurate than before. Table 2 displays the samples of each main and branched GHE.

A number of relationships confirmed the sample differentiation into hydraulic groups as Figure (3), as the relation between Reservoir Quality Index (RQI) and permeability (Fig. 4) illustrates the flow units distribution of the examined samples using r35 of the examined samples of Abu Roash ″E″ Member, AG-3 well in Abu El Gharadig field. Figure 5 displays the macro-port flow unit comprising the samples of GHE-4, GHE-5, and GHE-6 of Figure 3, where the examined samples (GHE-5 and GHE-6) have been differentiated in a way (the trend lines) that reflects the sub-GHEs of Figure 3. Finally, the calculated pore size distributions (PSD) were separated into different groups (Figure. 6) that assured the presence of the sub-flow units of Figure 3.

Petrographically, the depositional environments of microfacies types of the examinedexamined clastic samples were characterized by shallow marine conditions of the intertidal zone for Calcareous argillaceous quartz arenite, intertidal conditions for Argillaceous ferruginous quartz arenite, shallow marine conditions of the intertidal zone for Argillaceous quartz arenite, shallow marine intertidal conditions for Glauconitic quartz arenite, and finally shallow marine intertidal conditions for Evaporitic ferruginous quartz arenite.

Concerning the diagenetic processes of the examined samples, the effect of compaction gives (secondary porosity) overburden pressure as shown in Plate1 (A & E) during the middle stage, and it is shown in (Plate1-A) at a late stage of diagenetic processes. Cementation is represented by three kinds in the examined samples: The first is calcite (Plate-1B) during the early stage, the second is evaporites as shown in (Plate-1A), finally, by iron oxides as shown in Plate-1 (A, B &F) & Plate-2 (A&D). Hematite is the latest authigenic mineral in the examinedexamined sandstone. It occurs as rims on quartz grains that are commonly preserved between quartz grains and represent the later authigenic phases. Iron could be provided by intrastratal ferrosilicate solution from the clay beds in the examinedexamined section since the diagenetic environment was oxidizing.

Petrographical check showed the occurrence of iron minerals (hematite) as a cement replacing mineral in sandstone samples in Plate-1 (A&E).

The glauconite formation is facilitated with existing of decayed organic matter (Plate1-F). Leaching process (Plate1-A) is indicated by presence of oversize pores. These pores are formed by dissolving out or selective removal of the intergranular silicate minerals. This is the main diagenetic process to make high porosity during the late stage.

Mineralogy determination using X-ray diffraction analysis (XRD) helped determine the environmental conditions. SEM (Figure 8) distinguished different pore systems that can affect permeability values. The wider pore spaces are obvious for sample (6) which is the permeable one (56.9 mD), where the narrower pore spaces are clear for sample (16) that is the tight one (1.8 mD), also calcite cement was detected for sample#4 (Figure 9).

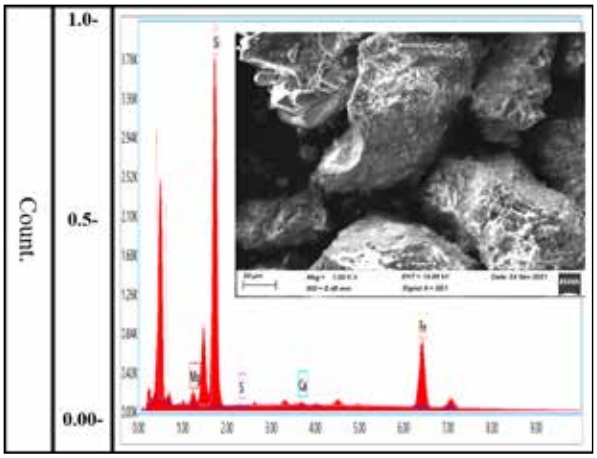

Figure 9. EDX and SEM showing calcite cement and replacement by iron oxide in Calereous quartz arenite microfacies, S#4, Abu Roash ″E″ Member, AG-3 well in Abu El Gharadig field.

6. Conclusion

The examinedexamined samples were classified into four zones of GHEs (GHE-3, GHE-4, GHE-5, and GHE-6). The new processing with GHE method permits adding sub-GHE flow units that enable better understanding of petroleum reservoir, where GHE-5 and GHE-6 were divided into two sub-units for each. The GHE method gives more details about flow units than r35 method. The effect of hematite in reducing the flow properties is obvious on GHE-3 unit. GHE-6B represents the best flow units where GHE-3 unit is the worst. Pore system similarity makes the samples have the same flow properties although they belong to different microfacies as in GHE-5 and GHE-6 flow units. SEM shows the positive/negative effects of pore geometry on the permeability values of the rocks. The results show that a specific microfacies can comprise several different reservoir flow units. Contrarily, similar flow units could be related to different microfacies.

Acknowledgments

The authors would like to thank Khalda Petroleum Company and General Egyptian Petroleum Corporation (E.G.P.C) for supplying the data required to achieve this study.

References

Abbey, C., Oniku, A., Meludu, C., Sebastian, A. (2020). Rock physics analysis of abnormal pore pressure regime offshore Niger Delta Basin. Jordan Journal of Earth and Environmental Sciences, 11: 224-233.

Abd El Rahman, A.A., Elnaggar, O.M., Mohamed, S.F. (2023). Magnetic susceptibility as an indication of reservoir properties of the Nubia Group in Aswan-Komombo, Southern Egypt. Egyptian Journal of Petroleum 32: 31-41.

Abd El-Wahab, A.A., and McBride, E.F. (1991). Digenetic control or reservoir quality of Araba and aqua diagenetic quartz arenites (Cambrian), Gebel Araba-Qabeliat, Southwest Sinai, Egypt. Egyptian Delta Journal of Science 15: 160-203.

Abuseda, H., and El_Sayed, A. M. (2022). Petrographical and petrophysical studies of some Upper Cretaceous rocks, Western Desert, Egypt. Jordan Journal of Earth and Environmental Sciences 13: 37-47.

Al-Jawad, S.N., and Saleh, A.H. (2020). Flow units and rock type for reservoir characterization in carbonate reservoir: case study, south of Iraq. Journal of Petroleum Exploration Production Technology 10: 1-20.

Amaefule, J.O., Altunbay, M., Tiab, D., Kersey, D., Keelan, D.K. (1993). Enhanced reservoir description, using core and log data to identify hydraulic (flow) units and predict permeability in un-cored interval wells SPE-26436. Society of petroleum engineers Conference, Houston, Taxes, U. S. A., 3-6 October, pp. 94-135.

Anderson, G. (1975). Coring and core analysis handbook, Petroleum Publishing Company. Tusla.

Bear, J. (2013). Dynamics of fluids in porous media. Courier Corporation, Chelmsford.

Berner, R.A. (1982). Burial of organic carbon and pyrite sulfur in the modern ocean: its geochemical and environmental significance, American Journal of Science 282: 451-473.

Besly, Y.B., and Turner, P. (1983). Origin of red beds in a moist tropical climate (Etruria Formation, Upper Carboniferous, UK). In: Wilson, R.C. (ed.) Residual Deposits: Surface Related Weathering Processes and Materials. Geological Society London Special publications 11: 131-147.

Biorlykke, K., and Ehrenberg, P.K. (1993). Quartz cementation in sedimentary basins. American Association of Petroleum Geologists Bulletin 77: 1538-1548.

Blatt, H., Middleton, G., Murray, R. (1972). Origin of sedimentary rocks. 2nd edition. Prentice Hall, Inc., Englewood Cliffs, New Jersey. U.S.A.

Brown, C. (1961). The X-Ray identification and crystal structure of clay minerals. A symposium, the Mineralogical Society, London, p. 544.

Chilingar, G.V., Bissel, H.J., Fairbridge, R.W. (1967). Carbonate rocks: origin occurrence and classification developments in sedimentology. Elsevier, publ. Co. London, New York.

Corbett, P.W.M., Ellabard, Y., Mohhammed, K. (2003). Global Hydraulic Elements-Elementary Petrophysics for Reduced Reservoir Modeling. EAGE 65th Conference and Exhibition.

Dakhanova, N.V. (1977). Determination of the petrophysical characteristics of sample. Russian, Nedra, Moscow, p. 41.

Deer, W., Howie, R.A., Zssman, J. (1963). Rock-forming minerals. John Willey and Sons, New York, comprehensive treatise, with excellent coverage on chemistry, crystal structure and paragenesis 5: 1788.

Ehrenberg, S.N. (1990). Relationship between diagenesis and reservoir quality in sandstones of the Garn Formation, Haltenbanken, mid-Norwegian continental shelf. American Association of Petroleum Geologists Bulletin 74: 1538-1558.

El-Desoky, H., Farouk, S., Heikal M., El-Mahallawy, M., Wahid, A. (2019). Geochemical and technical investigation of some clay materials in the Bahariya Oasis, Western Desert, Egypt: Implication in the vitrified clay pipes Industry. Journal of African Earth Sciences 160: 103612.

El Sharawy, M.S., and Nabawy, B.S. (2019). Integration of Electrofacies and Hydraulic Flow Units to Delineate Reservoir Quality in Uncored Reservoirs: A Case Study, Nubia Sandstone Reservoir, Gulf of Suez, Egypt. Natural Resources Research 28: 1587-1608.

Farouk, S., Sen, S., Abu-Alam, T., Al Kahtany, K. (2022a). Geomechanical assessment of the Lower Turonian AR-F limestone Member, Abu Gharadig Field, Egypt: Implications for unconventional resource development. Frontiers in Earth Science 10.

Farouk, S., Sen, S., Abuseda, H., El-Shamly, Y., Salam, A., Elhossainy, M.M. (2022b). Petrophysical Characterization of the Turonian and Cenomanian Intervals in the Abu Gharadig Field, Western Desert, Egypt: Inferences on Reservoir Quality and Resource Development. Natural Resources Research 31: 1793-1824.

Farouk, S., Sen, S., Ganguli, S.S., Ahmad, F., Abioui, M., Al-Kahtany, K., Gupta, P. (2022c). An integrated petrographical, petrophysical and organic geochemical characterization of the Lower Turonian Abu Roash-F carbonates, Abu Gharadig field, Egypt-Inferences on self-sourced unconventional reservoir potential. Marine and Petroleum Geology 145: 105885.

Flugel, E. (2004). Microfacies of carbonate rocks analysis, 1st interpretation and application Springer-verlag, Berlin Heideberg, Newyork. p. 956.

Flugel, E. (2010). Microfacies of carbonate rocks analysis, 2nd interpretation and application Springer-verlag, Berlin Heideberg, Newyork. P. 1006.

Harishidayat, D., Farouk, S., Abioui, M. and Aziz, O.A. (2022). Subsurface Fluid Flow Feature as Hydrocarbon Indicator in the Alamein Basin, Onshore Egypt; Seismic Attribute Perspective. Energies 15: 1-16.

Hayes, J.B. (1979). Sandstone diagenesis, the hole truth. S. E. P. M., Spec. publ., 26: 127-139

Khalid, M., Desouky, S.D., Rashed, M., Shazly, T., Sediek, K. (2020). Application of hydraulic flow units' approach for improving reservoir characterization and predicting permeability. Journal of Petroleum Exploration and Production Technology 10: 467-479.

Khalil, S.M., El-Baz, M.H., Abu-Assy, E.M. (1999). Petrography and diagenesis of Gabal El-Khashab. Red Sea, Egyptian Journal of Geology 5: 119-133.

Kobranova, V.N. (1962). Physical properties of rocks. In Russian Gestopechizdat, Moscow, p. 490.

Krauskopf, K.B. (1979). Introduction to Geochemistry, Mc, Graw-Hill, New York.

Lundegard, P.D., Land, L.S., Galloway, W.E. (1984). Problem of secondary porosity: Frio Formation (Oligocene), Texas Gulf Coast. Geology 12: 399-402.

Martin, A.J., Solomon, S.T., Hartmann, D.J (1997). Characterization of petrophysical flow units in carbonate reservoirs. American Association of Petroleum Geologists Bulletin 81: 734-759.

McBride, E.F., Abdel-Wahab, A.A., Salem, A.M.K. (1996). Influence of diagenesis on reservoir quality of Cambrian and Carboniferous sandstones, southwest Sinai, Egypt. Journal of African Earth Sciences 22: 285-300.

Michael, A.A., Matthias, D.G., James, W.C., Melissa, T. (2016). Egypt far Western Desert basins petroleum charge system as defined by oil chemistry and unmixing analysis. Marine and Petroleum Geology 77: 54-74.

Mohebian, R., Riahi, M.A., Kadkhodaie, A. (2017). Characterization of hydraulic flow units from seismic attributes and well data based on a new fuzzy procedure using ANFIS and FCM algorithms, example from an Iranian carbonate reservoir. Carbonates and Evaporites 34: 349-358.

Mohr, E.C.J., Van Baren, F.A., Van Schuylenborgh, J. (1971). Tropical soils, The Hague, the Netherland, In: Seghal et al., (1974), Genesis transformation and classification of clay minerals in Bulletin-Indian Society of Soil Science 9: 1-21.

Moraes, A.S., and De Ros, L.F. (1992). Depositional infiltrated and authigenic clays in fluvial sandstone of the Jurassic Sergio Formation. Reconocovo Basin, Northeastern Brazil, S.E.P.M. Special Publication 47: 197-208.

Mousa, A.S., El-Hariri, T.Y.M., El-Meligy, W.M. (2009). Assessing the influence of diagenetic processes at El-Gedida Mines, El- Bahariya Oasis, Egypt. Australian Journal of Basic and Applied Sciences 3: 1749-1762.

Obaidalla, N.A., (2005). Complete Cretaceous/Paleogene (K/P) boundary section at Wadi Nukhul, southwestern Sinai, Egypt: inference from planktic foraminiferal biostratigraphy. Rev. de Paléobiol., Gen. 24: 201-224.

Pettijohn, F.J. (1975). Sedimentary rocks. Harper and Row New York, 3rd ed.

Pittman, E.D. (1992), Relationship of porosity and permeability to various parameters derived from mercury injection-capillary pressure curves for sandstone. American Association of Petroleum Geologists Bulletin 76: 191-198.

Porras, J.C., and Campos, O. (2001). Rock typing: a key approach for petrophysical characterization and definition of flow units, Santa Barbara Field. Eastern Venezuela Basin. Presented at the SPE Latin American and Caribbean Petroleum Engineering Conference, Buenos Aires, Argentina, 25-28 March. Paper SPE-69458-MS.

Qian, W., Sun, Q., Jones, S.J., Yin, T., Zhang, C., Xu, G., Zhang, B. (2022). Diagenesis and controlling factors of Oligocene Huagang Formation tight sandstone reservoir in the south of Xihu sag, the East China Sea Shelf Basin. Journal of Petroleum Science and Engineering 215: 110579.

Qian, W., Yin, T., Zhang, C., Hou, G., He, M. (2020a). Diagenesis and diagenetic stages prediction of Ed2 reservoir in the west of Bozhong sag. Petroleum 6: 23-30.

Qian, W., Yin, T., Zhang, C., Tang, H., Hou, G. (2020b). Diagenetic evolution of the Oligocene Huagang Formation in Xihu sag, the East China Sea Shelf Basin. Scientific report 10: 19402.

Rzhevsky, Y., and Novik, G. (1971). The physics of rocks. Translation and Edited by A. A. Beknazarov, Mir publishers, Moscow, p. 320.

Scholle, P.A., and Spearing, D. (1982). Sandstone depositional environment. American Association of Petroleum Geologists Bulletin, Memoir 31. Tulsa, Oklahoma, U.S.A., pp. 1-320.

Selley, R.C. (1998). Elements of Petroleum Geology (2nd), Academic Press limited: California, USA.

Selley, R.C. (1996). Ancient sedimentary environments and their subsurface diagnosis. 4th edition, London.

Shalaby, M.R., Hakimi, M.H., Abdullah, W.H. (2013). Modeling of gas generation from the Alam El-Bueib formation in the Shoushan Basin, northern Western Desert of Egypt. International Journal of Earth Sciences 102: 319-332.

Sharaka, H. K., El-Desoky, H. M., Abd El-Moghny, M. W., Hafez, N. A. A., Abuelleban, S. A. (2022). Geological, Mineralogical and Physical Properties of Aswan Kaolinitic Clays, Egypt: Implications for Industrial Applications. Jordan Journal of Earth and Environmental Sciences 13: 64-73.

Turner, P. (1980). Continental Red Beds: Development in Sedimentology. Elsevier, Amsterdam.

Velde, B., and Nicot, E. (1985). Diagenetic clay mineral composition as a function of pressure, temperature and chemical activity. Journal of Sedimentary Petrology 55: 541-547.

Walker, T.R., Waugh, B., Grone, A.J. (1978). Diagenesis in first cycle desert alluvium of Cenozoic age, Southwest United States and Northwest Mexico. American Association of Petroleum Geologists Bulletin 89: 19-32.

Wang, W., Lin, C., Zhang, X. et al. (2020). Effect of burial history on diagenetic and reservoir-forming process of the Oligocene sandstone in Xihu sag, East China Sea Basin. Journal of Marine and Petroleum Geology 112: 1-23.

Welton, J.E. (1984). SEM Petrology Atlas. Volume 4 of American Association of Petroleum Geologists: AAPG methods in exploration series, Issue 4 of methods in exploration series, American Association of Petroleum Geologists.

Wood, J.R. (1989) Modeling the effect of compaction and precipitation/dissolution on porosity. In: Hutcheon. I.E. (ed.) Burial Diagenesis. Mineral Association of Canada Short Course 15: 311-362.

JJEES

JJEES (2025) 16 (1): 28-34
ISSN 1995-6681

Jordan Journal of Earth and Environmental Sciences

Flood Hazard Mapping from Dam Break: A Case Study of King Talal Dam

Radwan Al-Weshah[1*,2], Murad Al-Salahat[3], Saif Al-Omari[3]

[1]Civil Engineering Department, The University of Jordan, Amman 11942, Jordan.
[2]Department of Civil Engineering, Faculty of Engineering and Technology, Al-Zaytoonah University of Jordan, Amman 11733, Jordan.
[3]World Vision International, Amman 11855, Jordan.

Received on September 30, 2024; Accepted on November 10, 2024

Abstract

This paper assesses the flood hazard related to dam break analysis for King Talal Dam in Jordan. Probable Maximum Flood (PMF) was estimated by HEC-HMS using the Probable Maximum Precipitation (PMP) values. The PMF of Zarqa River Watershed (ZRW) was determined to be 3823 . Dam breach parameters were estimated using different models. A 2-dimensional unsteady flow simulation was used to route the breach flood in the downstream area of the dam. The maximum breach flows for overtopping and piping scenarios were estimated to be 65456 and 43748 , respectively. The study generated inundation, flood hazard, duration, and velocity maps for the dam's downstream areas. Most of the inundated areas were classified as extremely hazardous. The maximum water depth was approximately 107 meters on some agricultural lands. The paper provides valuable insights into the dynamics of dam breach floods and their effect on downstream regions. These findings help to develop plans and policies to minimize the risk of loss of life and property due to dam failure. The emergency preparedness strategies include the development a telemetry monitoring system for the dam body and spillway, an early warning system for the upstream watersheds, physical evacuation, and emergency response plans for residents downstream of the dam. The flooded areas include schools, hospitals, and other important public and private properties. This study demonstrates the importance of efficient emergency planning to minimize potential damage. The results of this analysis can help local authorities to prioritize their plans based on the observed arrival times and flood durations. It is very important to engage local communities, government agencies, and other stakeholders in the development of integrated flood preparedness strategies and management plans.

Keywords: *Dam Break Analysis, King Talal Dam, Flood Hazard Mapping, HEC-RAS, Flood Hydrology.*

1. Introduction

Failure of dams can result from internal and external factors. Studies show that dam failure events appear as a result of different reasons such as piping, overtopping, and settlement (Dincergok, 2007). Failure incidents until 1985 were 34 percent a result of overtopping, 30 percent because of foundation defects, 28 percent due to piping, and 8 percent for other reasons. Overtopping failure occurs as a result of poor spillway design, which causes a reservoir to fill high with water, especially during heavy rains (Goodarzi, 2013). In piping failure mode, a breach starts to emerge when water percolates through the dam's body. Then, a critical amount of flow and materials will come out through the piping hole until the breach becomes fully formed. This type of failure occurs in fair weather (sunny days). The analysis of a dam break involves identifying and detailing the consequences of flooding that occurred due to the dam's failure (Whitham, 1955). This analysis consists of three main tasks: estimation of the breach flow hydrograph, routing of the hydrograph through the downstream region, and creation of inundation maps (Aydemir and Güven, 2017).

The parameters of a dam breach, that have an impact on the flood downstream and the accompanying risks, are called dam breach parameters. Some crucial variables such as breach width, depth, time to breach, and side slope are used to simulate a dam breach and estimate its post-effects (Wahl, 1997). Researchers have predicted dam breach parameters through using many dam failures. The most common studies are MacDonald and Langridge-Monopolis (1984), Von Thun and Gillette (1990), Froehlich (1995), Froehlich (2008), and Xu and Zhang (2009). MacDonald and Langridge-Monopolis analyzed 42 events. Their study sample comprised an earthfill with a clay core, and rockfill dams. They established a relationship for the Breach Formation Factor. The factor was estimated by the volume of water that leaves the dam and the depth of water above the dam. Thereafter, the factor was utilized to correlate the amount of the material that was eroded from the dam (MacDonald and Langridge-Monopolis, 1984). In 1995, Froehlich performed a study that used 63 actual failures of embankment dams to determine the dam breach parameters. Based on his analysis, Froehlich concluded that most breaches have a trapezoidal shape with a horizontal bottom. In 2008, Froehlich updated his equations by adding 11 instances of dam failure events to his study. He then used the results of a statistical analysis in a Monte Carlo simulation to estimate the unpredictability of peak flows and water levels that could result from failed embankment dams

* Corresponding author e-mail: r.weshah@ju.edu.jo

(Froehlich, 2008). Von Thun and Gillette (1990) developed a guideline for estimating the parameters using data from Froehlich and MacDonald & Langridge Monopoli's studies. The guideline has a specific focus on estimating the breach side slopes, breach width at mid-height, and time until failure. The researchers found that their approach provided a more accurate fit for historical case study data than previous methods based on the breach formation factor proposed by MacDonald & Langridge Monopolis (Wahl, 1997). In 2009, Xu and Zhang provided empirical equations that possess a concrete basis to estimate the parameters. To elicit these equations, they utilized 182 instances of earthfill and rockfill dam failures. Approximately, half of the cases concerned sizable dams exceeding a height of 15 meters. They established empirical formulas between the characteristics of reservoirs and the breaching parameters using a multiparametric, non-linear regression technique (Xu and Zhang, 2009).

One of the most useful and popular hydraulic models was created by the U.S. Army Corps of Engineers (USACE). It is the Hydrologic Engineering Center's River Analysis System (HEC-RAS). It is employed for several tasks, including modeling water quality and water temperature, sediment transport, and 1-D and 2-D unsteady flow simulations (Brunner et al. 2016; Al-Azzam and Al-Kuisi, 2021; Al-Amoush et al., 2017; Al-Shibli et al., 2017). The most recent version of HEC-RAS offered by the US Army Corps of Engineers is 6.3.1. In order to provide precise hydraulic property tables based on the underlying topography utilized in the modeling process, HEC-RAS now features a 2D flow area pre-processor. Brunner (2018) employed the benchmark examinations devised by the Joint Defra Environment Agency of the UK to appraise the 2D proficiency of HEC-RAS. The outcomes demonstrated that HEC-RAS outclassed other models substantially, such as TUFLOW, MIKE FLOOD, and SOBEK.

The objective of this study is to perform a dam break analysis for the King Talal dam using a 2-D simulation approach to predict the characteristics of the flood wave, including peak flood flow, timing of the peak flood, and routing of the flood for different downstream regions. Additionally, the study generated inundation and hazard maps for overtopping and piping scenarios.

2. Materials and Methods

To create a flood map, this study employed an integration of rainfall-runoff and hydrodynamic models (Al-Salahat et al., 2024). High-resolution geometric data and meteorological and hydrological data were utilized in a rainfall-runoff simulation that estimated the flood magnitude. This integration was followed by simulation of overtopping and piping scenarios. The data are detailed in subsequent sections. The methodology employed in this study is graphically presented in Figure 1.

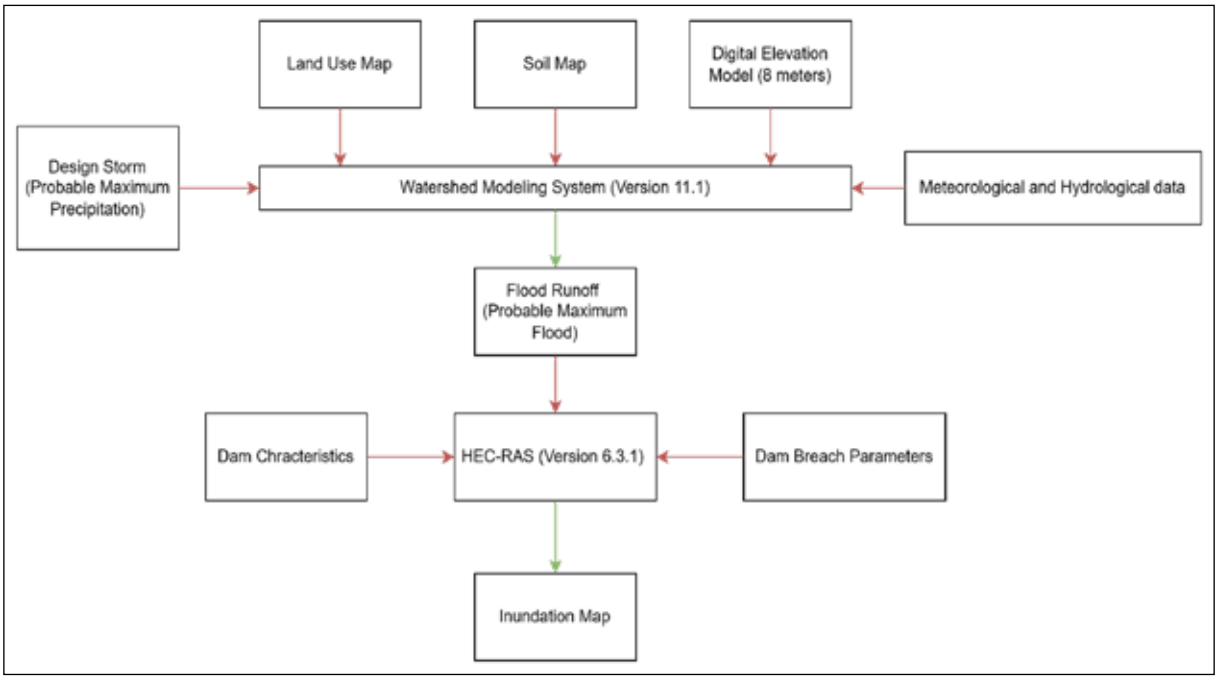

Figure 1. Flowchart of the modeling workflow

2.1 Study Area

Zarqa River Watershed (ZRW) is one of the major watersheds in Jordan that has coordinates of 32°12′ N and 35°35′ E. King Talal Dam (KTD) is located at the outlet of the ZRW with coordinates of 32°12′ N, 35°50′ E as shown in Figure 2. The dam is used for irrigation purposes in the Jordan Valley. The ZRW encompasses several cities and towns such as Amman, Zarqa, and Russeifa. The watershed covers about 4,300 square kilometers. It is a significant agricultural and industrial region and home to a substantial portion of Jordan's population. The KTD was built in 1978 as an earthfill dam with a spillway capacity of 4500 . The total storage capacity of the dam is 88.5 million cubic meters (MCM). The dead storage is approximately 8 MCM. Meanwhile, the live storage amounts to about 80.5 MCM. The reservoir's lake measures about 7.6 km in length and

spans a maximum width of 450 meters (El-Radaideh et al., 2017).

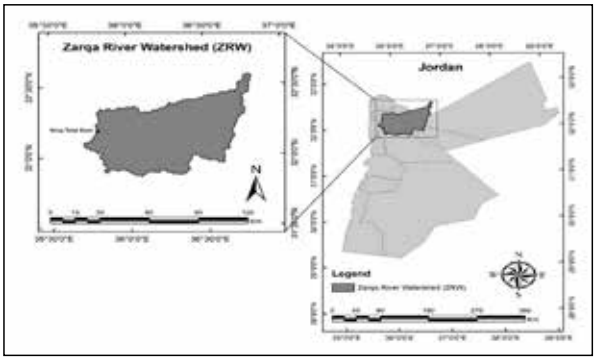

Figure 2. Location of the ZRW and KTD (El-Radaideh et al., 2017)

2.2 Geometric Data

A digital elevation model (DEM) is a depiction of a terrain's topography in a digital format. It provides a graphical illustration of elevation data that can be used to analyze and model various aspects of the terrain. Hydrological modeling, land-use planning, and infrastructure design are some of the most common applications of DEM. In this study, the DEM was generated using the Watershed Modeling System (WMS) with a resolution of 8 meters. Subsequently, it was converted to Triangulated Irregular Network (TIN) of maps using the HEC-RAS model for downstream area of the ZRW. The DEM of the ZRW is illustrated in Figure 3.

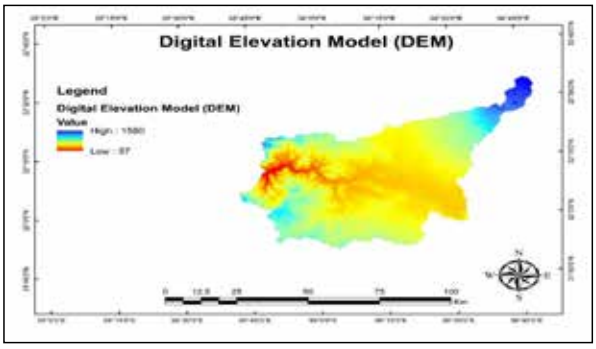

Figure 3. Digital Elevation Model of ZRW (Global Mapper, 2024)

In addition, the soil map was obtained from the Food and Agriculture Organization of the United Nations (FAO, 2022) website. Figure 4 illustrates that there are six types of soil presented in the ZRW. The ZRW is comprised solely of class D soil. According to USDA NRCS (1986), it tends to provide high surface runoff and has limited infiltration capacity when fully saturated.

For land use/cover maps, the Environmental Systems Research Institute (ESRI) website was utilized to maintain the map of the ZRW area. It offers a detailed and high-resolution depiction of land use with a resolution of 10 meters. The map classifies land use into seven major categories, including water, trees, grass, crops, scrubs, urban lands, and bare lands. Figure 5 presents the prominent land use areas of the ZRW.

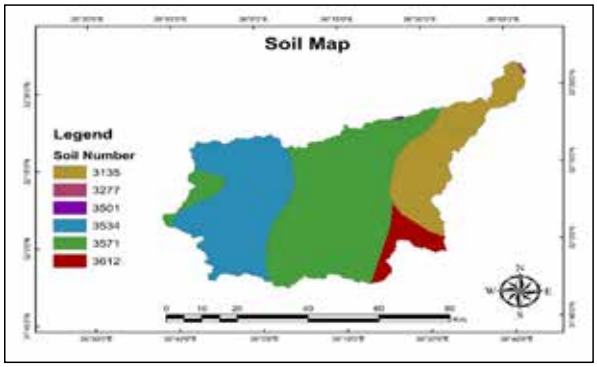

Figure 4. Soil map of ZRW (FAO, 2022)

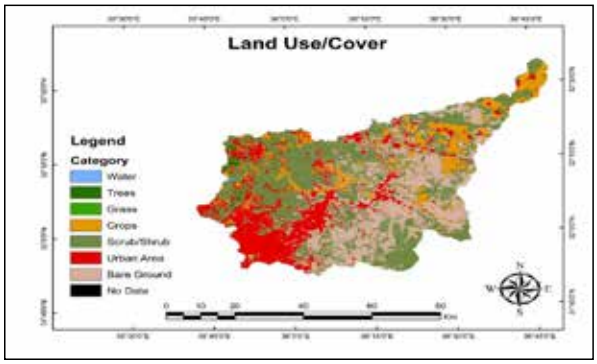

Figure 5. Land use/cover of ZRW (ESRI 2022)

3. Meteorological and Hydrological Data

The metrological and hydrological data were acquired from various governmental institutions. Specifically, the rainfall data for the ZRW were sourced from the Ministry of Water and Irrigation (MWI). The data were a daily rainfall measurement from 1987 to 2018, collected from 42 rainfall stations. However, due to incomplete records, only 36 stations were used in this study. In addition, data on the surface water elevation, storage, and discharge from the KTD were procured from the Jordan Valley Authority (JVA). The characteristics of the KTD such as dam type, crest width, height, and storage capacity were also collected from the JVA. Table 1 shows the characteristics of the KTD.

Table 1. General characteristics of KTD (MWI, 2024)

Type of the dam	Non-homogenous earthfill
Length (m)	350
Crest width (m)	11.5
Height (m)	108
Catchment area (km^2)	4300
Storage at full supply level (MCM)	88.5

4. Hydrologic Modeling

The use of Probable Maximum Flood (PMF) is a common practice to guarantee the safety of hydraulic structure and as a reference for flood disaster management (Alias et al., 2013a). To determine the PMF values, input data of Probable Maximum Precipitation (PMP) are required (Desa et al., 2001). The World Meteorological Organization (WMO) defines the PMP as the upper limit of precipitation that is expected to occur within a specific time and location (WMO, 2012). In this study, the values of the PMP are estimated

using the Hershfield statistical method. It is a well-establish technique that has been widely applied (Hershfield, 1961). The PMP can be estimated using the following equation:

$$X_{PMP} = X_n + S_n \times K_m \quad (1)$$

$$K_m = \frac{X_{max} - X_{n-1}}{S_{n-1}} \quad (2)$$

where X_n denotes the annual maximum rainfall average, and S_n represents the standard deviation of annual maximum rainfall. The K_m factor is the frequency factor, while X_{max} is the highest recorded rainfall value. Finally, X_{n-1} and S_{n-1} indicate the mean and standard deviation of the annual maximum rainfall data without the highest recorded value.

The simulation of inflows into the dam was conducted using the HEC-HMS rainfall-runoff model, which is proficient in generating runoff estimations from daily rainfall data (CEIWR-HEC, 2017). The preparation of HEC-HMS projects involved utilizing the WMS software to facilitate the requisite processes. WMS is a comprehensive watershed solution that automates delineation, as well as hydrologic and hydraulic modeling and facilitates floodplain and storm drain mapping. For the simulation, the soil conservation service-curve number (SCS-CN) method was used to estimate losses, the SCS unit hydrograph was employed to transform the inputs, and the Muskingum-Cunge method was used to determine channel routing.

5. Hydraulic modeling

Dam breach parameters were estimated using MacDonald and Langridge-Monopolis (1984), Von Thun and Gillette (1990), Froehlich (1995), Froehlich (2008), and Xu and Zhang (2009) equations. The breach shape was assumed to be a trapezoidal breach as shown in Figure 6. HEC-RAS can estimate the dam breach parameters of the previous models using the Parameter Calculator option. In this research, Parameter Calculator was used to estimate the parameters for the models mentioned above utilizing various variables such as dam characteristics and initial conditions at the time of failure.

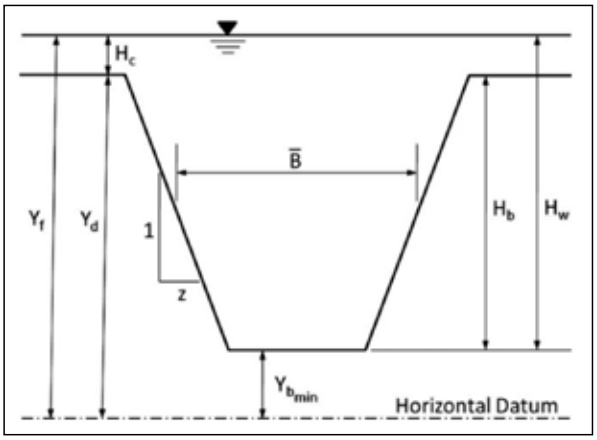

Figure 6. Dam breach shape and parameters (Froehlich, 2008)

In this study, two scenarios were simulated. They are overtopping and piping failures. It was assumed that the dam would fail when water would reach the crest of the dam in the overtopping scenario. In the piping scenario, the failure occurs in fair weather. Accordingly, the date 6/6/2020 was chosen for testing this scenario, as a typical day in the summer. At this date, the height of water and storage volume in the KTD was 99 m and 67.9 MCM. The data of water elevation-storage volume are a daily record of water elevation and storage from 2008 to 2020 for the KTD. Using this data, an elevation-storage volume diagram was formed as shown in Figure 7. A two-dimensional flow area was created using a square grid with a spacing of 75 m. To cover the entire area downstream of the dam, 270,000 square cells were generated. Moreover, a 30-second interval was selected as a time step for the simulation.

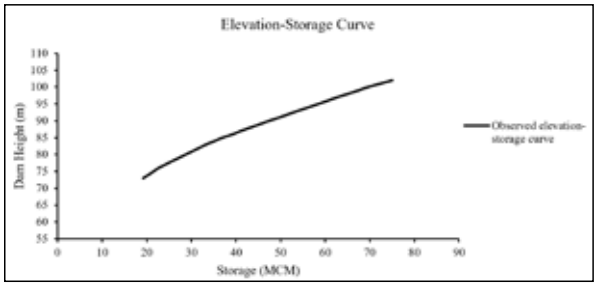

Figure 7. Elevation-Storage curve of the KTD

In this study, a 2D unsteady flow simulation was used to route the PMF hydrograph through the dam utilizing the 2D diffusion wave equations. The HEC-RAS model generates several maps such as inundation, velocity, duration, and arrival time maps. These maps were exported to the ArcGIS and the hazard map was classified according to the depth of the water resulting from the breach flood.

In summary, the paper investigates the hydrological analysis of the water upstream of the dam, the dam failures empirical models, and the hydraulic characteristics of the flood wave in the downstream areas of the dam.

6. Results and Discussion

The study aims to investigate the hydrologic characteristics of ZRW and estimate dam breach parameters for KTD. Also, a 2-D unsteady flow was simulated to predict the resulting flood in the downstream regions of the dam. Finally, flood mapping was performed to visualize the flood in these regions.

6.1 Probable Maximum Flood Hydrograph

Utilizing the features of the WMS software, the basin was divided into 8 sub-basins as shown in Figure 8, the CN values for these basins were entered, the PMP values that were calculated using Hershfield's equation were entered, and the channel routing was done using the Muskingum-Cunge method. After that, the final WMS model was exported to the HEC-HMS. Finally, a PMF hydrograph was computed using the SCS method.

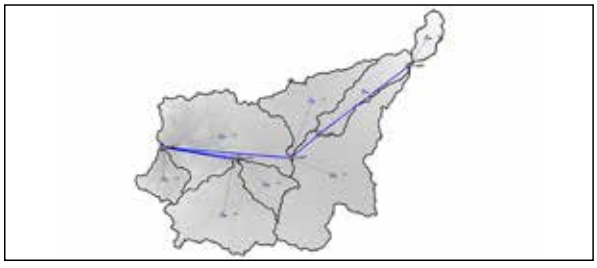

Figure 8. Hydrologic model using HEC-HMS

The CN of the basin was estimated to be approximately 88. Table 2 represents the values of the land use for the basin in general. It is noted from the table that most of the watershed area is composed of shrubs, approximately 40%. In addition, 28.7% of the land is bare, while urban land represents 19.3% of the ZRW.

Table 2. Land use of ZRW

Category	Land use (%)
Water	0.1
Trees	0.6
Grass	0.1
Crops	11.2
Scrub/Shrub	40.1
Urban Area	19.3
Bare Ground	28.7
Total	100

The PMF hydrograph from the HEC-HMS was used in HEC-RAS as an input. Figure 9 represents the PMF hydrograph of the PMP in the ZRW. The maximum flow was approximately 3823.

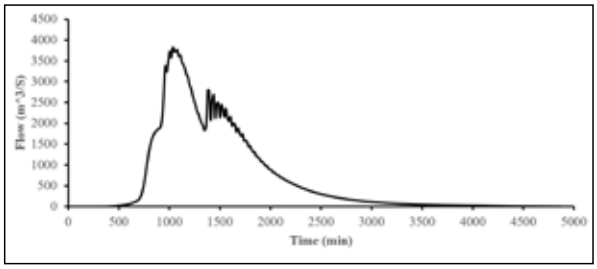

Figure 9. PMF hydrograph of the PMP

6.2 Breach parameters and breach flood hydrographs

Dam failure was simulated for both scenarios, piping and overtopping, and breach hydrograph curves were found at the outlet of the dam. Tables 3 and 4 show the dam breach parameters for overtopping and piping failures that were estimated using the five models mentioned previously. Compared to what is often utilized in HEC-RAS for breach development time, the Xu and Zhang data used in the equation for breach development time cover more of the initial and post-erosion times. Thus, the use of breach formation time would give inaccurate results (Brunner et al., 2016).

Table 3. Dam breach parameters for overtopping failure

Method	Breach Bottom Width (m)	Side Slope (H: V)	Breach Development Time (hrs.)
MacDonald et al.	47	0.5	2.65
Froehlich (1995)	96	1.4	0.83
Froehlich (2008)	70	1	0.68
Von Thun & Gillette	215	0.5	1.85
Xu & Zhang	151	1.08	1.94

Table 4. Dam breach parameters for piping failure

Method	Breach Bottom Width (m)	Side Slope (H: V)	Breach Development Time (hrs)
MacDonald et al	22	0.5	2.28
Froehlich (1995)	60	0.9	0.69
Froehlich (2008)	47	0.7	0.57
Von Thun & Gillette	192	0.5	1.67
Xu & Zhang	68	0.59	2.16

Figures 10 and 11 represent the breach flow hydrograph for overtopping and piping failures using the five equations. Froehlich's 1995 model has the greatest breach rate for overtopping failure, according to the data, with a value of 67782 . Von Thun is next, with a peak flow of roughly 65609 , and Froehlich 2008 results, with a peak flow value of 65456 . After that, the maximum discharge predicted by the Xu and Zhang equation is 35832 . Finally, the MacDonald and Langridge-Monopolis equation produced the lowest result, which amounted to 21499 . The breach flows for the five equations for pipe failure were as follows: 43748 for Froehlich 2008, 42049 for Froehlich 1995, 23534 for Von Thun and Gillette, 17487 for Xu and Zhang, and 13321 for MacDonald and Langridge-Monopolis.

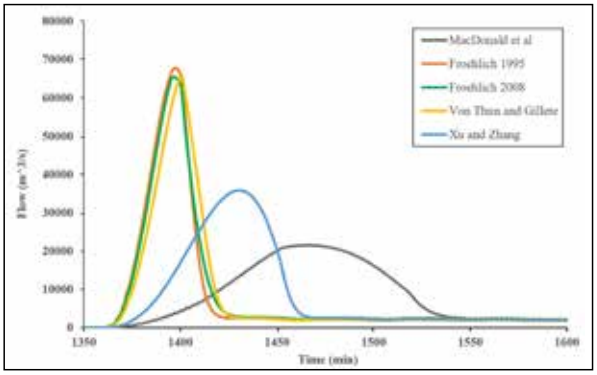

Figure 10. Breach flow hydrographs for overtopping failure

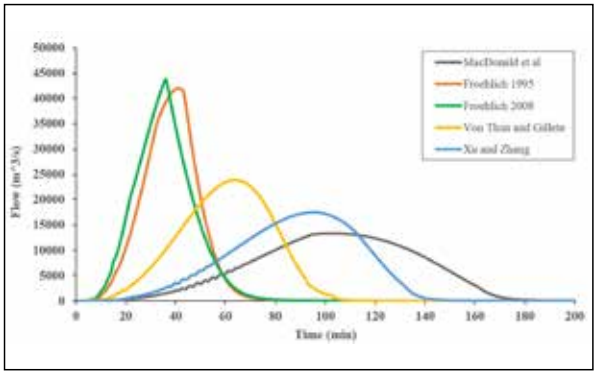

Figure 11. Breach flow hydrographs for piping failure

6.3 Flood Hazard Mapping

There are three urban regions located downstream of the King Talal dam, namely, Deir Alla, Twal Shamali, and Twal Janoobi, with a population exceeding 27,000 (Department of Statistics, 2020). Figure 12 displays the submersion map divided into several groups according to the MILT classification, as previously mentioned. It is noted that the majority of the flooded regions are categorized as H5, which stands for extremely hazardous regions. Deir Alla and Twal Shamali are fully included in this classification, whereas Twal Janoobi is only partially included. The remaining sections of this region are included in the H4 and H3 categories. In addition, Table 5 illustrates the area of the flooded areas for both scenarios. We note that the submerged areas, due to the overtopping scenario, are higher than the submerged areas due to the failure of the piping.

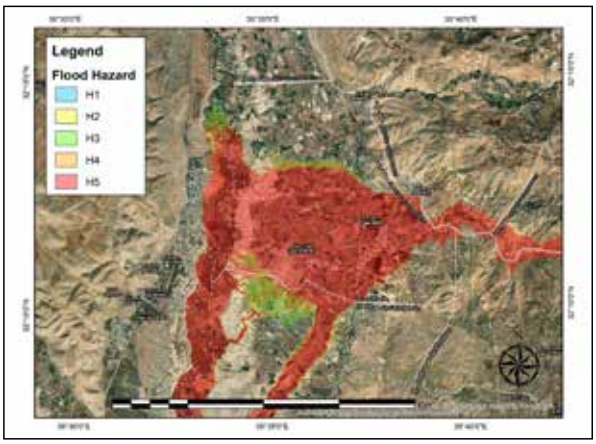

Figure 12. Flood hazard map due to dam failure

Table 5. Inundated area due to dam failure

Method	Inundated area (km^2)	
	Overtopping	Piping
MacDonald et al	163.0	129.7
Froehlich (1995)	162.1	132.5
Froehlich (2008)	161.9	132.6
Von Thun & Gillette	162.0	131.3
Xu & Zhang	160.4	129.8

Figure 13 represents the height of water resulting from the simulation of the dam failure. The maximum height in the Deir Alla region is 41 meters, while it is 25 and 17 meters in Twal Shamali and Twal Janoobi. These areas are considered residential areas. Also, the height of the water in the valleys and agricultural areas exceeds 100 meters.

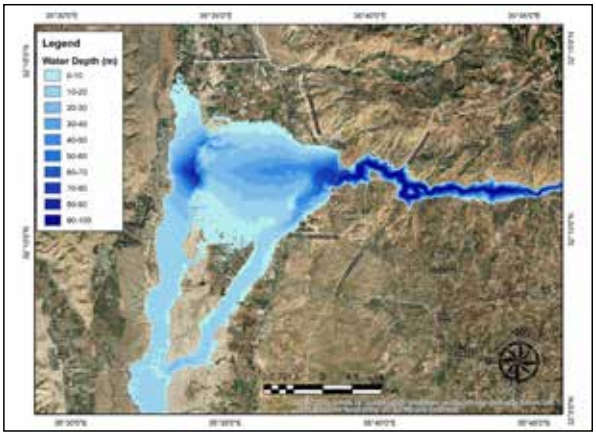

Figure 13. Inundation map for the downstream area of the dam

In terms of the flood's arrival time, Figures 14 and 15 show how long it would take for each urban region for the two failure scenarios. Since the dam's breakdown, the predicted flood takes around two and a half hours to reach Deir Alla and three hours to reach Tawal Shamali and Tawal Janoobi according to MacDonald model. The flood in the other models is comparatively faster than that in the MacDonald model.

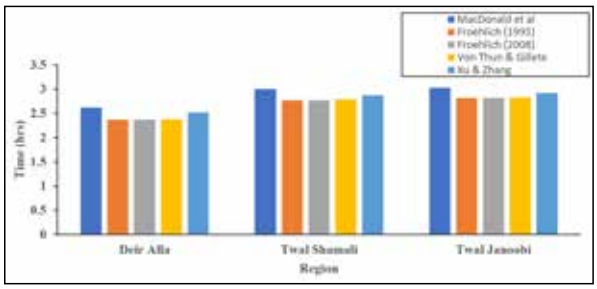

Figure 14. Arrival time for overtopping failure

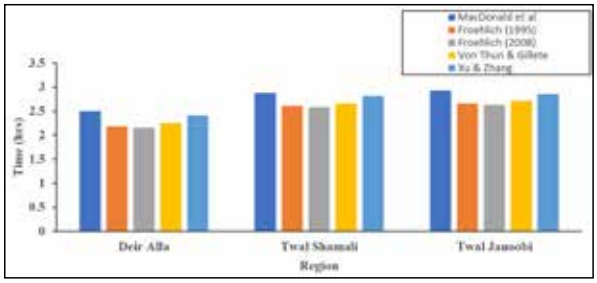

Figure 15. Arrival time for piping failure

Velocity maps provide important details regarding flood flow dynamics and potential erosion. Both the population and the infrastructure could be seriously affected. Figure 16 presents the velocity map that resulted from the simulation. The flood velocity in Deir Alla is about 85 m/s, which is higher than the other two urban regions. Figure 17 depicts how long the flood lasted in each area. Deir Alla's eastern region is subject to floods that last for more than 48 hours. With regard to the remaining areas, the flood continues for a maximum of eight hours. Tawal Shamali and Tawal Janoobi regions are affected by lengthy floods that persist for around 40 hours.

Figure 16. Velocity map due to dam failure

Figure 17. Flood duration period

7. Conclusions

Dam breach parameters were estimated using different models for two failure mode scenarios, namely, overtopping and piping failures. A 2-dimensional unsteady flow simulation was used to route the breach flood in the downstream area of the dam. The maximum breach flows for overtopping and piping scenarios were estimated to be 65456 and 43748 m^3/s, respectively. The study generated inundation, flood hazard, duration, and velocity maps for the dam's downstream areas. Most of the inundated areas were classified as extremely hazardous. The maximum depth of water was approximately 107 meters at some agricultural lands. More specifically, the inundation map shows that the depth of water ranged from 10 to 50 meters in Deir Alla, Tawal Shamali, and Tawal Janoobi regions. The velocity of the flood exceeds 100 meters per second in some steep places and wadis.

Furthermore, the fastest arrival time of the flood is estimated to be 2 hours after the breach occurred due to piping failure. Also, the flood in some regions lasts for about 40 hours. This underscores the importance of good emergency response plans and long-term flood management policies.

Overall, the paper provides valuable insights into the dynamics of dam breach floods and their effect on downstream regions. These findings could aid in developing plans and policies in order to minimize the risk of loss of life and property due to dam failure. The emergency preparedness strategies include developing a telemetry monitoring system for the dam body and spillway, an early warning system for the upstream watersheds, and physical evacuation and response plans for residents downstream of the dam. It is recommended to propose various flood mitigation and flood risk management tools and improvements for major infrastructures like roads, bridges, and hospitals.

The results of this analysis can help local authorities to prioritize their plans based on the observed arrival times and flood durations. It is important to engage local communities, government agencies, and other stakeholders in developing integrated flood preparedness strategies and management plans and raising their public awareness during a flood crisis.

It is recommended to conduct more national dam break studies to investigate possible dam breaks for the major dams in Jordan and link that to the National Crisis Management Center.

References

Al-Azzam, N.; Al-Kuisi, M. (2021). Determination of Flash Floods Hazards and Risks for Irbid Governorates Using Hydrological and Hydraulic Modelling. Jordan J. Earth Environ. Sci. (JJEES) 12, 81–91.

Alias N E, Luo P, Takara, Kaouru. (2013). Probable Maximum Precipitation Using Statistical Method for The Yodo River Basin Journal of Japan Society of Civil Engineers 69, 157-162

Al-Amoush, Hani & Alshabeeb, Abdel Rahman & Al-Adamat, Rida & Al-Fugara, A'Kif & Alayyash, Saad & Shdeifat, Akram & Al-Tarazi, Eid & Rajab, J.. (2017). The Use of GIS Techniques and Geophysical Investigation for Flood Management at Wadi Al-Mafraq Catchment Area. Jordan J. Earth Environ. Sci. (JJEES) 8, 97-103.

Al-Salahat, Murad, Radwan Al-Weshah, and Saif Al-Omari. (2024). 'Dam break risk analysis and flood inundation mapping: a case study of Wadi Al-Arab Dam', Sustainable Water Resources Management, 10: 74.

Al-Shibli, F. M., Maher, W. A., Thompson, R. M. (2017): The Need for a QuantitativeAnalysis of Risk and Reliability for Formulation of Water Budget in Jordan. – Jordan J. Earth Environ. Sci (JJEES) 8, 77-89

Aydemir, A. and Güven, A. (2017). 'Modified risk assessment tool for embankment dams: case study of three dams in Turkey.' Civil Engineering and Environmental Systems. 34 (1), 53-67.

Brunner, G. Benchmarking of the HEC-RAS Two-Dimensional Hydraulic Modeling Capabilities; U.S. Army Corps of Engineers: Davis, CA, USA, 2018; pp. 1–137.

Brunner, G. W., United States Institute for Water Resources (U.S.), and Hydrologic Engineering Center (U.S.). (2016). 'HEC-RAS river analysis system: Hydraulic reference manual.' Davis, CA: US Army Corps of Engineers, Institute for Water Resources, Hydrologic Engineering Center.

CEIWR-HEC; HEC-HMS. Hydrological Modeling System: Application Guide; US Army Corps of Engineers Hydrologic Engineering Center: Davis, CA, USA, 2017; pp. 3.1–3.19.

Department of Statistics. (2020). 'Estimated Population of the Kingdom by Municipality and Sex, at End-year 2020.' Jordan.

Desa M N, Noriah A, Rakhecha P. (2001). Probable Maximum Precipitation for 24 h Duration Over Southeast Asian Monsoon Region-Selangor Malaysia. Atmospheric Research 58(1) 41-54

Dinçergök, T. (2007). 'The Role of Dam Safety in Dam-Break Induced Flood Management.' International Conference on River Basin Management, May 23th -25th. pp. 683-691, Southampton, UK.

El-Radaideh, N., Al-Taani, A. A., & Al Khateeb, W. (2017). Status of sedimentation in King Talal Dam: case study from Jordan. Environmental Earth Sciences, 76, 132.

Froehlich, D. (1995). Peak Outflow from Breached Embankment Dam. Journal of Water Resources in Planning and Management,121, 90-97.

Froehlich, D. (2008). 'Embankment Dam Breach Parameters and Their Uncertainties'. Journal of Hydraulic Engineering, 134, 1708-1721.

Goodarzi, E., Lee, T. S., & Ziaei, M. (2013). Dam overtopping risk using probabilistic concepts – Case study: The Meijaran Dam, Iran. Ain Shams Engineering Journal, 4, 185-197.

Hershfield DM. (1961). Estimating the probable maximum precipitation. Journal of the Hydraulics Division, 87, 99–106

MacDonald, T. and Langridge-Monopolis, J. (1984). 'Breaching Characteristics of Dam Failures.' Journal of Hydraulic Engineering, 110, 567-586.

USDA NRCS. (1986). Urban Hydrology for Small Watersheds. US Department of Agriculture, Soil Conservation Service, Engineering Division: Washington, DC, USA.

Von Thun, J. and Gillette, D. (1990). 'Guidance on breach parameters' (Unpublished internal document, 17 p.). U.S. Bureau of Reclamation, Denver, Colorado, March 13, 17 p.

Wahl, T. L. (1997). Predicting embankment dam breach parameters-a needs assessment. In: Proceedings of the International Association for Hydraulic Research Congress, (pp. 48–53). San Francisco, California: IAHR.

Whitham, G. (1955). 'The effects of hydraulic resistance in the dam-break problem.' Proceedings of the Royal Society A, 227 (1170), 399–407.

World Meteorological Organization (WMO). (2012). Manual for estimation of probable maximum precipitation (PMP). Geneva, Switzerland: World Meteorological Organization.

Xu, Y., Zhang, L.M. (2009). Breaching parameters for earth and rockfill dams. Journal of Geotechnical and Geoenvironmental Engineering, 135, 1957–1970.

JJEES

JJEES (2025) 16 (1): 35-49
ISSN 1995-6681

Jordan Journal of Earth and Environmental Sciences

Cloud-based Rainfall-run-off Model for Assessment of Long-Term Rainfall Variability and Trends Using Google Earth Engine

D.Vetrithangam[1*], B. Arunadevi[2],
Naresh Kumar Pegada[3], Sukhpreet Kaur[4], B. KrishnaPrasad[5]

[1]Department of Computer Science & Engineering, Chandigarh University, Mohali, 140413, India
[2]Department of ECE, Dr. N.G.P Institute of Technology, Coimbatore, India
[3]Department of CSE (AI & ML), Keshav Memorial Engineering College, Telangana, India
[4]Department of Computer Science & Engineering, Chandigarh University, Mohali, 140413, India
[5]Department of CSE, Koneru Lakshmaiah Education Foundation, Vaddeswaram, Guntur, Andhra Pradesh, India.

Received on 31 August 2023; Accepted on 27 November 2024

Abstract

Several engineering constructions, such as canals, bridges, culverts, and road drainage systems, depend on rainfall for their creation. Different types of rainfalls normal, deficit, excessive, and seasonal are all understood using the daily rainfall data for the seven-year timeframe (2015–2021). Farmers, urban engineers, and planners of water resources will all benefit from the knowledge provided by this analysis as they determine the availability of water and plan the appropriate storage. To examine the variability in rainfall, the average, total monthly and annual rainfalls were determined. Most existing techniques used the curve number method to compute statistical rainfall runoff for a particular region; this technique ignores the effects of rain intensity and duration because it lacks an expression for time. The Soil Conservation Service curve number method is adaptable and widely used for runoff estimation. The main scope of this paper is to compute the statistical analysis of rainfall-runoff for the state of Andhra Pradesh. The SCS–CN method is implemented in Google Earth Engine (GEE) on the satellite images to estimate the runoff for the state of Andhra Pradesh. The result demonstrates that the average and total runoff values from 2015 to 2021 are 151.1786, and 1058.25, respectively, and their average and total precipitation values are 926.5884 and 6486.119. And this research work finds the facts: the year 2020 has the highest rainfall (1276.32 mm); the year 2016 has the lowest runoff (591.33). Engineers and farmers will be able to determine the necessary input value for the design and analysis of engineering constructions as well as for crop planning with the assistance of the computed detailed statistical analysis of this region.

Keywords: *Runoff, Precipitation, Curve Number, Land Cover, Land Use, Soil Texture, Google Earth Engine.*

1. Introduction

Water is indispensable to all life processes and cannot be replaced. In addition to being a source of power and beneficial resource consumption within the country, agriculture, and industry, water is also important in transportation. Rainfall is a region's primary source of water, and it has a significant impact on agriculture. Plants obtain water from both natural sources and irrigation. Forecasting the likelihood of rainfall is crucial because crop production, especially in rain-fed areas, depends on rainfall patterns that can be analyzed using historical hydrological data and statistical methods. Probability distribution or occurrence aids in connecting the size of extreme occurrences such as flooding, droughts, and violent storms with the amount of times they occur, so that the likelihood of occurrence over time can be predictably calculated. The collection of hydrological data can be fitted with a frequency distribution to determine the likelihood that a random parameter will occur. To match the distribution, statistical parameters are employed to assess the hydrological data and evaluate its variability. For planning water resources, a number of models, ranging from conceptual to empirical and physically based, have been developed. The most crucial hydrological component is run-off. The establishment of soil conservation procedures for projects was delegated to the Soil Conservation Services (SCS), which was established in 1933 (Abdul Ghani et al., 2016waterways, irrigation schemes, water harvesting, erosion control structures, and groundwater development strategies requires accurate estimation of surface runoff. However, hydrologists in Saudi Arabia face serious challenges, specifically due to the rare availability of surface runoff data. In this study, the soil conservation service-curve number (SCS-CN). In order to simulate the runoff process, the data-driven models identify the ideal correlation between the data inputs and the result series. In order to explain variations in runoff modeling and flood prediction, the benefits and drawbacks of the models above were finally explored (Ahmad et al., 2022). To estimate the surface run-off, Ahmad recommended taking into account factors such as soil, antecedent rainfall, geographical distribution, and land use/land cover (LULC) type. This classification represents a significant accomplishment for the SCS curve number (CN) method, which provides an

* Corresponding author e-mail: vetrigold@gmail.com

observational connection to estimate run-off and considers initial abstraction, depending on the soil variety and LULC (Al-Ghobari et al. 2020). The CN approach is also used to calculate surface run-off by several of the popular models, like SWAT and HEC-HMS (Anderson et al., 2004; Gholami and Khaleghi, 2021). The SCS model was initially created for the USA to calculate the actual surface water runoff from tiny basins' few rainfalls (Animashaun et al., 2020which is of prime importance in hydrological engineering, agricultural planning and management, environmental impact assessment, flood forecasting, and others fields. This article reviews the methodology and associated hydrological models used for runoff estimation along with their advantages and limitations. Furthermore, discussion focuses on the potential applications of Remote Sensing (RS, Arnold and Allen, 1996, Arvind et al., 2017). `

The incident in December 2014 is one example of how an unforeseen heavy rainfall storm contributed to rainfall totals those broke records. Many of its occurrences are proof of global warming and climate change, which will have an impact on these extreme rainfall events (Baquero et al., 2005). In the past, highly accurate classical rain gauges or wide-area microwave radars have been used to confirm rainfall measurements. Rainfall occurrences' drop size distribution (DSD) must be investigated in order to create and validate more precise rainfall forecast algorithms. The dispersion of drop sizes will be investigated and used in the analysis of rain acquisition with a disdrometer, utilizing observations from the NASA TRMM satellite and rain gauges (Baquero et al., 2005). Rapid development over the past few decades has significantly altered the LULC pattern, which affects CN and hydrological factors affecting catchment run-off. Geospatial technology advancements make it easier to incorporate these elements when spatially and temporally estimating run-off. The utilization of digital elevation models for hydrological modeling depending on an area's topography has been made possible by the application of GIS (Soulis and Dercas, 2007). The soil composition, drains, LULC, geography parameters, and other region features can be extracted using RS and stored as a georeferenced database in a GIS. In the GIS context, the retrieved layers are then integrated with meteorological information for further analysis, interpretation, and visualization of evolving rainfall-runoff models (Chormanski et al., 2008, Sayd and Mubi, 2020). Employing a high-quality land surface model, such as a Digital Elevation Model (DEM), alongside data from Earth observation satellites' visual and radar systems is essential for identifying flood-prone regions and analyzing the impacts of flood events. This integrated approach enhances the understanding of flood dynamics and facilitates more effective flood management strategies (Ebrahimian et al., 2009). In order to categorize and analyze watershed areas and runoff models, remote sensing methods can supply data about the land surface's space and time. In order to confirm the results of spatial models, they can measure surface characteristics (like surface hardness, LULC class, etc.) and their time-based variations on the one hand and relate geologically significant areal phenomena on the other (Eliza et al., 2016, Gupta and J. Dixit, 2022).

According to the current statistical study, which offers a clear picture of rainfall data, the region does not have enough rainfall to support wet crop production. Improved irrigation and crop production in this region depend on the coordinated use of groundwater and accessible rainfall. The Soil Conservation Service Curve Number (SCS-CN) method is a widely used hydrological model for estimating direct runoff or infiltration from rainfall. Developed by the USDA's Soil Conservation Service, this method relies on a curve number (CN) that reflects land use, soil type, and antecedent moisture conditions (Soulis and Valiantzas, 2012, Soulis and Valiantzas, 2009).

The synergistic approach of remote sensing and GIS techniques enables efficient flash-flood monitoring and damage assessment in the Thessaly plain area. This integration enhances the accuracy of flood prediction and provides valuable insights for disaster management and mitigation strategies (Psomiadis et al., 2019). Empirical data from typhoon occurrences was used to test the correctness of the surface runoff model (Psomiadis et al., 2020). For a few specific rainfall occurrences in the watershed, the runoff depth was calculated using the NRCS-curve number approach (Rajbanshi, 2016.) A revisit of NRCS-CN Inspired Models coupled with RS and GIS for Runoff Estimation examines enhanced runoff estimation by integrating the NRCS-CN model with remote sensing (RS) and GIS. This approach improves spatial accuracy by using satellite data to capture land use, soil, and rainfall variability (Verma et al., 2017). Rainfall-Runoff Risk characteristics of Urban Function Zones in Beijing Using the SCS-CN Model examines runoff risks across various urban zones in Beijing. The SCS-CN model is applied to assess how land use and soil types influence runoff potential, supporting targeted flood management strategies for diverse urban functions (Wei et al., 2018).

The application of the NRCS-CN method enhances watershed runoff estimation and disaster risk assessment by using land and soil data to predict runoff levels. Integrating geomatics tools with this method improves accuracy in assessing natural hazards. This approach aids in disaster preparedness and risk management (Zhang, 2019). Research on Rainfall Estimation Based on Improved Techniques explores advancements in methods for more accurate rainfall estimation. The improved approach enhances the integration of real-time data, leading to better rainfall predictions (Zhang et al., 2022).

The SCS-CN approach was a useful tool in this study since it made it easy but effective to determine the direct runoff reaction for each soil, land usage, and maintenance combination (Jehanzaib et al., 2022). It incorporates several of the parameters of soil, land utilization, and land maintenance factors that have an impact on runoff generation into a single CN factor and includes simple-to-obtain and well-documented environmental inputs (Ling et al., 2020, Attah et al., 2020). Studies on rainfall variability used the linear regression model (LRM), precipitation concentration index, and rainfall variability index. Nonparametric Mann-Kendall (MK) tests and the Kriging interpolation method were

utilized for trend analysis and change point identification, as well as for the spatial analysis of rainfall (Salahat and Al-Qinna, 2015). Hypothetical probability distributions for initial loss data were evaluated for their influence on design flood estimates. The Beta and Gamma distributions effectively approximate initial losses in Australia. Sample size significantly impacts the accuracy of probability distributions, with mixed results observed based on varying thresholds (Loveridge and Rahman, 2021). To examine the rainfall-runoff stake features of the research field, the SCS-CN model was used. High runoff risk cluster locations were primarily found in the study area's centre, while areas with a low likelihood of runoff were mostly found among the roads. The two CN system approach outperforms earlier methods focused on a completely asymptotic CN value determination and offers reasonable accuracy (Psomiadis et al., 2020). The observed CN value fluctuation cannot always be explained by CN value variation based solely on AMC group (Moglen et al., 2022). The major goal of the 7KH model is to offer a useful tool in regions with severe fresh water shortages, growing water needs, and a severe lack of hydrometric data (Musgrave., 1955). Rainfall data was acquired from a global weather station using the Thiessen polygon method, which is related to a Geographic Information System application. The findings indicated that two rainfall stations described the rainfall variation across the study object (Nganro et al., 2020).

Measuring rainfall runoff can be a challenging task due to various factors that can affect the accuracy of measurements. It presents several challenges. First, inadequate instrumentation can significantly impact accuracy; the quality and proper calibration of measurement devices are crucial, as some instruments may lack sensitivity to low flows or may become clogged with debris. Additionally, land use changes, such as deforestation and urbanization, can alter the surface properties of a catchment, thereby affecting its hydrological response to rainfall. For instance, urbanization often results in increased impervious surfaces and reduced infiltration, leading to higher and faster runoff. The topography of an area also plays a role; steep slopes can cause rapid runoff and erosion, while flat land may allow water to puddle and evaporate before it contributes to runoff. Furthermore, antecedent moisture conditions are significant, as the soil's moisture content before a rainfall event influences runoff behavior. Saturated soil reduces infiltration and leads to increased runoff. Lastly, measuring rainfall runoff through satellite data introduces its own challenges, as remote sensing techniques come with limitations and uncertainties that must be considered.

Measuring rainfall-runoff using satellite data presents several challenges. First, the spatial and temporal resolution of satellite data may be insufficient to capture the detailed hydrological processes that influence runoff, often being too coarse to detect small-scale variations in rainfall and runoff. Additionally, satellite measurements typically cover only limited areas, which may not represent the entire catchment, complicating efforts to extrapolate results, particularly in regions with complex topography. Calibration and validation of satellite data against ground-based measurements are essential for ensuring accuracy, but this process can be challenging due to the limited number of ground observations. Furthermore, cloud cover and atmospheric interference can significantly impact the accuracy of satellite-based rainfall measurements, as clouds may obscure the satellite's view of the Earth's surface, while atmospheric elements, such as water vapor, can distort readings. The cost and limited availability of satellite data, especially in developing countries, can hinder widespread use. Finally, the algorithms employed to derive rainfall-runoff from satellite data have inherent limitations and uncertainties; different algorithms may yield varying results, and their accuracy can be influenced by the location and type of rainfall event. While satellite-based measurements of rainfall-runoff have the potential to provide valuable insights, they come with their own set of challenges that need to be addressed to ensure their accuracy and reliability. Proper calibration, validation, and careful interpretation of the results are necessary to obtain meaningful insights from satellite-based measurements.

Our research work considered the following challenges and problems:

- Spatial and temporal resolution, data availability, land use, and limited coverage are needed to provide the solution.
- Most of the research work considered a small regional area for their study in rainfall-runoff estimation.
- No comparison is provided based on the metrology department's data in most of the research work.
- Finding the variation in the precipitation and runoff for every year and month will assist the researchers in performing predictions.

Based on the challenges, discussed above, a system is proposed to estimate the rainfall-runoff and precipitation for Andhra Pradesh from 2015 to 2021 by applying the SCS curve number technique to the land and land cover data and the soil texture class. The variation in precipitation and runoff for every year and the correlation among the years in rainfall is analyzed and presented. The remainder of the paper is organized as follows: Section 2 provides a comprehensive analysis of the various methods developed for estimating and assessing rainfall, runoff, and precipitation in a specific region. Section 3 covers the data collection, study area and methodologies used in this research. Section 4 explains the system model, architecture, and working principles of the current study. Section 5 describes the results produced by the proposed model and offers a detailed comparative analysis. Finally, Section 6 concludes the paper and discusses future directions.

2. Literature Review

Zhang et al. (2011) proposed a NRCS-CN approach for calculating watershed runoff and risk of disasters, which produced 90.8% accuracy. When runoff is poor, this strategy is useless for reducing errors. Ahmad et al. (2022) analyzed the long-term variation in rainfall and trends using satellite data by employing artificial neural networks. In Gujrat, the

maximum annual rainfall was found with a statistically significant upward trend (50.8 mm/decade). Wetchayont et al. (2023) used the geostatistical method to estimate rainfall in Bangkok by utilizing satellite, radar, and gauge rainfall datasets. In this work, the mean estimated rainfall ranged from 0.0012 to 3.80 mm h-1 and 0.02 to 2.53 mm h−1. Gupta et al. (2022) used the NRCS-CN approach while integrating GIS and remote sensing. The normal runoff depth and mean annual precipitation ranges are 444.50 to 1960 mm and 936 to 3520 mm, respectively. Fowler et al. (2022) described how rainfall-runoff interactions changed before, during, and after Australia's Millennium Drought. The Millennium Drought and droughts from 1950 to 1990 are contrasted with two droughts that occurred before 1950. Saragih et al. (2022) used observational rainfall data from Central MKG Region I Medan to evaluate the CHIRPS rainfall estimation data. November 2018 saw the highest CHIRPS monthly correlations of 0.520. Raza et al. (2023) proposed Irrigation Management Using GIS, which could help to comprehend rainfall calculation is that it measures the transference of soil, plants, and environment and produced accuracy 75.47%. Hassan et al. (2022) proposed a Machine Learning algorithm for Radar-Based Rainfall Assessment. The investigation also revealed that the RMG and RBRT(RC) estimators significantly overestimate the overall seasonal rainfall accumulation by around 60%. Soulis and Valiantzas (2012) proposed a rainfall estimation model, which will reduce the relative error to 3.18% and accounts for 43.5% of the precipitation estimate without filter wave calibration. Liu et al. (2023) suggested a deep learning-based approach to assess the impact of artificial precipitation, produced residual rainfall 9.98 mm in Shiyan region on 26th April 2018. Seong et al. (2022) Proposed Grid Rainfall-Runoff Model (GRM) for assessment of Uncertainty measures, which produced logarithmic Nash-Sutcliffe Efficiency 0.97. Loveridge and Rahman (2021) proposed Monte Carlo method to find variability in design flood estimates; it reduces the relative error to 3%. Sishah (2021) used SCS-CN approach to assess the rainfall runoff in the awash river basin located in Ethiopia, the correlation coefficient of 0.9253 is produced between the anticipated runoff and the actual runoff. Moglen et al. (2022) used the NRCS Curve Number Technique for Determining the Curve Number from Rainfall-Runoff values; it produced the mixed value from 0.05 to 0.20. Gholami and Khaleghi (2021) modelled the rainfall-runoff mechanism using a multilayer perceptron (MLP) network. For the date 15th, 1995, the correlation between the observed and simulated values is 0.6, and the correlation between the observed and simulated information is 0.6. Mohammadi et al. (2022) proposed a multi-conceptual method using machine learning for runoff and rainfall predictions, the model produced the accuracy of 68% of NSE.

3. Materials and Methods

3.1 Dataset

The Terra and Aqua combined Moderate Resolution Imaging Spectroradiometer (MODIS) Land Cover Type (MCD12Q1) Version 6.1 data package provides global land cover categories at yearly intervals from 2001 to 2021 (https://lpdaac.usgs.gov/products/mcd12q1v061/#tools). The MCD12Q1 V 6.1 data product is generated using trained classifications of MODIS. For information on soil texture categories (USDA system) for six typical soil depths, another dataset, called OpenLand Map Soil Texture Class (USDA System)(https://developers.google.com/earth-engine/datasets/catalog/OpenLandMap_SOL_SOL_ TEXTURE-CLASS_USDA-TT_M_v02), is used to derive from the soil texture package in R's expected soil texture fractions. One of the Curve Number approaches is mainly used in the current case research, which assumes determining the catchment's surface runoff. Calculating the amount of runoff from the land surface that enters rivers or streams is made more accessible by using the SCS-CN approach. The dataset, used as the rainfall dataset, is "CHIRPS Daily: Climate Hazards Group InfraRed Precipitation with Station data (Version2.0Final)" (https://developers.google.com/earth-engine/datasets/catalog/UCSB- CHG_CHIRPS _DAILY). A 30+ year quasi-global rainfall dataset is available under Climate Hazards Group InfraRed Precipitation with Station Data (CHIRPS), combining in-situ station data with 0.05° resolution satellite imagery.

3.2 Study Area

The present study concerns the state of Andhra Pradesh in India. As shown in Figure 1, the state is located in India's south-eastern coastline region. Its 162,975 km^2 make it the seventh-largest state in terms of size (62,925 sq mi).

The terrain of the state is diverse, spanning from the Nallamala Hills and Eastern Ghats Hills to the Bay of Bengal coastlines, which sustain a wide range of ecosystems and a vast diversity of flora and animals. The state is traversed by its two principal rivers: the Krishna and Godavari. The state's 975-km-long coastline stretches across the Bay of Bengal from Srikakulam to Nellore (606 mi). The entire population is made up of 14,610,410 urban residents and 34,776,389 rural residents, for a population share of 29.6%. Andhra Pradesh's economy is mostly dependent on agriculture and cattle. Four large Indian rivers—the Godavari, Krishna, Penna, and Tungabhadra—provide irrigation and pass through the state. 60 percent of the population works in agribusiness and associated sectors. Rice is the state's primary food crop and staple diet.

3.3 Data Pre-processing

In this study, using statistics and data processing on the MODIS/061/MCD12Q1 dataset, gridded rainfall products that are available weekly, seasonally, and annually were extracted, deploying the GEE platform using the 'ee. ImageCollection' technique and the filter command (ee. Filter.calendarRange). The 'clip' function was then applied to restrict the field of study and obtain relevant information in accordance with the field of study. The dataset SOL_ TEXTURE-CLASS_USDA-TT_M/v02 is processed to determine soil classes and convert hydrological soil categories like A, B, C, and D depending on their infiltration capacity. The operation 'ee.Filter.date' is applied to the CHIRPS dataset to filter the daily rainfall information for the specified duration.

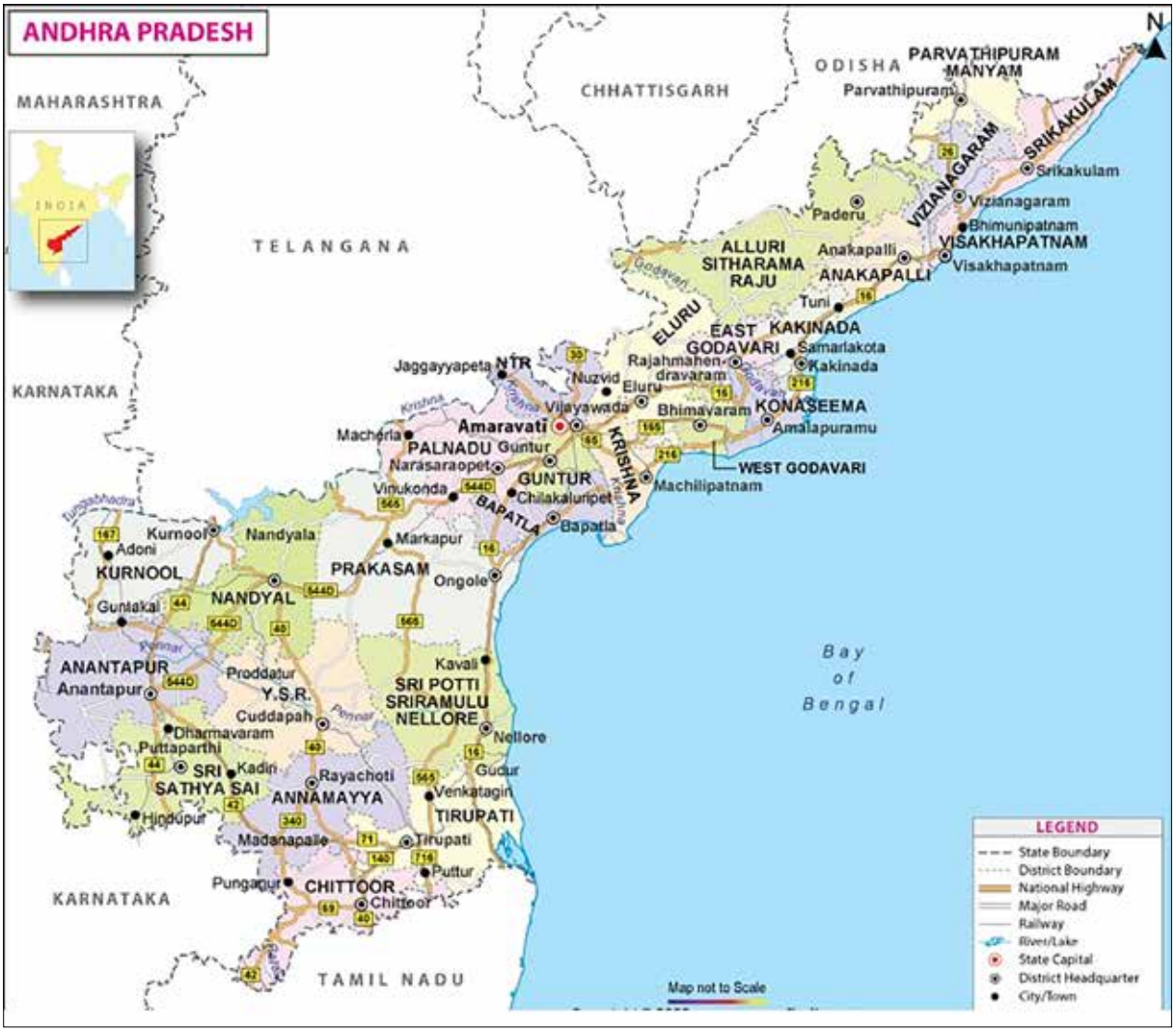

Figure 1. Map of the state of Andhra Pradesh

3.4 Methods

3.4.1 Curve Number (CN) Method

A common hydrological approach for calculating direct runoff from rainfall events in watershed modelling is the Curve Number (CN) method. It was created as a component of the Soil Conservation Service (SCS) methodology. The quantity of rainfall that results in direct runoff is estimated using the CN technique, which takes into account a number of variables including soil type, land use, and prior soil moisture conditions. It is particularly useful in predicting surface runoff in agricultural and urban areas. The CN method involves the following steps:

1. Determine Soil Hydrological Group: Soils are categorized into four hydrological classes (A, B, C, and D) depending on their infiltration features. These groups are assigned according to soil properties like texture, permeability, and depth. Each group has a corresponding range of CN values.
2. Assign Land Use Category: Different land use or land cover types within the watershed are classified into specific categories. Examples of land use categories include forest, agriculture, urban, and grassland. Each land use category has an associated CN value range.
3. 3. Establish Antecedent Soil Moisture Condition: Antecedent soil moisture is the amount of moisture in the soil prior to a rainfall occurrence, which affects the runoff response. Antecedent soil moisture conditions are classified into three categories: dry, normal, and wet. Each condition has a corresponding adjustment factor applied to the CN value.
4. Determine Curve Number (CN): Once the hydrological group, land use category, and antecedent soil moisture condition are known, the CN value is determined. This is typically done using lookup tables the SCS provides or through equations specific to the region or application.
5. Calculate Direct Runoff: With the CN value determined, the rainfall data for a specific event can be utilized to calculate the direct runoff.

4. Research Methodology

4.1 System Model

Two key theories have been put forth, and the SCS-CN technique depends on the water balance computation. The SCS-CN method is not represented by a single mathematical model but rather a set of equations and lookup tables. The process is based on empirical relationships and lookup tables

developed by SCS. These relationships are used to calculate direct runoff from precipitation occurrences depending on the hydrological, soil, and use of land factors. As shown in equation (5), the Curve Number (CN) parameter must be determined based on soil and land use characteristics. The CN value is typically determined using lookup tables provided by the SCS or through equations that consider the soil hydrological features and land use factors. The CN value is influenced by three key factors: Land usage, soil type, and previous soil moisture levels. This method assigns different CN values to different combinations of these factors, ranging from 0 to 100. Lower CN scores represent greater significance infiltration rates, while greater CN values indicate lower infiltration rates. The SCS-CN method provides lookup tables or equations to determine the CN value based on the soil hydrological group (A, B, C, or D), land use category (such as forest, agriculture, urban), and antecedent soil moisture condition (dry, normal, or wet). These lookup tables or equations vary depending on the region and specific application.

4.2 Architecture and working

The SCS-CN method does not have a specific architecture. Instead, it is a conceptual framework or methodology for calculating direct runoff from rainfall occurrences based on soil, land use, and hydrological features. The SCS-CN method involves the following key components:

- Rainfall Data: Rainfall data, such as precipitation depth and intensity, is collected or obtained for the field of study. This data serves as input to the SCS-CN method.
- Soil Hydrological Group: The SCS-CN method classifies soils into hydrological categories (A, B, C, or D) depending on their infiltration properties. The hydrological group is determined based on soil texture, permeability, and other soil characteristics. Lookup tables or equations are used to assign the appropriate hydrological group to each soil type in the field of study.
- Land Use Categories: Land use or land cover information is considered in the SCS-CN method as it affects the amount of runoff generated. Different land use categories, such as forest, agriculture, or urban areas, have different runoff characteristics. Lookup tables or equations are used to assign the appropriate land use category to each area within the study area.
- Antecedent Soil Moisture Conditions: The SCS-CN method considers the antecedent soil moisture conditions, which represent the moisture content in the soil before a rainfall occurrence. These conditions can be classified as dry, normal, or wet. Lookup tables or equations assign the appropriate antecedent soil moisture condition to each area within the study area.
- Curve Number (CN): It represents the cumulative impact of soil type, use of the property, and previous soil wetness conditions on the runoff process.
- Direct Runoff Calculation: The SCS-CN method uses the CN value and rainfall data to calculate the direct runoff from rainfall occurrences.

To estimate the direct runoff in the study region, empirical methods like the SCS-CN methodology are typically utilized as shown in Figure 2. Another cloud-based computing platform is GEE, which integrates Google's computational infrastructure with freely available GIS and remote sensing datasets. Any user can use any web browser to access GEE. It is freely accessible to everyone and effectively handles massive data thanks to automatic parallel processing. The vast collection of spatial data that GEE offers makes it easier to choose input data. Users can select their datasets from big sets of image collections using various filter techniques.

The SCS––CN equation is written by

$$Q = (P\text{-}I_a)^2 \,/\, P\text{-}I_a + S \quad \text{for} \quad P > I_a \tag{1}$$

$$Q = 0 \text{ for } \quad P < I_a \tag{2}$$

where P represents daily rainfall, I_a original simplification, F represents effective retention, Q represents straight surface run-off, and S represents the possible maximum durability. CN1, CN2, and CN3 values are calculated using the formula. Soil texture is converted into 4 types of soil groups: A == 1, B == 2, C == 3, and D == 4, where S is measured in millimeters and CN is a dimensionless run-off coefficient that is influenced by the type of soil, the use of the land, and the preexisting moisture conditions (AMC). The relative levels of dryness or moisture of a watershed, which varies continuously and has a big impact on run-off, is known as antecedent moisture.

Depending on the LULC and the soil category characteristics, CNs has been proposed. CN can be derived from the following equations:

$$CN1 = CN2 / (2.281\text{-}(0.0128*CN2)) \tag{3}$$

$$CN3 = CN2 / (0.427+(0.00573*CN2)) \tag{4}$$

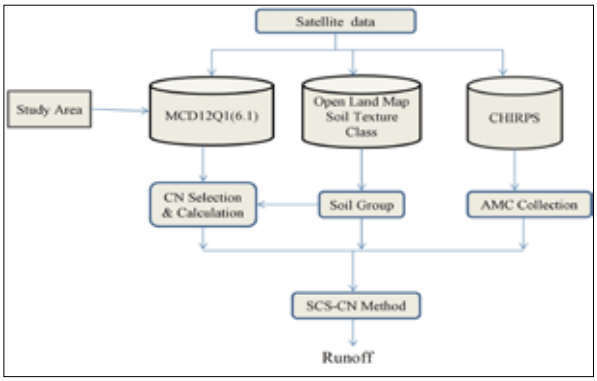

Figure 2. Overall flow diagram to estimate the rainfall-runoff

The required datasets, MCD12Q1 version 6.1 for land cover types, OpenLandMap Soil Texture Class for classifying the soil texture groups, and Climate Hazards Group Infrared Precipitation with Station Data (Version 2.0), are imported to the GEE through the JavaScript API. The soil texture map is transformed into different kinds of soil categories.

Procedure:

1. The required datasets are imported into GEE through the JavaScript API.
2. The soil texture map is transformed into different kinds of hydrologic soil groups, A, B, C, and D.
3. Curve number selection is done for all possible parameters of the four soil types and the LULC data

categories.

4. Daily rainfall information pictures are used to make daily AMC pictures.
5. To estimate run-off (Q), the equation (1) is used.

5. Results and Analysis

5.1 Experimental Setup

The experiment in this study is carried out using the Google Earth Engine platform. The GEE comprises a high-performance, intrinsically catalog computing service, and a multi-petabyte data catalog that is ready for examination. It may be accessed and managed online thanks to an application programming interface (API) and a web-based interactive development environment (IDE) that facilitate quick prototyping and result visualization as shown in Figure 3. The public data catalogue for the Earth Engine is a multi-petabyte curated collection of extensively used geospatial datasets. Earth-observing remote sensing images make up the majority of the catalog.

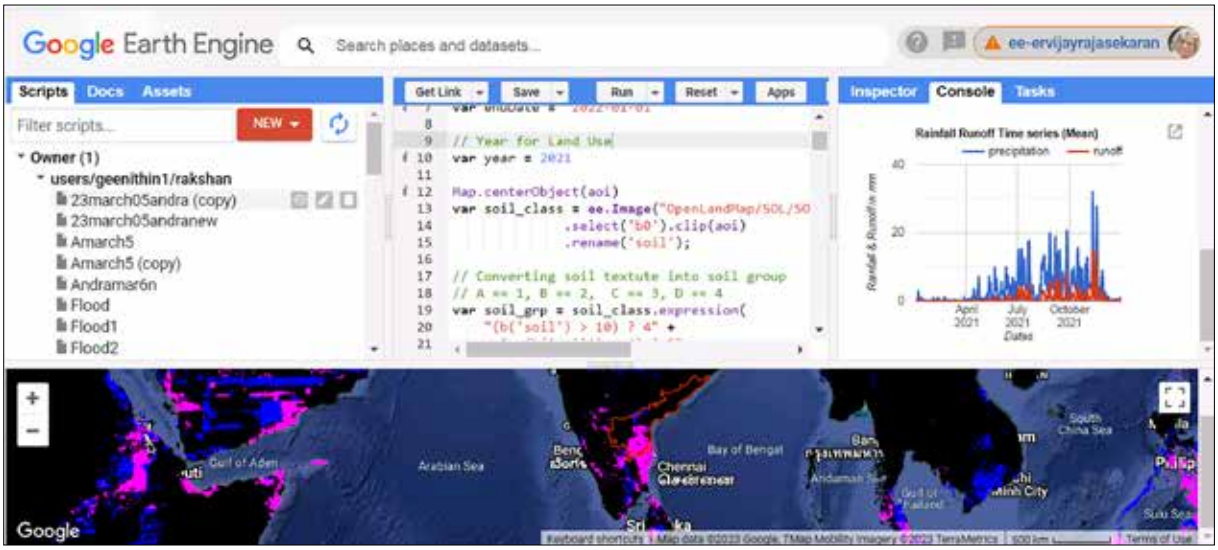

Figure 3. Experiment setup on the GEE platform

5.2 Performance Metrices

The rainfall runoff based on soil type, land use, antecedent moisture conditions, and rainfall characteristics is calculated using precipitation and retention values. The formula for calculating the rainfall runoff is given in Equation 5:

$$\text{Runoff} = \frac{(\text{Precipitation} - \text{The potential maximum retention} * 0.2)^2}{(\text{Precipitation} + \text{The potential maximum retention} * 0.8)} \quad (5)$$

The percent error formula for calculating the accuracy of precipitation is shown in equation 6:

$$\text{Percent Error} = \frac{(\text{Observed Value} - \text{Predicted/Measured Value})}{(\text{Predicted/Measured Value})} \times 100 \quad (6)$$

The "Observed Value" refers to the actual or observed precipitation amount. "Predicted / Measured Value" refers to the predicted or measured precipitation amount. The numerator of the formula calculates the difference between the observed and predicted/measured values. The denominator represents the predicted/measured value. The result is multiplied by 100 to obtain the percentage value. By calculating the percent error, you can determine the accuracy of the precipitation prediction or measurement. A lower percent error indicates a higher level of accuracy, while a higher percent error indicates a more significant deviation between the observed and predicted / measured values.

5.3 Results

5.3.1 Yearly Rainfall Analysis

Both the rainfall and runoff have followed a similar pattern: they began to rise in the middle of August, peaked in November, and then began to decline by the end of December. The total runoff for the year 2021 is 172.459. The maximum runoff value is 26.523, and the precipitation value is 47.222, which was observed on November 11, 2021. And second, the maximum runoff value is 24.102; the precipitation value is 43.711, which was observed on November 18th, 2021 as shown in Figure 4.

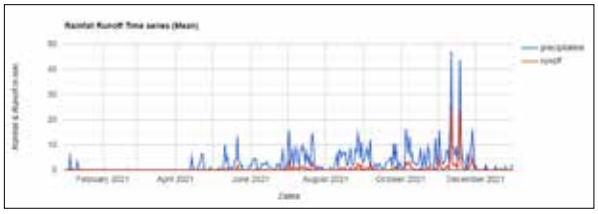

Figure 4. Time Series Plots of Yearly Rainfall Data for Andhra Pradesh State for the Year 2021

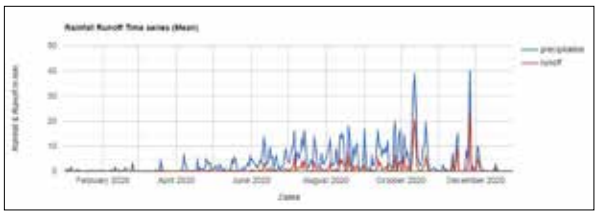

Figure 5. Time Series Plots of Yearly Rainfall Data for Andhra Pradesh State for the Year 2020

Similar trends in rainfall and runoff have been observed; both began increasing in August. The maximum runoff value is 20.677, and the maximum precipitation value is 39.107, observed on October 12th, 2020, as shown in Figure 2. The maximum precipitation value of 39.107 was also observed on October 12th, 2020, as shown in Figure 5.

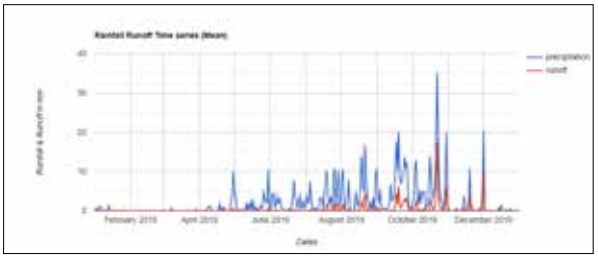

Figure 6. Time Series Plots of Yearly Rainfall Data for Andhra Pradesh State for the Year 2019

The total runoff and precipitation values for the year 2019 are 127.438 and 812.097. The maximum runoff value is 17.377 and the maximum precipitation value is 35.268, which were observed on October 22, 2019. And second, the maximum runoff value is 9.98 and the maximum precipitation value is 20.466, which were observed on December 1, 2019 as shown in figure 6.

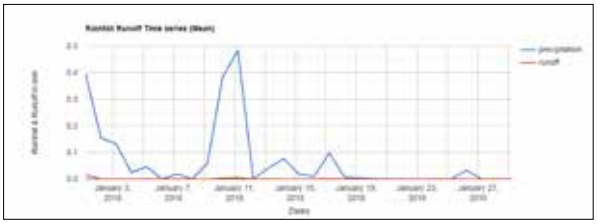

Figure 7. Time Series Plots of Yearly Rainfall Data for Andhra Pradesh State for the Year 2018

The total runoff and precipitation values for the year 2018 were 183.763 and 1198.909. The average runoff and precipitation values for the year 2018 were 0.50623 and 3.30278. The highest precipitation and runoff values of 12.914 and 30.604 occurred on November 16, 2018, with the dates of November 10, January 5, 6, and 7 receiving 0 runoff and precipitation as shown in Figure 7.

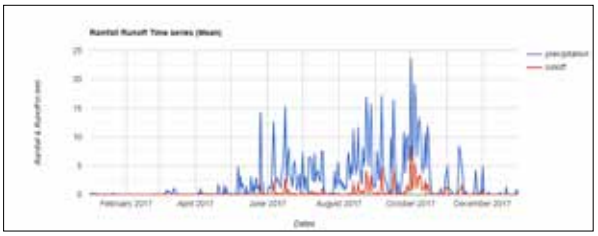

Figure 8. Time Series Plots of Yearly Rainfall Data for Andhra Pradesh State for the Year 2017

The total runoff and precipitation values for the year 2017 are 105.559 and 830.005. The average runoff and the amount of precipitation that fell in the year 2017 are 0.289203 and 2.273986. The highest precipitation and runoff values of 23.681and 8.402 occurred on October, 2017, with the dates of November 8, 9 and 18 receiving 0 runoff and precipitation as shown in Figure 8. The total runoff and precipitation values for the year 2016 are 63.49 and 591.33. The average runoff and precipitation values for the year 2016 are 0.17 and 1.615. The highest precipitation and runoff values of 19.225 and 8.046 occurred on December 12, 2016, with the dates of November 5, January 14, 18, and 28 receiving 0 runoff and precipitation as shown in Figure 9. The total runoff and precipitation values for the year 2015 are 124.612 and 783.482. The highest precipitation and runoff values of 38.225 and 18.20 occurred on December 18, 2015, with the dates of November 5, January 10, 14, and 18 receiving 0 runoff and precipitation as shown in Figure 10.

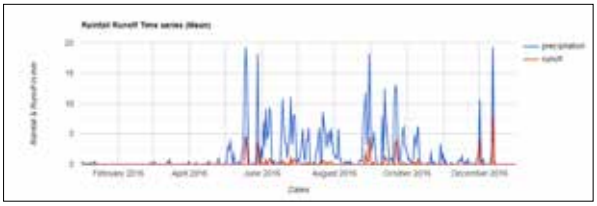

Figure 9. Time Series Plots of Yearly Rainfall Data for Andhra Pradesh State for the Year 2016

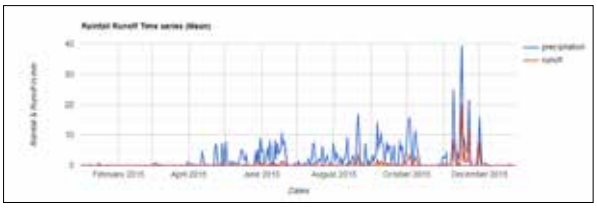

Figure 10. Time Series Plots of Yearly Rainfall Data for Andhra Pradesh State for the Year 2015

5.3.2 Monthly Rainfall Analysis

October and November months are taken into consideration for an in-depth analysis of rainfall. The total runoff and the amount of precipitation that fell in November 2021 are 99.05 and 283.372. The average runoff and the amount of precipitation that fell in November 2021 are 9.44 and 3.301. The total and average runoff values for the month of September are 9.08 and 0.30. The total runoff and the amount of precipitation that fell in November 2020 are 50.614 and 115.087. The average runoff and the amount of precipitation that fell in November 2020 are 1.687and 3.836. The highest precipitation and runoff values of 40.333 and 23.346 occurred on November 26, 2020, with the dates of November 18, 19, and 20, receiving 0 runoff and precipitation as shown in Figures 11 and 12.

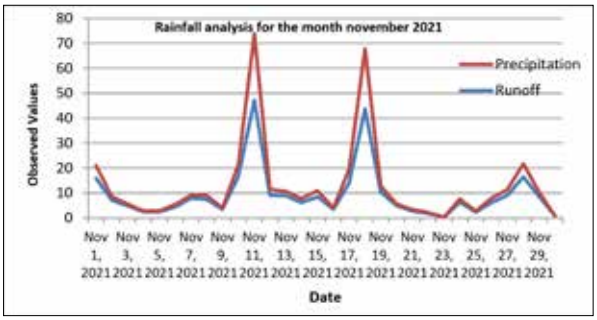

Figure 11. Rainfall analysis for the month of November 2020

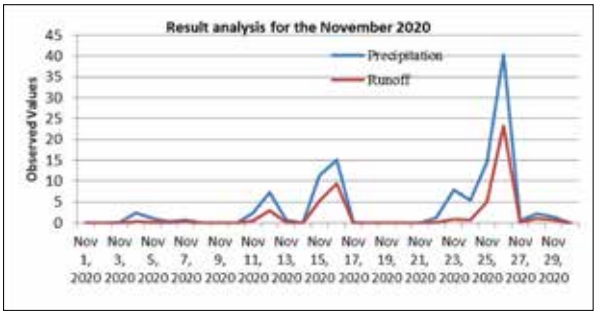

Figure 12. Rainfall analysis for the month of November 2020–2021

The total runoff and the amount of precipitation that fell in November 2019 are 6.16 and 29.539. The average runoff and the amount of precipitation that fell in November 2019 are 0.2 and 0.98, respectively. The total and average runoff values for the month of October are 51.163 and 1.65, respectively. The total and average runoff values for the month of September are 30.127 and 1.004 as shown in Figure 13.

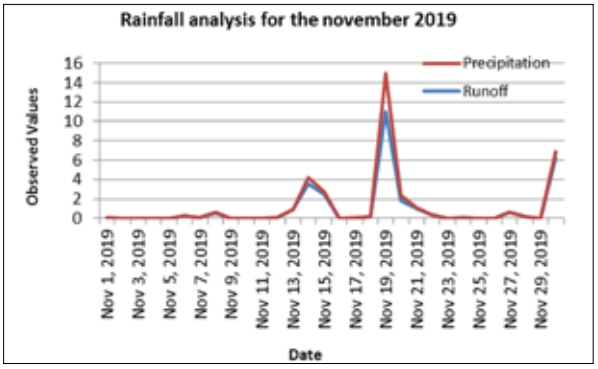

Figure 13. Rainfall analysis for the month of November 2019

The total runoff and the amount of precipitation that fell in November 2018 are 45.681 and 155.04539. The average runoff and the amount of precipitation that fell in November 2018 are 5.168 and 1.5227. The highest precipitation and runoff values of 30.604 and 12.914 occurred on November 16, 2018, with the dates of November 10, 25, and27 receiving 0 runoff and precipitation as shown in Figure 14.

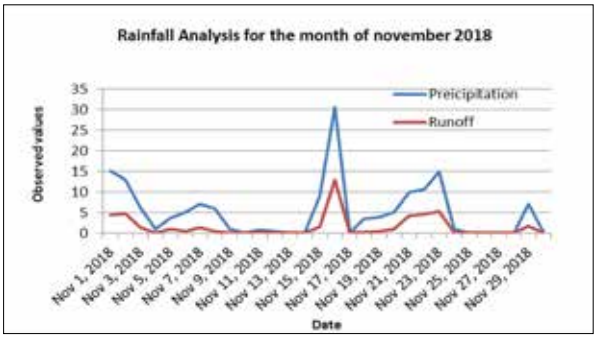

Figure 14. Rainfall analysis for the month of November 2018

The total runoff and the amount of precipitation that fell in November 2017 are 5.893 and 43.598. The average runoff and the amount of precipitation that fell in November 2017 are 0.1964 and 1.53, respectively. The highest precipitation and runoff values of 4.699 and 1.198 occurred on November 1, 2017, with the dates of November 8, 9, and 18 receiving 0 runoff and precipitation as shown in Figure 15.

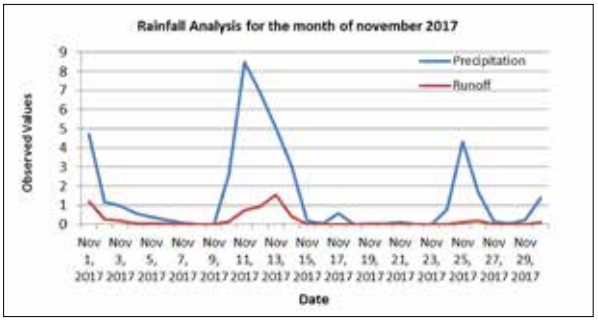

Figure 15. Rainfall analysis for the month of November 2017

The total runoff and the amount of precipitation that fell in November 2016 are 63.49 and 591.333. The average runoff and the amount of precipitation that fell in November are 2016 0.17347 and 1.615664. The highest precipitation and runoff values of 19.225 and 8.046 occurred on December 12, 2016, with the dates of November 30 and 31 receiving 0 runoff and precipitation as shown in Figure 16.

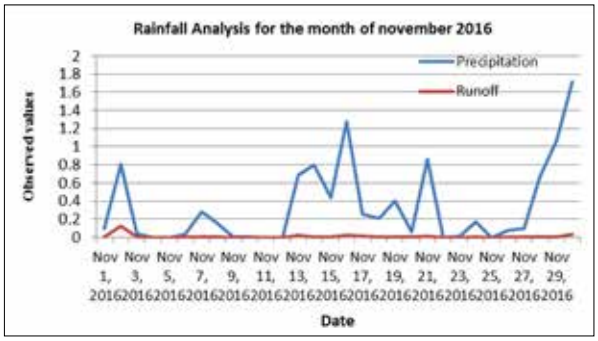

Figure 16. Rainfall analysis for the month of November 2016

The total runoff and the amount of precipitation that fell in November 2015 are 68.518 and 193.327. The average runoff and the amount of precipitation that fell in November 2015 are 0.544 and 2.99, respectively. The highest precipitation and runoff values of 39.466 and 19.905 occurred on November 16, 2015, with the dates of November 5 and 27 receiving 0 runoff and precipitation, as shown in Figure 17.

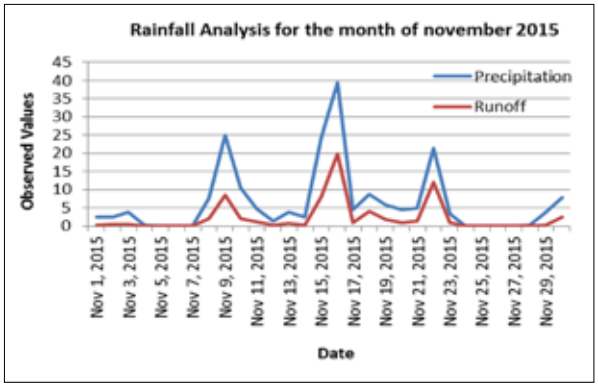

Figure 17. Rainfall analysis for the month of November 2015

Figure 18 shows the total runoff and the amount of precipitation that fell in September 2015 are 9.577 and 128.524. The average runoff and the amount of precipitation that fell in September 2015 are 0.319 and 4.28, respectively. The highest precipitation and runoff values of 14.356 and 1.934 occurred on September 6, 2015, with the dates of September 23 receiving 0 runoff and precipitation. The total runoff and the amount of precipitation that fell in October 2015 are 16.859 and 91.418. The average runoff and the amount of precipitation that fell in October 2015 are 0.544 and 2.99, respectively. On October 3, 2015, the highest precipitation and runoff values were 15.464 and 3.479 respectively, with October 13, 18, 21 to 25 receiving 0 precipitation runoff values.

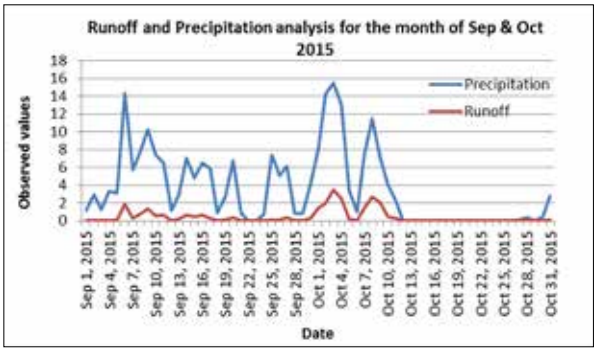

Figure 18. Runoff and precipitation analysis for Sep & Oct 2015

Figure 19 shows the total runoff and the amount of precipitation that fell in September 2016 are 13.068 and 112.718. The average runoff and the amount of precipitation that fell in September 2016 are 0.44 and 3.76. The highest precipitation and runoff values of 13.135 and 3.889 occurred on September 21 2016, with the dates of September 7 and 8 receiving 0 runoff and precipitation. The total runoff and the amount of precipitation that fell in October 2016 are 1.991 and 34.555. The average runoff and the amount of precipitation that fell in October 2016 are 0.064 and 1.114. The highest precipitation and runoff values of 6.236 and 0.807 occurred on October 10 2016, with the dates of October 14, 15, 17, and 25 to 27.

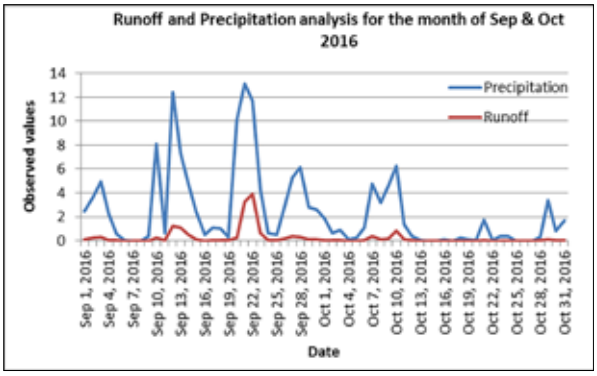

Figure 19. Runoff and precipitation analysis for the month of Sep & Oct 2016

Figure 20 shows the total runoff and the amount of precipitation that fell in September 2017 are 18.951 and 156.636. The average runoff and the amount of precipitation that fell in September 2017 are 5.22 and 0.6317. The highest precipitation and runoff values of 17.2 and 4.849 occurred on September 6 2017, with the dates of September 19 receiving 0.0001 and 0.094 runoff and precipitation. The total runoff and the amount of precipitation that fell in October 2017 are 41.794 and 180.108. The average runoff and the amount of precipitation that fell in October 2017 are 1.384 and 5.81, respectively. The highest precipitation and runoff values of 19.242 and 5.417 occurred on October 4 2017, with the dates of October 23 receiving 0 runoff and precipitation.

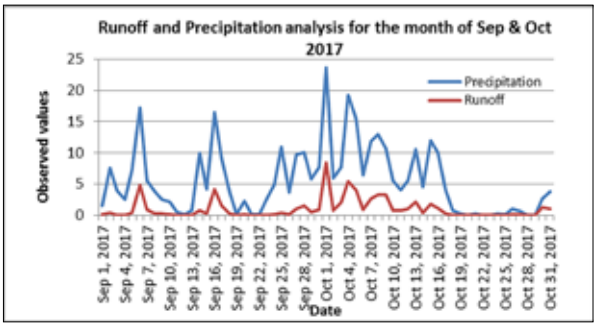

Figure 20. Runoff and precipitation analysis for the month of Sep & Oct 2017

Figure 21 shows the total runoff and the amount of precipitation that fell in September 2018 are 42.228 and 223.995. The average runoff and precipitation that fell in September 2018 are 3.766 and 0.438, respectively. The highest precipitation and runoff values of 2.336 and 11.972 occurred on September 16, 2018, with the dates of September 7 receiving 0 runoff and precipitation. The total runoff and the amount of precipitation that fell in October 2018 are 57.604 and 211.428. The average runoff and precipitation that fell in October 2018 are 1.203 and 6.254, respectively. On October 5, 2018, the highest precipitation and runoff values were 24.812 and 9.738 respectively, with October 30 receiving 0.293 precipitation and 0.011 runoff values.

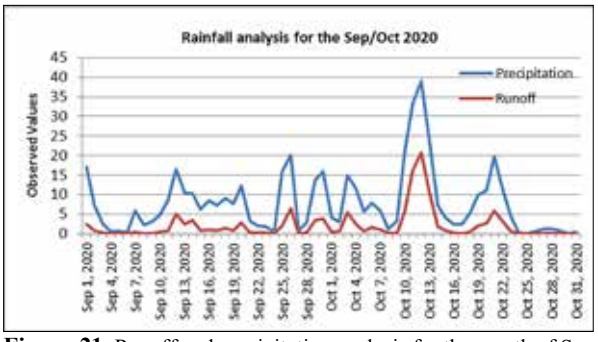

Figure 21. Runoff and precipitation analysis for the month of Sep & Oct 2018

The total runoff and the amount of precipitation that fell in September 2018 are 33.772 and 208.728. The average runoff and the amount of precipitation that fell in September 2018 are 1.004233 and 5.522867, respectively. The highest precipitation and runoff values of 19.957 and 6.219 occurred on September 19, 2019, with the dates of September 30 receiving 0.018 runoff and 0.095 precipitations. The total runoff and the amount of precipitation that fell in October 2019 are 68.571 and 254.534. The average runoff and the amount of precipitation that fell in October 2019 are 1.650419 and 6.824129, respectively. On October 22, 2019, the highest precipitation and runoff values were 35.268 and 17.377, respectively, with October 28 receiving 0.268 precipitation and 0.017 runoff values, as shown in Figure 22.

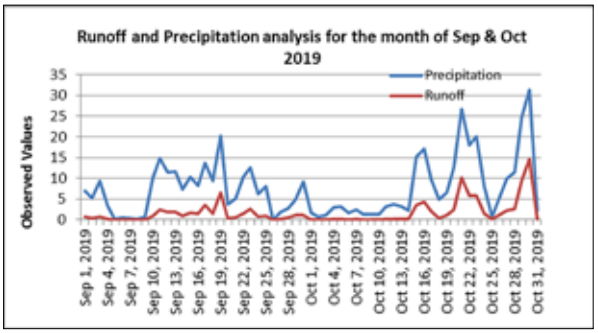

Figure 22. Runoff and precipitation analysis for the month of Sep & Oct 2019

The total runoff and the amount of precipitation that fell in September 2020 are 40.759 and 217.792. The average runoff and the amount of precipitation that fell in September 2020 are 1.3586 and 7.2597, respectively. The highest precipitation and runoff values of 20.136 and 6.492 occurred on September 26, 2020, with the dates of September 6 receiving 0.001 and 0.0338 runoff and precipitation respectively. The total runoff and the amount of precipitation that fell in October 2020 are 82.939 and 256.494. The average runoff and the amount of precipitation that fell in October 2020 are 2.675 and 8.274, respectively. On October 12, 2020, the highest precipitation and runoff values were 30.109 and 20.677 respectively, with October 25 receiving 0 precipitation and 0 runoff values as shown in Figure 23.

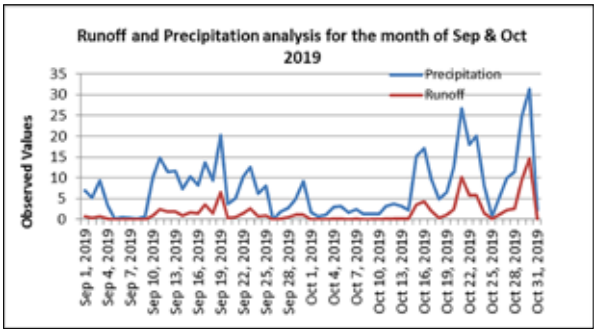

Figure 23. Runoff and precipitation analysis for Sep & Oct 2020

The total runoff and the amount of precipitation that fell in September 2021 are 9.088 and 105.518. The average runoff and the amount of precipitation that fell in September 2021 are 0.303 and 3.517, respectively. The highest precipitation and runoff values of 12.104 and 2.574 occurred on September 6, 2021, with the dates of September 16 receiving 0 and 0.195 runoff and precipitation, respectively. The total runoff and the amount of precipitation that fell in October 2021 are 20.475and 145.872. The average runoff and the amount of precipitation that fell in October 2021 are 0.66 and 4.706, respectively. On October 5, 2021, the highest precipitation and runoff values were 16.397 and 3.424 respectively, with October 25 and 26 receiving 0.001 precipitations and 0 runoff values as shown in Figure 24.

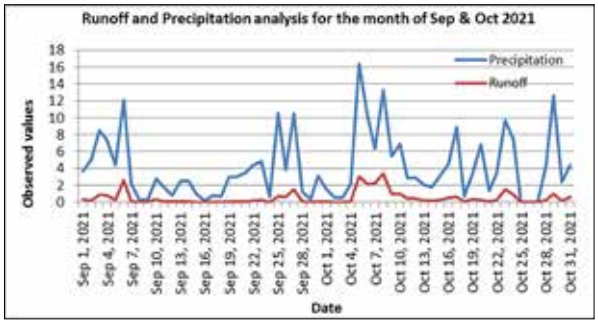

Figure 24. Runoff and precipitation analysis for the month of Oct & Nov 2021

5.4 Analysis

Table 1 shows the total runoff results computed for the years 2015–2021, which are 172.459; 209.666; 105.599; 63.49; and 124.612, respectively. The year 2020 has the highest runoff (209.666 percent), and the year 2016 has the lowest runoff (63.49 percent). As shown in Figure 25, the year 2018 has the highest precipitation of 1198.909 and the lowest precipitation of 591.33, and other precipitation values are 993.976, 1104.7, 812.097, 830.005, and so on. Table 2 shows the runoff and precipitation for the three months of September through November from 2015 to 2021. The month of September of the year 2020 received the highest precipitation value of 217.792. It shows that there will be a good correlation like 100 among the precipitation (105.518 to 156.636) and runoff (9.088 to 33.772) for the years 2015 to 2021, except for 2020. The years 2016 and 2018 have very near precipitation values of 112.718 and 112.968 in the month of September.

Table 1. Year-Wise Analysis (2015–2021)

Year	Runoff	Precipitation
2021	172.459	993.976
2020	280.889	1276.32
2019	127.438	812.097
2018	183.763	1198.909
2017	105.599	830.005
2016	63.49	591.33
2015	124.612	783.482

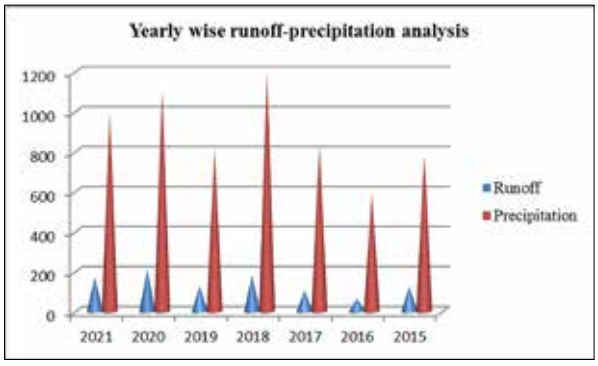

Figure 25. Year-wise runoff-precipitation analysis

Table 2. Three-month analysis for the years 2015-2021

Year	Month	Runoff	Precipitation
2021	Sep	9.088	105.518
	Oct	20.475	145.872
	Nov	99.05	283.372
2020	Sep	40.759	217.792
	Oct	82.939	256.494
	Nov	50.614	115.087
2019	Sep	33.772	208.728
	Oct	68.571	254.534
	Nov	39.466	134.546
2018	Sep	12.669	112.968
	Oct	37.3	193.88
	Nov	45.681	155.045
2017	Sep	18.951	156.636
	Oct	41.794	180.108
	Nov	5.893	43.598
2016	Sep	13.068	112.718
	Oct	1.991	34.555
	Nov	0.283	10.225
2015	Sep	9.577	128.524
	Oct	16.859	91.418
	Nov	68.518	193.327

As shown in Figure 26, November 2016 received a very low rainfall precipitation 10.225 than all the years. November 2021 received 283.372 highest precipitations. November has more variations in terms of runoff and precipitation values. There is a good correlation among the years 2016, 2018, and 2021 in September. The month of October 2016 received a very low precipitation value of 34.555 compared to all the years, and the year 2020 received the highest value for its October month of 256.494. There is more variation for the month of October in terms of its precipitation and runoff values.

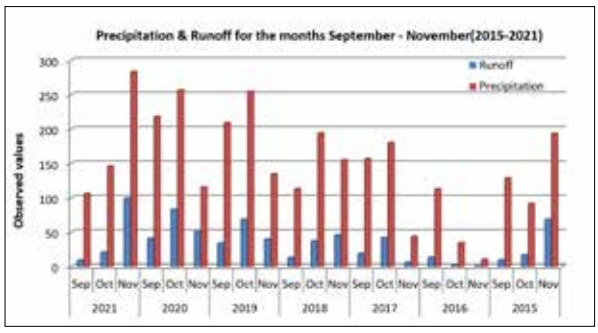

Figure 26. Three-month analysis for the months September – November

Figure 26: As shown in Table 3, there are abrupt changes in the precipitation values for the years 2016, 2017, 2018, and 2021. December of 2015 has received 18.352 mm; year 2016 has received more precipitation, 34.78 mm, which is 16.428 mm higher than 2015. December 2017 received a very low precipitation value of 8.932, which is less precipitation than the previous years. December 2018 received more precipitation than all of the year's December months combined. The years 2019 to 2021 received some variations. There will be no correlation in the precipitation values among the years as shown in Figure 27.

Table 3. Analysis for the month of December (2015-2021)

Year	Precipitation	Runoff
Dec-21	12.456	1.044
Dec-20	30.623	12.288
Dec-19	24.722	10.084
Dec-18	49.914	6.22
Dec-17	8.932	1.006
Dec-16	34.78	12.625
Dec-15	18.352	8.434

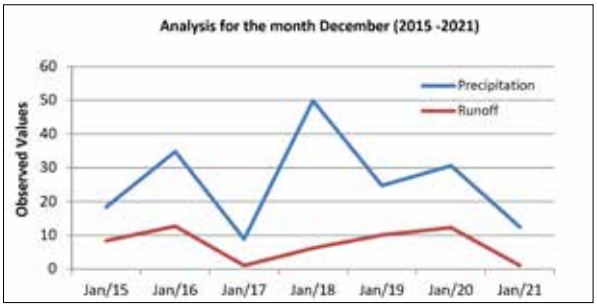

Figure 27. Analysis for the month of December (2015-2021)

As shown in Figure 28, January has seen a slow upgrade in precipitation and runoff values from 2015 to 2017, but there is an abrupt change in January 2018. This month received more rainfall when compared to January 2017. There is a correlation between January 2018 and January 2021.

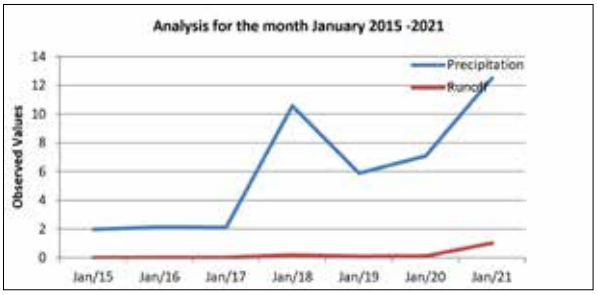

Figure 28. Analysis for January (2015-2021)

Table 4 shows the complete precipitation and runoff analysis for January from 2015 to 2021. Since 2018, every year has received more precipitation and higher runoff values than the previous years. The January of 2021 received the highest rainfall (12 mm); there was very little rainfall in December 2021 compared to previous years. It shows that there are more variations in the rainfall rate every year and that slow developments in climate change are happening in Andhra Pradesh.

Table 4. Analysis for the month of January (2015-2021)

Year	Precipitation	Runoff
Jan-21	12.508	1.008
Jan-20	7.1	0.106
Jan-19	5.888	0.082
Jan-18	10.567	0.189
Jan-17	2.094	0.02
Jan-16	2.121	0.021
Jan-15	1.963	0.016

For a comparison study, the data shown in the Table 5 is taken from the metrological department and the Ministry of Earth Sciences in India. The metrological department only has district-level data for Andhra Pradesh, but our research paper considered the entire state for the study. The total value of all the districts of Andhra Pradesh is compared with our result. As per the metrology department, 2020 received a rainfall of 1247 mm. the current research work estimated a rainfall of 1276.32 mm in the state of Andhra Pradesh for 2020. The accuracy of 97.72 percent is produced by our proposed model.

Table 5. Observed Values of Rainfall for the Year 2020 from the Metrological Department

Observed Rainfall values for the year 2020												
District	Jan R/F	Feb R/F	March R/F	April R/F	May R/F	June R/F	July R/F	Aug R/F	Sep R/F	Oct R/F	Nov R/F	Dec R/F
Anantapur	0.3	0	4.1	30.5	26.9	123.4	187.1	58.7	255.9	117.3	53.5	22.5
Chittoor	14.6	0	9.5	54.4	21.2	109.8	311.3	135.6	194.7	162.7	299.7	106.7
cuddapa	3.9	0	6.9	30	16.4	103.3	189.8	178.1	372.5	143.5	268.3	65.9
East Godavari	5.9	4.8	3.4	43.6	15.9	112.5	309.5	309.3	238.9	312.1	108.7	0.1
Guntur	17.6	11.9	10.4	6	11.7	143.6	286.5	168.5	251.6	185	118.6	0.2
krishna	10.6	21.8	8.9	31.3	3.8	126.7	302.4	186.8	231.2	293.5	142.5	0.6
kurnool	0	0	6.3	18.8	38.1	140.2	273.9	132.5	279.2	146.2	44.9	3.8
Nellore	50	0.4	5.5	60	6.3	98.2	162	130.3	164.8	99.6	522.3	180.3
prakasam	24.1	2.8	20.8	22.5	12.1	83.1	128.6	93.4	249.3	109.6	212	2.3
srikakulam	6.6	35.2	55.3	57.5	35.5	137.7	137	132.8	151	253.2	51.7	0.4
visakapattinam	8.4	24.3	49.4	84.6	47.5	128.4	167.4	137.5	163.3	281.4	82.3	0
vizianagaram	6.8	33	47.3	82.7	45.5	171.5	191.3	114.8	199.4	246.1	53.2	0
West Gadawari	14.3	4.5	0.6	33.6	5.4	139.4	379.9	293.1	278	286.6	117	0
Average	12.546	10.669	17.569	42.73	22.0	124.5	232.82	159.3	233.1	202.8	159.6	29.45
									Total Precipitation			**1247**

6. Conclusions and Future Scope

The rainfall in the state of Andra Pradesh has been studied for the period 2015-2021.The estimated result using the SCS-CN method and using the datasets of MCD12Q1 version 6.1 for land cover types, OpenLandMap Soil Texture Class for classifying the soil texture groups, and Climate Hazards Group Infrared Precipitation with Station Data was presented. Due to global warming and climate change, there are more variations in the rainfall every year. Among the study undertaken from 2015 to 2021, the year 2020 received more rainfall 1276.32 mm and the year 2015 received less rainfall 591.33 mm. There are more variations between the years 2019 and 2020; the difference value is 464 mm. The years 2018 and 2020 have a correlation in terms of their precipitation, and the years 2015, 2017, and 2019 have a correlation in terms of their precipitation. The month of January has seen a slow upgrade in precipitation and runoff values from 2015 to 2017, but there is an abrupt change in the month of January 2018. January 2017 received 2.094 mm of rainfall, but January 2018 has received 10.567 mm, which is 5 times higher than the 2017 rainfall. The January month of the year 2021 received the highest rainfall (12 mm); there was very little rainfall in the month of December 2021 when compared to previous years. Due to lacking of existing data, our research work is compared only for the year 2020.

In the future, more existing data will be collected, and a detailed comparative study will be done. Other algorithms will be integrated with our proposed model to estimate rainfall runoff, and a new algorithm will be developed for rainfall prediction.

Author contribution D.Vetrithangam: Conceptualization, methodology, data curation, writing—original draft, review and editing. B. Arunadevi: Project administration, writing—review and editing. Naresh Kumar Pegada: Methodology implementation. Sukhpreet Kaur: Formal analysis and methodology. B.KrishnaPrasad : Formal analysis. All authors have read, understood, and have complied as applicable with the statement on «Ethical responsibilities of Authors» as found in the Instructions for Authors.

Declarations:

- Data Availability Statement: Authors declare that all the data being used in the design and production cum layout of the manuscript is declared in the manuscript.
- Funding Statement: The authors received no specific funding for this study.
- Conflicts of Interest: The authors declare that they have no conflicts of interest to report regarding the present study.

References

Abdul Ghani, N. A., Mohamad, N. A., & Hui, T. W. (2016). Rainfall analysis to determine the potential of rainwater harvesting site in Kuantan, Pahang. ARPN Journal of Engineering and Applied Sciences, 11(11), 7264–7268.

Ahmad, A., Banerjee, W., Rashid, Z., Xia, S., Karim, S., & Asif, M. (2022). Assessment of long-term rainfall variability and trends using observed and satellite data in central Punjab, Pakistan. Atmosphere, 14(1), 60. https://doi.org/10.3390/atmos14010060

Al-Ghobari, A., Dewidar, A., & Alataway, A. (2020). Estimation of surface water runoff for a semi-arid area using

RS and GIS-based SCS-CN method. Water, 12(7), 1–16. https://doi.org/10.3390/w12071924

Anderson, Z., Chen, Q., Kavvas, M. L., & Feldman, A. (2004). Coupling HEC-HMS with atmospheric models for the prediction of watershed runoff. In Joint Conference on Water Resources Engineering and Water Resources Planning and Management 2000 Building Partnerships (pp. 312–318). https://doi.org/10.1061/40517(2000)135

Animashaun, P. G., Oguntunde, A. S., Akinwumiju, A. S., & Olubanjo, O. O. (2020). Rainfall analysis over the Niger central hydrological area, Nigeria: Variability, trend, and change point detection. Scientific African, 8, e00419. https://doi.org/10.1016/j.sciaf.2020.e00419

Arnold, J. G., & Allen, P. M. (1996). Estimating hydrologic budgets for three Illinois watersheds. Journal of Hydrology, 176(1–4), 57–77. https://doi.org/10.1016/0022-1694(95)02782-3

Arvind, P., Ashok Kumar, S., Girish Karthi, S., & Suribabu, C. R. (2017). Statistical analysis of 30 years rainfall data: A case study. In IOP Conference Series: Earth and Environmental Science (Vol. 80, No. 1). https://doi.org/10.1088/1755-1315/80/1/012067

Attah, U. E., Joshua, O. I., & Emmanuel, O. (2020). Susceptibility of agricultural land to soil degradation by rainfall using aggregates' stability indices in parts of Abia State, South Eastern Nigeria. Jordan Journal of Earth and Environmental Sciences, 11(4), 211.

Baquero, S., Cruz-Pol, S., Bringi, V. N., & Chandrasekar, V. (2005). Rain-rate estimate algorithm evaluation and rainfall characterization in tropical environments using 2DVD, rain gauges, and TRMM data. In International Geoscience and Remote Sensing Symposium (Vol. 2, pp. 1146–1149). https://doi.org/10.1109/IGARSS.2005.1525319

Chormanski, J., Van de Voorde, T., De Roeck, T., Batelaan, O., & Canters, F. (2008). Improving distributed runoff prediction in urbanized catchments with remote sensing-based estimates of impervious surface cover. Sensors, 8(2), 910–932. https://doi.org/10.3390/s8020910

Ebrahimian, L., See, L. F., Ismail, M. H., & Malek, I. A. (2009). Application of natural resources conservation service curve number method for runoff estimation with GIS in the Kardeh watershed, Iran. European Journal of Scientific Research, 34(4), 575–590.

Eliza, H., Mohamad, W. Y., & Yusop, Z. (2016). Rainfall analysis of the Kelantan big flood. Jurnal Teknologi, 4, 83–90.

Fowler, K., Peel, M., Saft, M., Peterson, T. J., Western, A., Band, L., & Nathan, R. (2022). Explaining changes in rainfall-runoff relationships during and after Australia's Millennium Drought: A community perspective. Hydrology and Earth System Sciences Discussions, in review. https://doi.org/10.5194/hess-2022-147

Gupta, N., & Dixit, J. (2022). Estimation of rainfall-induced surface runoff for the Assam region, India, using the GIS-based NRCS-CN method. Journal of Maps. https://doi.org/10.1080/17445647.2022.2076624

Gholami, V., & Khaleghi, M. R. (2021). A simulation of the rainfall-runoff process using artificial neural network and HEC-HMS model in forest lands. Journal of Forest Science, 67(4), 165–174. https://doi.org/10.17221/90/2020-JFS

Hassan, G. A., Isaac, P. A., Taylor, P. A., & Michelson, D. (2022). Optimizing radar-based rainfall estimation using machine learning models. Remote Sensing, 14(20). https://doi.org/10.3390/rs14205188

Jehanzaib, M., Ajmal, M., Achite, M., & Kim, T. W. (2022). Comprehensive review: Advancements in rainfall-runoff modelling for flood mitigation. Climate, 10(10), 1–17. https://doi.org/10.3390/cli10100147

Ling, Z., Yusop, Z., Yap, W. S., Tan, W. L., Chow, M. F., & Ling, J. L. (2020). A calibrated, watershed-specific SCS-CN method: Application to Wangjiaqiao watershed in the Three Gorges area, China. Water, 12(1). https://doi.org/10.3390/w12010060

Liu, H., Zhou, D., Li, D., Zeng, L., & Xu, P. (2023). Evaluation of artificial precipitation enhancement using UNET-GRU algorithm for rainfall estimation. Water, 15(8). https://doi.org/10.3390/w15081585

Loveridge, F., & Rahman, A. (2021). Effects of probability-distributed losses on flood estimates using event-based rainfall-runoff models. Water, 13(15), 1–18. https://doi.org/10.3390/w13152049

Mohammadi, M. J., Safari, S., & Vazifehkhah, S. (2022). IHACRES, GR4J and MISD-based multi conceptual-machine learning approach for rainfall-runoff modeling. Scientific Reports, 12(1), 1–21. https://doi.org/10.1038/s41598-022-16215-1

Moglen, G. E., Sadeq, H., Hughes, L. H., Meadows, M. E., Miller, J. J., Ramirez-Avila, J. J., & Tollner, E. W. (2022). NRCS curve number method: Comparison of methods for estimating the curve number from rainfall-runoff data. Journal of Hydrologic Engineering, 27(10), 1–10. https://doi.org/10.1061/(ASCE)HE.1943-5584.0002210

Musgrave, G. W. (1955). How much of the rain enters the soil? Yearbook of Agriculture, 1951–1960.

Nganro, S., Trisutomo, R. A., Barkey, M., & Ali, M. (2020). Rainfall analysis of the Makassar city using Thiessen polygon method based on GIS. Journal of Engineering and Applied Sciences, 15(6), 1426–1430. https://doi.org/10.36478/jeasci.2020.1426.1430

Psomiadis, K., Soulis, X., Zoka, M., & Dercas, N. (2019). Synergistic approach of remote sensing and GIS techniques for flash-flood monitoring and damage assessment in Thessaly plain area, Greece. Water, 11(3). https://doi.org/10.3390/w11030448

Psomiadis, K., Soulis, X., & Efthimiou, N. (2020). Using SCS-CN and Earth observation for the comparative assessment of the hydrological effect of gradual and abrupt spatiotemporal land cover changes. Water, 12(5). https://doi.org/10.3390/w12051386

Rajbanshi, R. (2016). Estimation of runoff depth and volume using NRCS-CN method in Konar catchment (Jharkhand, India). Journal of Civil and Environmental Engineering, 6(4), 4–9. https://doi.org/10.4172/2165-784x.1000236

Raza, A., et al. (2023). Water resources and irrigation management using GIS and remote sensing techniques: Case of Multan district (Pakistan). In C. B. Pande, M. Kumar, & N. L. Kushwaha (Eds.), Surface and groundwater resources development and management in semi-arid region. Springer Hydrogeology. Springer, Cham. https://doi.org/10.1007/978-3-031-29394-8_8

Salahat, M. A., & Al-Qinna, M. I. (2015). Rainfall fluctuation for exploring desertification and climate change: New aridity classification. Jordan Journal of Earth and Environmental Sciences, 7(1), 27–35.

Saragih, N. F., Sitepu, S., Simanungkalit, G. T., Sinambela, M., Rajagukguk, E., Larosa, F. G., & Jaya, I. K. (2022). Validation of CHIRPS estimation rainfall data using numerical accuracy test with precipitation observation data. In IOP Conference Series: Earth and Environmental Science (Vol. 1083, No. 1). https://doi.org/10.1088/1755-1315/1083/1/012095

Sayd, D., Yonnana, E., & Mubi, A. (2020). An analysis of rainfall and discharge relationship at the River Kilange catchment, Adamawa State, Nigeria. Jordan Journal of Earth and Environmental Sciences, 11(4).

Seong, C., Choi, K., & Jung, Y. (2022). Assessment of uncertainty in grid-based rainfall-runoff model based on

formal and informal likelihood measures. Water, 14(14). https://doi.org/10.3390/w14142210

Sishah, M. (2021). Rainfall runoff estimation using GIS and SCS-CN method for Awash river basin, Ethiopia. International Journal of Hydrology, 5(1), 33–37. https://doi.org/10.15406/ijh.2021.05.00263

Soulis, X., & Dercas, N. (2007). Development of a GIS-based spatially distributed continuous hydrological model and its first application. Water International, 32(1), 177–192. https://doi.org/10.1080/02508060708691974

Soulis, X., & Valiantzas, J. D. (2012). SCS-CN parameter determination using rainfall-runoff data in heterogeneous watersheds-the two-CN system approach. Hydrology and Earth System Sciences, 16(3), 1001–1015. https://doi.org/10.5194/hess-16-1001-2012

Soulis, X., Valiantzas, J. D., Dercas, N., & Londra, P. A. (2009). Analysis of the runoff generation mechanism for the investigation of the SCS-CN method applicability to a partial area experimental watershed. Soil Conservation, 605–615.

Verma, R. K., Verma, S. K., Mishra, A., Singh, A., & Jayaraj, G. K. (2017). A revisit of NRCS-CN inspired models coupled with RS and GIS for runoff estimation. Hydrological Sciences Journal, 62(12), 1891–1930. https://doi.org/10.1080/02626667.2017.1334166

Wei, Y., Yu, J., Xiao, J., & Chen, L. (2018). Rainfall-runoff risk characteristics of urban function zones in Beijing using the SCS-CN model. Journal of Geographical Sciences, 28(5), 656–668. https://doi.org/10.1007/s11442-018-1497-6

Wetchayont, C., Ekkawatpanit, S., Rueangrit, S., & Manduang, J. (2023). Improvements in rainfall estimation over Bangkok, Thailand, by merging satellite, radar, and gauge rainfall datasets with the geostatistical method. Big Earth Data, 1–25. https://doi.org/10.1080/20964471.2023.2171581

Zhang, F. (2019). Application of NRCS-CN method for estimation of watershed runoff and disaster risk. Geomatics, Natural Hazards and Risk, 10(1), 2220–2238. https://doi.org/10.1080/19475705.2019.1686431

Zhang, W., Fang, X., Jia, X., & Sheng, V. S. (2022). Research on rainfall estimation based on improved Kalman filter algorithm. Journal of Quantum Computing, 4(1), 23–37. https://doi.org/10.32604/jqc.2022.026975

Zhang, N., Wang, S., & Luo, L. (2011). Initial abstraction ratio in the SCS-CN method in the Loess Plateau of China. Transactions of the ASABE, 54(1), 163–169. https://doi.org/10.13031/2013.36271

JJEES

JJEES (2025) 16 (1): 50-60
ISSN 1995-6681

Jordan Journal of Earth and Environmental Sciences

Assessment of Groundwater Quality for Irrigation and Drinking Using Water Quality Indexes in the Upper Sebaou Valley (Tizi Ouzou-eastern Algeria)

Agrouche Sabrina[1], Mansouri Zineb[2*], Reghais Azzeddine[3], Kardache Ramdane[1], Dinar Haythem[4], Abdelkader Laafer[5]

[1]UMMTO University, Department of Geology, Algeria.
[2]MGRE Laboratory, Department of Geology, Batna2 University, Algeria.
[3]University Mohamed Seddik Benyahia of JijelGeological Engineering Laboratory (LGG)
[4]Centre de Recherche en Aménagement du Territoire (CRAT), Campus Zouaghi Slimane, Route de Ain el Bey, 25000 Constantine, Algérie.
[5](LSTM Laboratory, Department of Mechanic, Faculty of Technology, University of Blida 1, Soumâa Street No. 270, 09130 Blida, Algeria)

Received on 21 October 2023, Accepted on 29 November 2024

Abstract

This study assesses the suitability of groundwater for irrigation and drinking purposes in the Upper Sebaou Valley, using various methods. Eight water samples were collected during the high-water period in 2019 and were analyzed for major ions and physical parameters. The results revealed that the analyzed physical-chemical parameters were generally below the permissible limits of the World Health Organization (WHO), indicating good drinking water quality in 99% of the samples. The groundwater exhibited low alkaline characteristics, with pH values ranging from 7.5 to 7.8. The conductivity ranged between 843 and 1180 s/cm, and the total dissolved solids (TDS) levels ranged from 762 to 1009 in the research area. Hydrochemical facies analysis identified calcium and magnesium bicarbonate as the dominant types, with significant ions including Ca2+, Mg2+, Na+, HCO3-, Cl, and SO4-2. Multivariate statistical analysis, such as principal component analysis (PCA), provided insights into groundwater quality characterization. The analysis also highlighted the presence of high sodium levels, impacting soil permeability and causing water infiltration issues, which are crucial considerations for irrigation purposes. Overall, the results suggest that groundwater in the Upper Sebaou Valley is suitable for both drinking and irrigation purposes, with a few exceptions related to geogenic factors and excessive fertilizer use.

Keywords: *Drinking Water, Eastern Algeria, Hydrogeochemical Facies, Irrigation, Groundwater Quality, Upper Sebaou Valley, Water Quality Index.*

1. Introduction

One of the world's most valuable water sources is groundwater, which is located around three-fourths of the earth's surface. It provides a steady supply of freshwater, sustains ecosystems, and is a vital source of drinking water for numerous communities. Because of its subterranean location and filtration capabilities, groundwater is a valuable resource for the environment and humans (Soleimani et al., 2018; Muhammad and Ullah, 2022). It is a necessity for every person, including farmers, households, and manufacturers. Compared to other sources, it is regarded as pure (Jamshidzadeh et al., 2018; Boufekane et al., 2022). When rainfall hits the surface, it causes water to go through various processes that affect its chemical composition. These include the interactions between rocks and minerals as they move through the subsurface. This interaction helps shape the unique features of groundwater (Yousefi, Dehghani, et al., 2018; Muhammad and Usman, 2022). The water cycle affects the quality of groundwater. It is affected by various natural processes, such as ion exchange and mineral dissolution (Muhammad, 2023). Human activities, such as urbanization, overexploitation, and population growth can also have a significant impact on groundwater quality (Goyal et al., 2010; Kawo et al., 2018; Jasrotia et al., 2019; Asadi et al., 2019; Balamurugan et al., 2020; Adimalla et al., 2020; Haque et al., 2020; Panneerselvam et al., 2020; Aravinthasamy et al., 2021). However, the use of agrochemicals such as pesticides and fertilizers, as well as untreated industrial wastewater causes metals to infiltrate into water bodies (Khedidja et al., 2023).

In addition, industrial waste residues can leak into the groundwater, which can cause severe pollution (Muhammad, 2023). Although the Sebaou Valley has a lot of water, it is also heavily contaminated by agricultural, industrial, and urban sources (Din et al., 2023). The high stratum is the source of drinking water, while the rest is used for irrigation. It's important to monitor the water quality in a particular area (Muhammad and Ullah, 2022).

The evaluation of water quality involves assessing the various characteristics of groundwater, such as its pH level, color, temperature, turbidity, and dissolved oxygen. Hydrobiological features, including major anions and cations, are used as indicators for improving the classification process (Vadiati et al., 2016; Yousefi, Ghoochani, et al., 2018). The weighted and chosen parameters represent the end-uses of

* Corresponding author e-mail: z.mansouri@univ-batna2.dz

water, such as irrigation and drinking water (Sharma et al., 2006; Yousefi, Ghoochani, et al., 2018).

Various methodologies have been used to evaluate water quality to assess it more correctly, comparably, and realistically. The quality index (WQI) has been developed and invented since the 1960s. In 1848, the first investigations of the evolution of pollution levels and water quality were conducted in Germany. The Oregon Water Quality Index (OWQI) was developed by the Oregon Department of Environmental Quality (DEQ) in 1967 based on the transformation of water quality parameters without unity using sub-index equations, then, combining these sub-indices with mathematical expression to obtain a water quality index value. Following that, many indexes were devised in the 1970s, including Horton's index and Brown's index, used in 2010.

The Water Quality Index (WQI) serves as a convenient and standardized measure to evaluate water quality on a scale of 0 to 100. Higher WQI values indicate better water quality, while lower values signify poorer quality (Horton, 1965; Brown et al., 1970; Yousefi et al., 2017; Amin et al., 2021). WQI has been widely utilized by researchers to assess groundwater quality, examine regional variations in groundwater metrics, and evaluate the appropriateness of water for irrigation purposes (Stigter et al., 2006; Yousefi et al., 2017; Al-Hadithi et al., 2019; Hyarat et al., 2021; Hussien et al., 2022; Khaled et al., 2024).

Many studies, such as Djemai's hydrogeological study of the Sebaou Valley in 1985 (Djemai et al., 2017), conducted a study on physico-chemical water characteristics in the Upper Sebaou Valley (Great Kabylia), analyzing the variation of physico-chemical variables (pH) and electrical conductivity (EC), T°, Ca^{+2}, Mg^{+2}, Na^{+}, K^{+}, HCO_3^{-}, SO_4^{-2}, Cl-, and NO_3^{-}) and changes in water quality over time (2005–2007). This study's conclusions are geologically classic and broad in scope. The study analyzed the chemistry of groundwater and studied various hydrogeochemical processes. It also evaluated the Upper Sebaou groundwater's quality for irrigation and drinking water. Different indices, including the WQI, were used to analyze the region's water quality.

2. Materials and Methods

2.1. Study area:

The Sebaou plain is located 80 kilometres, east of northeast Algeria in the Tizi-Ouzou region. The area drained by the Sébaou River, and its watershed is confined by latitudes 36°27' and 36°55' North and longitudes 3°55' and 4°53' East. It has an estimated area of 1432 Km², extends from Boubhir upstream to the Belloua Pass downstream, and has a length of 30 km with a width ranging from 0.8 to 3 km (Figure 1).

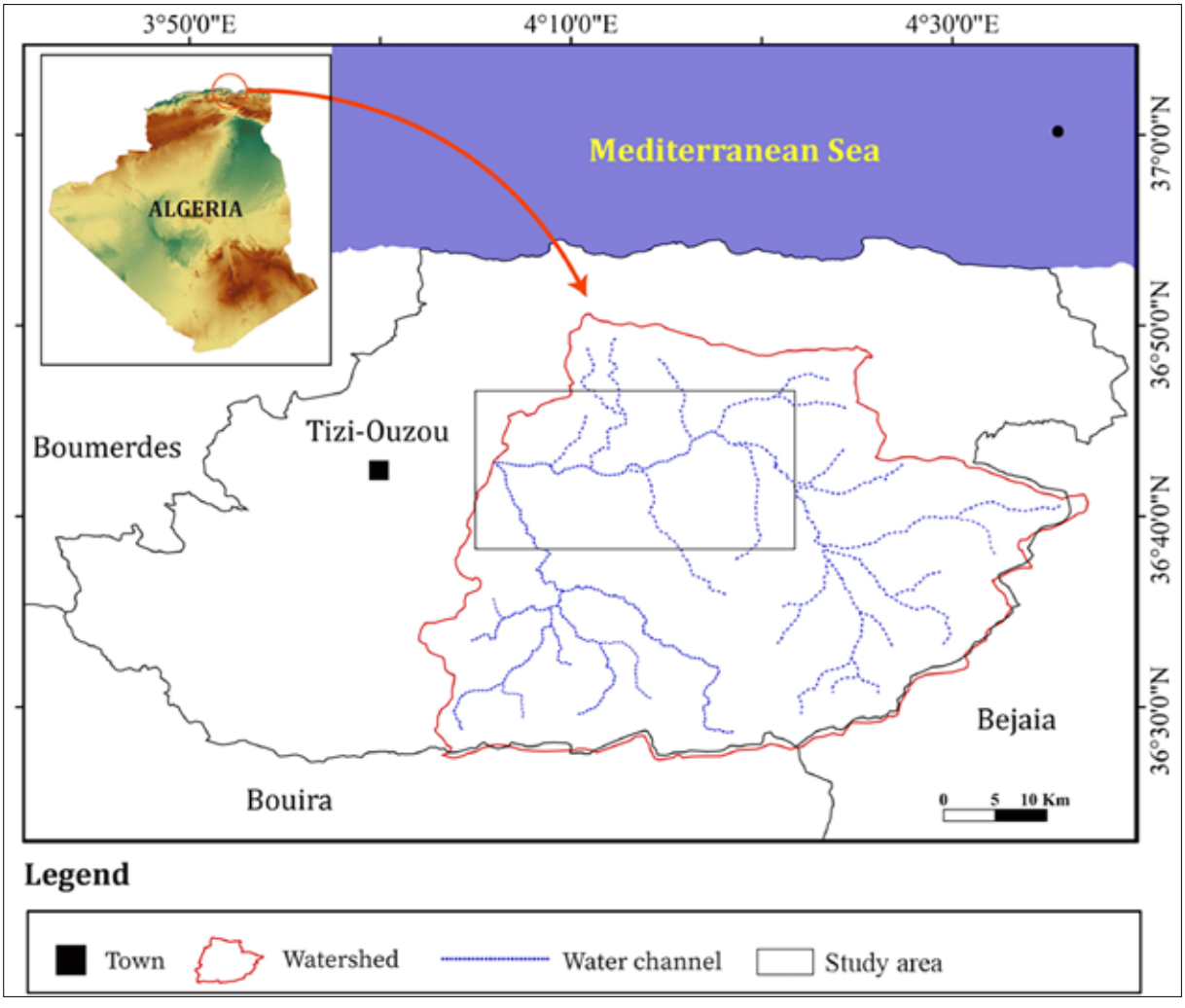

Figure 1. Geographical situation of the study area.

2.2. Agriculture and climate context:

Sebaou Valley, covering 50,000 hectares, is encompassed by densely inhabited areas, such as Oued Aisi, Freha, and Tizi Rached. The valley supports a population of 1,127,166 , with an EPA system connection rate of approximately 150 liters per capita per day as of 2020. The agricultural system in this region is predominantly multicultural, with mixed crop-livestock systems being the most prevalent.

The climate in the region is temperate, characterized by rainy winters and cool summers (Smail et al., 2013). The valley of Sebaou has a subhumid and mild climate with an average annual precipitation of around 824 mm per year. Between 2012 and 2019, the mean annual temperature was around 18.6 °C, and the Thornthwaite moisture index revealed a value of 944.05 mm. An average relative humidity of 70.5% is indicative of a humid season.

2.3. Geological and Hydrodynamical Setting:

The Upper Sebaou Valley has a free alluvial water table that runs east-west (Figure 2). It is surrounded by the Djurdjura mountains to the south and the Aftir coast to the north. This synclinal depression, filled with detrital materials derived from the crystalline rocks of the Kabyle socle, has resulted in the formation of stepped terraces. The underlying substrate comprises Miocene marls, which host a distinct hydraulic unit within the water table (Smail et al., 2013).

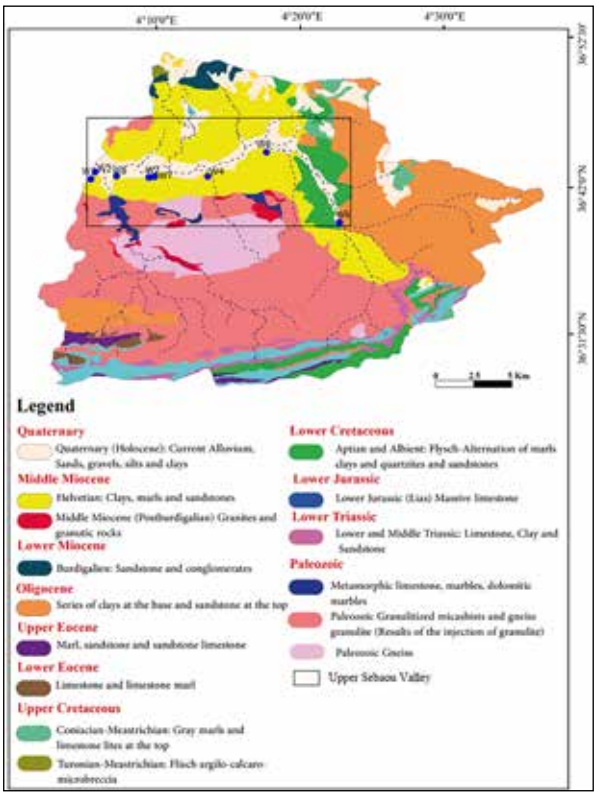

Figure 2. Geological formations of the Sébaou Valley.

23 water samples distributed throughout the plain of Sebaou were measured during the high-water and low-water periods of 2019. The piezometric maps revealed lateral flows from the east to west of the valley, which constitute an NE-SW-oriented drainage axis in the direction of the wadi flow (Figures 3 and 4).

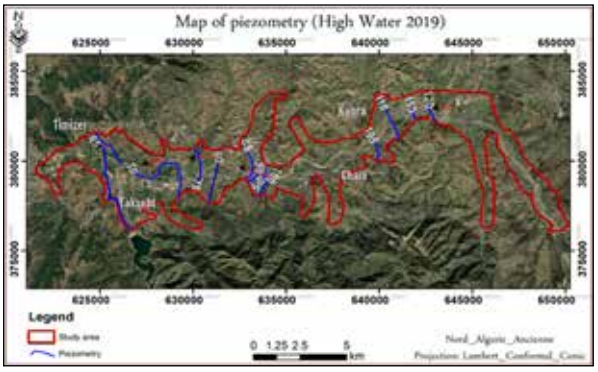

Figure 3. Map of piezometry (High Water 2019) ANRH 2019.

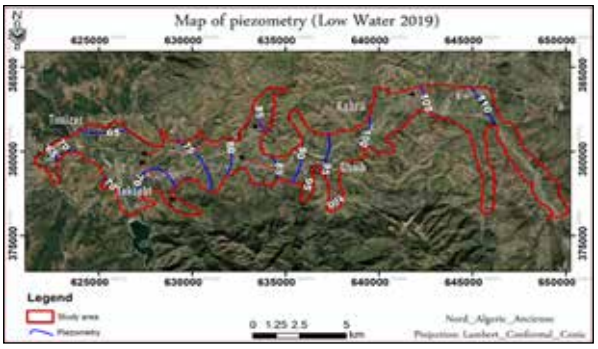

Figure 4. Map of piezometry (Low Water 2019) ANRH 2019.

2.4. Sampling and analysis:

The study aimed to assess the water quality of both irrigation and drinking water on the alluvial plain of the Sebaou Valley. By employing analytical techniques such as conductivity and pH measurements, it was feasible to acquire a more profound comprehension of the water's behavior. A total of eight boreholes was employed for the purpose of sample collection. The analysis was carried out at ANRH's laboratory in Tizi Ouzou, and the samples were gathered, using high-density polyethylene bottles. Subsequently, these bottles were securely closed in order to avoid any air contact . A filter was employed to exclude contaminants and particle matter from the samples. To mitigate the deposition of metal ions on the surfaces of the bottles, a solution of hydrochloric acid that has been acidified was employed. The study collected and prepared the samples in a way that ensured their reliability and accuracy. This was done to ensure that the results of the analysis were reliable. The concentration of Ca and Mg ions was estimated, using the EDTA sodic titration method, which is a complexometric approach. The concentration of Cl ions was measured using the Mohr method. On the other hand, the concentration of SO_4^{-2} ions was examined using the conductimetric titration method. The concentrations of potassium ions (K^+) and sodium ions (Na+) were determined using a flame photometer. The data obtained in milligrams per liter (mg/L) were converted to milliequivalents per liter (meq/L).

2.5. Multivariate statistical analysis :

Multivariate statistical analysis is a quantitative and independent method used to classify groundwater samples. Furthermore, a connection can be established between metals and groundwater samples, as demonstrated by Cloutier et al. in 2008. Furthermore, the present study

employed principal component analysis (PCA) and cluster analysis (CA), utilizing R Language version 4.1.1. (2021). Key statistical measures are the mean, range, and standard deviation (Khanoranga et al., 2019). K-means clustering was performed to group the sites into groups. The process of splitting a dataset into discrete groups or clusters based on a pattern optimizes certain clustering criteria.

2.6. Assessment for Drinking:

The index water quality was one of the most successful methods for measuring drinking water quality for policymakers (Reghais et al., 2023; Bezai et al., 2024). WQI is a rating that indicates the combined impact of many physico-chemical parameters on water quality (Belkhiri et al., 2018).

The relative weight (Wi) of each parameter was estimated as follows (Fehdi et al., 2009):

WQI =∑ Qi *Wi and Qi =∑ Vn/Sn*100

Wi is the weight and number of each parameter, for each parameter, the consistency rating scale (Qi) is assigned by dividing its concentration by its respective norm in each water sample (Al-Mashhadany, 2021).

2.7. Assessment Irrigation water quality indexes:

The following equations express the index: the concentration units were transformed from [mg/L] to [meq/L] according to the conversion factors given by (Lesch et al., 2009).

SAR (eq. 1) Laboratory of the USDA (Wilcox et al., 1995):

$$SAR = \frac{Na^{+}}{\sqrt{Ca^{+2}+Mg^{+2}/2}} \quad (1)$$

PI This parameter was estimated as follows (eq. 2), according to (Dinka, 2016):

$$PI = \frac{Na^{+}+\sqrt{HCO_3^{-}}}{Ca^{+2}+Mg^{+3}+Na^{+}} x100 \quad (2)$$

RSC (Residual Sodium Carbonate) index (eq. 3) (Richards, 1954);

$$RSC = [HCO_3^{-} + CO3^{-2}] - [Ca^{+2} + Mg^{+2}] \quad (3)$$

The sodium content percent (percent Na) was calculated using the following equation 4 (Todd, 1980):

$$Na\% = \frac{Na^{+}+K^{+}}{Ca^{+2}+Mg^{+2}+Na^{+}+K^{+}} x100 \quad (4)$$

Kelly's Ratio (KR) was calculated using the following equation 5 (Kelley, 1963):

$$KR = \frac{Ca^{+2}}{Ca^{+2}+Mg^{+2}} \quad (5)$$

Total Hardness (TH) was calculated using the following equation 6 (Crittenden et al., 2012):

$$TH\left(\frac{mg}{L}\right) = 2.497Ca^{+2} + 4.1152Mg^{+2} \quad (6)$$

3. Results and Discussion

3.1. Groundwater Chemistry:

Table 1 summarizes the results of the hydrogeochemical analysis hydrogeochemical of the collected data.

Table 1. Hydrogeochemical analysis of the Groundwater outputs.

Wells name	year	Ca^{+2} (meq/L)	Mg^{+2}	Na^{+}	K^{+}	HCO_3^{-}	Cl^{-}	SO_4^{-2}	NO_3^{-}	TH	TA	TDS	pH	CE
														µ/cm
W1	June 2018	6,943	3,006	1,435	0,051	5,998	1,517	1,416	0	49,743	0	779	7.6	1063
W2	June 2018	6,075	3,006	2,088	0,102	5,998	2,022	2,249	0,403	45,404	0	781	7.6	1060
W3	June 2018	7,377	1,288	2,262	0,026	7,747	1,657	1,874	0,065	43,324	0	842	7.5	987
W4	June 2018	6,509	2,147	1,348	0,051	6,748	1,32	1,624	0	43,279	0	726	7.8	846
W5	June 2018	6,292	1,718	2,088	0,026	6,248	1,798	1,145	0	40,047	0	696	8.2	843
W6	June 2018	8,244	3,865	1,957	0,077	7,747	1,742	3,31	0,887	60,546	0	1009	7.6	1290
W7	June 2018	7,377	2,147	1,522	0,077	7,248	1,404	1,166	0,339	47,618	0	781	7.6	905
W8	June 2018	7,81	4,079	2,262	0,051	8,747	1,742	2,561	0	59,5	0	979	7.7	1180
752	October 2018	6,719	3,716	1,174	0,072	6,498	1,882	2,457	0,032	52,176	0	806	7,6	1010
753	October 2018	7,905	2,347	2,392	0,038	7,498	2,247	1,999	0,29	51,259	0	895	7,37	1193
754	October 2018	5,929	2,738	2,218	0,026	5,998	2,36	1,416	0,29	43,334	0	737	7,6	963
755	October 2018	8,695	4,694	2,088	0,128	7,498	2,5	3,748	0,758	66,946	0	1025	7,43	1386
756	October 2018	5,533	2,738	1,653	0,026	5,498	2,303	1,353	0,032	41,358	0	681	7,6	847
757	October 2018	6,719	2,542	1,348	0,23	6,498	2,022	1,416	0,508	46,309	0	569	7,27	950
758	October 2018	2,569	2,347	0,913	0,486	4,499	1,77	0,208	0,161	24,58	0	448	7,3	604
W01	May 2013	5,3	3,15	1,78	0,06	3,99	2,022	3,331	0,08	43	20	727	7,4	1 101
W02	May 2013	2,65	3,67	0,91	0,05	5,49	0,562	1,062	0,08	32	28	468	7,4	750
W03	May 2013	1,59	6,61	0,95	0,05	7,99	0,534	1,499	0,24	41	40	560	7,4	1 000
W04	May 2013	3,18	7,35	1,95	0,12	6,99	0,674	5,663	0,59	53	35	847	7,2	1 284
W05	May 2013	3,39	5,04	1,87	0,04	6,99	0,758	1,457	0,35	43	35	532	7,3	919
W06	May 2013	3,61	4,83	1,26	0,05	6,49	0,646	1,707	0,43	43	33	562	7,5	903
W07	May 2013	2,65	3,67	1,6	0,03	4,99	0,787	1,499	0,29	32	25	590	7,3	900
W08	May 2013	3,71	3,67	1,13	0,06	5,99	0,646	1,145	0,22	37	30	527	7,4	800

Table 1 presents the descriptive data for groundwater, indicating that the conductivity levels range from 800 to 1386 µS/cm. Some of these samples exhibit unsuitable water quality, which can be attributed to excessive salinity in the Basale section of Great Kabylia. This salinity issue arises from contamination by wastewater and agricultural practices involving the extensive use of chemical fertilizers.

The pH of groundwater varied from 7,2 to 8,2, indicating a low alkaline kind. HCO3 can increase the pH and affect corrosion rates due to importing alkalinity into the water (Fijani et al., 2023). TDS levels ranged from 527 to 1025 in the research area. The dissipation of the dolomitic limestone terrains of Chellata-Djurdjura is also responsible for the high TDS levels detected in the dissolved matter. TDS levels are lower due to dilution from rainfall and the influent nature of surface water. Chloride and sodium concentrations in groundwater range from 0,53 to 1,88 meq/L and 0,91 to 2,26 meq/L. respectively, calcium ion concentrations are moderately greater than other cations, ranging from 1,5 to 8,6 meq/L, and magnesium concentrations range from 1,2 to 7,3 meq/L.

The concentrations of HCO3 and SO_4^{-2} vary from 3,9 to 8,7 and from 0,2 to 3,7 meq/L. During the rainy season, the dissolution of limestone-dolomite rocks in the sedimentary rocks of the Kabila basement frequently results in high magnesium, calcium, bicarbonate, and sulfate concentrations. However, potassium K concentrations in sample water ranged from 0.02 to 0.4 meq/L, with the greater value of K^+ possibly related to the excessive usage of lime in agricultural zones.

3.2. Groundwater classification:

The physical-chemical data are provided in Figure 5 to determine the chemical facies of Upper Sebaou Valley groundwater. Hydrochemical facies characterize calcium and magnesium bicarbonate and chloride and sulfate calcium and magnesium types, with Ca2+> Mg > Na and HCO3>Cl> SO4> NO3 as significant ions. The first group consists of samples (W1, W5, and W7), dominated by bicarbonate and chloride. The second group comprises wells (W2, W3, W4, W6, and W8), with HCO3 > SO4>Cl > NO3 as significant ion abundance, sulfate as the dominant element, and bicarbonate and calcium being the most prevalent in this group.

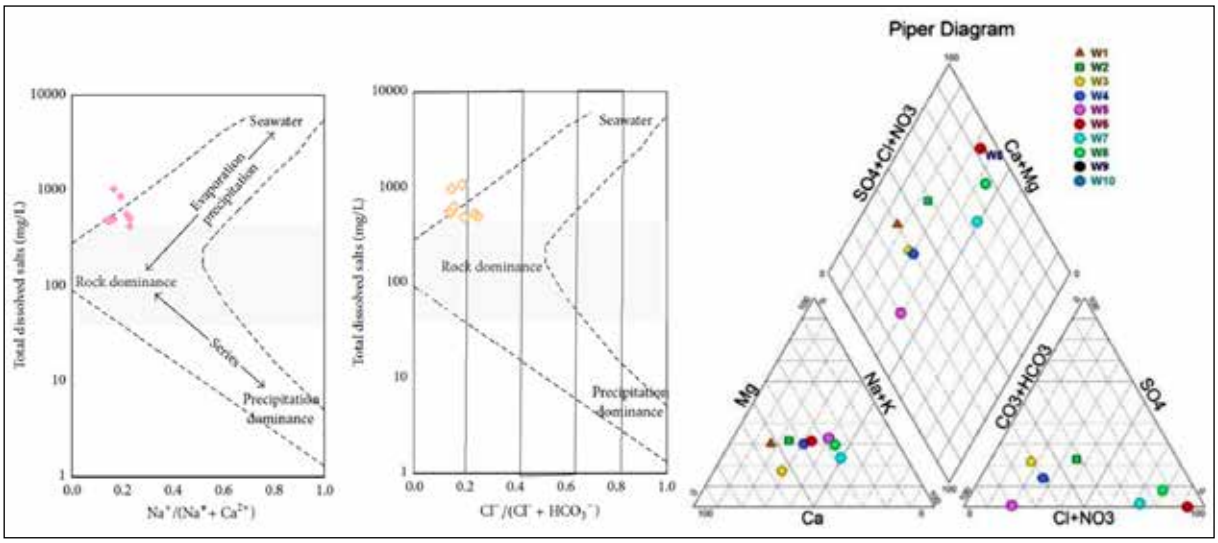

Figure 5. Piper diagram for water samples, and the ratio of Na+K/(Na+K+Ca) and Cl/(Cl+HCO3) as a function of TDS (High waters, Low waters).

3.3. Chemical weathering:

The ratio-I for cations [(Na+K)/(Na+K+Ca)] and ratio-II for anions [Cl/(Cl+HCO3)] as a function of TDS is commonly used to analyze the functional sources of dissolved chemical constituents, as shown in Figure 6 (Polemio et al., 2005). The location of the samples obtained in TDS > 500 mg/L segments. However, the majority of water samples in Sebaou Valley had high TDS concentrations and low I/I ratios and were found on the left side, indicating the preponderance of rock weathering. The phreatic water is controlled by the water rock.

3.4. Multivariate statistical analysis:

It is critical to do a statistical analysis of the given results. The basic statistics and correlation analysis provided insights into groundwater quality characterization. However, principal component analysis (PCA) uses 8 groundwater samples for 13 variables, including chemical-physical parameters (EC at 25°C, TH, TAC, TD, and pH) and major ions (Na^+, K^+, Ca^{2+}, Mg^{+2}, Cl^-, NO_3^-, $SO4^{-2}$, and HCO_3^-). Table 2 illustrates the physico-chemical element correlation matrix, with the latter indicating the correlateable elements by a high correlation coefficient ratio. A strong 0.82 connection exists between Ca, HCO3, and an average 0.77 correlation exists between (Mg, SO4). The chemical facies calcium-magnesium bicarbonate contains related components of the same origin. Ca (0.863), SO4 (0.7), and TDS are all substantially associated with electrical conductivity (0.962). It's also worth noting that chlorides have a relationship with Na and other elements, probably the result of the invasion by the sea.

Table 2. Correlation coefficient matrix of hydrochemical parameters (June 2018).

Variables	Ca2+	Mg2+	Na+	K+	Cl-	SO42-	HCO3-	NO3-	pH	EC	Rsc	TH	TAC
Ca2+	1	0,4739	0,1839	-0,009	-0,149	0,4906	0,8224	0,4428	-0,462	0,6843	0,8144	0,8122	0,8224
Mg2+	0,4739	1	0,1099	0,5111	0,2937	0,7720	0,3431	0,4266	-0,250	0,8437	0,7877	0,8986	0,3431
Na+	0,1839	0,1099	1	-0,159	0,7910	0,0779	0,4383	0,0861	0,0450	0,3704	0,4506	0,1644	0,4383
K+	-0,009	0,5111	-0,159	1	0,2635	0,2861	-0,157	0,6693	-0,438	0,3823	0,1922	0,3337	-0,157
Cl-	-0,149	0,2937	0,7910	0,2635	1	0,2450	-0,060	0,2916	0,0878	0,4235	0,3312	0,1201	-0,060
SO42-	0,4906	0,7720	0,0779	0,2861	0,2450	1	0,1765	0,4142	-0,489	0,8897	0,7953	0,7559	0,1765
HCO3-	0,8224	0,3431	0,4383	-0,157	-0,060	0,1765	1	0,1313	-0,295	0,4726	0,6834	0,6371	1,0000
NO3-	0,4428	0,4266	0,0861	0,6693	0,2916	0,4142	0,1313	1	-0,357	0,5955	0,4813	0,5032	0,1313
pH	-0,462	-0,250	0,045	-0,438	0,0878	-0,489	-0,295	-0,357	1	-0,500	-0,454	-0,396	-0,295
EC	0,6843	0,8437	0,3704	0,3823	0,4235	0,8897	0,4726	0,5955	-0,500	1	0,9604	0,8999	0,4726
Rsc	0,8144	0,7877	0,4506	0,1922	0,3312	0,7953	0,6834	0,4813	-0,454	0,9604	1	0,9276	0,6834
TH	0,8122	0,8986	0,1644	0,3337	0,1201	0,7559	0,6371	0,5032	-0,396	0,8999	0,9276	1	0,6371
TAC	0,8224	0,3431	0,4383	-0,157	-0,060	0,1765	1,0000	0,1313	-0,295	0,4726	0,6834	0,6371	1

The link between the variables is explained in the graph Variable-PCA in Figure 6. NO3, Mg, SO4, Cl, Na, Ca, CE, TDS, and HCO3 dominated component 1 on this axis, accounting for 50,9% of the total variations. Component 2 accounts for approximately 18,4 percent of unlimited variations; the pH is highly represented on this axis, opposite the first factor.

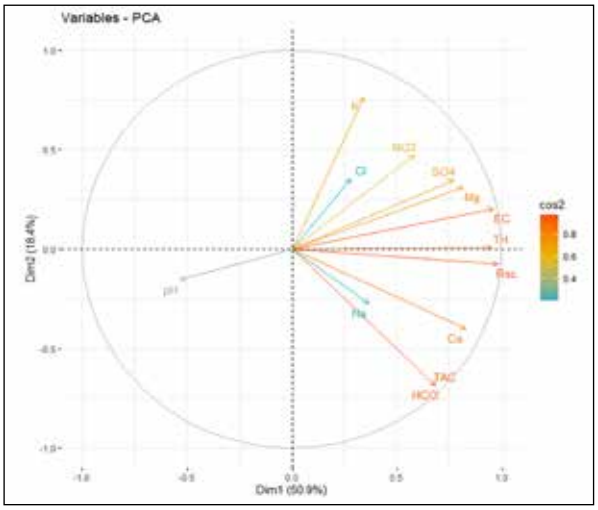

Figure 6. PCA of physical-chemical parameters of wells.

Figure 7's Boxplot results revealed the maximum and minimum values for Ca (121.73 mg/L and 165.21 mg/L, respectively) and Mg (15.65 mg/L and 49.56 mg/L, respectively), which fall within the permissible limits set by WHO in 2017. However, significant variations were observed in the values of Na (ranging from 21 mg/L to 57 mg/L), surpassing the prescribed permissible limit of 200 mg/L by WHO in 2017. The potassium concentration in groundwater exhibited variability, ranging from 1 mg/L to 4 mg/L, which is below the permissible limit according to WHO guidelines.

In all regions, chloride concentrations ranged from 47 to 72 mg/L, and Cl values in water samples did not surpass the WHO-recommended limit of 250 mg/L for drinkable water. The sulfate concentration fluctuates from a minimum of 55 mg/L to a maximum of 159 mg/L; current readings were below the WHO limit of 250 mg/L, and the concentration was at a level that did not pose a health risk. The concentrations of nitrates have not exceeded the allowed level of 50 mg/L (WHO 2017).

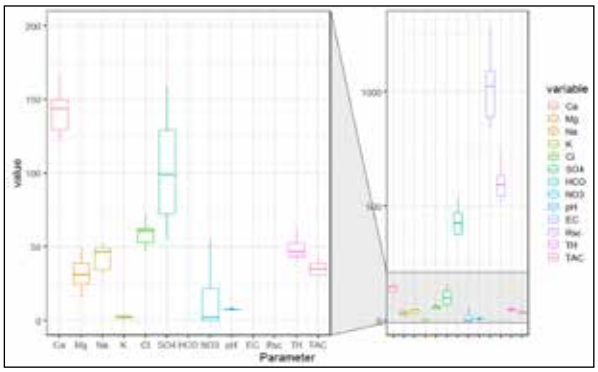

Figure 7. Boxplot of geochimical parameters.

3.5 Drinking water quality assessment:

Table 3 shows the water samples used to calculate the Water Quality Index (WQI). According to WHO 2017 (Table 4) based on the World Health Organization's 2017 report (Table 6), the drinking water quality index indicates a high standard of drinking water quality, with 90% of the samples meeting the criteria for good quality. Additionally, we found exceptional water quality in one specific well (W3).

Table 3. Water quality index.

	W1	W2	W3	W4	W5	W6	W7	W8
WQI	30.208	37.635	23.795	33.413	40.952	41.834	34.164	35.998

Table 4. WQI range according to WHO,2017.

WQI range	Water quality
0-25	Excellent
26-50	Good
51-75	Poor
76-100	Very Poor
Above 100	Unsuitable

3.6. Irrigation water quality assessment:

We demonstrate in this part indexes of irrigation water quality, data is presented in Table 5.

Table 5. Irrigation water quality evaluation

SAR	RSC	Na%	PI	MH	TH	KR
0,643591	-3,951	12,99995	34,12257	30,21453	49,7427	0,144
0,979845	-3,083	19,43208	40,62248	33,10208	45,40356	0,230
1,086676	-0,917	20,88551	46,17407	14,86757	43,32398	0,261
0,648163	-1,908	13,91858	39,44403	24,80505	43,27898	0,156
1,043318	-1,761	20,87788	45,43254	21,44548	40,04712	0,261
0,795486	-4,362	14,38216	33,70279	31,91591	60,54558	0,162
0,697659	-2,276	14,37708	38,15437	22,54472	47,61813	0,160
0,927663	-3,143	16,28542	36,88169	34,31012	59,44954	0,190

Table 6. Classification of irrigation water based on SAR, KR, Na%, TH RSC, and PI values (Eaton, 1950; Richards, 1954; Kelley, 1963; Doneen, 1964).

		Class
SAR	<10	Excellent
	10-18	Good
	18-26	Fair
Total hardness (TH) mg/L	<75	Soft
	75-150	moderately
	150-300	hard
KR	KR> 1 KR<1	Unsuitable Safe
Na%	<20	Excellent
	20-40	Good
	40-60	Permissible
	60-80	Doubtful
	>80	Unsuitable
PI	>75	Good
	25-75%	Doubeful
	<25	unsuitable
RSC	<1.25	Good
	1.25-2.5	Doubeful
	>25	unsuitable

Figure 8 and Table 6 highlight the common use of EC (Electrical Conductivity) and SAR (Sodium Adsorption Ratio) in conjunction. High sodium levels in water pose a challenge as they affect soil permeability and lead to issues with water infiltration. Sodium displaces calcium and magnesium that are absorbed by clay particles, resulting in soil compaction. This compaction reduces the rate of water infiltration during irrigation cycles, leading to insufficient soil saturation for crop roots before the next watering. All groundwater samples analyzed in this study exhibited SAR values within the excellent class, indicating satisfactory irrigation water quality. SAR values ranged from 0.60 to 1.08.

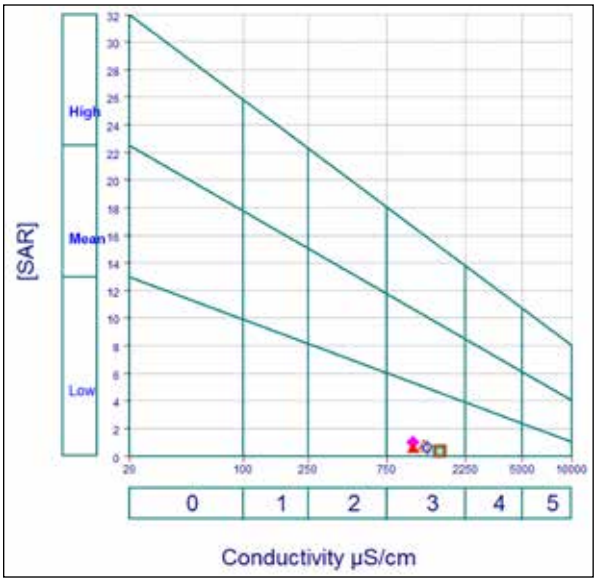

Figure 8. Classification of irrigation water quality according to Richards (1954).

The carbonate and bicarbonate ratios of residual sodium carbonate (RSC) are used to assess the groundwater for irrigation suitability (Selvakumar et al., 2017). The negative value of RSC indicate that the concentration of Ca^{+2} and Mg^{+2} is in excess (Rawat et al., 2018). The high value of RSC points to a high concentration of calcium and magnesium related to the reaction of HCO3-, generating calcium bicarbonate and magnesium bicarbonate (Chitsazan et al., 2019). High alkalinity of water could increase the pH value of the soil or plant development environment to the point of damaging their growth (Khedidja et al., 2014). The RSC values are -0,917 to -4,362 indicate a considerable risk of sodization degrading the soil's physical qualities (Feraga et al., 2021).

The Permeability Index (PI) is a useful tool to assess irrigation water suitability. It outlines the effect of sodium, calcium, magnesium, and bicarbonate ions concentrations on soil permeability (Doneen, 1964; Singh et al., 2020). It suggests water classification criteria according to the PI, which is related to water quality and displays the rate of water penetration (irrigation) into and through the soil (Mandal et al., 2019). A criterion for assessing the suitability of water for irrigation is based on PI water and can be classified into

classes I, II, and III. Class I and II water were categorized as good for irrigation with more than 75% of permeability (Khedidja et al., 2021). However, class III water was unsuitable with 25% of maximum permeability (Figure 9). All samples fall into class I, thus reflecting a good suitability for irrigation (Wu et al., 2014).

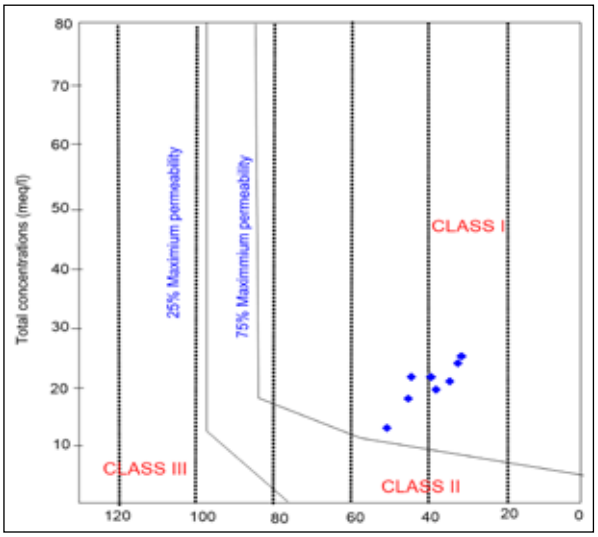

Figure 9. Classification of irrigation water based on the permeability index (June 2018).

The sodium percentage (Na%) in water is one of the criteria used to define the appropriateness of irrigation water (Tiwari et al., 1985). Sodium could indirectly harm vegetation by weakening the soil's physical quality (Richards, 1954). Moreover, the soil develops compact. The ability of plants to receive water or nutrients from their growth environment is hampered by high osmotic pressure in the soil-plant interface (Naseem et al., 2012). The percentage of Na in the examined sites varied from 12 to 22% (Figure 10). Sebaou Valley irrigation waters are grouped into class 2 (good).

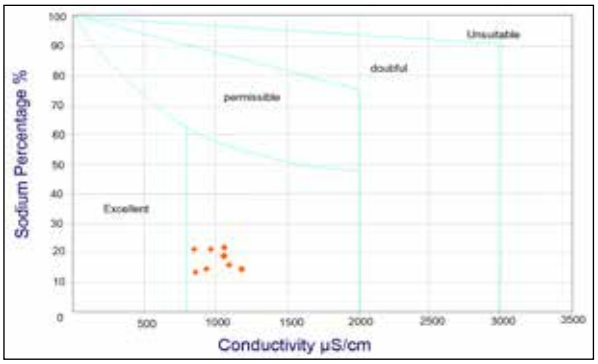

Figure 10. Suitability of Groundwater for irrigation in Wilcox diagram (June 2018).

The ratio between the concentration of sodium Na^{+} and the total of Ca^{+2} and Mg^{+2} is known as Kelly's Ratio (KR).

Groundwater with a Kelly ratio of less than one is generally considered suitable for irrigation (Paliwal et al., 1967). RK readings in this study are in the safe category, indicating that it is adequate for irrigation (Table 6).

3.7. Distribution of Spatial and Temporal Irrigations Index

The water quality for irrigation purposes via irrigation index spatiotemporal was calculated for a time period from 2013 to2018 (Docheshmeh Gorgij et al., 2023) . The results, depicted in Figure 12, exhibit notable variations in SAR values over a span of four years. Specifically, the SAR values observed in 2018 were considerably higher compared to those in 2013. Intensive cultivation practices and the expansion of agricultural lands, which result in higher concentrations of sodium in the soil, are likely responsible for this increase in SAR values. The excessive presence of sodium ions in the soil has a detrimental effect on the behavior of the colloidal fraction and leads to the dispersion of soil aggregates, subsequently reducing soil permeability and causing soil hardening (Tijani, 1994; Herrero et al., 2005).

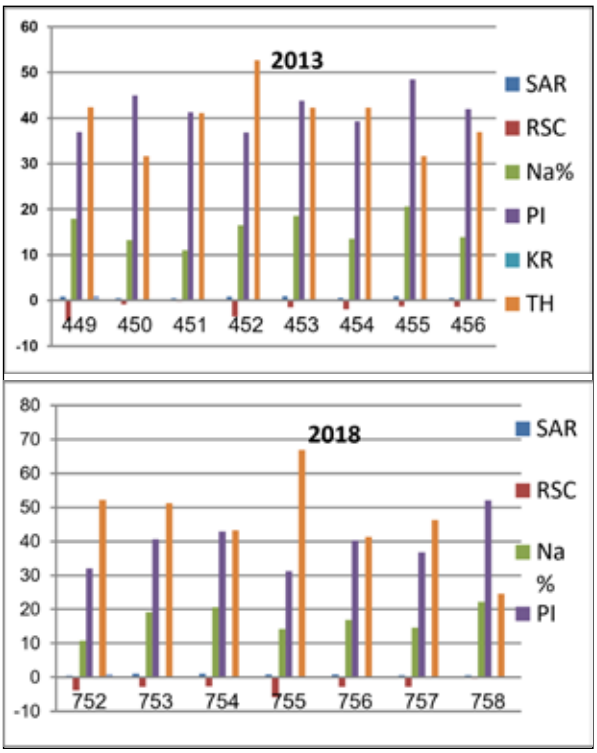

Figure 11. Evolution temporal of SAR, RSC, Na%, PI, KR and TH in 2013 and 2018.

4. Conclusions

This research employed multiple approaches to enhance the understanding of water quality in Sebaou, Tizi Ouzou. These approaches included Principal Component Analysis (PCA), Cluster Analysis (CA), and Correlation Matrix to examine the origin of mineralization and assess suitability for drinking water. The multivariate statistical techniques utilized evaluated the Sebaou Valley plain in Northeastern Algeria.

The research findings indicated that the groundwater quality in the study area was acceptable for irrigation purposes. Although the anatomical results showed satisfactory groundwater quality, thunderstorm effects led to changes in quality, including reduced rainfall, runoff, seepage, and alterations in the composition of precious water stones.

The identified significant chemical facies were primarily Ca-HCO3 (with variations of Mg, Cl, SO4, and Na), reflecting the mineralization patterns of the geological facies in the Sebaou Basin.Djemai et al. (2017) attributed the presence of HCO3 to limestone deposits in the Djurdjura mountains to

the south of the Sebaou River Valley (SRV) and attributed the origin of SO4 to agricultural and domestic effluents in the upstream agglomerations of the Sebaou valley. However, the samples fell within the medium to high salinity range (843–1290 µS/cm) based on electrical conductivity (EC) values, making them suitable for horticultural crops.

Nearly 99% of the water samples exhibited water quality above the allowed standards for irrigation, while the remaining samples exceeded the acceptable limits due to the influence of sulphate stones in the evaporator. The waters of the Sebaou Valley were categorised into category three, namely C3S1, based on their sodium adsorption ratio and electrical conductivity. This classification indicates their appropriateness for irrigation purposes. In addition, the water was categorized into four irrigation appropriateness categories based on its sodium percentage, with the majority falling into the "excellent" category. According to the Water Quality Index (WQI), groundwater from three districts was also safe for drinking, indicating that it was of good quality.

Acknowledgment

This work was supervised by the MGRE Laboratory, Department of Geology, Batna2 University, Algeria. And the ANRH Tizi Ouzou. Acknowledgments to the DGRsDT-mesRs for the technical support.

References

Adimalla, N. Taloor., Ajay, K. (2020), Hydrogeochemical Investigation of Groundwater Quality in the Hard Rock Terrain of South India Using Geographic Information System (GIS) and Groundwater Quality Index (GWQI) Techniques. Groundwater for Sustainable Development, 10: 100288. available at https://www.sciencedirect.com/science/article/pii/S2352801X19302231

Al-Hadithi, M., Hasan, K., Algburi, A. and Al-Paruany, K. (2019), Groundwater Quality Assessment Using Irrigation Water Quality Index and GIS in Baghdad, Iraq. Jordan Journal of Earth and Environmental Sciences, 10(1): 15–20.

Al-Mashhadany, M.H. S. (2021), Application of the CCME Water Quality Index to Evaluate the Groundwater Quality of Shouira Village for Drinking and Domestic Purposes in Nineveh Governorate. IOP Conference Series: Earth and Environmental Science, 722(1): 012029. available at

Amin, Sehrish, Muhammad, Said and Fatima, Hina (2021), Evaluation and Risks Assessment of Potentially Toxic Elements in Water and Sediment of the Dor River and Its Tributaries, Northern Pakistan. Environmental Technology & Innovation, 21: 101333.

Aravinthasamy, P., Karunanidhi, D., Subramani, T. and Roy, Priyadarsi D. (2021), Correction to: Demarcation of Groundwater Quality Domains Using GIS for Best Agricultural Practices in the Drought-Prone Shanmuganadhi River Basin of South India. Environmental science and pollution research international, 28(15): 18436. available at http://dx.doi.org/10.1007/s11356-020-09225-x

Asadi, Esmaeil, Isazadeh, Mohammad, Samadianfard, Saeed, Ramli, Mohammad Firuz, Mosavi, Amir, Nabipour, Narjes, Shamshirband, Shahaboddin, Hajnal, Eva and Chau, Kwok-Wing (2019), Groundwater Quality Assessment for Sustainable Drinking and Irrigation. Sustainability: Science Practice and Policy, 12(1): 177. available at https://www.mdpi.com/2071-1050/12/1/177 [8 July 2023].

Balamurugan, P., Kumar, P. S. and Shankar, K. (2020), Dataset on the Suitability of Groundwater for Drinking and Irrigation Purposes in the Sarabanga River Region, Tamil Nadu, India. Data in brief, 29: 105255. available at http://dx.doi.org/10.1016/j.dib.2020.105255

Belkhiri, Lazhar, Mouni, Lotfi, Tiri, Ammar, Narany, Tahoora Sheikhy and Nouibet, Razki (2018), Spatial Analysis of Groundwater Quality Using Self-Organizing Maps. Groundwater for Sustainable Development, 7: 121–132. available at https://www.sciencedirect.com/science/article/pii/S2352801X1730070X

Bezai, Abderrahim, Brinis, Nafaa, Reghais, Azzeddine, Djenba, Samir and Bouzid, Khadidja (2024), Hydrochemical Analysis and Groundwater Quality Assessment for Irrigation in the Remila Plain, Khenchela, Northeast Algeria. Geomatics Landmanagement and Landscape, (3): 35–57. available at http://gll.ur.krakow.pl/

Boufekane, Abdelmadjid, Belloula, Moufida, Busico, Gianluigi, Drias, Tarek, Reghais, Azzeddine and Maizi, Djamel (2022), Hybridization of DRASTIC Method to Assess Future GroundWater Vulnerability Scenarios: Case of the Tebessa-Morsott Alluvial Aquifer (Northeastern Algeria). NATO Advanced Science Institutes series E: Applied sciences, 12(18): 9205.

Brown, R. M., McClelland, N. I. and Deininger, R. A. (1970), A Water Quality Index-Do We Dare. Water and sewage.

Chitsazan, M., Aghazadeh, N., Mirzaee, Y. and Golestan, Y. (2019), Hydrochemical Characteristics and the Impact of Anthropogenic Activity on Groundwater Quality in Suburban Area of Urmia City, Iran. Environment, Development and Sustainability, 21(1): 331–351. available at https://doi.org/10.1007/s10668-017-0039-1

Crittenden, John C., Rhodes Trussell, R., Hand, David W., Howe, Kerry J. and Tchobanoglous, George (2012), MWH's Water Treatment: Principles and Design. John Wiley & Sons.

Din, Imran Ud, Muhammad, Said and Rehman, Inayat ur (2023), Groundwater Quality Assessment for Drinking and Irrigation Purposes in the Hangu District, Pakistan. Journal of food composition and analysis: an official publication of the United Nations University, International Network of Food Data Systems, 115: 104919.

Dinka, Megersa Olumana (2016), Quality Composition and Irrigation Suitability of Various Surface Water and Groundwater Sources at Matahara Plain. Water Resources, 43(4): 677–689. https://doi.org/10.1134/S0097807816040114

Djemai, Mohammed, Saibi, Hakim, Mesbah, Mohamed and Robertson, Andrew (2017), Spatio-Temporal Evolution of the Physico-Chemical Water Characteristics of the Sebaou River Valley (Great Kabylia, Algeria). Journal of Hydrology: Regional Studies, 12: 33–49.

Docheshmeh Gorgij, A., Askari, Gh, Taghipour, A. A., Jami, M. and Mirfardi, M. (2023), Spatiotemporal Forecasting of the Groundwater Quality for Irrigation Purposes, Using Deep Learning Method: Long Short-Term Memory (LSTM). Agricultural water management, 277: 108088.

Doneen, Lloyd David (1964), Notes on Water Quality in Agriculture. Department of Water Science and Engineering, University of California, Davis.

Eaton, Frank M. (1950), SIGNIFICANCE OF CARBONATES IN IRRIGATION WATERS. Soil science, 69(2): 123.

Fehdi, Ch, Rouabhia, Aek, Baali, F. and Boudoukha, A. (2009), The Hydrogeochemical Characterization of Morsott-El Aouinet Aquifer, Northeastern Algeria. Environmental geology, 58(7): 1611–1620. https://doi.org/10.1007/s00254-008-1667-4

Feraga, Touhami and Pistre, Séverin (2021), Qualitative and Comparative Study of Different Methods of Interpolation for the Mapping of Groundwater Salinity: Case Study of Thermal Waters Used for Irrigation in Northeastern Algeria. Journal of

geoscience and environment protection, 09(07): 115–132.

Fijani, Elham and Meysami, Sahar (2023), Assessment of Hydrochemical Characteristics and Groundwater Suitability for Drinking and Irrigation Purposes in Garmsar Plain, Iran. Geopersia, 13(1): 83–102.

Goyal, Sanjay Kumar, Chaudhary, B. S., Singh, Omvir, Sethi, G. K. and Thakur, Praveen K. (2010), GIS Based Spatial Distribution Mapping and Suitability Evaluation of Groundwater Quality for Domestic and Agricultural Purpose in Kaithal District, Haryana State, India. Environmental Earth Sciences, 61(8): 1587–1597. available at https://doi.org/10.1007/s12665-010-0472-z

Haque, Skmafizul, Kannaujiya, Suresh, Taloor, Ajay Kumar, Keshri, Dipika, Bhunia, Rakesh Kumar, Champati Ray, Prashant Kumar and Chauhan, Prakash (2020), Identification of Groundwater Resource Zone in the Active Tectonic Region of Himalaya through Earth Observatory Techniques. Groundwater for Sustainable Development, 10: 100337.

Herrero, J. and Pérez-Coveta, O. (2005), Soil Salinity Changes over 24 Years in a Mediterranean Irrigated District. Geoderma, 125(3): 287–308. available at https://www.sciencedirect.com/science/article/pii/S0016706104002204

Horton, Robert K. (1965), An Index Number System for Rating Water Quality. Journal - Water Pollution Control Federation, 37(3): 300–306.

Hussien, H., Samuel, Z. A. and Bokke, A. S. (2022), Assessment of Surface Water Resources Based on Different Growth Scenarios, for Borkena River Sub-Basin, Awash River Basin, Ethiopia. , (JJEES 13 (3): 199-214).

Hyarat, T. and Al, Kuisi M. (2021), Comparison between Weighted Arithmetic and Canadian Council of Ministers of the Environment Water Quality Indices Performance in Amman-Zarqa Area, Jordan. Earth Environ. Sci, 12(4): 295–305.

Jamshidzadeh, Zahra and Barzi, Majid Tavangari (2018), Groundwater Quality Assessment Using the Potability Water Quality Index (PWQI): A Case in the Kashan Plain, Central Iran. Environmental Earth Sciences, 77(3): 59. available at https://doi.org/10.1007/s12665-018-7237-5

Jasrotia, Avtar Singh, Kumar, Rajesh, Taloor, Ajay Kumar and Saraf, Arun Kumar (2019), Artificial Recharge to Groundwater Using Geospatial and Groundwater Modelling Techniques in North Western Himalaya, India. Arabian Journal of Geosciences, 12(24): 774. available at https://doi.org/10.1007/s12517-019-4855-5

Kawo, Nafyad Serre and Karuppannan, Shankar (2018), Groundwater Quality Assessment Using Water Quality Index and GIS Technique in Modjo River Basin, Central Ethiopia. Journal of African Earth Sciences, 147: 300–311.

Kelley, W. P. (1963), USE OF SALINE IRRIGATION WATER. Soil science, 95(6): 385.

Khaled, Eman Bani, Obeidat, Mutawakil, Al-Ajlouni, Ahmad, Awawdeh, Muheeb and Dalo, Muna Abu (2024), Demarcation of Groundwater Quality Using Drinking Water Quality Index (DWQI), Nitrate Pollution Index (NPI), and Irrigation Indices: A Case Study from Jerash Region. Jordan Journal of Earth and Environmental Sciences (JJEES), 15 (1): 37-52.

Khanoranga and Khalid, Sofia (2019), An Assessment of Groundwater Quality for Irrigation and Drinking Purposes around Brick Kilns in Three Districts of Balochistan Province, Pakistan, through Water Quality Index and Multivariate Statistical Approaches. Journal of Geochemical Exploration, 197: 14–26.

Khedidja, Abdelhamid and Boudoukha, Abderrahmane (2014), Risk Assessment of Agricultural Pollution on Groundwater Quality in the High Valley of Tadjenanet-Chelghoum Laid (Eastern Algeria). Desalination and water treatment, 52(22–24): 4174–4182.

Khedidja, Abdelhamid and Boudoukha, Abderrahmane (2021), Quality Assessment of Shallow Groundwater for Irrigation Purposes in Tadjenanet – Chelghoum Laid Area (Eastern Algeria). International Journal of River Basin Management, 19(2): 141–148. available at https://doi.org/10.1080/15715124.2019.1628031

Khedidja, Abdelhamid, Drias, Tarek and Reghais, Azzeddine (2023), Assessment of Groundwater Vulnerability to Pollution Using DRASTIC and the SI Methods: Case of the Alluvial Aquifer in Tadjenanet-Chelghoum Laid (East Algeria). Acque Sotterranee-Italian Journal of Groundwater, 12(2): 37–47. available at https://acquesotterranee.net/acque/article/view/644

Lesch, S. M. and Suarez, D. L. (2009), A Short Note on Calculating the Adjusted SAR Index. available at https://pubag.nal.usda.gov/catalog/30435

Mandal, S. K., Dutta, S. Kole, Pramanik, S. and Kole, R. K. (2019), Assessment of River Water Quality for Agricultural Irrigation. International Journal of Environmental Science and Technology, 16(1): 451–462. available at https://doi.org/10.1007/s13762-018-1657-3

Muhammad, Said (2023), Evaluation of Heavy Metals in Water and Sediments, Pollution, and Risk Indices of Naltar Lakes, Pakistan. Environmental science and pollution research international, 30(10): 28217–28226. available at http://dx.doi.org/10.1007/s11356-022-24160-9

Muhammad, Said and Ullah, Insha (2022), Spatial and Seasonal Variation of Water Quality Indices in Gomal Zam Dam and Its Tributaries of South Waziristan District, Pakistan. Environmental science and pollution research international, 29(19): 29141–29151. available at http://dx.doi.org/10.1007/s11356-022-18524-4

Muhammad, Said and Usman, Qazi Ahmed (2022), Heavy Metal Contamination in Water of Indus River and Its Tributaries, Northern Pakistan: Evaluation for Potential Risk and Source Apportionment. Toxin reviews, 41(2): 380–388. available at https://doi.org/10.1080/15569543.2021.1882499

Naseem, Shahid, Hamza, Salma and Bashir, Erum (2012), Assessment of Geochemistry of Soils for Agriculture at Winder, Balochistan, Pakistan. Water quality, soil and managing irrigation of crops, InTech-Open Access Publisher, Croatia: 73–94.

Paliwal, K. V. and Singh, S. (1967), Effect of Gypsum Application on the Quality of Irrigation Waters. Madras Agric J.

Panneerselvam, Balamurugan, Paramasivam, Suresh Kumar, Karuppannan, Shankar, Ravichandran, Nagavinothini and Selvaraj, Pauline (2020), A GIS-Based Evaluation of Hydrochemical Characterisation of Groundwater in Hard Rock Region, South Tamil Nadu, India. Arabian Journal of Geosciences, 13(17): 837. available at https://doi.org/10.1007/s12517-020-05813-w

Polemio, M., Limoni, P. P., Mitolo, D. and Santaloia, F. (2005), Nitrate Pollution and Quality Degradation of Ionian Coastal Groundwater (Southern Italy).

Rawat, K. S. and Singh, Sudhir Kumar (2018), Water Quality Indices and GIS-Based Evaluation of a Decadal Groundwater Quality. Geology, Ecology, and Landscapes, 2(4): 240–255. https://doi.org/10.1080/24749508.2018.1452462

Reghais, Azzeddine, Drouiche, Abdelmalek, Zahi, Faouzi and Debieche, Taha-Hocine (2023), Hydrogeochemical Evaluation of the Terminal Complex Aquifer System in an Arid Area: A Case Study from the Biskra Region, North-East Algeria. Environmental Earth Sciences, 82(7): 182. https://doi.org/10.1007/s12665-023-10786-6

Richards, L. A. (1954), Diagnosis and Improvement Of. Saline

and Alkali Soils. Handbook.

Selvakumar, S., Chandrasekar, N. and Kumar, G. (2017), Hydrogeochemical Characteristics and Groundwater Contamination in the Rapid Urban Development Areas of Coimbatore, India. Water Resources and Industry, 17: 26–33.

Sharma, M. P., Sharma, S., Gael, V. and Sharma, P. (2006), Water Quality Assessment of Behta River Using Benthic Macroinvertebrates. Life sciences.

Singh, Kshitindra Kr, Tewari, Geeta and Kumar, Suresh (2020), Evaluation of Groundwater Quality for Suitability of Irrigation Purposes: A Case Study in the Udham Singh Nagar, Uttarakhand. Journal of chemistry and chemical engineering, 2020.

Smail, Ali Si, Bouheraoua, Ali and Abdesselam, Malek (2013), Caractérisation Hydrodynamique Des Sols de La Haute Vallée de l'oued Sébaou (Algérie) : Étude Expérimentale, Numérique et Analytique. Physio-Géo, (Volume 7): 261–283.

Soleimani, Hamed, Abbasnia, Abbas, Yousefi, Mahmood, Mohammadi, Ali Akbar and Khorasgani, Fazlollah Changani (2018), Data on Assessment of Groundwater Quality for Drinking and Irrigation in Rural Area Sarpol-e Zahab City, Kermanshah Province, Iran. Data in brief, 17: 148–156. http://dx.doi.org/10.1016/j.dib.2017.12.061

Stigter, T. Y., Ribeiro, L. and Carvalho Dill, A. M. M. (2006), Application of a Groundwater Quality Index as an Assessment and Communication Tool in Agro-Environmental Policies – Two Portuguese Case Studies. Journal of Hydrology , 327(3–4): 578–591.

Tijani, M. 'N (1994), Hydrogeochemical Assessment of Groundwater in Moro Area, Kwara State, Nigeria. Environmental geology, 24(3): 194–202. http://dx.doi.org/10.1007/bf00766889

Tiwari, T. N. and Mishra, M. A. (1985), A Preliminary Assignment of Water Quality Index of Major Indian Rivers. Indian Journal of Environmental Protection.

Todd, David Keith (1980), Groundwater Hydrology. Brisbane, QLD, Australia: John Wiley and Sons (WIE).

Vadiati, M., Asghari-Moghaddam, A., Nakhaei, M., Adamowski, J. and Akbarzadeh, A. H. (2016), A Fuzzy-Logic Based Decision-Making Approach for Identification of Groundwater Quality Based on Groundwater Quality Indices. Journal of environmental management, 184(Pt 2): 255–270. http://dx.doi.org/10.1016/j.jenvman.2016.09.082

WHO (World Health Organization) (2017), Guidelines for Drinking-Water Quality: Fourth Edition Incorporating the First Addendum. World Health Organization, Geneva, Switzerland.

Wilcox, B. J., Applegate, M. D., Portera-Cailliau, C. and Koliatsos, V. E. (1995), Nerve Growth Factor Prevents Apoptotic Cell Death in Injured Central Cholinergic Neurons. The Journal of comparative neurology, 359(4): 573–585. http://dx.doi.org/10.1002/cne.903590405

Wu, Jianhua, Li, Peiyue, Qian, Hui, Duan, Zhao and Zhang, Xuedi (2014), Using Correlation and Multivariate Statistical Analysis to Identify Hydrogeochemical Processes Affecting the Major Ion Chemistry of Waters: A Case Study in Laoheba Phosphorite Mine in Sichuan, China. Arabian Journal of Geosciences, 7(10): 3973–3982. https://doi.org/10.1007/s12517-013-1057-4

Yousefi, Mahmood, Dehghani, Mohammad Hadi, Nasab, Saba Maghsoudi, Taghavimanesh, Vahid, Nazmara, Shahrokh and Mohammadi, Ali Akbar (2018), Data on Trend Changes of Drinking Groundwater Resources Quality: A Case Study in Abhar. Data in brief, 17: 424–430. http://dx.doi.org/10.1016/j.dib.2018.01.032

Yousefi, Mahmood, Ghoochani, Mahboobeh and Hossein Mahvi, Amir (2018), Health Risk Assessment to Fluoride in Drinking Water of Rural Residents Living in the Poldasht City, Northwest of Iran. Ecotoxicology and environmental safety, 148: 426–430. http://dx.doi.org/10.1016/j.ecoenv.2017.10.057

Yousefi, Mahmood, Saleh, Hossein Najafi, Mohammadi, Ali Akbar, Mahvi, Amir Hossein, Ghadrpoori, Mansour and Suleimani, Hamed (2017), Data on Water Quality Index for the Groundwater in Rural Area Neyshabur County, Razavi Province, Iran. Data in brief, 15: 901–907. http://dx.doi.org/10.1016/j.dib.2017.10.052

JJEES

JJEES (2025) 16 (1): 61-66
ISSN 1995-6681

Jordan Journal of Earth and Environmental Sciences

Environmental Governance in Jordan: Addressing Legislative Gaps, Preserving Natural Heritage, and Aligning with Global Climate Commitments

Mahmoud Abu-Allaban[1] and Safeia Hamasha[2]

1 Department of Water Management & Environment, The Hashemite University, Zarqa 13133, Jordan
2 Department of Physics, The Hashemite University, Zarqa 13133, Jordan

Received on 2 October 2024, Accepted on 20 December 2024

Abstract

Environmental legislation in Jordan has evolved significantly since the establishment of the country in 1921 to cope with growing local environmental challenges and international commitments. Still, there are significant gaps in enforcement and integration among different sectors. This paper examines Jordan's environmental policies by tracking the historical evolution of local environmental legislation with a particular focus on important issues including integrated water management, air quality, soil conservation, and sustaining natural and cultural heritage. We also analyze the effectiveness of Jordanian frameworks of environmental legislation, detecting gaps and inadequacies in areas such as implementation, policy consistency, and coping with international environmental obligations and commitments. Actionable recommendations recognized in international best practices, such as the Polluter Pays Principle as well as the Integrated Environmental Management (IEM) model are offered to fill gaps in local environmental governance, improving Jordan's legislative framework and ensuring long-term sustainability. Implementing the presented recommendations would lead to a referendum on the local legislative framework, enhance environmental practices, promote long-term sustainability, and address gaps in legislation and implementation to preserve natural and cultural heritage.

Keywords: *Environmental governance, Azraq wetland, Soil degradation, Pollution, Environmental policy, Cultural heritage.*

1. Introduction and Geologic setting

Jordan which is characterized by an arid climate and scarce natural resources, faces significant environmental challenges (Hadadin & Tarawneh, 2007; Al-Qinna et al., 2011). Since the establishment of the country in 1921, local environmental policy has evolved to address growing worries, including water scarcity, air pollution, soil contamination, and conserving cultural and natural heritage (Al-Momani, 2010; El-Anis and Poberezhskaya, 2023). Local environmental legislations face challenges in enforcing environmental laws, especially sustainable resource management and the prevention of industrial pollution (MoEnv, 2021). Recent years witnessed increased efforts at all levels to strengthen local environmental policies to align with global climate commitments including the Montreal Agreement to protect ozone, the Kyoto Protocol, the Paris Accord, and the outcomes of COP27 and COP28. However, the contamination of the food chain due to the overuse of herbicides and pesticides and the deterioration of some important natural ecosystems, such as the Jordan River and the Azraq Wetland, draws attention to significant gaps that need to be addressed and resolved in local environmental legislation.

The main questions of this research is to find out how efficient environmental legislative frameworks are in managing Jordan's key environmental challenges and what they lack to guarantee effective enforcement, consistency, integrity, and coping with international climate obligations.

The paper follows a dual approach: Firstly, it tracks the evolution of Jordan's environmental legislation since the British mandate to Transjordan, focusing on important areas such as the preservation of natural and cultural heritage, integrated water management, soil conservation, and air quality management. Secondly, it examines the effectiveness of frameworks of the existing laws and instructions, detecting shortcomings and gaps that need to be addressed and filled. It also assesses responses of Jordan's legislation to COP28–30 and other global climate initiatives. The Integrated Environmental Management (IEM) model and the Polluter Pays Principle are among the best practices that are highlighted in the paper and are recommended to strengthen the environmental legislative framework in Jordan and promote long-term sustainability.

2. Evolution of Jordanian Environmental Legislation

Environmental issues in Jordan are increasingly attracting the attention of competent authorities and public sectors to increase resilience and face vulnerability and stressed water bodies and scarce natural resources (Hadadin & Tarawneh, 2007; Alshamaila et al., 2024). Local environmental policies have evolved tremendously,reflecting Jordan's commitment to international climate treaties including the Paris Accord (MoEnv, 2017). However, the nation faces growing pressure to enhance its environmental governance, particularly in

* Corresponding author e-mail: mlaban@hu.edu.jo

sectors that contribute to global warming, in order to cope with the goals and outcomes of COP27-COP30 (UNEP, 2023; MoEnv, 2022).

In the following sections, we will trace the development of Jordanian environmental laws and instructions, identify deficiencies in regulatory frameworks, and analyze Jordan's environmental policy in the global context to develop a climate action plan for climate goal attainment (Babiker & Fehaid, 2012).

2.1. Early Environmental Regulation (19211946-)

Environmental governance, declared and enforced upon the establishment of the nation in the twenties of the 20th century, was limited aiming at protecting public health and natural resources. This is evident in the Health Law of 1926, the early regulatory framework that established provisions for sanitation and waste management in urban areas and laid the foundation for later environmental laws (Al-Momani, 2010, Al-Shamaileh, 2016, Combaz, 2019).

2.2. Post-Independence Developments (19461980-s)

The earliest post-independence law that influenced environmental governance was the Municipalities Law of 1955 which forced municipalities to manage urban planning and waste disposal to control solid waste and prevent pollution (Arabeyyat, 2024). The Water Resources Law of 1977 followed suit, forming a benchmark for protecting water resources to address the emerging water scarcity crisis.

2.3. Institutionalization of Environmental Policy (1990s)

The 1990s witnessed active governmental and public mobilizations to consolidate the environmental regulatory framework, culminating in the creation of the Jordanian Ministry of Environment (MOENV) in 1995, which enabled the centralization of efforts to address environmental pollution and waste management, and promote sustainable development. In that era, Jordan became more actively engaged in global efforts to protect the planet, including the 1992 Earth Summit in Rio de Janeiro, which significantly influenced Jordan's environmental legislation by promoting the principles of sustainable development (Combaz, 2019). The Environment Protection Law of 1995 strengthened Jordan's commitment to addressing environmental challenges and formed the milestone for subsequent regulations to address pollution control, waste disposal, and ecosystem preservation (MoEnv, 2020).

2.4. Modern Environmental Governance (2000s-present)

In the 2000s, Jordanian legislators passed more comprehensive laws: the Environment Protection Law of 2006, which replaced the 1995 Environment Protection Law, and the Agricultural Law of 2015. The amendments, made to the 2006 Environment Protection Law, established a comprehensive environmental management framework. They aimed at safeguarding all environmental components from anthropogenic pollution by introducing stricter controls on industrial pollution and hazardous waste, along with practices such as environmental impact assessments and environmental audits. The Agricultural Law of 2015 regulates the use of agrochemicals to protect agricultural lands by preventing (or minimizing) soil contamination, resulting from the excessive use of fertilizers, pesticides, and herbicides (MoAg, 2020). The nationwide ratification of the Paris Agreement in 2016 underscores Jordan's commitment to reducing greenhouse gas emissions. It also highlights the country's awareness of the global challenges, posed by ongoing climate change, with particular emphasis on its vulnerability to extreme weather events and decreasing rainfall, which negatively impact its fragile ecosystems and depleted water resources. Nevertheless, the enforcement of the best agricultural practices remains limited and insufficient to prevent soil degradation, hindering Jordan's efforts to increase agricultural productivity and strengthen food security (El-Anis and Poberezhskaya, 2023). This underscores the need for stricter enforcement, robust compliance mechanisms, and improved coordination among government agencies (UNDP, 2021). Achieving these targets presents significant challenges in strengthening regulatory governance and promoting inter-agency cooperation (El-Anis and Poberezhskaya, 2023).

3. Cross-Sectoral Influence on Environmental Policy

3.1. Health Sector Contributions

Public health is closely tied to Jordanian environmental legislation, as exemplified by the 2003 Instructions for Hazardous Waste Handling and Management enacted by the Ministry of Environment (MOENV). These instructions outline comprehensive guidelines for the safe storage, transportation, treatment, and disposal of hazardous materials, particularly chemicals and toxic substances, to ensure full protection of public health and occupational safety (MoENV, 2006). The instructions require contractors responsible for collecting, transporting, and disposing hazardous substances to sort, label, and securely containing them at their sources to prevent chemical spills and environmental contamination. They also emphasize using the best available technologies and disposal facilities that comply with international environmental guidelines and directives to minimize the risks of environmental degradation and health hazards (MOENV, 2006). The Public Health Law No. 47 of 2008 complements these instructions by requiring the safe disposal of hazardous waste and the controlled release of air contaminants. It requires systematic monitoring and management of local pollution sources to minimize the risks of public health exposure to toxic substances, thereby, reducing the potential for respiratory illnesses, cancers, and other chronic diseases (MoH, 2008). The Ministry of Health took a step forward by providing stricter and more detailed instructions (The Hazardous Materials Management Instructions of 2015) to enhance the effective management of hazardous chemicals and toxic substances. Capacity building and regular training of professionals, involved in handling hazardous materials, are vital components of the instructions and practices enforced by the Ministry of Health to ensure compliance with strict safety standards (MOH, 2015).

Together, the Hazardous Waste Handling and Management Instructions (2003) and the Hazardous Materials Management Instructions (2015) provided a robust regulatory framework that supported the environmentally responsible management of hazardous waste. These measures

reflect Jordan's commitment to improving environmental governance and safeguarding public health by minimizing the risks associated with the hazardous substances.

3.2. Role of Municipalities

Municipalities play a pivotal role in managing urban environmental issues, with responsibilities outlined in the Municipalities Law of 1955, revised in 2015. This law covers areas such as waste management, urban planning, and the enforcement of local environmental regulations. It serves as the foundation for local governance and environmental initiatives, aiming at improving urban sustainability and quality of life (Alshamaila et al., 2024).

In conjunction with the National Solid Waste Management Strategy (2015), municipalities have implemented initiatives to enhance environmental sustainability, such as creating green spaces and introducing recycling programs in cities like Amman and Irbid. These initiatives contribute to Jordan's broader environmental objectives by improving air quality, reducing waste, and promoting resource sustainability (United Nations, 2018).

Municipalities are also responsible for enforcing environmental regulations related to urban development, zoning, and land use. They ensure that construction projects comply with environmental standards, manage urban sprawl, and encourage green building practices. This role has become more critical as Jordan faces challenges related to rapid urbanization and the environmental impacts of climate change, including increased air pollution and waste generation (MOENV, 2020; Al-Kraimeen et al., 2024).

Collaboration between municipalities and central government agencies has been vital in aligning local and national environmental objectives, facilitating the implementation of policies at the local level, and strengthening municipalities' capacity to address urban environmental challenges effectively (MOENV, 2019).

3.3. Internal Affairs and Civil Defense

The Civil Defense Law No. 18 of 1999 is the cornerstone of disaster response in Jordan, addressing environmental hazards such as floods, droughts, and other climate-related risks. It establishes a framework for national coordination in disaster preparedness, response, and recovery, safeguarding communities from environmental hazards. As climate change intensifies, particularly with water resources and agricultural land, the importance of this legislation in protecting public safety and minimizing environmental damage has grown (McMurray, 2023).

Amendments to the Civil Defense Law in 2002 (Law No. 57 of 2002) strengthened the legal framework by introducing additional guidelines for managing large-scale disasters, including environmental emergencies. These provisions improve disaster response capacity and enhance coordination among government agencies, municipalities, and the private sector. As climate change exacerbates environmental challenges, such as water scarcity and land degradation, the law remains essential for addressing the increasing frequency of natural disasters.

Climate change consideration into disaster response policies is critical to ensuring Jordan's preparedness for the growing frequency of extreme weather events like heatwaves, droughts, and floods. These climate-induced disasters often worsen the vulnerabilities in water resources, agriculture, and public health. The evolution of the Civil Defense Law reflects Jordan's growing recognition of these risks and its efforts to build a more resilient disaster response framework (Al-Kharabsheh, 2020).

4. Environmental Policies Since the Paris Agreement

Jordan's National Climate Change Policy (2013-2020) and its updates offer a comprehensive framework for mitigating and adapting to climate change (El-Anis and Poberezhskaya, 2023). The policy emphasizes reducing greenhouse gas emissions and boosting renewable energy production, particularly in energy, water management, and agriculture—the sectors most vulnerable to climate impacts. These efforts aim to transforming Jordan to a low-carbon economy while enhancing resilience to climate challenges, especially water scarcity and agricultural productivity (MoEnv, 2013).

In line with international commitments, Jordan submitted its Nationally Determined Contribution (NDC) to the UNFCCC in 2016, with an updated version in 2021. The 2021 NDC includes more ambitious targets, particularly for resilience and adaptation in sectors like water and agriculture. These targets are essential for tackling climate challenges such as improving water efficiency, developing sustainable agriculture, and promoting climate-resilient infrastructure. The NDC reflects Jordan's determination to reduce emissions while acknowledging the unique challenges posed by its geographic location, limited resources, and reliance on external water sources (World Bank, 2020).

4.1. Renewable Energy and Energy Efficiency

Jordan has made significant progress in renewable energy development through the Renewable Energy and Energy Efficiency Law of 2012, which aims to expand the country's renewable energy capacity. It enabled various solar and wind energy projects, such as the Tafila Wind Farm and the Shams Ma'an Solar Plant, supporting the nation's commitment to reduce its carbon footprint and enhance energy security (MOEMR, 2012). To further support these efforts, Bylaw No. 13 of 2015 introduces financial incentives, including exemptions from customs duties and sales taxes on renewable energy equipment (MOEMR, 2012).

Jordan's renewable energy initiatives should have benefited from broader regional projects in the Middle East and North Africa (MENA) region such as Morocco that developed the renowned Noor Solar Complex, which enabled the country to reduce its carbon footprint while attracting international investment. Noor Solar Complex demonstrates the economic and environmental benefits of large-scale renewable energy projects and offers a potential model for Jordan and other developing countries (Hamouchene, 2016).

4.2 COP and Jordan's Path Forward

The outcomes of COP27-COP29 underscored the need for Jordan to revise and strengthen its environmental policies, particularly in the climate change resilience. This section introduces a roadmap to improve the country's resilience and adaptation to climate change.

4.3. Adaptation to Climate Change

Fresh water availability, which is increasingly impacted by global warming and regional instability, is a vital issue in Jordan. Therefore, water management is critical for Jordan as climate risks intensify. The National Water Strategy (2016-2025) integrates climate resilience into water conservation and wastewater management to sustain water resources nationwide. It emphasizes the improvement of water infrastructure for water harvesting, desalination, and the reclamation of domestic wastewater (MOWI, 2016).

4.4. Financing and International Cooperation

Securing climate finance to Jordan as well as other developing countries to support climate resilience efforts is one of the main actions called upon by COP27. Green Climate Fund (GCF) and the Adaptation Fund are crucial mechanisms for helping Jordan to ratify its water strategy and other climate resilience initiatives. Therefore, competent authorities are encouraged to participate in established funding bodies to secure external financial resources for large-scale projects in water management, renewable energy, and agricultural adaptation. This would strengthen Jordan's adaptive capacity, ensuring the well-preparedness of its economy and ecosystems for climate impacts. These efforts will also help the country to meet its commitments to the Paris Agreement regarding financing for mitigation and adaptation initiatives.

5. Critical Analysis of Current Environmental Legislation

As can be readily seen from previous sections, it is evident that Jordan has made progress in environmental legislation. However, there exist many challenges in the effectiveness of laws addressing environmental pollution and control of effluents. In addition, there are gaps between legislative goals and practical outcomes, which requires stronger enforcement, better coordination, and increased public awareness and involvement.

5.1 Air Quality

Ambient air pollution is a pressing issue in urban centers where anthropogenic activities contribute significantly to pollution. Despite regulations like the Public Health Law No. 47 of 2008, enforcement remains inconsistent, and air pollution levels occasionally exceed national standards or international guidelines (World Health Organization, 2021; Al-Kraimeen et al., 2024; World Bank, 2018). Ground-level ozone (O3) and CO levels also remain a concern in urban areas, particularly during peak traffic times (UNEP, 2020).

Developed countries like Germany and France imposed stringent regulations, forced carbon taxes, and promoted investments in renewable energy, which resulted in significant reductions in harmful emissions. Jordan's Renewable Energy and Energy Efficiency Law No. 13 of 2012 have promoted investment in solar and wind energy, but they did not foster integrating air quality management with renewable energy projects. This demonstrates the importance of strengthening law enforcement, integrating air quality with renewable energy policies, and introducing a carbon tax to help Jordan reduce air pollution and meet national climate goals and international obligations.

5.2 Water Management and Legislative Gaps

Jordan, which is classified as one of the poorest nations in fresh water resources, faces unprecedented challenges due to declining precipitation, increasing evaporation, and the high rates of population growth due to cultural inheritance and regional political instability. Water crises are exacerbated by unsustainable water management practices, weak enforcement, increasing demand from various sectors, and the fragmentation of responsibilities between authorities (Al-Kharabsheh, 2020). Integrated water management practices to link water management with agriculture, energy, and climate adaptation are essential for sustainable water use.

The Water Resources Law of 1977 and the National Water Strategy (2016-2025) regulate the extraction, allocation, distribution, and reclamation of traditional and nontraditional water resources, but they failed to prevent vandalism or overexploitation of water resources, which depleted most surface and ground water aquifers. hinders effective governance. Technologies, although recognized in the National Water Strategy, have not been expanded sufficiently. The government should invest in the best available technologies for desalination and water recycling to maximize water efficiency.

5.3 Soil Degradation and Pollution in the Food Chain

Excessive use of agrochemicals in fertilizers, herbicides, and pesticides continues to harm soil and the food chain. Agricultural Law No. 13 of 2015 is meant to regulate chemical use, but enforcement remains weak, which hinders the efforts of the agricultural sectors to take part in international markets. Tarawneh et al. (2019) pointed out that a ban in 2017 by neighboring countries on Jordanian vegetables due to pesticide residues resulted in a $100 million export loss. This implies that Jordan must strengthen its regulatory framework and promote organic farming, integrated pest management, and other sustainable farming practices to maintain a high quality of agricultural products, protect population and retain its international reputation. Additionally, a comprehensive review of Jordan's sectoral laws, including those for agriculture, water, and health is needed to align with climate goals and ensure effective, integrated responses to environmental challenges.

6. Preserving Cultural and Natural Heritage

6.1 Cultural Heritage Conservation

Jordan's cultural heritage, including unique sites like Petra, is integral to the nation's identity and economy, particularly through tourism. However, these sites face environmental pressures from urbanization, mass tourism, air pollution, and climate change. Rapid urban development and infrastructure projects threaten archaeological sites due to land confiscation and environmental deterioration which place immense strain on ecosystems. Acid rain and global warming intensify these issues, with extreme weather and fluctuating temperatures that accelerate the erosion of ancient structures and monuments (Abu-Allaban and El-Khalili, 2014).

6.1.1 Legislation and Challenges

The Antiquities Law No. 21 of 1988 was enacted to protect Jordan's cultural heritage sites. While it provides a framework for heritage protection, enforcement has been inconsistent, leaving sites vulnerable to environmental threats. The law lacks sufficient provisions to address the environmental aspects of heritage conservation, and inadequate monitoring and limited resources hinder enforcement.

6.1.2 Policy Recommendation

Jordan should strengthen legal frameworks by integrating environmental considerations into heritage site management. Comprehensive site management plans that address both conservation and sustainability are necessary. Sustainable tourism practices should be prioritized to reduce the ecological footprint of tourism and encourage eco-friendly behaviors among visitors. Stricter regulations, such as limiting access to fragile areas, controlling waste disposal, and mandating low-impact materials for site maintenance, would prevent further environmental damage. Strengthening collaboration between the Ministry of Antiquities, the Ministry of Environment, and other stakeholders would foster a more integrated approach to heritage protection.

6.2 Azraq Wetland

The Azraq Wetland, a vital natural habitat in Jordan's eastern desert, has suffered severe degradation due to excessive groundwater extraction. Since the 1960s, overexploitation of the Azraq Aquifer for agricultural, industrial, and domestic use has led to the near-total depletion of the wetland. By the 1990s, over-extraction had dried it up almost entirely, severely impacting biodiversity, including migratory birds and endemic plants (Damhoureyeh et al., 2004). Despite restoration efforts, including reducing water extraction and rehabilitating the ecosystem, the wetland has not fully recovered. Water levels remain critically low, and ecological imbalances threaten its long-term viability.

6.2.1 Restoration Efforts

The Azraq Wetland has faced significant degradation due to groundwater over-extraction, urbanization, and climate change. Since the 1990s, restoration efforts have focused on reducing groundwater extraction and restoring the wetland's natural hydrology. Despite these efforts, the wetland has not fully recovered, with water levels remaining low.

The scarcity of water in the region, exacerbated by population growth and agricultural expansion, continues to strain the aquifers feeding the wetland. Jordan's low per capita water availability makes it increasingly difficult to allocate water for environmental conservation (Mohammad, 2023). Additionally, climate change has altered the natural hydrological cycle, reduced aquifer replenishment, and increased evaporation rates (Wehrey et al., 2023). This creates a feedback loop, where the wetland's degradation worsens due to direct and indirect climatic effects.

To enhance restoration efforts, it is essential to integrate climate change adaptation into water management strategies. These should include using climate-resilient crops, improved irrigation technologies, and techniques to enhance water retention (UNEP, 2020). Artificial wetlands and wastewater treatment systems could help restore some functions of the wetland, reducing pressure on groundwater extraction. Additionally, modern irrigation systems surrounding the wetland would alleviate excessive groundwater extraction.

Effective governance and coordination between stakeholders, including the Ministry of Environment, the Ministry of Water and Irrigation, and local communities, are critical to the success of restoration efforts. Financial support from international funding sources for climate adaptation and conservation is also necessary to sustain rehabilitation initiatives.

A comprehensive approach, combining water management, sustainable agriculture, climate change adaptation, and innovative technologies, is essential for restoring the Azraq Wetland and preserving its ecological functions for future generations.

7. Summary and Conclusion

Jordan has made notable strides in environmental legislation since the establishment of the nation in the twenties of the previous century. However, significant gaps remain in enforcement, policy coherence, and the protection of both natural and cultural heritage. To meet the targets of the Paris Agreement and the outcomes of COP27-COP30, Jordan must address these gaps by strengthening climate change integration across sectors, improving air quality legislation, and expanding efforts in renewable energy.

By comparing Jordan with developed nations, it becomes clear that there are areas where its legal frameworks can be enhanced. Additionally, lessons from other developing countries provide valuable insights into scaling up renewable energy and climate adaptation initiatives. The degradation of critical ecosystems, such as the Azraq Wetland, further underscores the urgency for robust policy interventions.

Looking ahead, Jordan must prioritize institutional capacity building, secure international climate finance, and engage the public to ensure a sustainable environmental future. By adopting the best international practices like the Integrated Environmental Management (IEM) model and the Polluter Pays Principle, Jordan can strengthen its environmental governance and legislative framework. These steps will safeguard the country's natural and cultural heritage for future generations. Immediate action is essential to address these challenges and ensure a resilient and sustainable future for the environment and society.

Conflict of Interest

The authors declare no conflict of interest.

References

Abu-Allaban, M. and El-Khalili, MM. (2014). Antiquity Impact Of Air Pollution At Gadara, Jordan. Mediterranean Archaeology and Archaeometry 14(1), 191-199.

Al-Kharabsheh, A. (2020). Challenges to sustainable water management in Jordan. Jordan Journal of Earth and Environmental Sciences, 11(1), 38-48.

Al-Kraimeen, A., Hamasha, S., Abu-Allaban, M. (2024). Spatial and temporal variation of air quality index in Amman-Zarqa urban area. Nature Environment and Pollution Technology, 23(3), 1697-1708.

Al-Momani, N. (2010). Improving Jordan's law towards

sustainable solid and hazardous waste management: Lessons from USA's environmental laws. American Journal of Environmental Sciences, 6(4), 338-343.

Al-Qinna, M., Hammouri, N., Obeidat, M., & Ahmad, F. (2011). Drought analysis in Jordan under current and future climates. Climatic Change, 106(3), 421-440.

Al-Shamaileh, A. (2016). An evaluation of the effectiveness of environment policy in Jordan. International Journal of Business and Management, 11(2), 92. https://doi.org/10.5539/ijbm.v11n2p92

Alshamaila, Y., Papagiannidis, S., Alsawalqah, H. (2024). Smart cities in Jordan: Challenges and barriers. Cities, 154, 105327. doi:10.1016/j.cities.2024.105327.

Arabeyyat, A., Alnsour, J., L-Bazaiah, S., & Al-Habees, M. (2024). Managing urban environment: Assessing the role of planning and governance in controlling urbanization in the city of Amman, Jordan. Journal of Environmental Management and Tourism, 15(2), 263-271. doi:10.14505/jemt.v15.2(74).03.

Babiker, M. H. & Fehaid, M. A. (2012). Climate change policy in the MENA region: Prospects, challenges and the implication of market instruments. In Hala Abou-Ali (Ed.), Economic Incentives and Environmental Regulation (pp. 73-94). Edward Elgar Publishing.

Combaz, E. (2019). Jordan's environmental policies and engagement on climate change. K4D Helpdesk Report. Brighton, UK: Institute of Development Studies.

Damhoureyeh, Said, Disi, Ahmad, Al-Khader, I., & Al-Jboor, Sh. (2004). The Azraq Oasis: Biodiversity, threats and conservation. Annals of Arid Zone, 43, 317-334.

El-Anis, I., & Poberezhskaya, M. (2023). Responding to climate change in Jordan: Understanding institutional developments, political restrictions and economic opportunities. British Journal of Middle Eastern Studies, 1–19. doi:10.1080/13530194.2023.2279332.

Hamouchene, H. (2016). The Ouarzazate solar plant in Morocco: Triumphal 'green' capitalism and the privatization of nature. Jadaliyya. Retrieved from https://jadaliyya.com.

Hadadin, Nidal & Tarawneh, Zeyad. (2007). Environmental issues in Jordan, solutions and recommendations. American Journal of Environmental Sciences, 3, 30-36. doi:10.3844/ajessp.2007.30.36.

McMurray, S. (2023). Integrating climate security into policy frameworks: Jordan. adelphi research gemeinnützige GmbH. Retrieved from https://weatheringrisk.org/sites/default/files/document/Integrating_Climate_Security_into_Policy_Frameworks_Jordan_2.pdf.

MoAg-Jordan Ministry of Agriculture. (2020). National Agricultural Strategy (2018-2030). Ministry of Agriculture Annual Report.

MoEMR-Jordan Ministry of Energy and Mineral Resources. (2012). Renewable Energy and Energy Efficiency Law No. 13 of 2012. Ministry of Energy and Mineral Resources.

MoEnv-Jordan Ministry of Environment. (2006). Environment Protection Law No. 52 of 2006. Ministry of Environment.

MoEnv-Jordan Ministry of Environment. (2017). Jordan's Third National Communication on Climate Change to the UNFCCC. Ministry of Environment.

MoEnv-Jordan Ministry of Environment. (2019). Environmental governance in Jordan: Policy analysis and recommendations. MEE Report.

MoEnv-Jordan Ministry of Environment. (2020). Waste Sector Green Growth National Action Plan 2021-2025. Ministry of Environment.

MoEnv-Jordan Ministry of Environment. (2021). Environmental governance in Jordan: Challenges and opportunities. Ministry of Environment.

MoEnv-Jordan Ministry of Environment. (2022). Jordan's Nationally Determined Contributions (NDCs) Report. Ministry of Environment.

MoEnv-Jordan Ministry of Environment. (2022). National Climate Change Policy (2013-2020). Ministry of Environment.

MoH-Jordan Ministry of Health. (2008). Hazardous materials management instructions. Ministry of Health Publications

MoH-Jordan Ministry of Health. (2015). Hazardous materials management instructions. Ministry of Health Publications.

MoWI-Jordan Ministry of Water and Irrigation. (2016). National Water Strategy (2016-2025). Ministry of Water and Irrigation.

Mohammad, A.H., Ghanem, M., de la Hera Portillo, Á., Laftouhi, N.E. (2023). Sustainable water management for Azraq Geopark: Enhancing environmental sustainability and geotourism. International Journal of Design & Nature and Ecodynamics, 18(5), 1061-1067. doi:10.18280/ijdne.180506.

Tarawneh, I. N., Alawi, M. A., Saph, R. H., & Shmeis, R. M. (2019). Pesticide residues in commonly consumed fruits and vegetables in Jordan and their associated health risk assessments. Jordan Journal of Chemistry, 14(2), 69-80.

UNDP. (2021). Soil degradation and agricultural productivity in Jordan: Policy recommendations. United Nations Development Programme Report.

UNEP. (2020). Adapting to climate change in the Middle East: Integrated water management strategies. United Nations Environment Program.

UNEP. (2023). COP27 outcomes and their implications for developing countries. United Nations Environment Program.

United Nations. (2018). National Solid Waste Management Strategy in Jordan. United Nations Environmental Program.

Wehrey, F., Dargin, J., Mehdi, Z., Muasher, M., et al. (2023). Climate change and vulnerability in the Middle East. The Carnegie Endowment for International Peace. Retrieved from https://carnegieendowment.org/posts/2023/07/climate-change-and-vulnerability-in-the-middle-east.

World Bank. (2018). Air pollution in Jordan: Challenges and policy responses. World Bank Report.

World Bank. (2020). Climate change and water scarcity in Jordan: Strategies for adaptation and mitigation. World Bank Report.

World Health Organization. (2021). Air quality guidelines. WHO Publications

JJEES

JJEES (2025) 16 (1): 67-74
ISSN 1995-6681

Jordan Journal of Earth and Environmental Sciences

Modeling Recharge Rates of Stormwater Ponds into the Vadose Zone: A Case Study in a Semi-Arid Region

Tamer Eshtawi*

Department of Engineering and Smart Systems, University College of Applied Sciences, P.O. Box 1415, Palestine

Received on 28 May 2024, Accepted on 30 December 2024

Abstract

In this study, the basic soil hydrologic processes within the vadose zone were simulated using the Hydrus-2D/3D package, which presented a numerical solution to Richards equation (derived from Darcy's law). The flow through the vadose zone was modeled for five cases of moderate periods of infiltration (≤ 10 days), as practiced in stormwater harvesting ponds in the Gaza Strip. The five cases comprise: (a) three cases of surface infiltration, including three sizes of infiltration ponds, namely 25 × 25 m, 50 × 50 m, and 100 × 100 m and (b) two cases of dry well infiltration, with two sizes of infiltration ponds, namely 25 × 25 m having 9 dry wells, and 50 × 50 m, having 49 dry wells. For the surface infiltration cases, Darcy's gradient fit equation was determined to be (i = 2.4 − 0.24 ln (Pond Area, A)). In the case of dry wells, the infiltration capacity decreased from 93 m^3/day to 90.9 m^3/day using 9 dry wells and further declined to 81.7 m^3/day with 49 dry wells. Results reveal that infiltration rates decrease over time, with surface infiltration showing a notable reduction due to groundwater mounding, especially in larger ponds. Despite lower initial rates, dry well infiltration maintains greater stability and reduced mounding impact, suggesting its suitability for sustained recharge in semi-arid areas. The general empty dry well equation can be modified by a factor of 0.25 to 0.3 for large infiltration ponds to fit the case of a dry well filled with gravel. The study provides insight into the dynamic interactions between pond size, infiltration method, and groundwater mounding, highlighting essential design considerations.

Keywords: *Vadose zone; Infiltration rate; Stormwater harvesting; Dry wells infiltration, Hydrus 2D/3D*

1. Introduction

Recharge could be classified according to the source (De Vries and Simmers, 2002). Natural recharge is related to precipitation that infiltrates beneath the ground. In contrast, artificial recharge is a process of replenishing groundwater by the percolated surface water into the aquifer layer through various methods depending on the topographic, geologic, and groundwater conditions. The vadose zone influences the hydrologic cycle, which includes two major components of the water budget: surface runoff and percolation (Dillon, 2002). Quantifying water recharge in the vadose zone is still a research topic, especially in the context of urban water resources (He et al., 2024). There are different techniques, that could be utilized to estimate the infiltration rate into the vadose zone, e.g., Darcy's flux method, Green-Ampt models, and Richards' equation models. The Richards' equation, known for its detailed representation of unsaturated flow through porous media, is often regarded as the most accurate approach for modeling infiltration rates (Hsu et al., 2002). The Green-Ampt model, although simpler and less computationally demanding, has shown comparable performance to the Richards' equation in many practical cases (Williams et al., 1998).

Surface infiltration through ponds is a common recharge technique requiring permeable soil layers as well as an unconfined aquifer, whereas sufficient lateral flow is required to reduce groundwater mounding impact. Thus, a hydrogeological assessment is required to do the first screening and to select the proper sites. Where suitable geological layers, as well as suitable land areas for surface infiltration, are not available, vertical infiltration systems should be raised as a proper solution, such as dry wells in the vadose zone. Vadose zone wells are carried out using a bucket auger, and they could be about 0.6 – 1.2 m in diameter and reach 80 m deep. Clogging of the infiltration surface is a debatable problem that could result in a dramatic reduction of the infiltration rate into the topsoil and vadose zone (Bouwer, 2002).

Despite the simplicity of Darcy's law for one-dimensional saturated flow (Darcy, 1856), which is a function of the saturated hydraulic conductivity and the hydraulic gradient. The hydraulic gradient reflects the potential flow forces (e.g., gravity and capillary suction) causing water to infiltrate beneath the recharge facility. The variation of the hydraulic gradient is a function of the time of the infiltration event, the geology of the infiltration layers, and the groundwater depth. For a very short period of potential infiltration (e.g., less than a day for sandy soil), the initial infiltration is greater than the saturated hydraulic conductivity (K_s) since the hydraulic gradient value is greater than 1.0. Whereas infiltration will be around the (K_s) values for longer periods, then decrease to less than the (K_s) values as the wetting front (Green-Ampt concept) reaches the water table (Massmann et al., 2003).

* Corresponding author e-mail: teshtawi@ucas.edu.ps

In light of the above, some research has been carried out to estimate the hydraulic gradient under these circumstances using imperial methods. For example, Drost et al. (1999) performed different computer simulations to derive the effective gradient empirical formula under steady-state conditions for surface infiltration as well as infiltration trenches. However, there is a need for research depicting the unsteady state behavior of the infiltration process, including the change of the hydraulic gradient, especially for cases of short to medium infiltration periods, e.g., storm events in a semi-arid area.

The Richards' equation is a very common partial differential equation to simulate the vertical flow in the vadose zone, taking into account the variation of the hydraulic gradient (Zha et al., 2019). In spite of the applicability of the analytical solution, the numerical solution is recommended for its flexibility in dealing with boundary and initial conditions (Pachepsky et al., 2003).

Using finite element software is a significant approach to modeling the unsteady-state infiltration rate, considering the Richards' equation. The Hydrus software is a physical/numerical-based model, utilizing a finite-element method to simulate the movement of water as well as multiple solutes in different saturated media. Simunek and Weihermüller (2018) used Hydrus-1D to investigate the impact of soil, the initial water content of soil, and potential boundary conditions on the infiltration rate. Farasati and Shakeri (2018) used Hydrus-1D to infer the hydraulic parameters to model water infiltration rates in loamy soil for four pre-identified locations, considering the reverse method. Ying et al. (2020) utilized the Hydrus-1D to investigate a modified Green-Ampt model to quantify infiltration through a column of 3.0 m and five soil layers. Rasheed and Sasikumar (2015) used neural networks and white numerical models based on system knowledge to simulate the unsaturated flow process, taking feed-forward neural network architecture into account. With a recent update of Hydrus modeling techniques, Sasidharan et al. (2020) compared the efficiency of the dry wells as well as the surface infiltration basins under similar conditions using the Hydrus (2D/3D) software.

In the Gaza Strip, a semi-arid region, there are several ponds for stormwater infiltration as well as treated wastewater recharge; however, some of these ponds failed to meet the estimated infiltration rates. Several issues could be raised as reasons for system failure, including design criteria or equations and clogging during operation. Infiltration via dry wells, which are filled with gravel (0.6 - 0.8 m borehole diameter), has been used in Gaza to overcome the existence of shallow impermeable soil layers that can dramatically reduce a pond's infiltration rate. However, there are a lot of debates about the effectiveness of this alternative. Additionally, the chemical composition of groundwater depends on the recharge rate from anthropogenic sources, such as stormwater ponds, which can disrupt fragile groundwater systems either by polluting them or altering the hydrological cycle (Onwuka et al., 2010; Okogbue and Ukpai, 2013). The investigation of different infiltration systems and the simulation of their infiltration rates using a comprehensive technique can support future infiltration facilities as well as solve efficiency problems in similar current ponds. In this study, the vertical infiltration through the soil layers was addressed by Richards' equation to simulate the basic soil hydrologic processes in the vadose zone.

Not only does the study reflect the modeling of surface infiltration rate scenarios, but it also simulates the overall transient infiltration capacity of different sets of dry wells during discrete storm events in Gaza.

The study aims to simulate the infiltration rates of two main recharge techniques practiced in Gaza, namely surface infiltration and dry wells, taking into account soil hydraulic conductivity and groundwater level. The objectives of this study are to carry out (1) a 3D modeling of surface infiltration rates for different cases or combinations of pond areas and (2) a 3D modeling of dry well infiltration rates for a different combination of pond areas reflected in different numbers of dry wells. The study demonstrates a temporal simulation of the infiltration rates with different systems and sizes to be used as a guide for the proper design of stormwater infiltration facilities.

2. Study Area and Existing Recharge Facilities

The Gaza Strip is located in the eastern part of the Mediterranean; its climate is characterized as that of a semi-arid region. In Gaza, around 2.2 million people live within an area of 365 km^2, according to 2021 statistics (PCBs, 2021). Stormwater harvesting is considered a crucial policy that should be continuously embraced by the Palestinian Authority and implemented in different large projects, e.g., roads, industrial estates, etc. Large-scale infiltration facilities were taken into account over the last 10 years as a major non-conventional water resource in Palestine, particularly in the Gaza Strip (Hamdan et al., 2007). Gaza has faced continuous depletion of its underground resources due to withdrawals exceeding the total recharge of the aquifer. Consequently, the stored volume continues to decrease, similar to other semi-arid regions like Jordan, making efficient groundwater recharge essential (Bentahar et al., 2023). No specific location in Gaza was used in this study; however, the average period of storm events, the average groundwater elevation for most of the harvesting ponds, and soil hydraulic parameters are the main characteristics of the study area reflected in the model parameters.

2.1 Topography

The land surface topography of the Gaza Strip ranges from 0 (near the sea) to around 108 meters of elevation. Figure 1 (a) exhibits the digital elevation model of the Gaza Strip with a raster resolution of 30 m (USGS, 2021).

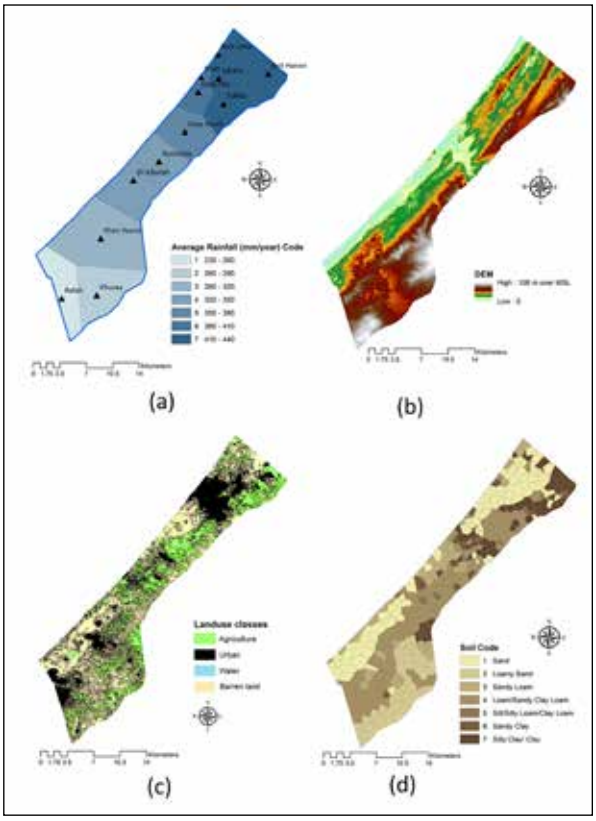

Figure 1. Gaza Strip: (**a**) Rainfall distribution (MoA, 2021); (**b**) Topography; (**c**) Landuse (developed by the author for year-2023; (**d**) Soil (MoA, 2021)

2.2 Climate

The climate of the study area varies, taking rainfall into account; the average annual rainfall for the Gaza strip is around 315 mm (around 415 mm for the north and 225 mm for the south). The annual pan evaporation is about 1620 mm in Gaza City (MOA, 2021), and the mean temperature varies between 14 °C in January and 28 °C in August (MOA, 2021). Rainfall is the main source of replenishment for the Gaza coastal aquifer. In the Gaza Strip, there are 12 daily rainfall stations distributed among the five Gaza governorates. Figure 1 (b) shows the average annual rainfall quantities of the 12 rainfall stations for the period 1976–2021. The daily rainfall data depicts that continuous storm events could, at their maximum before a significant stop, range between 5 and 10 days, which is a crucial factor in stormwater pond design in terms of hydraulic gradient calculation.

2.3 Soil and landuse

Three dominant land-use classes can be depicted in the Gaza Strip, namely, agricultural land, barren land, and urbanized areas representing more than 20 % of the Gaza Strip area (Figure 1 (c). Figure 1(d) depicts a soil map of the Gaza Strip, classified into seven soil textures according to the percentage of sand, silt, and clay. The main composition of the coastal soil (sand dunes) of the Gaza Strip is quartz and alumina silicate. Its layer thickness ranges from 2 m to about 50 m and extends up to 4 to 5 km, especially in the northern and southern areas. Sandy loess soils, loessial sandy soils, and loess soils prevail in the southeast part of the Strip. The soil in the north and east of Gaza is richer in silt, clay, and loess. Loess soil represents the main soil class around the valleys with a thickness of around 25 to 30 m (MoA, 2021).

2.4 Vadose Zone Characteristics

The vadose zone is the unsaturated zone above the groundwater level that represents the space between the topsoil and the water table. The vadose zone is functionally similar to that of aquifer media in terms of its permeability. The vadose zone media within the study area is classified as sandstone layer (50%), sand and sandstone (30%), and clay and sandstone (20%) (Al-Hallaq and Elaish, 2012). According to different experimental and technical studies, the saturated vertical hydraulic conductivity ranges from 2 to 6 m/day (4 m/day on average) for the sandstone layers that could be suitable for infiltration techniques. Under the stormwater ponds, the typical geological characteristics depict different formations of sandy layers and sandy loam layers that are suitable for infiltration as well as clay, silty clay, or sandy silty clay layers that have very low permeability. In some cases, the low permeable soil is shallow, which raises the need for a dry well technique to penetrate this layer to a more suitable one for infiltration. The groundwater depth beneath the majority of the stormwater infiltration ponds ranges between 15 and 25 meters.

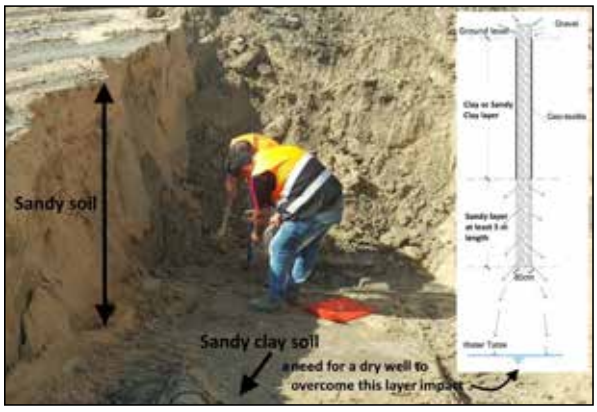

Figure 2. A real photo taken during the excavation for a stormwater pond depicting the need for dry well technique to penetrate a low permeable layer

Figure 2 shows a real photo taken during the excavation to construct a stormwater pond. The first 2 m were sandy soil, followed by a sand clay layer (very low permeable soil) with a thickness ranging from 8 m to 12 m before reaching a sandstone layer (sandy soil) with a saturated hydraulic conductivity of 4 m/day.

3. Vadose zone flow modeling

Vadose zone flow for five infiltration cases was modeled using the Hydrus-2D/3D package. The Hydrus, including its additional modules, solves the Richards' equation, using numerical techniques for saturated and unsaturated water flow and convection-dispersion type equations for heat and solute transport (Yu and Zheng, 2010).

Considering Richards' equation as the governing equation for the targeted model, Darcy's law for one-dimensional saturated flow is the basis for this equation, which can be expressed as equation (1).

$$q = K_s i = -K_s \frac{dH}{dl} \quad (1)$$

where K_s is the saturated hydraulic conductivity, H is the hydraulic pressure head, and (i) or dl/dl is the hydraulic gradient (defined as the change in total head per the unit length of the flow pathway). However, for unsaturated conditions, the hydraulic conductivity is a function of moisture content θ (it ranges between 0 and 1), so Darcy's law for unsaturated media (in one dimension) can be depicted as in equation (2).

$$q = -K(\theta)\frac{dH}{dl} \quad (2)$$

when the hydraulic pressure head (H) is a function of h (the capillary pressure head, which is a function of the moisture content θ) and z (the elevation head), then, Darcy's law can be written as in equation (3).

$$q = -K(\theta)\frac{d(h(\theta)+z)}{dz} \quad (3)$$

Given this relationship $\partial\theta/\partial t=-\partial q/\partial z$, the mass-conservative form of the Richards equation for 3D flow can be written as follows in equation (4) (Gasiorowski and Kolerski, 2020):

$$\frac{\partial\theta}{\partial t} = \frac{\partial}{\partial z}\left(K_z(h)\frac{\partial h}{\partial z} - K_z(h)\right) + \frac{\partial}{\partial x}\left(K_x(h)\frac{\partial h}{\partial x}\right) + \frac{\partial}{\partial y}\left(K_y(h)\frac{\partial h}{\partial y}\right) \quad (4)$$

where θ (h) represents volumetric water content; h refers to the pressure head (unsaturated zone has negative pressure), t is time; x, y, and z represent spatial variables, (m), and $K_x(h)$, $K_y(h)$, and $K_z(h)$ are unsaturated hydraulic conductivity in the mentioned spatial variables, (m/s).

The vadose zone hydraulic properties (e.g., soil water retention parameters) could be depicted by Mualem–van Genuchten (MVG) formulas (Simunek et al., 2006); however, this study utilized Modified Mualem–van Genuchten that improves the hydraulic conductivity characterization near saturation to get a converged solution (Schaap and Genuchten, 2005), especially regarding dry-wells cases. In the transient simulation process, the minimum time step was 0.001 days (1.44 min), which is a very important parameter; Hydrus could diverge with larger values when there was a sudden change in boundary fluxes.

3.1 Surface infiltration cases

Three cases of surface infiltration were simulated, taking into account three sizes of infiltration ponds, namely 25 × 25 m, 50 × 50 m, and 100 × 100 m. The water table is estimated to be approximately 20 meters below the soil surface (an average value among different stormwater ponds in Gaza). The soil water pressure head, an initial condition, was defined to be a constant pressure head of 0.5 m for the infiltration domain as depicted in Figure 3. The model domain for different cases was discretized into a three-dimensional triangular finite element mesh utilizing the MESHGEN tool under the umbrella of Hydrus, as tabulated in Table 1. The mesh was refined at the bottom of the infiltration area where a large water flux was expected. The depth of the overall domain was 30 m for all cases. The saturated hydraulic conductivity was 4 m/day.

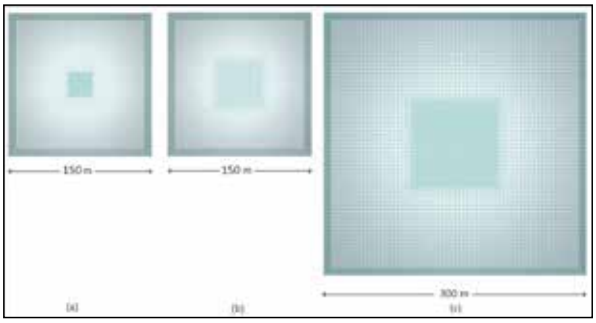

Figure 3. Finite element meshes (top plan) for the surface infiltration cases: (**a**) the modeling domain of 150 × 150 m and 25 × 25 m top infiltration domain; (**b**) the modeling domain of 150 × 150 m and 50 × 50 m top infiltration domain; (**c**) the modeling domain of 300 × 300 m and 100 × 100 m top infiltration domain.

3.2 Dry well infiltration cases

Two cases of dry well infiltration were simulated, taking into account two sizes of infiltration ponds namely, 25 × 25 m comprising 9 dry wells, and 50 × 50 m comprising 49 dry wells. The dry wells have a diameter of 0.8 m and were filled with gravel. The distance between the bottom of the dry well and the water table is 5 m for the two dry well cases. The soil moisture was considered to be uniform throughout the infiltration zone, whereas the capillary fringe was considered to be below the bottom of the dry well, and the soil domain surrounding the dry well installation was considered an unsaturated zone.

Table 1. Numerical model characteristics (surface infiltration)

Case	Characteristics
(a)	Total Domain: 150 × 150 × 30 m, 114,186 3D-elements Mesh size: 3.6 m (large), 0.9 m (small) Constant head: 0.5 m Infiltration space: 25 × 25 m Ks: 4 m/day GW depth: –20 m
(b)	Total Domain: 150 × 150 × 30 m, 104,691 3D-elements Mesh size: 3.6m (large), 1.8m (small) Constant head: 0.5 m Infiltration space: 50 × 50m Ks: 4 m/day GW depth: –20 m
(c)	Total Domain: 300 × 300 × 30 m, 162,906 3D-elements Mesh size: 5 m (large), 2.5 m (small) Constant head: 0.5 m Infiltration space: 150 × 150 m Ks: 4 m/day GW depth: –20 m

The soil water pressure head, an initial condition, was defined to be a constant pressure head of 0.5 m for the infiltration domain as depicted in Figure 4. The simulation domain was discretized into a three-dimensional triangular finite element mesh using the MESHGEN tool available within the Hydrus (2D/3D) as tabulated in Table 2. The mesh was refined at the bottom of the infiltration area where a large water flux was expected. The depth of the overall domain was 32 m for all cases. The saturated hydraulic conductivity was estimated for the infiltration sandstone layer (after a 10-m clay layer) to be 4 m/day. A top 2-meter sandy layer was

added as a natural filter to improve stormwater quality (as implemented in previous existing projects) with a saturated hydraulic conductivity of 8 m/day, making the water table 22 meters below the top of the added sand (or 20 meters, not considering this added layer).

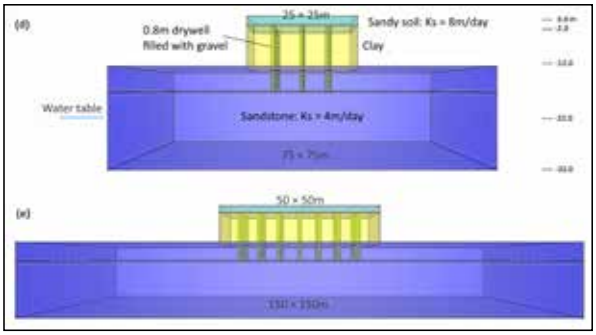

Figure 4. Finite element meshes for the drywells infiltration cases: (**d**) 9 dry wells; (**e**) 25 dry wells.

Table 2. Numerical model characteristics (dry wells)

Case	Characteristics
(d)	Total Domain: 173,612 3D-elements Mesh size: 2.4 m (soil layers), 0.8 m (dry wells) Constant head: 0.5 m Infiltration space: 25 × 25 m, 9 (diam. 80cm) Geological layers: 2 m top sand, 10 m clay, 5 m sandy layer, water table, 15 m sandy layer K_s for infiltration layer: 4 m/day K_s for top sandy layer: 8 m/day GW depth: –22 m
(e)	Total Domain: 185,739 3D-elements Mesh size: 5.0 m (soil layers), 0.8 m (dry wells) Constant head: 0.5 m Infiltration space: 50 × 50 m, 49 (diam. 80cm) Geological layers: 2 m top sand, 10 m clay, 5 m sandy layer, water table, 15 m sandy layer K_s for infiltration layer: 4 m/day K_s for top sandy layer: 8 m/day GW depth: –22 m

4. Results and Discussion

Modeling of recharge beneath stormwater ponds shows how the wetting front reaches the water table in terms of velocity as well as flux. The results illustrate a spatial-temporal behavior of infiltration taking into account two infiltration techniques, namely surface infiltration and dry well infiltration. The results show that there are negative relationships between the infiltration rate and the area of infiltration, as well as between the infiltration rate and the time of infiltration. The simulation results are depicted in Figures 5 to 10. The figures show the Darcy's velocities as well as the infiltration rates (from the output mass balance information) after 1 day, 5 days, and 10 days of simulation.

Regarding the surface infiltration cases, the infiltration rate obviously decreased from 4.1 m/day (case a) to 3.5 m/day (case c which has a higher infiltration area) on day 1, and similarly from 3.5 m/day to 0.9 m/day on day 10. The impact of groundwater mounding that occurs beneath stormwater ponds is obvious in case (c) exhibiting a dramatic decrease in the infiltration rate (from 3.5 m/day to 0.9 m/day). This impact is clear in the lag in colored contours of Darcy's velocity with time from day 1 to day 10 (decreased from 4 m/day to around zero in the middle of the pond for case (c)).

After 10 days of the simulation, a pond area of 625 m^2 (case a) lost around 15% of its initial infiltration rate. Similarly, cases (b) (pond area 2,500 m^2) and (c) (pond area 10,000 m^2) show losses of their initial infiltration capacities of around 47% and 74%, respectively. Referring to Darcy's equation (Equation 1) (the hydraulic gradient (i) was simulated to be 0.88, 0.51, and 0.23 for cases (a), (b), and (c), respectively.

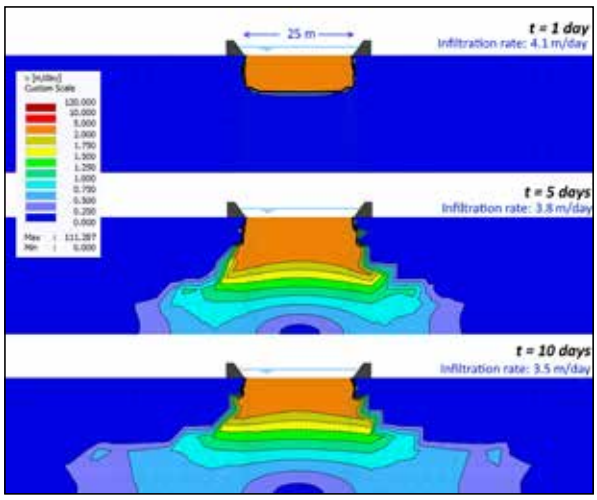

Figure 5. Darcy's velocity and infiltration rate in the vadose zone (20 m) (Case a).

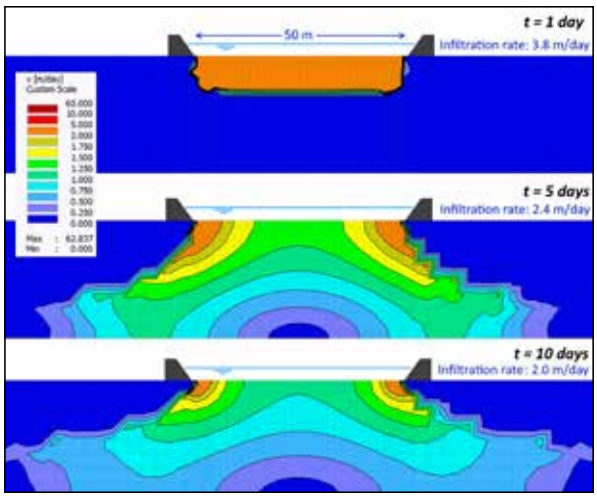

Figure 6. Darcy's velocity and infiltration rate in the vadose zone (20 m) (Case b).

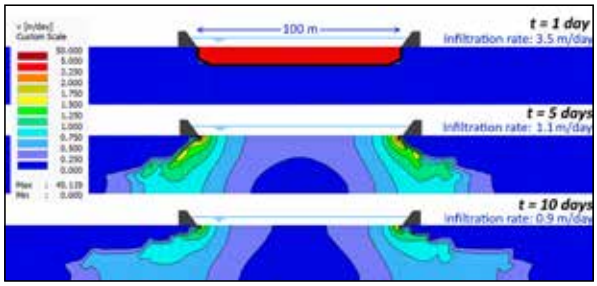

Figure 7. Darcy's velocity and infiltration rate in the vadose zone (20 m) (Case c).

Figure 8 depicts the relationships between the stormwater pond area (A) (> 500 m^2) and the gradient (*i*) for the three surface infiltration cases. Taking into account that a 10-day infiltration rate is suitable for the rainfall pattern in the

Gaza Strip, equation 5 is a deduced equation to estimate the Darcy gradient for general cases of stormwater ponds in the Gaza Strip as well as in other semi-arid regions with similar groundwater levels.

$$i = 0.24(10.1 - \ln(A)) \quad (5)$$

A comparison between the hydraulic gradient results obtained and those obtained using the empirical formula proposed by Massmann et al., 2003 is illustrated in Figure 8. Massmann equation is a steady state equation (Equation 6), to estimate hydraulic gradient (i) considering water depth in the pond (D_{pond}) (m), water table depth (D_{wt}) (m), infiltration area (A) (m^2), and saturated hydraulic conductivity (K_s) (m/s). It provides more conservative hydraulic gradient results because it deals with a steady-state situation rather than short to moderate infiltration periods (≤ 10 days).

$$i = 8.46 \times \frac{D_{wt}+D_{pond}}{K_s^{0.1}} A^{-0.76} \quad (6)\ \text{(Massmann et al., 2003)}$$

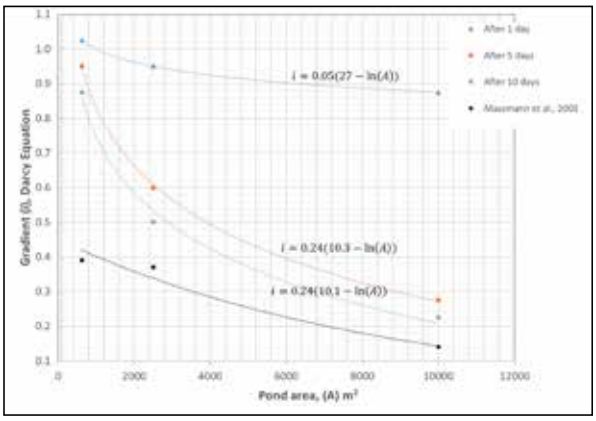

Figure 8. The relationship between the stormwater pond area (A) and the gradient (i) for the three surface infiltration cases

For the dry wells' infiltration cases, Figures 9 and 10 illustrate Darcy's velocity and the infiltration capacity for a dry well. The infiltration rates for the two cases were slightly lower compared with the surface infiltration cases, reflecting the lower impact of groundwater mounding. The dry well infiltration capacity decreased from 93 m^3/day to 90.9 m^3/day for case (d) and to 81.7 m^3/day for case (e) due to the grouping impact (multiple dry wells in one infiltration pond). The slight impact of groundwater mounding is clear in Case (e) on day 10, where the Darcy's velocity in some areas was reduced. Taking into account the dry well equation for empty boreholes (Equation 7) (not filled with gravels) (Bouwer, 2002):

$$Q = K_s 2\pi L_w^2 / \left\{ ln\left[\frac{L_w}{r_w} + \sqrt{\left(\frac{L_w^2}{r_w^2} - 1\right)}\right] - 1 \right\} \quad (7)$$

where Q is the infiltration rate (L^3/t), K_s represents the saturated hydraulic conductivity value (L/t), L_w refers to the length of the infiltration portion of the borehole (L), and r_w is the radius of the borehole (L). Figure 11 depicts these parameters.

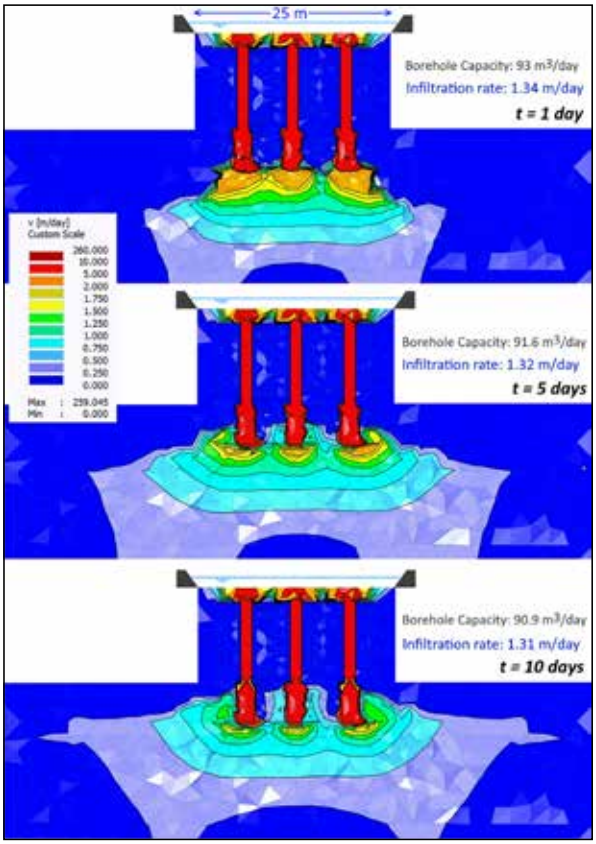

Figure 9. Darcy's velocity and infiltration rate (Case d)

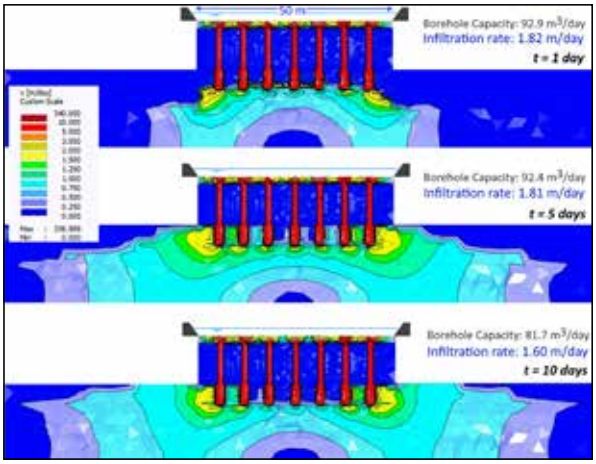

Figure 10. Darcy's velocity and infiltration rate (Case e)

The estimated Q for one borehole in the two-dry well cases was 283.2 m^3/day, not considering the grouping efficiency of the boreholes. This research result promotes a factor of around 0.3 (The model results, considering a gravel-filled dry well, show a value of 81.7, which is divided by the estimation from Equation 7 for an empty dry well = "81.7 / 283.2 = 0.3") to be used for modifying the dry well equation to fit the situation as well as the practice in Gaza (dry wells filled with gravel). This factor was deduced for a pond area of around 2,500 m^2 (around 50 m^2 for each dry well). According to the slight differences between the resulting values, this factor could be valid for larger ponds; however, it could be reduced to 0.25 for relatively larger ponds.

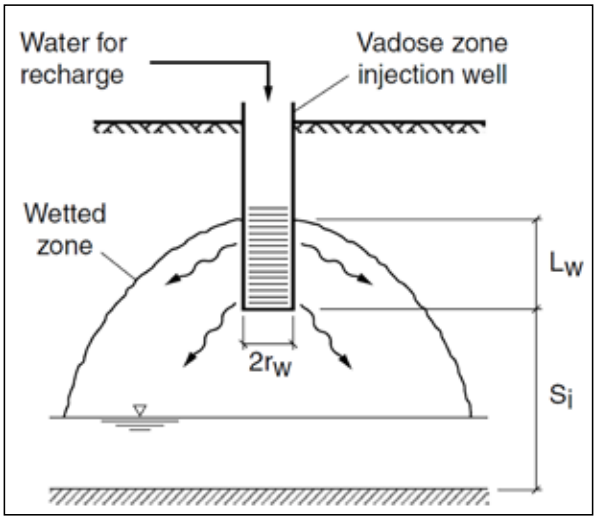

Figure 11. Dry wells parameters

The results of this study provide significant insights into the behavior of infiltration beneath stormwater ponds using both surface and dry well infiltration methods. The decreasing infiltration rates, observed over time, reflect the natural processes of soil saturation and groundwater mounding. In particular, the rapid decline in infiltration capacity for larger pond areas (e.g., case (c)) highlights the critical influence of pond size on groundwater recharge dynamics. This trend aligns with previous studies (e.g., Massmann et al., 2003), which indicate that larger infiltration areas result in lower hydraulic gradients, thereby reducing infiltration efficiency over time.

The comparison of surface and dry well infiltration also offers valuable practical insights. While the dry well method exhibited lower infiltration rates than surface methods, the reduced impact of groundwater mounding suggests its suitability for semi-arid regions, like Gaza, where maximizing infiltration over extended periods is crucial for groundwater recharge. Furthermore, the application of the Bouwer (2002) equation (Equation 7) for dry wells, combined with the deduced modification factor (0.3), provides a practical adjustment for engineers and hydrologists working in areas with similar geohydrological conditions. This factor allows for more accurate predictions of dry well performance, particularly when filled with gravel, as commonly practiced in Gaza.

However, there are several broader implications of these findings. The relationship between pond area and infiltration efficiency suggests that optimizing pond size for specific rainfall patterns and groundwater levels could enhance stormwater management strategies in semi-arid regions. This optimization could be particularly relevant for areas facing water scarcity, as more efficient infiltration designs could increase the recharge rate of local aquifers.

5. Conclusion and Recommendation

Hydrus-2D/3D was employed to estimate the infiltration rate into the vadose zone using two infiltration techniques, namely surface infiltration and dry well infiltration. Groundwater mounding, related to the infiltration pond area, has an obvious impact on reducing the infiltration rate for the surface infiltration technique.

The surface infiltration for a moderate infiltration period (10 days) was around 0.9 m/day for a pond area (A in m^2) of 10,000 m^2, which could be estimated as . Whereas, for the dry well technique, around 82 m^3/day is the capacity for one borehole after 10 days of infiltration. The hydraulic gradient (i) was estimated to be around 0.23 for large infiltration ponds on the 10^{th} day of the simulation. This value can be used for large infiltration ponds (around 10,000 m^2) utilized for stormwater harvesting purposes (10 days of infiltration simulates two storm events in a semi-arid region like Gaza). Equation 3, used for flow estimation through a dry well, can be modified by a factor of 0.25 to 0.3 for large infiltration ponds to fit the case of a dry well filled with gravel (a vertical trench). This factor comprises the impact of constructing several dry wells in one pond, and the time of infiltration. Extending the research cases to include a longer simulation time as well as a larger infiltration pond area to cover the infiltration of continuous effluent from treated wastewater is recommended. Although Massmann et al. (2003) equation (Equation 6) reflects a slight change in the hydraulic gradient (i) due to any significant change in the saturated hydraulic conductivity (in the equation, K_s was raised to a small power ($K_s^{0.1}$)), investigating the sensitivity of saturated hydraulic conductivity and its impact on the hydraulic gradient will be useful in supporting more design practices for infiltration techniques in Gaza.

From another side, the Massmann equation provides a conservative estimate of hydraulic gradients under steady-state conditions, the differences observed between the empirical and model results suggest that more research is needed to adapt these general equations to the short- to medium-term infiltration periods typical in stormwater management practices. Future work could also focus on refining the modified Bouwer equation for dry wells to better account for variations in pond size and groundwater levels, as well as other influencing factors such as soil heterogeneity and compaction.

Moreover, the sensitivity of the infiltration rates to groundwater mounding raises questions about long-term sustainability. While the model results provide a 10-day snapshot, longer-term simulations are necessary to assess how continued stormwater recharge might impact groundwater quality, particularly in areas with high contamination risk. Studies on the transport of pollutants during infiltration events (especially in urban areas) could help determine the suitability of these methods for both quantity and quality management of groundwater.

Finally, this research demonstrates the concept of effective blue-green infrastructure that depicts natural systems and artificial facilities covering urban water systems (blue infrastructure, e.g., stormwater harvesting ponds, and green infrastructure, e.g., natural habitats, ecosystems, and urban greenspace).

Acknowledgments

This research was supported by MEDRC Water Research Innovation Initiative Award – Palestine.

Conflict of Interest

The author declares that he has no known competing financial interests or personal relationships that could have appeared to influence the work reported in this paper.

References

Al-Hallaq, A., and Elaish, B. (2012). Assessment of aquifer vulnerability to contamination in Khanyounis Governorate, Gaza Strip—Palestine, using the DRASTIC model within GIS environment. Arabian Journal of Geosciences, 5: 833–847.

Bentahar, F., Mesbah, M., and Ribstein, P. (2023). Hydrogeological modeling of the sandstone aquifer of Mostaganem Plateau (North-West Algerian) and perspectives on the evolution of withdrawals. Jordan Journal of Earth and Environmental Sciences, 14(2): 113-125.

Bouwer, H. (2002). Artificial recharge of groundwater: Hydrogeology and engineering. Hydrogeology Journal, 10(1): 121–142.

Dillon, P.J. (Ed.) (2002). Management of aquifer recharge for sustainability: Proceedings of the 4th International Symposium on Artificial Recharge of Groundwater (ISAR-4), Adelaide, South Australia, 22–26 September 2002. A.A. Balkema Publishers, Lisse, Netherlands, 561p.

De Vries, J.J., and Simmers, I. (2002). Groundwater recharge: An overview of processes and challenges. Hydrogeology Journal, 10: 5-17.

Farasati, M., and Shakeri, H. (2018). Simulation of water infiltration in the soil using HYDRUS-1D software and field data. Journal of Water and Soil Conservation, 25(3): 113-128.

Gasiorowski, D., and Kolerski, T. (2020). Numerical solution of the two-dimensional Richards equation using alternate splitting methods for dimensional decomposition. Water, 12: 1780.

Hamdan, S.M., Troeger, U., and Nassar, A. (2007). Stormwater availability in the Gaza Strip, Palestine. International Journal of Environment and Health, 1(4): 580.

He, Y., Wang, Y., Liu, Y., Peng, B., and Wang, G. (2024). Focus on the nonlinear infiltration process in deep vadose zone. Earth-Science Reviews, 252: 104719.

Hsu, S.M., Ni, C.F., and Hung, P.F. (2002). Assessment of three infiltration formulas based on model fitting on Richards equation. Journal of Hydrologic Engineering, 7(5): 363-374.

Massmann, J. (2003). Implementation of infiltration pond research. Washington State Transportation Commission Department of Transportation in cooperation with U.S. Department of Transportation Federal Highway Administration. WA-RD 578.1.

MoA (Ministry of Agriculture) – Palestine. (2021). Archived data.

Okogbue, C.O., and Ukpai, S.N. (2013). Geochemical evaluation of groundwater quality in Abakaliki area, southeast Nigeria. Jordan Journal of Earth and Environmental Sciences, 5(1): 1-8.

Onwuka, S.O., Ezeh, C.S., and Ekwe, A.C. (2010). Application of chemometric technique in the assessment of groundwater quality in Udi and its environs, South-eastern Nigeria. Jordan Journal of Earth and Environmental Sciences, 3(2): 63-78.

Pachepsky, Y., Timlin, D., and Rawls, W. (2003). Generalized Richards' equation to simulate water transport in unsaturated soils. Journal of Hydrology, 272(1-4): 3-13.

PCBS (Palestinian Central Bureau of Statistics). (2021). Palestinians at the end of year 2017. Ramallah–Palestine. Retrieved from http://www.pcbs.gov.ps.

Rasheed, S., and Sasikumar, K. (2015). Modeling vertical infiltration in an unsaturated porous media using neural network architecture. Aquatic Procedia, 4: 1008-1015.

Sasidharan, S., Bradford, S., Simunek, J., and Kraemer, S. (2020). Comparison of recharge from dry wells and infiltration basins: A modeling study. Journal of Hydrology, 594(4): 125720.

Schaap, M.G., and Van Genuchten, M.T. (2006). A modified Mualem-van Genuchten formulation. Vadose Zone Journal, 5: 27–34.

Simunek, J., Van Genuchten, M.T., and Sejna, M. (2006). The HYDRUS software package for simulating two- and three-dimensional movement of water, heat, and multiple solutes in variably-saturated media. Technical manual. Version 1.0. Prague: PC Progress, 241p.

Simunek, J., and Weihermüller, L. (2018). Using HYDRUS-1D to simulate infiltration. Retrieved from https://www.pc-progress.com.

USGS (US Geological Survey). (2022). EarthExplorer [Online]. Available from: http://earthexplorer.usgs.gov.

Williams, J.R., Ying, O., Chen, J.S., and Ravi, V. (1998). Estimation of infiltration rate in the vadose zone: Application of selected mathematical models. Volume 2.

Ying, M., Shaoyuan, F., Dongyuan, S., Guangyao, G., and Zailin, H. (2010). Modeling water infiltration in a large layered soil column with a modified Green–Ampt model and HYDRUS-1D. Computers and Electronics in Agriculture, 71(1): 40-47.

Yu, C., and Zheng, C. (2010). HYDRUS: Software for flow and transport modeling in variably saturated media. Software Spotlight, Groundwater, 48(6): 787-791.

Zha, Y., Yang, J., Zeng, J., Tso, C.H.M., Zeng, W., and Shi, L. (2019). Review of numerical solution of Richardson–Richards equation for variably saturated flow in soils. WIREs Water. First published: 19.

JJEES

JJEES (2025) 16 (1): 75-82
ISSN 1995-6681

Jordan Journal of Earth and Environmental Sciences

Morphometry and Paleoenvironment of Pebbles from the Agbani Sandstone, southeast Nigeria

Henry Yemagu Madukwe [1*], Adeyinka Oluyemi Aturamu [2], Amos Oluwafemi Ilori[3]

[1] Department of Geology, Ekiti State University Ado-Ekiti, Nigeria, https://orcid.org/0000093-7147-0001-X
[2] Department of Geology, Ekiti State University Ado-Ekiti, Nigeria, https://orcid.org/00002731-0745-0003-
[3] Department of Geology, Ekiti State University Ado-Ekiti, Nigeria

Received on 17 September 2023, Accepted on 31 December 2024

Abstract

Pebbles from outcrops of Agbani sandstone at Amuri town southeast Nigeria were subjected to morphometric analysis in order to investigate the depositional environment. The pebbles are sub-rounded to well-rounded, monomictic, and matrix-supported sandy conglomerates. Morphometric analysis indicates the following range values: The Flatness Ratio (FR) 0.23 to 1.24 (average = 0.61), Elongation Ratio (ER) 0.40 – 1.43 (Average = 0.81), Flatness Index 0.36 to 1.03 (average = 0.81), Maximum Projection Sphericity Index (M.P.S.I) 0.44 to 1.03 (average = 0.77), Oblate–Prolate Index -4.9 to 15.89 (average = 0.11), roundness 30 and 85% (average = 56.9%), and preponderance of equant/spherical pebbles are indicative of fluvial process. The dominant forms of the pebbles are the compact, compact-bladed, compact platy, and bladed forms which are synonymous with fluvial setting. The bivariate plots indicated that river processes deposited the pebbles while some of the pebbles might have also been deposited in a transitional environment. The roundness of the pebbles suggests a long distance travel and random orientation suggests turbulence or bedload deposits under low energy environment.

Keywords: *Agbani sandstone, Environment, Fluvial, Pebbles, Roundness.*

1. Introduction

The utilisation of pebble indices in paleo-environmental analysis has been established and observed to be valuable, in both modern and ancient pebble deposits (Dobkins and Folks, 1970; Stratten, 1974). A pebble is a clastic coarser, loose gravel material with a particle size of 4 to 64 millimetres (-2 to -6 Phi) based on the Udden-Wentworth scale. When pebbles are lithified, they are called pebble conglomerates. The nature of sediment varies in origin, size, shape, and composition; particles such as grains and pebbles may be derived from the erosion of older rocks or directly ejected from volcanoes (Nichols, 2009). The rounding of gravel results from abrasion in transport by streams, glaciers, and sea waves. Pebbles mutually abrade each other, defining the time evolution for the abraded pebble and for the abrading environment, represented by other particles subject to particle transport (Domokos and Gibbons, 2012). Because of changing conditions, gravel formations generally are more limited and more variable in coarseness, size, and configuration than sand or clay deposits sediments. The size, shape, and distribution of particles all provide clues to how the materials were carried and deposited (Nichols, 2009). It has been shown and proved that pebble morphometric parameters may be helpful, as additional indicators, in deciphering the processes of transport and depositional environment (e.g., Sneed & Folk, 1958; Lutig, 1962; Sames, 1966; Dobkins & Folk, 1970; Stratten, 1974; Gale, 1990, 2021; Widera, 2010; Okoro et al., 2012; Odumodu & Israel, 2014; Ocheli et al., 2018; Madi & Ndlazi, 2020; Oluwajana et al., 2021).

Zigede et al. (2015) studied the paleoenvironment of sandstones within Enugu State University of Science and Technology, Agbani Campus using pebble morphometry and textural analysis. The authors utilized only fifteen pebbles and the Maximum Projection Sphericity Index (MPSI), Flatness Index (FI), and Oblate-Prolate Index (OPI) for their analyses.

This study aims to carry out a morphometric analysis of pebbles in the Agbani sandstone to infer the depositional environment. The scope entails measuring the pebble roundness, Elongated Ratio (ER), Flatness ratio (FR), Coefficient of Flatness (CF), Maximum Projection Sphericity Index (M.P.S.I), Oblate-Prolate index (OPI), Flatness Index (FI), long (L), Intermediate (I), Short axes (S) and using bivariate and ternary plots.

2. The Study Area

The study area is located in Nkanu-West local government area, southeast of Enugu State and lies within latitudes 6^0 15. 53^1N and 6^0 15. 53^1N and longitudes 7^0 31. 32^1 E and 7^0 31. 23^1 E in the Lower Benue Trough (Figure 1). The major access route to the area is by a roadcut linking Enugu Port Harcourt expressway to Ebonyi through Ozilla, Obe, Umueze, Agbani, Akpugo, and a minor road linking Agbani to Amurri. The Benue Trough is comprised of three segments: The Lower, Middle and Upper (Fig. 2). The study area is located in the southern part of the Lower Benue Trough. There is no obvious definition for each segment, the major towns, localities, or settlements that form the hub of various areas. They are widely conveyed in published materials (Petters, 1982; Nwajide, 1990; Idowu and Ekweozor, 1993).

* Corresponding author e-mail: henry.madukwe@eksu.edu.ng

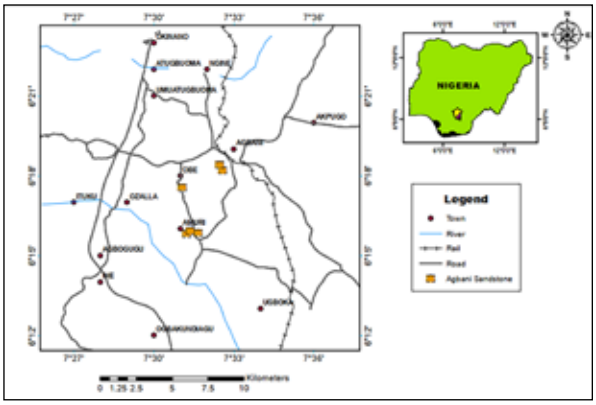

Figure 1. Location map of the study area.

The origin of the basin is generally linked to the Santonian tectonics of the Abakaliki-Benue Basin, during which an N-S compression between the African and Europeans plates folded the Abakaliki Anticlinorium (Maluski et al., 1995). The structural evolution of the Lower Benue Trough has been described by Binks and Fairhead (1992), Obi et al. (2001), Obi and Okogbue (2004). Prior to the tectonic event the Lower Benue Trough was a thinly covered platform by sediments. The folding of the anticlinorium laterally shifted the depositional axis into the Anambra platform which then began to accumulate sediments shed largely from the Abakaliki Anticlinorium (Murat, 1972; Hoque and Nwajide, 1984; Amajor, 1987). The Benue Rift was known as the failed arm of a trilete fracture (rift) system (Figure 2), during the breakup of the Gondwana supercontinent and the opening of the Southern Atlantic Ocean during the Jurassic (Hoque and Nwajide, 1984).

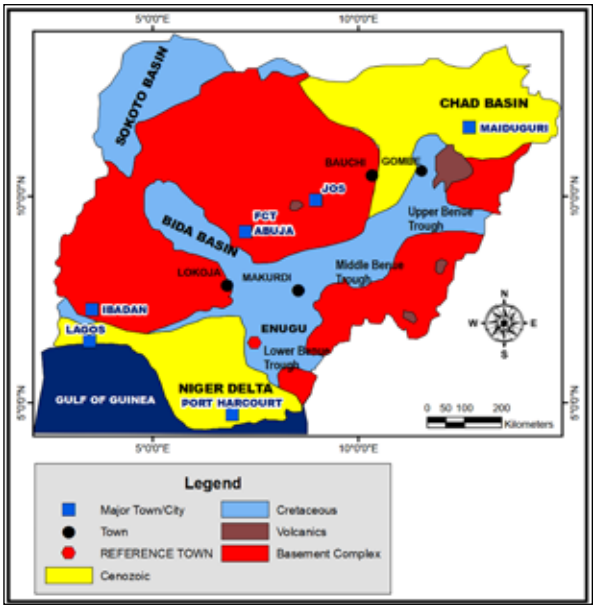

Figure 2. Map of the Benue Trough showing the study location. (Modified from Obaje et al., 2009).

The initial syn-rift sedimentation in the embryonic trough occurred during the Aptian to early Albian and comprised alluvial fans and lacustrine sediments of the Mamfe formation in the Southern Benue Trough (Obaje, 2009). Ojoh and Popoff (1989) established three principal subsidence trends in the region: It was high during the Albian, low in the Cenomanian, and high during the Turonian-Coniacian. According to Ramanathan and Fayose (1990), the Benue Trough has four key depositional cycles that are concomitant with transgression and regression: The first cycle occurred between Middle Albian to Upper Albian and postulated to be the result of the opening of the South Atlantic Ocean, the second ranged from Upper Cenomanian to Middle Turonian, the third spanned from the Upper Turonian to the Lower Santonian and concomitant with the deposition of Awgu shale and Agbani sandstone, and the fourth cycle marked the transgressive Campanian-Maastrichtian stage in the Lower Benue Trough (Figure 3).

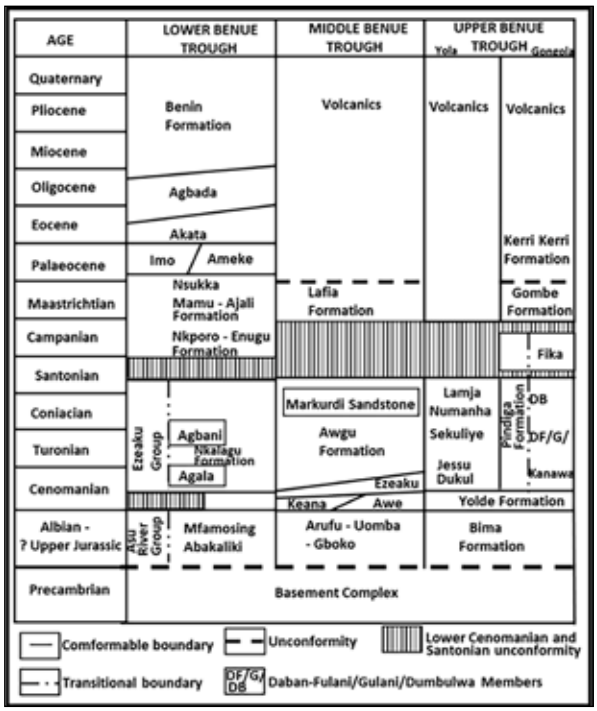

Figure 3. Stratigraphy of the Benue Trough (from Abubakar, 2014)

The Agbani sandstone is the siliciclastic facies of the Santonian sediment influx that ended the Coniacian-Santonian marine sedimentation (Nwajide, 2013). The sandstones are white, medium to coarse grained, poor to moderately sorted and cross laminated, depicting a fluviatile environment as a result of regression during Coniacian to Lower Santonian (Agagu and Ekweozor, 1982). The Agbani sandstone is a rough time equivalent of the Agwu shale (Reyment, 1965). It is a NE-SW trending lensoidal sandstone body which is difficult to trace and map laterally due to poor exposures; it is estimated to be 40 km long and 10 km wide with an exposed thickness of 30-50 m (Agumanu, 2011). Amuri, the study area, has an elevation of about 140m above sea level. The Coniacian Agbani sandstones exposed at Amuri are coarse grained, poorly sorted and contain sub-rounded to well-rounded quartz pebbles with random orientation.

3. Materials and Methods

More than three hundred pebbles were collected from three different outcrops at Amuri. These pebbles were washed, screened to exclude pebbles that were cracked or broken, numbered, and sent to the laboratory for analysis: Only isotropic pebbles that have high resistance to wear were considered representative of the pebbles (Figure 4).

Figure 4. Field photograph of the pebbles at Amuri

Measurements of the scale of the long (L), intermediate (I), and the short axes (S) of the pebbles were made using a Vernier Caliper. The dimension of pebble axes is based on the method suggested by Folk (1980). Pebble roundness were also estimated based on the set of pebble images given by Powers (1953); the image set is based on the proportion of the grain surface that is convex.

From the measurements of pebble axes and roundness, the following morphometric parameters were determined: Flatness Ratio (FR), Elongation Ratio (ER), Coefficient of Flatness (CF), Flatness Index (FI), Maximum Projection Sphericity Index (MPSI), and Oblate-Prolate index (OPI).

Flatness Ratio (FR) is the ratio between the short axis to the long axis (Lutig, 1962) and is evaluated via equation 1:

$$FR = \frac{S}{L} \quad (1)$$

Elongation Ratio (ER) is the ratio between the intermediate to the long axis based on Lutig (1962) and is evaluated via equation 2:

$$ER = \frac{I}{L} \quad (2)$$

The Coefficient of Flatness (CF) was determined usingequation 3 (Lutig, 1962):

$$CF = \frac{S}{L} \times 100 \quad (3)$$

Equation 4 by Illenberger (1991) was utilized to obtain the Flatness Index (FI) and expressed as:

$$FI = \frac{L-I+S}{L} \quad (4)$$

The measure of equidimensionality (sphericity) of the pebbles was determined using the Maximum Projection Sphericity Index (Sneed and Folk, 1958); it is the cube root of the ratio between the square of the short axis and the product of the long and intermediate axis and calculated via equation 5:

$$MPSI = \sqrt[3]{\frac{S^2}{LI}} \quad (5)$$

The Oblate-Prolate (OP) index shows how close the intermediate (I) axis of a pebble is to the short axis or long (L) axis (Dobkins and Folk, 1970). The Oblate-Prolate Index (OPI) is given by equation 6:

$$OPI = 10\left[\frac{L-I}{L-S} - 0.50\right]^{S}/_{L} \quad (6)$$

The mean and standard deviation of each of the indices were calculated and computed. Form measures the relationship between the three mutually perpendicular axes of a pebble. It is used to accommodate the fact that particles, having the same numerical value of maximum projection sphericity, may have different ratios between their three axes (Odumodu and Ephraim, 2007). Sneed and Folk's sphericity form diagram (1958) and Zingg's shape classes (1935) were used to determine the form name of each pebble set. These parameters were used independently to interpret the paleoenvironment of deposition and as dependent variables in binary plots such as MPSI vs OPI (Dobkins and Folk, 1970); Flatness index vs MPSI (Folk, 1955), and Roundness vs elongation.

4. Results

The pebbles are in a coarse sandstone (Figure 4). The pebbles are sub-rounded to well-rounded monomict (Figure 5), matrix-supported sandy conglomerates. The result, obtained from the morphometric analysis of the pebbles, is shown in Table 1: the long axis of the pebbles ranges from 0.41 to 3.30 cm in length with an average of 1.08 cm, while the intermediate and short axes range from 0.31 to 2.20 cm, and 0.20 to 1.52 cm, with averages of 0.86 cm and 0.65 cm respectively. The Flatness Ratio (FR) ranges from 0.23 to 1.24 (average = 0.61). The Elongation Ratio (ER) ranges between of 0.40 – 1.43 (Average = 0.81). The Flatness Index range from 0.36 to 1.03 (average = 0.81). The maximum projection sphericity index (M.P.S.I) range from 0.44 to 1.03 (average = 0.77), while the Oblate–Prolate Index ranges between -4.9 to 15.89 (average = 0.11). The particle roundness for the pebbles under investigation ranges between 30 and 85%, (average = 56.9%) and indicates sub-rounded to well-rounded status.

Figure 5. Pebbles studied.

Table 1. Summary of pebble measurements and morphometric parameters

Morphometric Parameters	Pebble Sets S-1 (n = 100)	Pebble Sets S-2 (n = 100)	Pebble Sets S-3 (n = 100)	Total Pebble Sets (n = 300)		
	Average	Average	Average	Minimum	Maximum	Average
Long axis (L) cm	0.76	0.96	1.52	0.41	3.3	1.08
Intermediate axis (I) cm	0.58	0.76	1.23	0.31	2.2	0.86
Short axis (S) cm	0.42	0.58	0.95	0.2	1.52	0.65
Mean size	0.59	0.77	1.23	0.34	2.19	0.86
Roundness (%)	56.9	60.65	53.15	30	85	56.9
Flatness Ratio (F.R)	0.57	0.62	0.64	0.24	1.25	0.61
Elongation Ratio (E.R)	0.77	0.81	0.83	0.4	1.43	0.8
Flatness Index	0.79	0.81	0.62	0.36	1.03	0.81
M.P.S.I	0.74	0.78	0.79	0.44	1.03	0.77
O.P. Index	0.11	-0.04	0.25	-4.9	15.89	0.11

Sneed and Folk (1958) diagram revealed two dominant forms for the pebbles examined (Figure 6). The result shows that the dominant shapes are the compact-bladed (28.33%) and the compact (26.67%) forms. Other notable forms are bladed (14.67%) and compact platy (11.55%). The distribution of the various pebble forms as defined by Sneed and Folk (1958) is presented in Table 2.

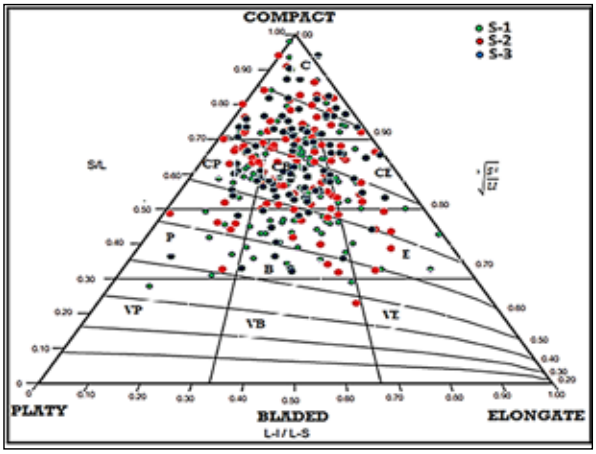

Figure 6. Sphericity-form diagram of the pebbles studied (after Sneed and Folk, 1958)
C = Compact, P = Platy, B = Bladed, E = Elongate, CP = Compact-platy, CB = Compact-bladed, CE = Compact-elongate, VP = Very-platy, VB = Very-bladed, VE = Very-elongate

Table 2. Form classification for the pebbles studied (after Sneed and Folk, 1958)

Form	Count	Percent
Compact	80	26.67
Compact-Platy	34	11.33
Compact-Bladed	85	28.33
Compact-Elongate	30	10
Platy	12	4
Bladed	44	14.67
Elongate	12	4
Very-Platy	1	0.33
Very-Bladed	2	0.67
Very-Elongate	0	0
TOTAL	300	100

5. Discussion

The pebbles examined are quartzose, with a mean size of 0.86 cm (8.6 mm). The sub-rounded to well-rounded nature of the pebbles suggests a long-distance journey from the source (extra formational). According to Madi and Ndlazi (2020), pebbles that are quartzose in composition are common river pebbles that have traveled for a long distance.

Geometric forms depict the three-dimensional aspects of a pebble utilized for their classification. Sneed and Folk (1958) proposed ten geometric forms: compact, compact platy, compact bladed, compact elongated, bladed, elongated, platy, very platy, very bladed, and very elongated that are diagnostic of certain environments. The compact (C), compact platy (CP), compact bladed (CB), and compact elongated (CE) pebbles are diagnostic of fluvial environments. Platy, bladed, and elongated pebbles are diagnostic of a transitional environment, while very platy, very bladed, and very elongated are diagnostic of a marine (beach) environment (Ocheli et al., 2018). The distribution of the various pebble forms as defined by Sneed and Folk (1958) is presented in Table 2 and Figure 6 which revealed that the dominant shapes are the compact-bladed (28.33%) and the compact (26.67%). Other notable forms are bladed (14.67%) and compact platy (11.55%), these percentages suggest a fluvial environment. Because river and beach environments contain bladed pebbles, the bladed forms were probably deposited under tidal influences, which is suggestive of a fluvial–tidal (transitional) environment of deposition

The mean roundness value of 57% for the studied samples falls within the 55 - 65% range which Lutig (1962) depicted as typifying fluvial pebbles and below 80 - 95% range for marine pebbles. This mean roundness value also shows that the pebbles are predominantly rounded, suggesting a long travel distance. The pebbles are scattered in the Agbani sandstone with no definite orientation; this suggests turbulence or bedload deposits under low energy. According to Tucker (2011), rocks with a uniform composition and structure, such as several granites, dolerites, and thick-bedded sandstones will give rise to equant/spherical pebbles, thin-bedded rocks will generally form tabular and disc-shaped clasts, and highly cleaved or schistose rocks such as slates, schists or some gneisses will generally form bladed or rod-shaped

pebbles. Figure 7 shows that 70% of the pebbles are plotted in the equant/spherical zone, the discoidal/tabular forms make up approximately 17%, and the rod-shaped constitute about 10% of the pebbles. The equiaxial nature of the pebbles signifies a propensity towards sphericity, which decreases downstream. Consequently the high amount of equant/ spherical pebbles signifies a fluvial influence. According to Barudžija et al. (2020), homogeneous rocks such as massive limestones, dolomites, quartzites, or marbles form sphere, and disc pebble shapes. The distribution of pebbles' shapes into mainly disc-, rod-, and sphere-shaped may signify different clast fabrics and multiple sources (e.g., Sremac et al., 2018; Barudžija et al., 2020). The Flatness Ratio for the pebbles ranges between 0.23 and 1.24 with an average of 0.61. The percentage of Flatness Ratio can be used to discriminate between fluvial and beach pebbles, a value of more than 45% is indicative of fluvial pebbles (Stratten, 1974). The majority of pebbles (87%) have values more than 45%, suggesting a fluvial environment. The Elongation Ratios for the samples range from 0.40 to 1.43 (average = 0.8). According to Hubert (1968); the elongation ratio values for fluvial environment range between 0.6 and 0.9. The majority of the values of elongation ratio, obtained (> 80%) for the pebbles in this study, fall within Hubert's range for fluvial environment.

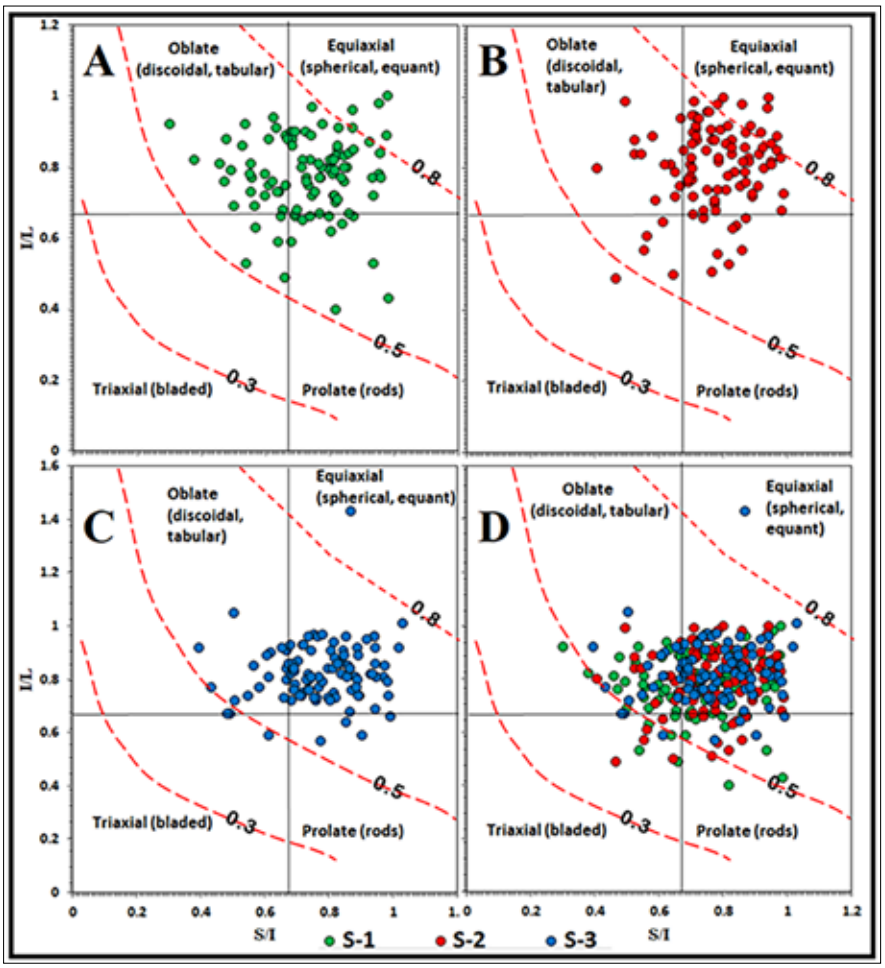

Figure 7. Classification of Amuri pebble shapes, after Zingg (1935) showing lines of equal Wadell (1932) sphericity. Curves represent grains of the same sphericity by the formula . A, B and C represents plots of the outcrops S-1, S-2 and S-3 respectively, while D is a combination of the three.

The Maximum Projection Sphericity Index (MPSI) for the pebbles fall within 0.44 and 1.03 with a mean of 0.77. According to Dobkin and Folk (1970), Hubert (1968), and Sneed and Folk (1958), the maximum projection sphericity of pebbles is generally high for fluvial environment than for beaches. Pebbles whose values fall within 0.65 and above were likely deposited via fluvial processes, while pebbles whose values fall below 0.65 are indicative of a beach environment (Dobkins and Folk, 1970). The percentage of pebbles with maximum projection sphericity values greater than 0.65 is approximately 90%, indicating a fluvial setting. 99.7% of the measured pebbles have flatness index values greater than 45% which indicate deposition by fluvial-influenced processes. The values for the Oblate-Prolate Index (OPI) range from -4.9 to 15.89 with 88% above -1.5 which Dobkins and Folk (1970) classified as fluvial. The bivariate plot of Flatness Index against Maximum Projection Sphericity Index (Figure 8), Coefficient of Flatness against Maximum Projection Sphericity Index (Figure 9), and bivariate plot of Maximum Projection Sphericity Index against Oblate-Prolate Index (Figure 10) for the pebbles show that majority of the pebbles plotted in the fluvial zone. This suggests that the pebbles were largely deposited by river processes while some of the pebbles might have also been deposited in a transitional environment.

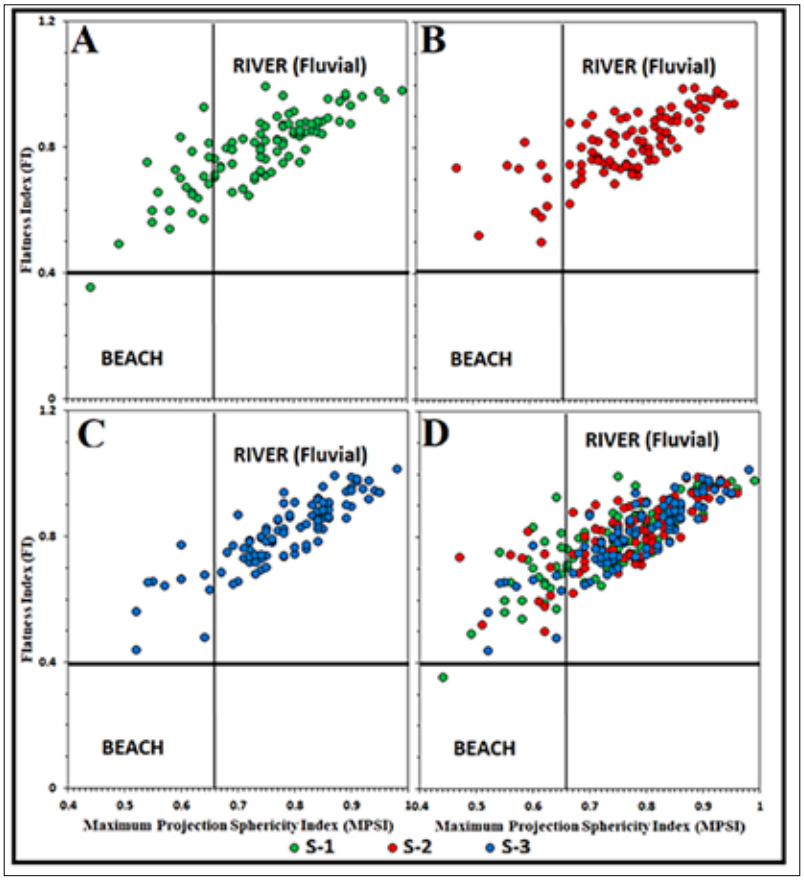

Figure 8. Bivariate plot of Flatness Index (FI) against Maximum Projection Sphericity Index of the studied pebbles (After Dobkins and Folk, 1970). A, B and C represents plots of the outcrops S-1, S-2 and S-3 respectively, while D is a combination of the three.

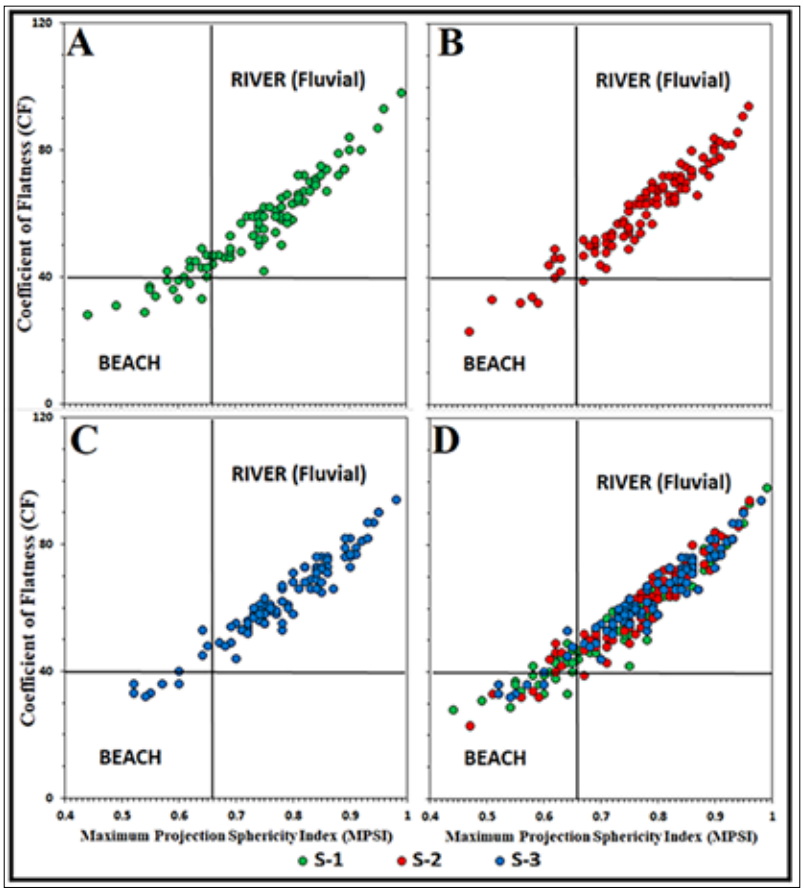

Figure 9. Plot of Coefficient of Flatness against sphericity of the studied pebbles (After Stratten, 1974). A, B and C represents plots of the outcrops S-1, S-2 and S-3 respectively, while D is a combination of the three.

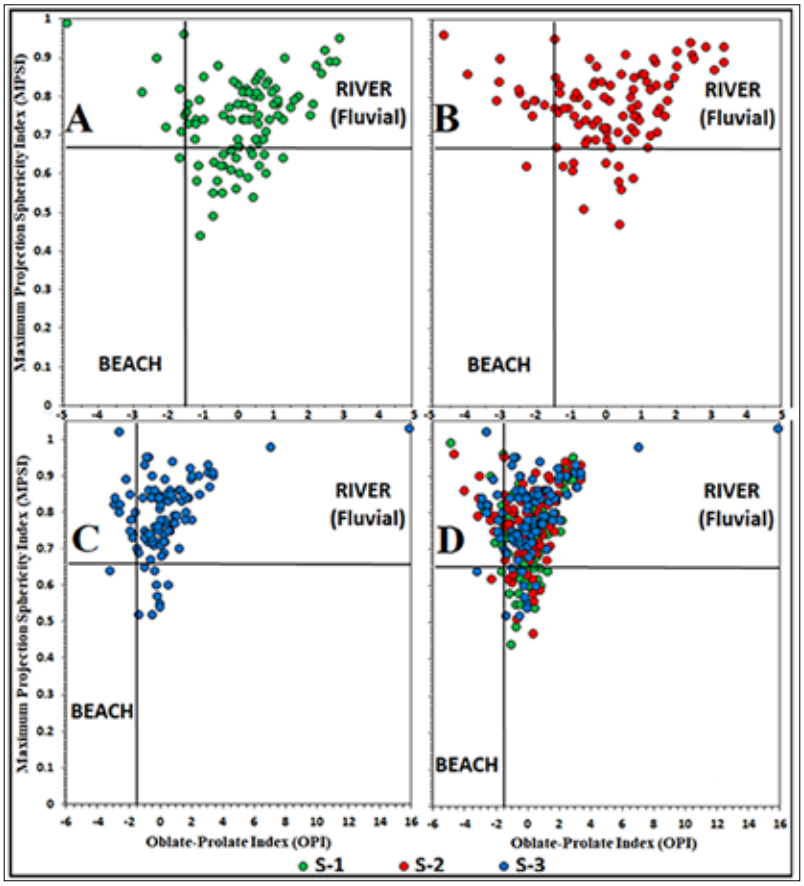

Figure 10. Bivariate plot of Maximum Projection Sphericity against Oblate-Prolate Index of the pebbles studied (After Dobkins and Folk, 1970). A, B and C represents plots of the outcrops S-1, S-2 and S-3 respectively, while D is a combination of the three.

6. Conclusion

1. The Coniacian Agbani sandstones exposed at Amuri contain quartz pebbles with no definite orientation and are sub-rounded to well-rounded. The pebbles are monomict, matrix-supported sandy conglomerates.
2. The rounded nature of the pebbles suggests a long distance travel from the source.
3. The mean roundness (57%), Flatness Ratio (0.61), Elongation Ratios (0.8), Maximum Projection Sphericity Index (0.77), Oblate-Prolate Index (0.11), and preponderance of equant/spherical pebbles suggest a fluvial setting.
4. The dominant shapes are the compact-bladed (28.33%), compact (26.67%), bladed (14.67%), and compact platy (11.55%). These percentages suggest a fluvial dominant environment.
5. Bivariate plots of Flatness Index against Maximum Projection Sphericity Index, Coefficient of Flatness against Maximum Projection Sphericity Index, and bivariate plot of Maximum Projection Sphericity Index against Oblate-Prolate Index for the pebbles suggest that the pebbles were largely deposited by river processes while some of the pebbles might have also been deposited in a transitional environment.
6. The pebbles are scattered in the sandstone and this suggests turbulence or bedload deposits under low energy.

Declaration

This paper has not been submitted/ published elsewhere in the same form, in English or in any other languag. The paper is the original work of the author(s) and not copied (in whole or in part) from any other work.

References

Abubakar, M.B. (2014): Petroleum potentials of the Nigerian Benue Trough and Anambra Basin: A regional synthesis, Natural Resources, 5(1), 25-58.

Agagu, O.K. and Ekweozor, C.M. (1982): Source-rock characteristics of Senonian shales in the Anambra Syncline, Southern Nigeria. Journal of Mineralogy and Geology, 19(2), 52-61.

Agumanu, A.E. (2011): Environment of deposition of the Awgu Formation (Late Cretaceous), Southern Benue Trough, Nigeria. Global Journal of Geological Sciences, 9(2), 215-228.

Amajor, L.C. (1987): Major and trace element geochemistry of Albian and Turonian shales from the Southern Benue trough, Nigeria. Journal of African Earth Sciences 6(5), 633-641.

Barudžija, U., Velić, J., Malvić, T., Trenc, N. and Božinović, N.M. (2020): Morphometric Characteristics, Shapes and Provenance of Holocene Pebbles from the Sava River Gravels (Zagreb, Croatia). Geosciences 10, 92. doi:10.3390/geosciences10030092

Binks, R.M. and Fairhead, J.D. (1992): A plate tectonic setting for the Mesozoic rifts of Western and Central Africa. In: Ziegler, P.A. (Ed.), Geodynamics of Rifting, Volume II. Case History Studies on Rifts North and South America, Tectonophysics 213, 141-151.

Britannica, The Editors of Encyclopaedia. "gravel". Encyclopedia Britannica, 31 Mar. 2019, available via

https://www.britannica.com/science/gravel. Accessed 28 May 2022.

Dobkins, J.E. and Folk, R.L. (1970): Shape development on Tahiti-Nui. Journal of Sedimentary Petrology 40, 167-1203.

Domokos, G. and Gibbons, G.W. (2012): The evolution of pebble size and shape in space and time. Proceedings of Royal Society A. 468, 3059-3079.

Folk, R.L. (1955): Student operator error in determination of roundness, sphericity and grain size. Journal of Sedimentary Petrology, 25(4), 297-301.

Folk, R.L. (1980): Petrology of Sedimentary Rocks. Hemphill Pub. Co., Austin.

Gale, J., (1990). The Shape of Beach Gravels. Journal of Sedimentary Petrology, pp 787-789.

Hoque, M. and Nwajide, C.S. (1984): Tectono-sedimentological evolution of an elongate Intracratonic basin (Aulacogen): the case of the Benue Trough of Nigeria. Nigerian Journal of Mining Geology, 21(1 & 2), 19-26.

Hubert, F.L. (1968): Selection and Wear of pebbles on gravel Beaches. University of Groningen Geological Institute Publication Number 190, 144pp.

Idowu, J. and Ekweozor, C. (993): Petroleum potential of Cretaceous shales in the Upper Benue trough, Nigeria. Journal of Petroleum Geology, 16(3), 249-264

Illenberger, W.K. (1991): Pebble shape and size. Journal of Sedimentary Petrology, 61(5), 756-767.

Krynine, P.D. (1960): On the antiquity of 'sedimentation' and hydrology. Bulletin Geological Society America, 71, 1721–1726. (doi:10.1130/0016-7606(1960)71[1721:OTAOSA]2.0.CO;2)

Lutig, G. (1962): The shapes of pebbles in continental, fluviatile and marine facies. International Association of Hydrogeologists 59, 253-258.

Madi, K. and Ndlazi, N.Z. (2020): Pebble morphometric analysis as signatures of the fluvial depositional environment of the Katberg Formation near Kwerela River around East London, Eastern Cape Province, South Africa. Arabian Journal of Geosciences 13(235), 1-16.

Maluski, H., Coulon. C., Popoff, M. and Baudin, P. (1995): 40Ar/39Ar chronology, petrology, and geodynamic setting of Mesozoic to early Cenozoic magmatism from the Benue Trough, Nigeria. Journal of Geological Society of London 152, 311-326.

Murat. R.C. (1972): Stratigraphy and paleogeography of the Cretaceous and Lower Tertiary in Southern Nigeria. In: Dessauvagie, T.F.J., Whiteman, A.J. (Eds.), African Geology, University of Ibadan Press, Nigeria, 251-266.

Nichols, G. (2009): Sedimentology and stratigraphy, 2nd ed. Wiley-Blackwell Publishing, London.

Nwajide, C.S. (1990): Sedimentation and paleogeography of the Central Benue Trough, Nigeria. In: Ofoegbu C.O. (ed) The Benue Trough structure and evolution. Vieweg, Braunschweig, 19–38

Nwajide, C.S., 2013. Geology of Nigeria's Sedimentary Basins. CSS Bookshops, Lagos, 565 pp.

Obaje, N.G. (2009): Geology and Mineral Resources of Nigeria. Springer-Verlag Berlin Heidelberg.

Obi. G.C. and Okogbue C.O. (2004): Sedimentary response to tectonism in the Campanian-Maastrichtian succession, Anambra Basin, South-eastern Nigeria. Journal of African Earth Sciences, 38, 99-108.

Obi. G.C., Okogbue, C.O. and Nwajide, C.S. (2001): Evolution of the Enugu Cuesta: A tectonically driven erosional process. Global Journal of Pure Applied Sciences 7, 321-330.

Ocheli, A., Okoro, A.U., Ogbe, O.B. and Aigbadon, G.O. (2018): Granulometric and pebble morphometric applications to Benin Flank sediments in western Anambra Basin, Nigeria: proxies for paleoenvironmental reconstruction. Environ. Monit. Assess., 190, 286.

Odumodu, C.F.R. and Ephraim, B.E. (2007): Pebble morphometry as an indicator of the depositional environment of the Ajali Sandstone, Nigeria. Natural and Applied Sciences Journal 8(2). 132-143.

Odumodu, C.F.R. and Israel, H.O. (2014) Pebble form indices as paleoenvironmental reconstruction toolsfFor the Ogwashi – Asaba Formation, Southeastern Nigeria. International Journal of Geology, Earth & Environmental Sciences, 4(3), 149-159.

Ojoh, K.A. (1990): Cretaceous Geodynamic Evolution of the Southeastern Parts of the Benue Trough (Nigeria). In: the equatorial Domain of the South Atlantic Stratigraphic Basin Analysis and Palaeooceanography. Bull. Center Research. Explor – Prod. Elf-Aquitaine 14(2), 419-442.

Ojoh, K.A. and Popoff, M. (1989): Tectono-sedimentary evolution of the southerm part of Benue Through: from an asymetric basin in middle Albian to an infilled basin in mid-Cenomanian. American Association of Petroleum Geologists 73, 396.

Oluwajana, O.A., Adebambo, B.A., Olawuyi, G.T., Ewuji, J.O., Adejayan, B.A., Ayodele, O.D., Adeniran, P.M., Arabi, D.O. and Adedokun, T.A. (2021): Paleoecologic implications of foraminiferal assemblages in the Upper Cretaceous-Paleogene strata, eastern Dahomey (Benin) Basin, southwestern Nigeria. Arabian Journal of Geosciences. 14, 9, 1-16.

Petters, S.W. (1982): Central West African Cretaceous-Tertiary benthic foraminifera and stratigraphy. Palaeontographica Abteilung A, 1-104.

Powers, M.C. (1953): A new roundness scale for sedimentary particles. Journal of Sedimentary Petrology 23, 117-119.

Ramanathan, R.M. and Fayose, E.A. (1990): Cretaceous Transgression and regressions in Calabar Flank, SE Nigeria. In: Ofoegbu, C.O. (eds): The Benue Trough, Structure and Evolution. Vieweg and Sohn, Braunschweig, 59-75.

Reyment, R.A. (1965): Aspects of the Geology of Nigeria: The Stratigraphy of the Cretaceous and Cenozoic Deposits. Ibadan University Press, 144 pp.

Sneed, E.D. and Folk, R.L. (1958): Pebbles in the lower Colorado River, Texas: a study in particle morphogenesis. Journal of Geology 66(2), 114-150.

Sremac, J., Velić, J., Bošnjak, M., Velić, I., Kudrnovski, D. and Troskot-Čorbić, T. (2018): Depositional Model, Pebble Provenance and Possible Reservoir Potential of Cretaceous Conglomerates: Example from the Southern Slope of Medvednica Mt. (Northern Croatia). Geosciences, 8, 456.

Stratten, T. (1974): Notes on the application of shape parameters to differentiate between beach and river deposits in Southern Africa. Transactions of the Geological Society of South Africa, 59-64.

Tucker, M.E. (2011): Sedimentary Rocks in the Field - A Practcal Guide. 4th Edition. Ho Printing, Singapore Pte Ltd, Singapore.

Wadell, H. (1932): Volume, shape, and roundness of rock particles. Journal of Geology 40, 443-451.

Widera M.(2010). The morphology of fossil pebbles as a tool for determining their transport processes [Koźmin South lignite open-cast pit, central Poland]. Annales Societatis Geologorum Poloniae. 80, 315–325

Zigede, L.J., Ezeh, C.C. and Okonkwo, A.C. (2015) Paleoenvironmental Analysis of Sandstone Deposits within ESUT Agbani Campus, Enugu State, Nigeria, using Pebble Morphometry and Textural Analysis. Civil and Environmental Research, 7(10), 35-52.

Zingg, T. (1935): Beiträge zur Schotteranalyse: Min. Petrog. Mitt. Schweiz., 15, 39-140.

JJEES

JJEES (2025) 16 (1): 83-95
ISSN 1995-6681

Jordan Journal of Earth and Environmental Sciences

Time-Series Analysis for Forecasting Climate Parameters of Kashmir Valley Using ARIMA and Seasonal ARIMA Model

Khalid Hussain[1], Fahad Farooq J.[1], Mir Salim N.[1], Sheikh Umar Farooq[2], and Insha Altaf[1]

1Department of Computer Science and Engineering, University of Kashmir, North Campus, Delina, Baramulla, India
2Department of Computer Science, University of Kashmir, North Campus, Delina, Baramulla, India

Recieved on 28 December 2023, Accepted on 31 December 2024

Abstract

The Kashmir Valley, a sensitive ecological zone within the Indian Himalayan Region (IHR), demands urgent attention regarding climate change. Home to multiple rivers and glaciers, the region holds significant geopolitical and economic importance. This work presents an analysis of three major climate variables—precipitation, cloud cover, and temperature—in the Kashmir Valley by leveraging the CRU TS4.04 time series data from 1901 to 2021, thereby revealing some key and concerning trends. Further, this study aims to predict the future trends of these variables for the next 80 years (2020–2100) utilizing ARIMA and SARIMA models. The projections show a significant increase of approximately 2.0ºC in the mean temperature, compared to 2019 levels by the end of the 21st century. The projections also point to a substantial reduction in the frequency of winter months experiencing mean temperatures below 2.0ºC, potentially ceasing altogether by 2048, which could have devastating consequences for the region's ecosystem. The insights, gathered in this study, may serve as a presage for the concerned government and stakeholders and will pave the way for the development of robust and efficient plans to tackle climate change in the area. The findings also shed light on the limitations of the ARIMA model, particularly its inability to forecast erratic changes in climate variables, thereby emphasizing the need for more sophisticated approaches to capture the complexities inherent in regional climate systems.

Keywords: *ARIMA; Climate; Kashmir Valley; Analysis; Time-series Forecasting; Weather.*

1. Introduction

Climate change is a pervasive phenomenon, manifesting as prolonged alterations in diverse climate variables, notably temperature and precipitation, within a given region. The scope of the investigation may encompass a localized area or extend to dimensions as vast as a continent or the entire globe. Rigorous studies, dedicated to comprehending climate change, typically involve meticulous analyses of fluctuations in various climatic parameters, aiming to gauge the magnitude of alterations occurring within the specified region over defined periods. The climate time-series data can have trends (long-term changes in the data) and seasonality (changes and variations in the data that occur regularly at short intervals). Accurate predictions and estimations of the impending alterations in a region are indispensable for effective planning and management of natural disasters such as floods, droughts, and extreme temperature events. Recognizing the gravity of climate change, the United Nations Organization (UNO) underscores its significance, calling it a "defining issue of our time" and the present era as a "defining moment" (Nations Organization United, 2021), emphasizing the urgency for immediate global actions to analyze, prevent, and address climate change in diverse regions. A 2007 Intergovernmental Panel for Climate Change (IPCC) report by UNO highlights the potential damages associated with a 2.0ºC rise in global temperatures (IPCC, 2007). However, recent findings from a special report on global warming caution that adverse impacts may occur even with a 1.5ºC increase (IPCC, 2022). The IPCC's 2021 report amplifies concerns, branding the current global climate scenario as "code red for humanity" (IPCC, 2021). The dire consequences of climate inaction are expounded in the IPCC's Assessment Report-6 of the year 2023, which underscores the colossal risks and the imperative for unprecedented changes on a global scale. While the report provides unprecedented insights into the gravity of the climate emergency, it also highlights the critical need for immediate, substantial, and efficacious efforts to analyze, mitigate, and potentially reverse the climate change trajectory (IPCC, 2023).

Despite the global scale of efforts to combat climate change, certain regions warrant increased focus due to the potential catastrophic consequences, arising from adverse climate effects in these specific areas. A prime example is the Kashmir Valley, strategically positioned at an elevation of 1600 meters above sea level in the North-Western corner of the Himalayas, with an area ranging from (33.25◦N, 73.75◦E) to (34.5◦N, 75.25◦E) and geopolitically divided between India and Pakistan as shown in Figure 1. The region's environmental, geographical, and economic significance is substantial. The region is considered to have a sub-tropical climate, which is sometimes also classified as Sub-Mediterranean due to the rainfall distribution pattern (Meher-Homji, 1971). Mild summers and severe winters are considered characteristic features of the climate in the region. Multiple rivers such as Jhelum, Lidder, etc.,

* Corresponding author e-mail: suf.cs@uok.edu.in

originating from the glaciers located in the upper reaches of the valley, and then flowing through the valley, as well as towards other regions, such as Pakistan and Punjab, are acting as a source of irrigation. The high-altitude origins of these rivers confer a substantial hydroelectric potential of around 20,000 Megawatt, with an estimated annual export revenue of $13 billion. Nevertheless, only about 20% of this potential has been recently realized (Ahmad, 2019; Smith, 2010). Any drastic climate change can be disastrous to the hydroelectric potential of the region since it is directly dependent on the glaciers in the region. A glaring example of climate impact is evident in the saffron industry, an integral part of the region's heritage for over 2500 years. The industry has witnessed a substantial decline in the 2018 harvest to be merely half of that produced in 1998 (Chakravarty, 2022; Economic Times, 2020).

Numerous studies and reports on climate change in the region reveal alarming findings, including a 27 − 38% decrease in glacier sizes (Romshoo et al., 2020a), a 19.44% reduction in daily rainfall (Wani et al., 2015), and a projected 6.93 ºC temperature increase by 2100 in the RCP 8.5 Scenario (Romshoo et al., 2020b). Recent anomalous events, such as the exceptionally hot and humid summers of 2020 and 2021, the devastating floods of 2014, sporadic surges in rainfall, and shifts in horticulture practices (Das et al., 2011), underscore an apparent alteration in the region's overall climate. This necessitates thorough analysis, study, and forecasting to comprehend the extent of climate change, devise strategies for prevention, and develop measures to mitigate its impacts. While various machine learning-based forecasting methods, including ARIMA, S-ARIMA, ASTAR, SVM, and KNN, offer effective predictions of climate variables, studies in our region have predominantly relied on traditional forecasting methods (Zaz et al., 2019; Shafiqul et al., 2019).

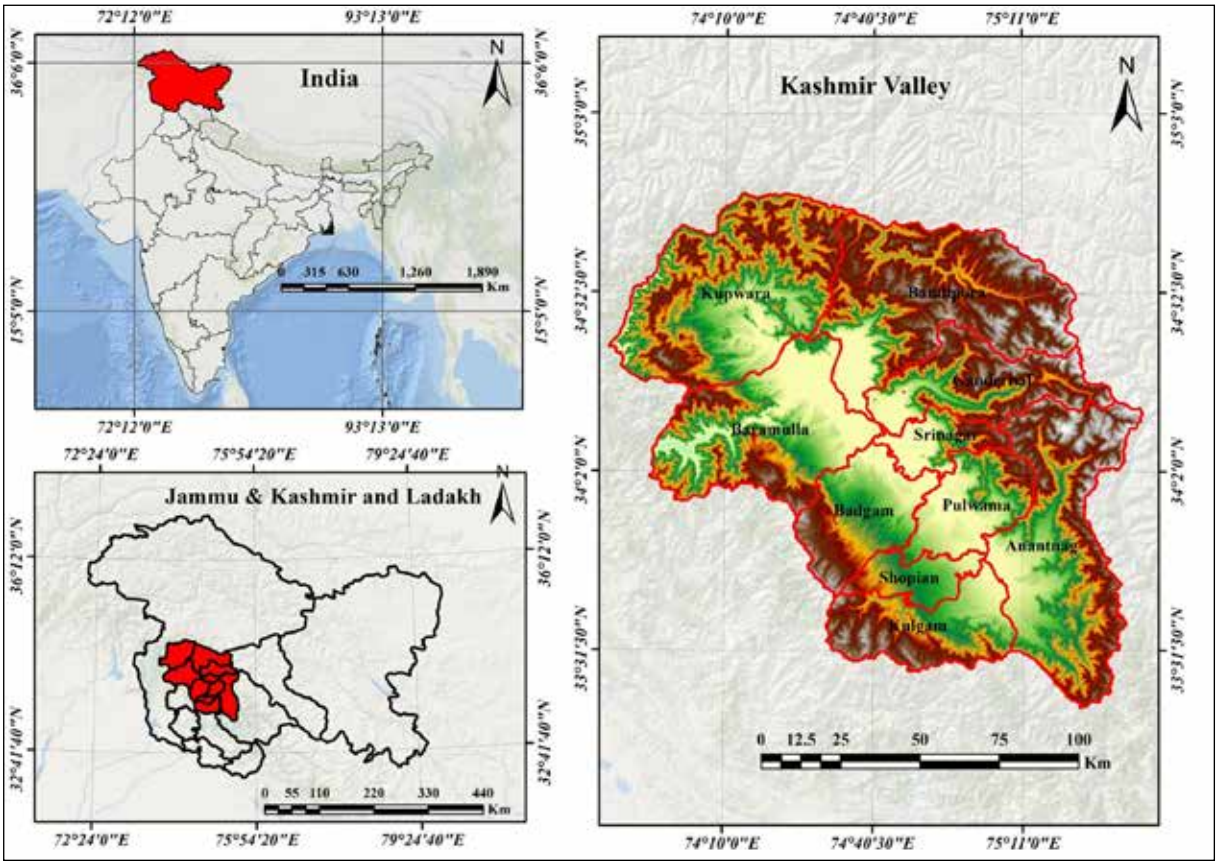

Figure 1. Area of study (33º 15' N, 73º 45' E to 34º 30'N, 75º 15'E)

Notably, limited exploration has been undertaken using machine learning and deep learning models, despite their demonstrated potential to yield superior results, compared to conventional mathematical models, as evidenced by several studies (Jebeile et al., 2021). This research aims to address this gap by leveraging advanced forecasting techniques to enhance the precision and reliability of climate predictions for the Kashmir Valley. The major contributions of this study are the following:

I. Forecasting future trends: One of the significant contributions of the study is forecasting the future climate trends of the valley for the next 80 years (2020−2100), based on a pre-processed large dataset ranging from 1901 to 2019. Despite being an ecologically sensitive and geographically important area, not enough efforts have been made to estimate the future trends of the climate variables such as temperature (mean, max, and min) and precipitation using machine learning models on the large high-quality dataset. This study aims to build upon the past results by using the proven ARIMA model for forecasting climate variables in the region. The validated forecasts will help in early planning and strategizing methods to tackle the changes in the future, which can prove beneficial to the

surrounding regions, as well as, the rest of the world.

Identifying key trends: Apart from forecasting climate change for the future, we also performed some basic analysis to identfy key trends in climate change that have occurred over the years (1901-2019) in the region of interest.

In this study, analysis has been done on a much larger dataset, with some noteworthy findings that have been discussed, in detail, in section 4 of the study. The analysis would help us better visualize how climate has changed over the past decades. The analysis can pave the way for an immediate decision and policy-making regarding climate change in the region.

II. Providing ready-to-use data: A major hurdle in studying and analyzing climate change in Kashmir valley is the availability of ready-to-use, clean and readable data. The data used in the study is provided by the CRU (Climate Research Unit) and requires various pre-processing steps that may appear daunting to researchers of a non-technical background. The high-quality, processed, and ready-to-use CRU dataset has been made available publicly in a public repository (JK Climate Data Github repository (k3rnelpanik, 2022)). This repository can be used by further studies for replications or analyzing other variables such as potential evapotranspiration, vapor density, etc.

The paper is further divided into multiple sections, with section 2 discussing the previously undertaken research focusing on the subject matter. Section 3 follows, discussing the dataset used in the study, and section 4 discusses inferences and notable observations made from the historical data. Section 5 discusses the methodology followed in the study. Section 6 discusses the forecasting results for each of the climate parameters: temperature, precipitation, and cloud cover. The conclusion and future scope of the study are discussed in sections 7 and 8 of the study, respectively.

2. Related Work

Many studies in the past have been conducted to forecast and study climate change in Kashmir Valley. The studies conducted differ in terms of variables used to study climate change, the area used in the study, the dataset, and/or the technique(s) used to carry out the forecasting. The studies conducted in the region of Kashmir present varying findings and results.

Linear regression analysis was used to examine the rate of change of climatic indices using data from 1961-2005 and an overall increasing trend was found in the seasonal and annual average temperatures (Ul and Khan, 2013). Another study, including observational data from six stations within Kashmir Valley, used the Weather and Research Forecasting (WRF) model and ERA-Interim data. The main findings from the study were that the higher altitude stations exhibited a steep increase of 1.04ºC to 1.13ºC in the annual mean temperatures from 1980−2016 (Zaz et al., 2019). Investigation of future climate change trends for the 21st century was done under 3 emission schemes (AIB, RCP4.5, RCP8.5) with the baseline period of the data being 1961-1990. The study used the GFDL CM2.1 model and the conclusion was that the annual mean temperature was projected to increase by 4.5ºC, 3.98ºC, and 6.93ºC respectively under the 3 emission schemes. The study also found out that the different climatic zones would experience significant changes (Romshoo et al., 2020b). Changes in the glacier sizes have also been studied, by comparing satellite images from 1980 to 2018, showing a decrease of 27 − 38% in the sizes of different glaciers, suggesting increasing temperatures and a decline in winter solid precipitation in the region, which if continues in the future, would adversely affect the economy in the region (Romshoo et al., 2020a). Similarly, glacier behavior estimation has been performed under climate change using a GRASS GIS module in Italy, with the results showing that the module can be used for a large number of glaciers to obtain spatial simulations to assess future scenarios (Strigaro et al., 2016). Another study uses SDSM to make projections for maximum and minimum mean temperatures, showing an increase of 0.3ºC to 2.3ºC in future decades, from 2030−2100 (Shafiqul et al., 2019). A study by (Ahsan et al., 2021) focusing on climatic extremes in the valley uses IMD data, ranging from 1980−2010, with future projections being generated for 2006−2100, showing clear upward trends in temperature extremes, and a general decreasing trend in precipitation. Several studies have been conducted across different regions to analyze climate variable trends using basic statistical models (Baig et al., 2021; Hossain et al., 2014; Shama and Najim, 2014). The utilization of the ARIMA model has shown very promising results in various domains including climate change analysis. A study by Narayanan et al. (2013) used the ARIMA model for analyzing trends and modelinglk; pre-monsoon rainfall data with results indicating a significant rise in the pre-monsoon rainfall over the northwest part of the country. Air pollution modeling and forecasting have also been done using the ARIMA model, with findings showing that meteorological variables have a definite influence on the life cycle persistence of air pollutants (Naseem et al., 2018). Climate change has also been assessed along with a monthly rainfall forecast over Khordha District in Odisha, India, with outstanding accuracy using the ARIMA model (Swain et al., 2018). Precipitation and temperature changes in India's Bhagirathi River basin have been studied and forecasted using ARIMA, with the results showing an increasing trend for temperature in one station and a decreasing trend for another, while the precipitation is found to be over-predicted in case of extreme rainfall events (Dimri et al., 2020).

Other domains where the ARIMA model has been successfully applied and has produced exceptionally accurate results include stocks, the economy, and the COVID-19 Pandemic. ARIMA has been used for forecasting the GDP (Gross Domestic Product), which is a monetary measure of the market value of all the final goods and services produced in a specific time period by countries, for Portugal and Germany until the year 2031 with results suggesting a steady growth in both countries (Pires et al., 2021). The Nigerian economy has also been studied using the ARIMA model,

with a study showing that the living standards in Nigeria would most likely worsen over the next decade unless the economic policy stance is not reviewed (Nyoni, 2019).

For analyzing and forecasting the COVID-19 pandemic, in terms of the spread and infection rates in different regions, ARIMA has produced acceptable and proven results. A study focused on analyzing the top five affected countries, with the resulting forecasts being found concurring the observed data and predictions of exponential curves in certain countries such as India, the US, and Brazil turning out to be true (Sahai et al., 2020). COVID-19 cases in India were also forecasted in another study using ARIMA, with data from the Ministry of Health and Family Welfare (MOHFW), with results showing an increasing trend of COVID-19 cases with approximately 1500 cases per day (Khan and Gupta, 2020). No studies focusing on the analysis of climate change in this specific region have harnessed the potential of machine learning approaches for forecasting future climate trends and variable values, such as temperature and precipitation despite the demonstrated superiority and stability of machine learning approaches over traditional models. Another aspect requiring improvement is the limited scope of data utilized in existing studies, as most have relied on small datasets with records spanning only a few decades (Ul and Khan, 2013). Additionally, certain studies have confined their investigation to narrower regions within the valley, excluding statistically and environmentally significant areas. This limitation diminishes the significance and applicability of their findings and conclusions. Addressing these gaps, the current study seeks to overcome these shortcomings by leveraging a substantial dataset covering the period from 1901 to 2019. Moreover, it aims to broaden the geographical scope by encompassing all regions of Kashmir Valley.

3. Dataset Description

The time series data used in the study is sourced from the CRU TS4.04 dataset (Centre for Environmental Data Analysis (CEDA), 2020), which is in the public domain of the Tyndall Centre for Climate Change Research, School of Environmental Sciences, University of East Anglia in Norwich, UK. The main motive of the division is to provide data to the general public for research purposes. The data is an interpolated high-resolution gridded dataset (0.5º x 0.5º grids) consisting of global monthly mean temperature, precipitation, cloud cover, potential evapotranspiration, etc. Itranges from 1901 to 2019. The 'Subsetter' tool from the web processing service (WPS) available on the CEDA web archive portal (Centre for Environmental Data Analysis (CEDA), 2025) was used to extract the monthly precipitation, average cloud cover, and mean temperature data for our region of study. While other datasets were available as well, such as the one from the Indian Meteorological Department (IMD) Pune which is available on the Open Governmental Data Platform and one from Berkeley Earth (Berkeley Earth Climate Data). These datasets have significantly a lower number of entries than the CRU dataset and in some cases, the datasets provided are derivatives of the CRU time series dataset itself like the data available on the Indian Water Portal. The CRU data is also well documented, credible, accurate, and used extensively in research (Dimri et al., 2020; Harris et al., 2020; Salvacion et al., 2018; Shi et al., 2017). Another reason for the selection of the CRU time series data in this study is that previous studies have used sparsely populated datasets, with data only available for the past 3-4 decades, and using an extensive dataset populated with data-points from over a century as is the case with the CRU dataset, provides the potential for better understanding of the past trends as well as more accurate forecasting.

I. Pre-processing: The CRU data obtained in its original form required some pre-processing before being used for analysis and forecasting purposes. While the data is originally being provided a gridded time series, it needs to be averaged over the region of interest for each month, which is done by calculating the mean for cloud cover (%) and temperature (ºC). To convert the gridded time series data points to numeric values, the sum of the total precipitation (mm/month) is considered for each month.

II. Detection and removal of outliers: Detection and removal of outliers allow machine learning models to better understand the underlying trends in the data and to model them more accurately. The 'z-score' of the distribution is calculated for this purpose and any values that had a z-score greater than 3 or less than -3, as is the norm with Gaussian (Normal) distributions, were replaced by the mean of the immediately neighboring values.

$$z = \frac{x-\mu}{\sigma^2} \quad (1)$$

where μ denoting the mean of the distribution and , the standard deviation.

III. Training and testing values: The total collected data spanned over the time period of 1901 to 2019. The data (1901-2019) is split into two parts, with data from 1901-1999 being used for training the model and that from 2000-2019 used for validation of the forecasts made for the time period of 2000-2100.

4. Data Analysis and Notable Observations

A key part of our study was to analyze and visualize the extent of climate change that has occurred over the years up until now, especially since it has been a topic that has not received much attention when it comes to the Valley of Kashmir (Ahmad, 2018). The time series data was plotted using specialized software Seaborn and trend lines fitted upon the graphs to better visualize the direction and change in the temperatures, precipitation, and cloud cover over the period of study. Results are analyzed and discussed in the subsequent sections of the paper.

4.1 Drastic changes in temperature

The change in mean temperature over the period of 119 years in the region can be observed from the temperature (Figures 2 - 5), showing about 10 − 25% change in mean temperature in springs, summers, and autumns. The more worrying part is the gradual but extreme increase of about 200% in the mean temperatures over the past winters, as shown in Table 1 and Table 2. This is a worrying sign for

the region, considering its ecologically sensitive nature. Such drastic and extreme increase in the mean temperature, especially for winters, can result in the accelerated melting of glaciers which may result in flooding and even affect the perennial nature of the rivers originating from them. The rise in mean temperature is also a problem for most of the fruit-bearing trees in the region such as apples, apricots, and walnuts, all of which have their own "Chilling hour" requirements, the insatiability of which can cause abnormalities in the yield (Salama et al., 2021; Patel et al., 2019; Das et al., 2011; Stafne, 2017).

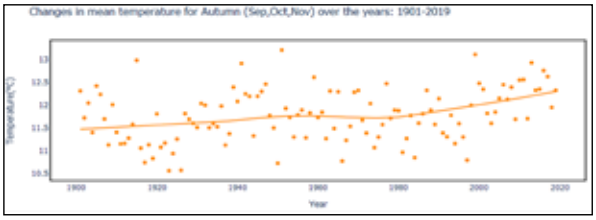

Figure 2. Changes in mean temperature over 1901-2019 in the autumn season (Sep., Oct., and Nov.)

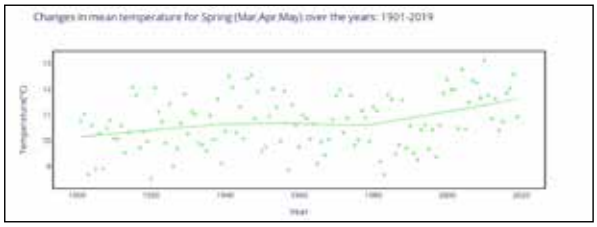

Figure 4. Changes in mean temperature over 1901-2019 in the spring season (Mar., Apr., and May)

Figure 3. Changes in mean temperature over 1901-2019 in the winter season (Dec., Jan., and Feb.)

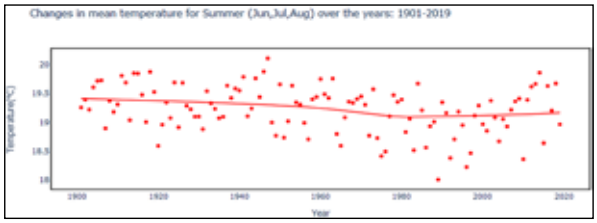

Figure 5. Changes in mean temperature over 1901-2019 in the summer season (June, July, and Aug.)

Table 1. Changes in mean temperature for winter (1901-1990) and (1991-2019).

Years	Mean	Standard Deviation	Min	25%	50%	75%	Max
1901-1990	0.870	1.509	-3.275	-0.266	1.003	1.942	4.488
1991-2019	1.506	1.420	-1.206	0.359	1.669	2.709	5.000

Table 2. Changes in mean temperature for autumn (1901-2000) and (1991-2019).

Years	Mean	Standard Deviation	Min	25%	50%	75%	Max
1901-1990	11.685	0.555	10.567	11.285	11.683	12.036	13.206
1991-2019	12.231	0.391	11.602	11.875	11.875	12.524	12.929

4.2 Precipitation spikes

Upon analysis of the precipitation data, extreme spikes in precipitation were noticed in summers and autumns, causing flash floods in localized areas such as that in 2010 (Guardian, 2010) and major floods like that of (Greater Kashmir, 2015) and that of 2022 in Pakistan which resulted in a loss of more than 1600 lives and estimated damage of $30 billion (Devi, 2022; Zhong, 2022; UNICEF, 2022). The precipitation data, when separately plotted for 1901-1990 and 1991-2019, shows a lower mean and deviation in the former time period and a higher mean and deviation, pointing to more erratic rainfalls. The precipitation keeps peaking in late summer and early autumn, as shown in Table 3 and Figure 6.

4.3 Potential for using temperature and cloud cover forecasts to predict heavy rainfall

Cloud cover is one of the most overlooked climate factors when it comes to analyses of the Valley's climate. A trend line was fitted upon the data points to analyze the co-dependence of the variables. The trend line is a locally weighted polynomial regression line fit using weighted least squares giving more weight to points near the point whose response is being estimated and less weight to the points further away. Upon analysis of the data and the trend line, it was observed that the cloud cover usually sits around a small range of 41 − 47% and a relatively larger range of 23 − 34% in summers and autumns respectively, correlating to precipitations of 3000 − 8000 mm in summers and 1000 − 3000 mm in autumns. The deviances and spikes in precipitations can be correlated to cloud covers greater than 55% in summers and 40% in autumns, as shown in Figure 7 and Figure 8. A multi-variate approach, using the precipitation and cloud cover data, can thus be taken in early prediction of such spikes, which can thus aid in the prevention of catastrophic loss of property and life, such as the ones caused in 2010 and 2014.

Table 3. Total yearly precipitation compared over the years, (1901-1990) vs. (1991- 2019).

Years	Mean	Standard Deviation	Min	25%	50%	75%	Max
1901-1990	11960.7	2278.3	7490.7	10227	11651	13350	17319
1991-2019	13295.7	2427.7	10421	11490	12620	14761	18997

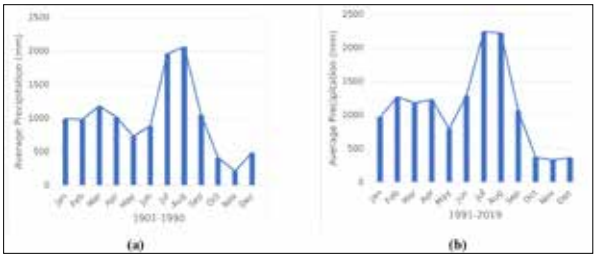

Figure 6. Comparison between mean monthly precipitation for 1901-1990 and that for 1991-2019.

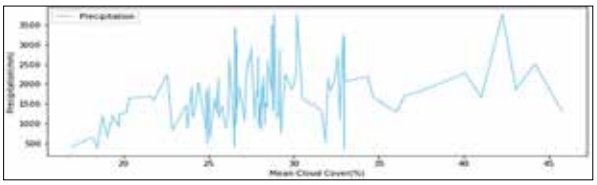

Figure 7. Correlation between cloud cover and precipitation spikes for the autumn season (Sep, Oct, and Nov).

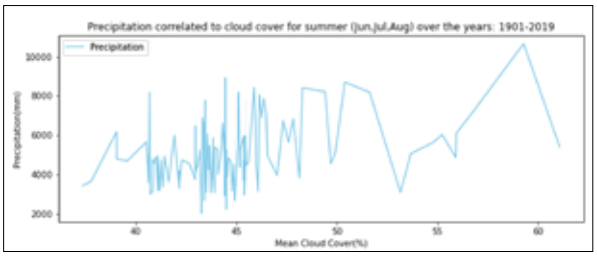

Figure 8. Correlation between cloud cover and precipitation spikes for the summer season (Jun, Jul, Aug).

5. Methodology

The data considered for the study includes temperature (mean, maximum and minimum), precipitation, and cloud cover from the year 1901-2019. The data is provided in the gridded form and is prepared as monthly mean values, except for precipitation, which is taken as the sum total of precipitation observed in the entire region. Upon preparation of data files, the models that produce the best results in terms of forecast need to be identified, provide a factual background, clearly define the problem, propose a solution, and include a brief literature survey along with the scope and justification of the work done.

5.1 Model Description

Auto-Regressive Integrated Moving Average (ARIMA) model is used for time series analysis to better understand the underlying trends in the data and to produce forecasts based on the mean, deviation, and differences of the past values (Pires et al., 2021; Youssef et al., 2021; Sahai et al., 2020; Khan and Gupta, 2020; Ding et al., 2020; Nyoni, 2019). The usage of the ARIMA model involves three main hyper-parameters:

- p-term which denotes the order of the AR (auto-regressive) term i.e., the number of prior values the current value in a time series is regressed upon.
- d-term which denotes the I (integrated) term i.e., numbers of differencing required for the time series to make it stationary.
- q-term which denotes the order of the MA (moving average) term i.e., the number of error values occurring at various time intervals in the past that the regression error is a linear combination.

These p(AR), d(MA) and q(I) values need to be selected, so that the model fits the data in the best way possible. If the time series to be used is non-stationary, its trend is removed by differencing to obtain a stationary time series. Non-seasonal ARIMA models are denoted as ARIMA (p, d, q) and seasonal ARIMA models as ARIMA (p, d, q) (P, D, Q) m where "m" denotes the number of periods in each season. ARIMA is considered to be one of the best models to use, when dealing with long and stable time series data, especially for approximating historical patterns for the future (Jebeile et al., 2021; Rolnick et al., 2019; YoosefDoost et al., 2017). An ARIMA model can be mathematically described as:

$$\hat{y}_t = \mu + \phi_1 y_{t-1} + \cdots + \phi_p y_{t-p} - \theta_1 e_{t-1} - \cdots - \theta_q e_{t-q} \quad (2)$$

The equation follows the Box-Jenkins convention wherein the MA parameters (θ) are defined so that their signs are negative. Identifying the appropriate ARIMA model for some data begins by determining the order of differencing (d) required to make the time series stationary and remove any seasonality. Stationary series can still have auto-correlated errors, which is suggestive of the need for some number of AR terms (p≥1) and possibly some MA terms (q≥1) in the forecasting equation. Separate ARIMA models have been fitted to forecast mean temperature, maximum temperature and minimum temperature, and cloud cover following the methodology presented in Figure 9. Precipitation achieved a relatively higher RMSE value, due to the inability of the ARIMA model to adapt to extreme changes in the data, with values ranging from 60mm/month, all the way up to around 19000 mm/month. Identification of the best fit models was done using the metrics discussed in detail in section 5.2.

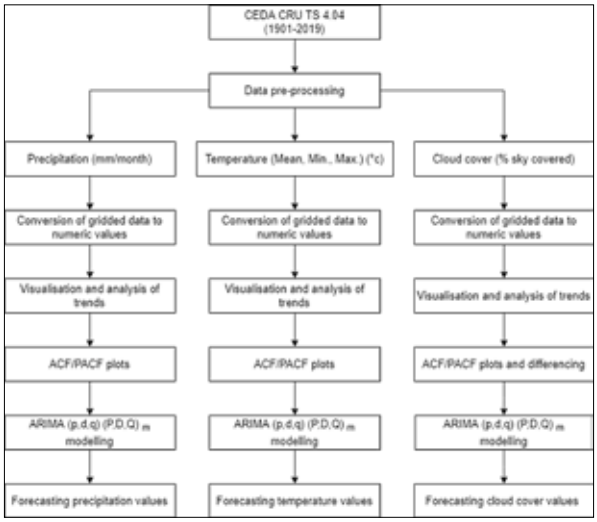

Figure 9. Methodology followed for forecasting three major climate variables

5.2 Evaluation Metrics

The results are graded using multiple evaluation metrics, such as RMSE, AIC, BIC as well as distribution metrics such as skew, kurtosis, and stationarity R2, all of which are inherent to the ARIMA model.

i. Akaike Information Criterion (AIC):

AIC is an estimator of prediction error. When a statistical model is used to represent the process that generated the provided data, the representation is never exact, some information is always lost. AIC simply estimates this

relative amount of information such as a part of the climate observations lost by our model. A lower AIC value implies a better model:

$$AIC = 2 \times K - 2 \times \ln(\text{loglikelihood}) \quad (3)$$

where, K being the number of parameters in the data.

ii. Bayesian Information Criterion (BIC):

BIC tries to find the "True" model amongst a finite set of models. BIC introduces penalty terms into a model for each parameter that may increase the likelihood, thus preventing overfitting, i.e., preventing the model from simply repeating temperature or precipitation values instead of actually trying to understand the basis for the patterns. Similar to AIC, lower BIC values are preferred and considered to make for better models:

$$BIC = -2 \times loglikelihood + K \times \log(N) \quad (4)$$

where, K being the number of parameters in the data and N being the size of the dataset.

iii. Root Mean Square Error (RMSE):

The RMSE denotes how close the values predicted by the trained model are to the actual observed values. The differences between the observed and predicted values, such as temperature or precipitation, known as residuals, help in the determination of a model's quality.

$$RMSE = \sqrt{mean(forecast - observed)^2} \quad (5)$$

iv. R-squared:

The R-squared value denotes how well the model has fit on the training data, thus providing a measure for the model's evaluation instead of the forecasts, i.e., how well the model has understood previous trends from the weather data, the closer the value to 1, the better the model is considered.

$$R^2 = 1 - \frac{unexplained\ variation}{total\ variation} \quad (6)$$

v. Stationarity Tests

The first step while dealing with any time series data is to determine whether it is stationary or not, which can be done using multiple tests. In this study, we used one such test known as the Augmented Dickey-Fuller Test (ADF). The p- value from the test is used to test the null hypothesis and any values higher than the significant threshold of 0.05 (5%) deem the rejection of the null hypothesis false. The conclusion from the results thus reached was that only the cloud cover time series data was nonstationary, while the rest of the data were stationary. To make the cloud cover data stationary, first-order differencing was performed. As auto-correlated errors could still exist in the differenced time series, AR (p≥1) and MA (q≥1) terms could be added to compensate for any mild under-differencing or over-differencing respectively. The ADF test results are shown in Table 4 and the differencing plots in Figure 10.

Table 4. Augmented Dickey-Fuller Test results for the dataset.

	Mean Temperature	Avg. Min. Temperature	Avg. Max. Temperature	Precipitation	Cloud Cover
Test Statistics	-4.519	-4.186	-4.938	-5.494	-0.629
p-value	0.000	0.001	0.000	0.000	0.864
Lags	23	23	23	24	23
Observations	1404	1404	1404	1403	1404
Reject	True	True	True	True	False

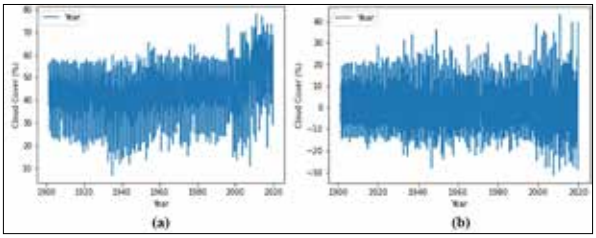

Figure 10. Differencing plots for cloud cover: (**a**). Before Differencing and (**b**). After Differencing

5.3 Determination of AR(p) and MA(q) terms

Auto-correlation function (ACF) and partial auto-correlation function (PACF) plots are used for determining the values for AR (p) and MA (q) terms. The ACF and PACF plots showing large values decomposing very slowly over time shows the need for differencing. The plots also show a confidence level (95%), towards which, if the values show a sharp cut-off in ACF, denotes some over differencing in the series and the need for an MA(q) term. In case of PACF, a sharp cut-off represents under differencing and the need for an AR (p) term. The ACF-PACF plots are shown in Figures 11-15. It is found that in case of mean temperature, maximum and minimum temperature, the ACF plot showed a sharp cut-off after the 3rd lag, thus providing the value for MA(q) term. The PACF plot shows a sharp cut-off after the 12th lag and a dip after the 4th lag, providing with a value of either 12 or 4 for AR(q) term. Both of them are used in the ARIMA model and the better performing AR(q) term is selected. The AR(p) term for mean temperature is 12 and that for minimum and maximum temperature is either 12 or 4, and MA(q) term for all the three temperature variables is 3. This results in the selection of ARIMA (12, 1, 3) for mean temperature, ARIMA (12, 1, 3) for maximum temperature, ARIMA (4, 1, 3) for minimum temperature. Similar steps are followed to determine the 'p' and 'q' terms for both cloud cover and precipitation, with ACF plots for cloud cover showing a cut-off after the 12th lag and the PACF plot also showing a cut-off after the 12th lag, resulting in the selection of ARIMA (12, 1, 12). The ACF plot for precipitation shows a repeating pattern, indicative of one of the pattern cut-offs being the ideal value for the 'q' term, while its PACF plot shows a cut-off after the 11th lag, and ARIMA (11, 1, 12).

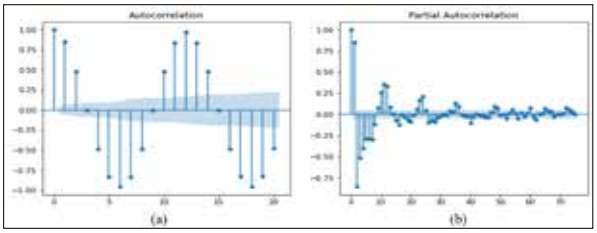

Figure 11. ACF and PACF plots for Mean Temperature.

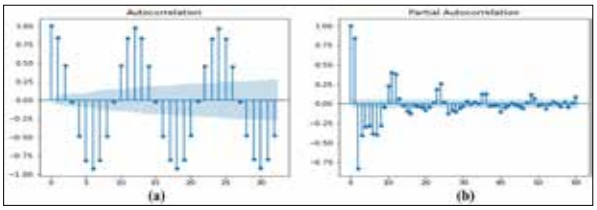

Figure 12. ACF and PACF plots for Average Minimum Temperature.

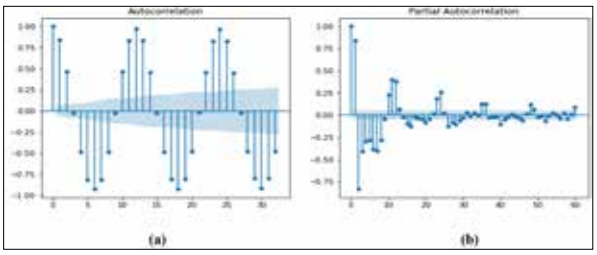

Figure 13. ACF and PACF plots for Average Maximum Temperature.

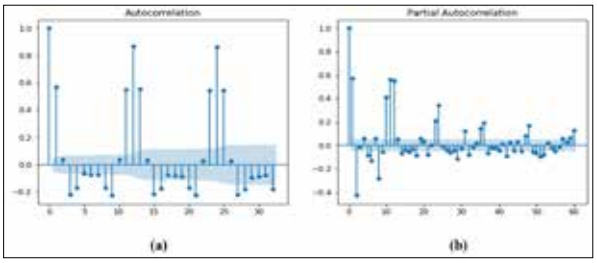

Figure 14. ACF and PACF plots for Cloud Cover.

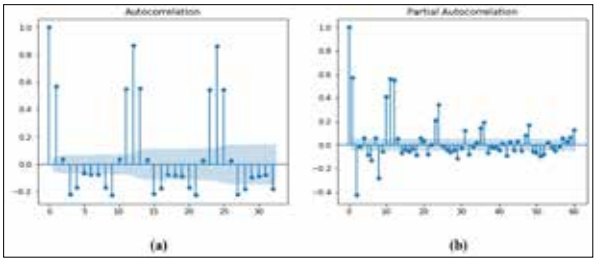

Figure 15. ACF and PACF plots for total precipitation.

5.4 Determination of the 'm' term

The 'm' term is used to remove seasonality in the time series. Since the data is a monthly dataset, with each year having 12 months, the same value was chosen, i.e., m = 12. Appropriate values for P, D, and Q are then chosen for m = 12 in a similar manner as the values for p, d, and q.

5.5 Selection of the best ARIMA model

Once the appropriate values for hyper-parameters (p, d, q) and (P, D, Q) are calculated, the best-fitting model is determined based on the residual values of ARIMA models. Data from the years 1901-2000 is used for training the models and forecasting is performed from 2001-2100, with the data from 2001-2019 acting as validation sets for the fitted models. The models are tested using the evaluation metrics described before in section 5.2. The most appropriate model for mean temperature is found to be ARIMA (12,0,3) $(0,0,3)_{12}$ and ARIMA (12,1,3) $(0,1,3)_{12}$ for maximum temperature and minimum temperature, ARIMA (4,1,3) $(0,1,3)_{12}$. The model selected for precipitation is ARIMA (11,1,12). In a similar manner, ARIMA (12, 1, 12) is selected for modelling the cloud cover data.

6. Results

Each variable's time-series data, encompassing mean temperature, maximum temperature, minimum temperature, precipitation, and cloud cover, underwent individual training and forecasting using distinct ARIMA models. The training dataset spanned from 1901 to 1999, with forecasts extending into the subsequent century (2000-2100). The validation of forecasts utilized data from 2000 to 2019. Despite the ADF tests confirming the stationarity of precipitation, mean temperature, minimum and maximum temperature data, certain seasonality was detected through ACF/PACF plots in the minimum and maximum temperature variables. These plots revealed the presence of seasonal properties, including sequentially recurring trends in lags and a gradual decay over time in the respective time series.

A computer system with an AMD Ryzen 5 4500U APU, 16 GB RAM and AMD Vega 8 GPU is used for training and visualizing the data, as well as making forecasts. The modeling and forecasting process is undertaken using Python 3.9 and Python libraries viz., as Matplotlib, Seaborn, Statsmodels, Pyplot, Plotly, NumPy, Pandas, SciKit Learn.

6.1 Temperature Forecasting Results

The results for mean temperature, minimum temperature, and maximum temperature show a very low RMSE value, considering the fact that average values of parameters in the region lies around 18-23°C. The mean temperature shows the most prominent change, doubling by the end of century for January and showing an increase of about 50% on average for the other two months of winter (December and February). Springs are also predicted to get hotter, which further worsens the issue regarding lack of "chilling period" required by fruit trees in the region, as discussed earlier in the analysis phase. The summers and autumns are seen to be getting cooler when looking at the mean temperature for Jun-Nov, whilst also seeing an increase in the minimum and maximum temperatures, pointing to an increase in the erratic behavior seen in the said seasons over recent years.

The models fit for each of the temperature variables (mean, maximum and minimum) have been shown in detail in Figures 16-18, and their evaluation results in Table 5. The forecast results have been made yearly and shown as values in 20-year intervals between 2020 and 2100 in table 6-8, and to better visualize the change predicted in the temperature, plots showing the same are provided in Figures 19-21.

Table 5. ARIMA model evaluation results for mean, minimum and maximum temperature.

Climate Variable	AIC	BIC	RMSE	Skew	Kurtosis	R^2
Mean Temperature	3442.07	3537.94	1.1296	-0.06	3.92	0.973
Minimum Temperature	3288.46	3343.84	1.1504	0.17	3.70	0.970
Maximum Temperature	3432.28	3527.93	1.1514	0.09	3.84	0.974

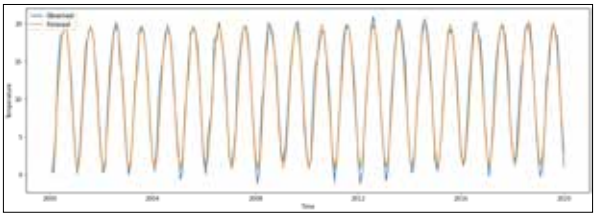

Figure 16. ARIMA (12,0,3) (0,0,3)12 model validation plot for mean temperature (°C).

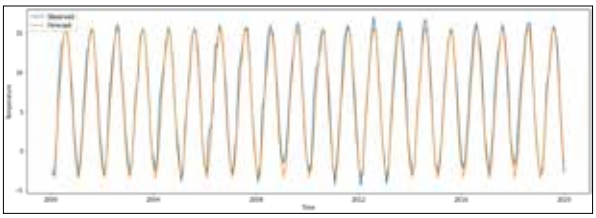

Figure 17. ARIMA (12,1,3) (0,1,3) 12 model validation plot for minimum temperature (°C).

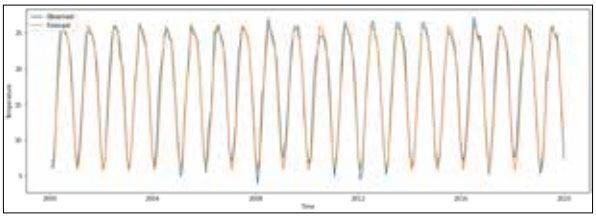

Figure 18. ARIMA (4,1,3) (0,1,3)12 model validation plot for maximum temperature (°C).

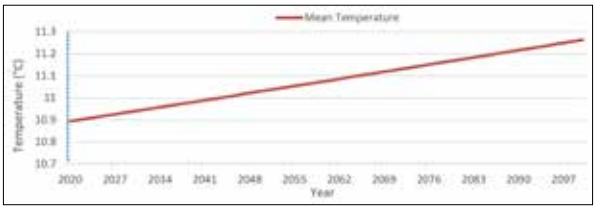

Figure 19. Yearly mean temperature (°C) changes over the years 2020-2100.

Table 6. Mean temperature (°C) forecasts for the years 2020-2100.

Month	Year				
	2020	2040	2060	2080	2100
JAN	**1.264**	1.837	2.246	2.574	**2.874**
FEB	**2.243**	2.723	3.165	3.544	**3.880**
MAR	5.773	5.951	6.251	6.565	6.856
APR	10.664	10.596	10.685	10.846	11.027
MAY	15.376	15.287	15.232	15.233	15.270
JUN	18.657	18.698	18.617	18.521	18.442
JUL	19.864	19.972	19.927	19.813	19.681
AUG	18.904	18.894	18.856	18.769	18.652
SEP	16.029	15.823	15.748	15.697	15.639
OCT	11.773	11.527	11.444	11.440	11.463
NOV	7.050	7.033	7.053	7.131	7.247
DEC	**3.132**	3.475	3.696	3.899	**4.114**

Figure 20. Yearly average minimum temperature (°C) changes over the years 2020-2100.

Table 7. Average minimum temperature (°C) forecasts for the years 2020-2100.

Month	Year				
	2020	2040	2060	2080	2100
JAN	-3.335	-3.289	-3.247	-3.206	**-3.165**
FEB	-2.127	-2.074	-2.034	-1.993	-1.952
MAR	2.133	2.163	2.203	2.244	2.284
APR	6.710	6.746	6.788	6.829	6.870
MAY	10.222	10.277	10.318	10.359	10.400
JUN	13.827	13.864	13.904	13.945	13.985
JUL	15.638	15.668	15.709	15.750	15.791
AUG	15.081	15.131	15.173	15.214	15.255
SEP	11.638	11.684	11.724	11.765	11.806
OCT	6.584	6.612	6.652	6.693	6.734
NOV	1.629	1.672	1.714	**1.755**	1.796
DEC	**-1.579**	-1.527	-1.486	-1.445	-1.404

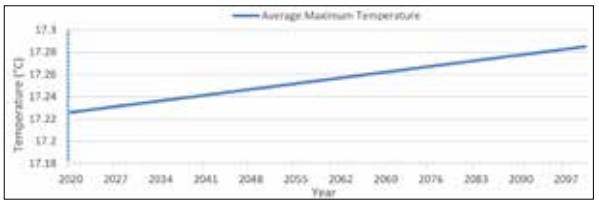

Figure 21. Yearly average maximum temperature (°C) changes over the years 2020-2100.

Table 8. Average maximum temperature (°C) forecasts for the years 2020-2100.

Month	Year				
	2020	2040	2060	2080	2100
JAN	5.799	5.814	5.829	5.844	5.858
FEB	7.324	7.339	7.354	7.369	7.383
MAR	11.890	11.905	11.920	11.934	11.949
APR	17.580	17.595	17.609	17.624	17.639
MAY	21.982	21.997	22.012	22.027	22.041
JUN	25.899	25.914	25.929	25.944	25.958
JUL	**25.623**	25.638	25.653	25.667	**25.682**
AUG	24.672	24.687	24.702	24.717	24.731
SEP	23.565	23.580	23.595	23.610	23.624
OCT	19.675	19.689	19.704	19.719	19.734
NOV	14.185	14.200	14.215	14.229	14.244
DEC	8.516	8.531	8.545	8.560	8.575

6.2 Cloud Cover Forecasting Results

The ARIMA model fitted for cloud cover showed an increase in the RMSE than that achieved for the model fitted for temperature values. The model thus tends to underestimate the peaks of the cloud and makes forecasts that are around 4-8% lower than what the actual values may be.

The evaluation metrics for the model are shown in Table 9 and the model fit values are compared to actual observed values for validation in Figure 22. The cloud cover values for different seasons have also been visualized in Figures 23-26, with springs showing a very slight decrease, winters showing a relatively larger decline in values, summers and autumns showing slightly increasing values as the years go on. The forecast results from the model are presented in table 10, in 20-year intervals.

Table 9. ARIMA model evaluation results for cloud cover.

	AIC	BIC	RMSE	Skew	Kurtosis	R^2
Cloud Cover	6262.51	6389.22	11.8918	-0.462	-0.967	0.2483

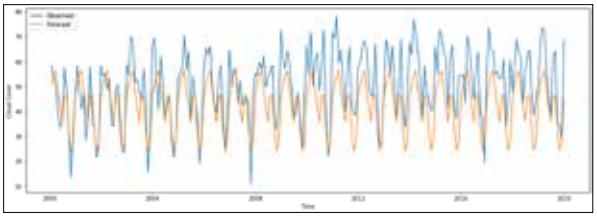

Figure 22. ARIMA (12,1,12) model validation plot for cloud cover (%).

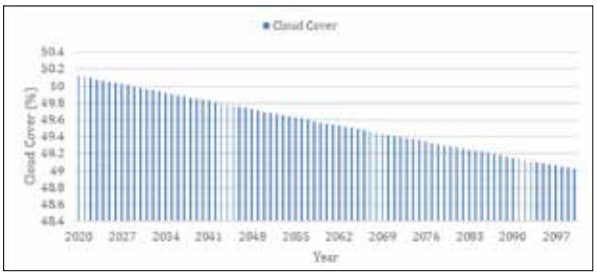

Figure 23. Cloud cover (%) forecast changes for winter (Dec, Jan, Feb) over the years 2020-2100.

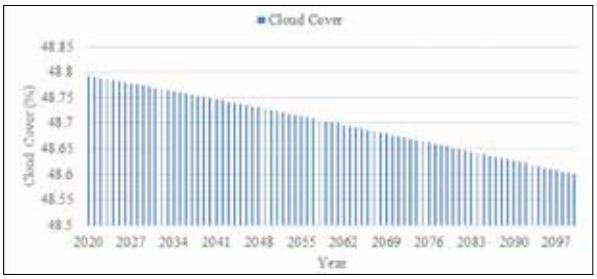

Figure 24. Cloud cover (%) forecast changes for spring (Mar, Apr, May) over the years 2020-2100.

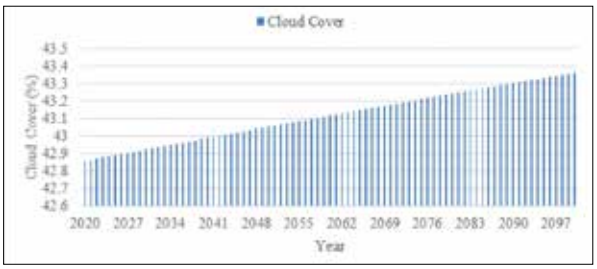

Figure 25. Cloud cover (%) forecast changes for summer (Jun, Jul, Aug) over the years 2020-2100.

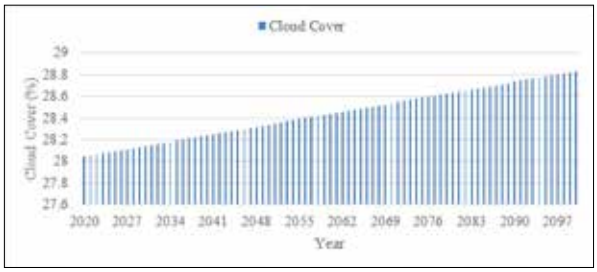

Figure 26. Cloud cover (%) forecast changes for autumn (Sep, Oct, Nov) over the years 2020-2100.

Table 10. Forecasts for average yearly cloud cover (%).

Month	Year				
	2020	2040	2060	2080	2100
JAN	50.845	50.598	50.356	50.122	49.894
FEB	54.339	54.054	53.778	53.509	53.247
MAR	56.310	56.225	56.127	56.020	55.904
APR	48.436	48.314	48.201	48.094	47.992
MAY	41.633	41.708	41.776	41.841	41.902
JUN	36.039	36.447	36.850	37.243	37.628
JUL	46.171	46.194	46.212	46.225	46.236
AUG	46.365	46.330	46.297	46.264	46.231
SEP	32.266	32.273	32.288	32.314	32.351
OCT	24.373	24.717	25.054	25.382	25.701
NOV	27.485	27.730	27.970	28.207	28.441
DEC	45.190	44.861	44.541	44.228	43.923

6.3 Precipitation Forecasting Results

The ARIMA model produces a high RMSE value for the precipitation dataset, mainly due to its inability to adapt to erratic changes in the precipitation which is essentially a high variance between the data points. The model is unable to replicate the peaks that are expected when comparing the forecasted values with the observed values and thus creates a curve with smaller peaks. The model evaluation results are discussed in Table 11. The validation fit for the model has been shown as a plot in Figure 27, and the values forecast using the model are presented in Table 12, with visualizations for the same in fig 28, showing an overall decrease in the total precipitation in almost all seasons, especially the summers, pointing to drier climates.

Table 11. ARIMA model evaluation results for precipitation.

	AIC	BIC	RMSE	Skew	Kurtosis	R^2
Precipitation	18005.49	18127.13	504.923	-0.073	-1.106	0.457

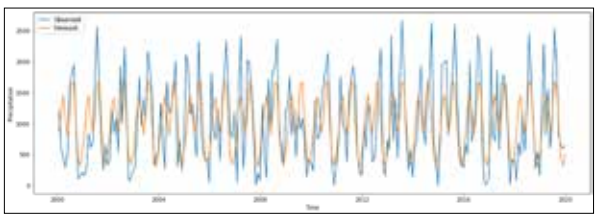

Figure 27. ARIMA (11,1,12) model validation plot for precipitation (mm/month).

Table 12. Forecasts for total precipitation (mm/month) for the years 2020-2100.

Month	Year				
	2020	2040	2060	2080	2100
JAN	827.259	822.059	829.926	846.947	873.467
FEB	1292.45	1353.94	1408.87	1463.19	1515.35
MAR	1482.47	1513.28	1544.88	1571.42	1592.40
APR	1135.92	1144.92	1153.38	1163.77	1179.93
MAY	850.69	877.804	909.056	949.669	997.282
JUN	1163.02	1196.69	1236.43	1271.64	1298.92
JUL	1659.21	1655.83	1634.69	1600.16	1555.79
AUG	**1612.55**	**1547.77**	**1479.96**	**1415.04**	**1353.35**
SEP	983.912	945.346	921.974	904.800	891.905
OCT	434.783	458.288	471.460	478.244	478.894
NOV	336.650	317.251	290.615	258.438	220.468
DEC	483.213	427.805	381.267	**339.437**	**304.823**

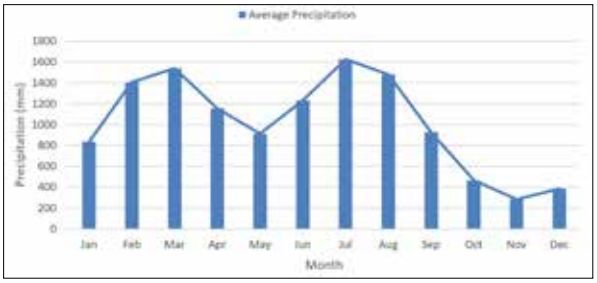

Figure 28. Forecasted average precipitation (mm/month) for the years 2020-2100.

7. Conclusion

The climatic attributes of a geographic area are fundamentally shaped by the observed variables of temperature, precipitation, and cloud cover. This research utilized the ARIMA model to conduct an in-depth analysis of these factors in the context of the Kashmir Valley, offering predictions for the region.

Across temperature variables, encompassing mean, maximum, and minimum values, the ARIMA model yielded predictions with low error values. A noteworthy observation is the discernible shift in mean temperatures, particularly evident during winter seasons, indicating an overall warming trend. The forecast points to an estimated temperature increase of approximately 2°C by the end of the century relative to 2019 levels, with a significant implication being the absence of winter months featuring temperatures below 2°C from 2048 onwards. Such alterations carry substantial ramifications for the local ecosystem and the economic landscape of the Kashmir Valley.

While minimum and maximum temperatures exhibit an ascending trend, the impact is comparatively less pronounced than that on mean temperatures. Projected outcomes suggest a marginal cooling effect during summers and autumns, compared with a relatively more substantial temperature increase during springs. These alterations may disrupt traditional low-temperature periods in spring, adversely affecting fruit and crop yields during autumn, thereby posing economic challenges for a considerable segment of the population dependent on agriculture.

Despite the ARIMA model's inherent limitations in predicting extreme precipitation events, mean precipitation forecasts demonstrated a closer alignment with actual observations. The study envisions a reduction in precipitation and an increase in cloud cover during summers, signaling a rise in humidity that could have adverse repercussions given the region's susceptibility.

A particularly disturbing finding is the cumulative impact of projected changes across all climate parameters, pointing towards potential catastrophes for vital economic sectors such as hydroelectricity, tourism, and agriculture. The projected temperature shifts and heightened cloud cover are anticipated to accelerate glacier melting, compounded by erratic precipitation, thereby elevating the risk of recurrent flooding. Urgent collaborative efforts involving governmental bodies, stakeholders, scientists, and researchers are imperative to formulate strategies and roadmaps addressing the foreseen climate changes. The proactive approach holds paramount significance in mitigating potential economic, environmental, and human losses in the region.

The primary purpose of this study is to bring attention to the imminent dangers of climate change in the region. Nevertheless, amidst the challenging projections, there remains a glimmer of hope. It is crucial to emphasize that these potential threats are not inevitable catastrophes. Meaningful and collective action can be taken to avert such scenarios. Recent global commitments, such as those emerging from The Paris Agreement signed in 2015 [45], UN Climate Change Conference (COP28) held recently in Nov-2023 [46] and other such inititaives exemplify the growing awareness and dedication to addressing climate change on a global scale. It is our fervent hope that governments across the country, and indeed the world, will take proactive initiatives inspired by these commitments, implementing effective policies and fostering international collaboration to secure a sustainable and resilient future for the world and to our region of interest.

8. Future Scope

While the mean, average minimum, and average maximum temperature variables exhibited precise results with minimal errors, the outcomes for cloud cover and precipitation diverged due to the ARIMA model's limitations in capturing and reproducing peaks and abrupt changes. Consequently, exploring alternative machine learning and deep learning models holds promise for enhancing prediction accuracy, especially for extreme events.

Another area that can be improved upon, is the use of higher-resolution datasets, which can allow for finer, cluster-wise analyses and forecasts. Such datasets can allow for the separation of data for planes, and mountainous regions, providing a clearer picture of the impact on glaciers and snow-caps in the region.

The utilization and integration of diverse datasets, including but not limited to the CRU dataset and satellite imagery datasets focusing on glaciers, within a unified research framework, present an opportunity to rectify

potential shortcomings inherent in studies reliant on singular datasets. Expanding the scope of the investigation involves incorporating additional variables associated with greenhouse gas emissions, notably carbon dioxide (CO2) levels—a pivotal factor in regional climate health. This extended study aims to assess the magnitude of the region's climate degradation, particularly in light of the escalating industrialization trends in the area.

Enhancing climate forecasting accuracy and efficacy could be achieved through the incorporation of additional variables into the forecasting algorithm. While temperature and precipitation stand as pivotal factors in climate analysis, the inclusion of variables such as humidity, solar radiation, topography, latitude etc. holds the potential to yield substantial insights for region-specific climate forecasting.

Funding

This research received no specific grant from any funding agency in the public, commercial, or not-for-profit sectors.

Data Availability

The dataset used in the study and the codebase is available at https://github.com/fahad-farooq/climchange_jk

Disclaimer

The authors have no financial or non-financial conflicts of interest to declare

References

Ahmad, M. (2018). "It's High Time the Government Took Notice of Kashmir's Changing Climate". https://thewire.in/environment/high-time-government- took-notice-kashmirs-changing-climate (Jan. 13, 2025).

Ahmad, M. (2019). Development of hydropower projects in Jammu And Kashmir. International Journal of Trend in Research and Development, 6(1), 6–8.

Ahsan, S., Bhat, M. S., Alam, A., Farooq, H., & Shiekh, H. A. (2021). Evaluating the impact of climate change on extreme temperature and precipitation events over the Kashmir Himalaya. Clim Dyn, 1–19.

Baig, M. A., Zaman, Q., Baig, S. A., Qasim, M., Khalil, U., Khan, S. A., Ismail, M., Muhammad, S., & Ali, S. (2021). Regression analysis of hydro-meteorological variables for climate change prediction: A case study of Chitral basin, Hindukush region. Science of The Total Environment, 793, 148595. https://doi. org/https://doi.org/10.1016/j.scitotenv.2021.148595

Centre for Environmental Data Analysis (CEDA). (2020). " CRU TS 4.04: Climatic Research Unit (CRU) Time-Series Dataset Version 4.04". https://data.ceda. ac.uk/badc/cru/data/cru ts/cru ts 4.04 (Jan. 13, 2025).

Centre for Environmental Data Analysis (CEDA). (2025). " CEDA WPS User Interface". https://ceda-wps-ui.ceda.ac.uk/processes (Jan. 13, 2025).

Chakravarty, P. (2022). " Global warming forces Kashmir farmers to grow saffron indoors". https://rfi.my/8u1l.X (Jan. 13, 2025).

Das, B., Krishna, H., Attri, B. L., Ahmad, N., & Ranjan, J. K. (2011). Harvest maturity standards and fruit quality of some apple cultivars under high altitude conditions. Indian Journal of Horticulture, 68(2), 170–179.

Devi, S. (2022). Pakistan floods: Impact on food security and health systems. The Lancet, 400(10355), 799–800.

Dimri, T., Ahmad, S., & Sharif, M. (2020). Time series analysis of climate variables using seasonal arima approach. Journal of Earth System Science, 129(1), 1– 16.

Ding, G., Li, X., Shen, Y., & Fan, J. (2020). Brief analysis of the ARIMA model on the covid-19 in Italy. MedRxiv.

Economic Times. (2020). " Climate change ravages Kashmir's 'red gold' saffron crop". https://ecoti.in/4FoSLa (Jan. 13, 2025).

Greater Kashmir. (2015). " The 2014 Kashmir Flood: The Extreme of the Extremes". https://www.greaterkashmir.com/gk-magazine/the-2014-kashmir- flood-the-extreme-of-the-extremes (Jan. 13, 2025).

Guardian, T. (2010). " Kashmir flash floods leave dozens dead". https://www. theguardian.com/world/2010/aug/06/kashmir-flash-floods (Jan. 13, 2025).

Harris, I., Osborn, T. J., Jones, P., & Lister, D. (2020). Version 4 of the CRU TS monthly high-resolution gridded multivariate climate dataset. Sci Data, 7(1), 1–18.

Hossain, M. Z., Mondal, M. N. I., Sarkar, S. K., & Haque, M. A. (2014). Seasonal variation of temperature in Dhaka metropolitan city, Bangladesh. Jor dan Journal of Earth and Environmental Sciences, 6(2), 93–97.

IPCC. (2007). Climate change 2007: Synthesis report. contribution of working groups I, II, and III to the fourth assessment report of the intergovernmental panel on climate change (C. W. Team, R. Pachauri, & A. Reisinger, Eds.) (Jan. 13, 2025). Intergovernmental Panel on Climate Change (IPCC). Geneva, Switzer- land. https://www.ipcc.ch/report/ar4/syr/

IPCC. (2021). Climate change 2021: The physical science basis. contribution of working group i to the sixth assessment report of the intergovernmental panel on climate change (V. Masson-Delmotte, P. Zhai, A. Pirani, S. Connors, C. P´ean, S. Berger, N. Caud, Y. Chen, L. Goldfarb, M. Gomis, M. Huang, K. Leitzell, E. Lonnoy, J. Matthews, T. Maycock, T. Waterfield, O. Yelek¸ci,

R. Yu, & B. Zhou, Eds.) (Jan. 13, 2025). Intergovernmental Panel on Climate Change (IPCC). Cambridge, United Kingdom, New York, NY, USA, Cambridge University Press. https://www.ipcc.ch/report/ar6/wg1/

IPCC. (2022). Global warming of 1.5ºC: Ipcc special report on impacts of global warming of 1.5ºC above pre-industrial levels in context of strengthening response to climate change, sustainable development, and efforts to eradicate poverty. Intergovernmental Panel on Climate Change. Cambridge, Cambridge University Press.

IPCC. (2023). Summary for policymakers. in: Climate change 2023: Synthesis re- port. contribution of working groups i, ii and iii to the sixth assessment re- port of the intergovernmental panel on climate change (C. W. Team, H. Lee, & J. Romero, Eds.). Intergovernmental Panel on Climate Change. Geneva, Switzerland. https://doi.org/10.59327/IPCC/AR6-9789291691647.001

Jebeile, J., Lam, V., & Ra¨z, T. (2021). Understanding climate change with statistical downscaling and machine learning. Syntheses, 199(1), 1877–1897.

k3rnelpanik. (2022). " Climate Data for The Valley of Kashmir (1901-Present)". https://github.com/k3rnelpanik/climchange jk (Jan. 13, 2025).

Khan, F. M., & Gupta, R. (2020). Arima and nar based prediction model for time series analysis of covid-19 cases in india. Journal of Safety Science and Resilience, 1(1), 12–18.

Meher-Homji, V. M. (1971). On the mediterranean climatic regime of west Pakistan. Archive for Meteorology, Geophysics und Bioclimatology, Serie B, 19, 277– 286.

Narayanan, P., Basistha, A., Sarkar, S., & Kamna, S. (2013). Trend analysis and arima modelling of pre-monsoon rainfall data for western India. Comptes Rendus Geoscience, 345(1), 22–27.

Naseem, F., et al. (2018). An integrated approach to air pollution modeling from climate change perspective using ARIMA forecasting. Journal of Applied Agri- culture and Biotechnology, 2(2), 37–44.

Nathaniel, A., Jacob, A., Joshua, A., & Solomon, A. (2024). Estimation of global solar radiation, sunshine hour distribution and clearness index in three geopolitical regions of Southern Nigeria. Jordan Journal of Earth and Environmental Sciences, 10(2), 97–103.

Nations Organization United. (2021). " Global Issues - Climate Change". https://www.un.org/en/global-issues/climate-change (Jan. 13, 2025).

Nyoni, T. (2019). Is Nigeria's economy progressing or backsliding? implications from arima models (MPRA Paper No. 91396). University Library of Munich, Germany. https:// ideas.repec.org/p/pra/mprapa/91396.html

Patel, N. R., Akarsh, A., Ponraj, A., & Singh, J. (2019). Geospatial Technology for Climate Change Impact Assessment of Mountain Agriculture. Springer Singapore.

Pires, F., Gouveia, J., Perestrello, F., Melo, A., & Gomes, M. (2021). " Using an ARIMA Model to Forecast GDP Until 2031 for Portugal and Germany". https://ssrn.com/abstract=3855082 (Jan. 13, 2025).

Rolnick, D., et al. (2019). Tackling climate change with machine learning. arXiv preprint arXiv:1906.05433.

Romshoo, S. A., Fayaz, M., Meraj, G., & Bahuguna, I. M. (2020a). Satellite-observed glacier recession in the Kashmir Himalaya, India, from 1980 to 2018. Environ Monit Assess, 192(9), 1–17.

Romshoo, S. A., Bashir, J., & Rashid, I. (2020b). Twenty-first century-end climate scenario of jammu and Kashmir Himalaya, India, using ensemble climate models. Clim Change, 162(3), 1473–1491.

Sahai, A. K., Rath, N., Sood, V., & Singh, M. P. (2020). Arima modelling & forecasting of covid-19 in top five affected countries. Diabetes & Metabolic Syndrome: Clinical Research & Reviews, 14(5), 1419–1427.

Salama, A.-M., et al. (2021). Temperate fruit trees under climate change: Challenges for dormancy and chilling requirements in warm winter regions. Horticulturae, 7(4), 86.

Salvacion, A. R., Magcale-Macandog, D. B., Cruz, P. C. S., Saludes, R. B., Pangga,

I. B., & Cumagun, C. J. R. (2018). Evaluation and spatial downscaling of cru ts precipitation data in the philippines. Model Earth Syst Environ, 4(3), 891–898. https://doi. org/10.1007/s40808-018-0450-6

Shafiq ul, M., Ramzan, S., Ahmed, P., Mahmood, R., & Dimri, A. P. (2019). Assessment of present and future climate change over Kashmir Himalayas, India. Theoretical and Applied Climatology, 137(3), 3183–3195.

Shama, L. F. Z., & Najim, M. M. M. (2014). Analysis of rainfall trends in three selected rain gauging stations from wl3, il1a, and dl1f agroecological regions in Sri Lanka. Jordan Journal of Earth and Environmental Sciences, 14(3), 175–181.

Shi, H., Li, T., & Wei, J. (2017). Evaluation of the gridded CRU TS precipitation dataset with the point rain gauge records over the three-river headwaters region. J Hydrol (Amst), 548, 322–332.

Smith, G. (2010). " In Kashmir, water treaty means less power to the people". https://www.theglobeandmail.com/news/world/ in-kashmir-water-treaty-means-less-power-to-the-people/ article1389907/ (Jan. 13, 2025).

Stafne, E. T. (2017). Chilling-hour requirement of fruit crops (Jan. 13, 2025). Missis- sippi State University Extension. http://extension.msstate.edu/publications/chilling-hour-requirements-fruit-crops

Strigaro, D., Moretti, M., Mattavelli, M., Frigerio, I., Amicis, M. D., & Maggi, V. (2016). A grass GIS module to obtain an estimation of glacier behavior under climate change: A pilot study on Italian glacier. Comput Geosci, 94, 68–76.

Swain, S., Nandi, S., & Patel, P. (2018). Development of an ARIMA Model for Monthly Rainfall Forecasting over Khordha District, Odisha, India. In P. K. Sa, S. Bakshi, I. K. Hatzilygeroudis, & M. N. Sahoo (Eds.), Recent Findings in Intelligent Computing Techniques (pp. 325–331). Springer Singapore.

Ul, I. Z., & Khan, R. L. A. (2013). Climate change scenario in Kashmir Valley, India, based on seasonal and annual average temperature trends. Disaster Advances, 6(4), 30–40.

UN Climate Change Conference. (2023). " UAE-2023: COP28". https://unfccc.int/ cop28 (Jan. 13, 2025).

UNFCCC. (2018). " Paris Climate Change Conference - November 2015, Session COP 21". https://unfccc.int/ documents/184656 (Jan. 13, 2025).

UNICEF. (2022). " Devastating floods in Pakistan". https : //www . unicef . org / emergencies/devastating-floods-pakistan-2022 (Jan. 13, 2025).

Wani, M. H., Baba, S. H., Bazaz, N. H., & Sehar, H. (2015). Climate change in Kashmir Valley: Is it initiating transformation of mountain agriculture? Indian J Econ Dev, 3(2), 142–154.

YoosefDoost, A., Sadeghian, M. S., NodeFarahani, M., & Rasekhi, A. (2017). Com- parison between performance of statistical and Low Cost ARIMA Model with GFDL, CM2.1 and CGM 3 Atmosphere-Ocean General Circulation Models in assessment of the effects of climate change on temperature and precipitation in Taleghan Basin. American Journal of Water Resources, 5(4), 92–99.

Youssef, J., Ishker, N., & Fakhreddine, N. (2021, June). GDP Forecast of the Biggest GCC Economies Using ARIMA (MPRA Paper No. 108912). University Library of Munich, Germany. https://ideas.repec.org/p/pra/mprapa/108912. html

Zaz, S. N., Romshoo, S. A., Krishnamoorthy, R. T., & Viswanadhapalli, Y. (2019). Analyses of temperature and precipitation in the Indian Jammu and Kashmir region for the 1980–2016 period: Implications for remote influence and extreme events. Atmos Chem Phys, 19(1), 15–37.

Zhong, R. (2022). " In a First Study of Pakistan's Floods, Scientists See Climate Change at Work". https://www.nytimes. com/2022/09/15/climate/pakistan- floods-global-warming. html (Jan. 13, 2025).

JJEES

JJEES (2025) 16 (1): 96-107
ISSN 1995-6681

Jordan Journal of Earth and Environmental Sciences

The Relative Impact of Urbanization Expansion and Climate Change on Flood Hazard in Amman City

Ibrahim M. Oroud*

Mutah University, Karak, Jordan

Received on 21 September 2024, Accepted on 2 February 2025

Abstract

The effect of land use changes and climate change on flooding frequency and magnitude was evaluated in the rapidly expanding Amman City, Jordan. A high spatial resolution hydrological model was run on a daily timestep from 1985 through 2021 to simulate the evolution of flooding events using three land use scenarios, 1986, 2001, and 2024. Land use derived from Landsat images indicated a large urban expansion, with urban areas expanding from ~83 km^2 in 1986 to 137 km^2 in 2024. Simulation results were commensurate with observed and archived datasets. Aridification and warming were observed in the study area. Precipitation decreased and the minimum and maximum temperatures rose significantly during the past 20 years. It is expected that aridification and warming will provide a buffering effect on flooding events, but the effect of urbanization is far more important in increasing flooding hazards as demonstrated by the frequency and magnitude of flooding events during recent years. The rapid urban expansion altered the ability of the surface to absorb and retain rainwater, leading to recurrent severe flooding events in recent years as revealed by the frequency of reported flooding events and the simulation results. The simulated average annual surface runoff for the 1986 land use scenario from 1985 to 2021 was 71 mm, whereas its corresponding values for the 2001 and 2024 scenarios were 78 mm and 87 mm, respectively. The total number of flooding events with a runoff value above 10 mm was simulated to be 88 for the 1986 land use scenario while the number for the 2001 and 2024 scenarios were 100 and 106, respectively. The number of flooding events exceeding 20 mm for 1986 scenario was 25, increased to 30 and 39 for land use scenarios of 2001 and 2024. Results show that urban expansion is a major driving force in flood generation and the projected warming and drying will not alleviate this emerging hazard. The present study highlights that urban expansion has a more significant impact on flood intensity and frequency than decreasing precipitation and rising temperatures. The study emphasizes the urgent need to integrate urban hydrology and geomorphology into land-use planning policies. The flood related information presented in this investigation is quite operational to assist in mitigating potential flood damages and future land use planning for Amman City and other urban areas in Jordan and the nearby region.

Keywords: *natural hazard, climate change, urban hydrology, Amman City, flooding hazard, urban planning, remote sensing*

1. Introduction

Rapid urban expansion has deleterious consequences on many environmental issues such as air quality, energy consumption, and thermal comfort (e.g., Chung et al., 2011; Jahan et al., 2021; Oroud, 2022). Of particular importance is flooding, which poses significant challenges to cities worldwide, particularly in third-world countries due to a lack of adequate infrastructure and poor zoning criteria. Urban areas are prone to extensive flooding events due to the widespread impermeable surfaces which impede the absorption and retention of rainwater (Guo et al., 2021; Agonafir et al., 2023). Population growth causes inward and outward urban expansion. Inward growth fills the void spaces, causing a substantial increase of the impermeable surfaces while the outward expansion adds additional impervious landscapes to the total area contributing to flooding events.

Urban landscape has numerous negative effects on the hydrological cycle including increasing surface runoff, decreasing infiltration, and degrading water quality (e.g., Miller and Hutchins, 2017; Odeh et al., 2022). Recurrent flooding in Amman City has become ubiquitous during the rainy season in recent years. The rapid population growth, poor zoning measures, and the topography of the city go hand in hand in exacerbating the recurrence of this damaging natural hazard. Significant property losses and human casualties have been increasing in the city in recent years. A major flooding catalyst has been the substantial expansion of the impermeable urban fabrics over the steep topography during the past four decades, resulting from the rapid population growth. The population of Amman increased from ~0.8 million people in 1986 to more than 2.25 million people in 2024. The risk of flooding events is further intensified by the rugged topography and poor urban planning. Significant parts of the city are situated along the wadies, draining higher portions of the city. Improper zoning measures contributed significantly to this damaging hazard. Planners did not pay attention to the hydrology of the city prior to zoning new lands into urban land use over the higher portions of the city which caused water to significantly flood to the downtown area.

* Corresponding author e-mail: ioroud@mutah.edu.jo

In recent years, the southeastern Mediterranean witnessed aridification and warming trends , precipitation declined, and temperature showed a significant increase. This aridification and warming trends are expected to influence flood hazard in the study area provided that the intensity of precipitation did not witness any alterations.

Numerous studies were conducted to assess flooding in Amman City and nearby areas (Alhasanat, 2014; Oroud, 2015a, Oroud, 2015b; Engicon, 2019; Gharaibeh et al., 2019; Tabari et al., 2020; Al Azzam and Al Kuisi, 2021; Oroud, 2024). For instance, Ecogen (2019) reported that the intensity of precipitation that fell on the 28 of February 2019 did not justify the massive flooding in downtown Amman and attributed the flood disaster to an inadequate municipal drainage network. Other studies focused on the effect of climate change on individual and community response to flood disasters (Al Saodi et al., 2023; Gammoh et al., 2023). The relative influence of land use changes and the recent aridification-warming trends on flooding have not been addressed in earlier studies, and thus the objective of the present study is to examine the effect of land use changes and recent climate change on flooding events within the catchment area draining the city of Amman using a spatially distributed hydrological model, remote sensing data and GIS tools. The model is run on a daily timestep with a spatial resolution of 250 m to capture the fine spatial details caused by the large variations in topography and land cover. The hydrological model was run for three land use scenarios: 1986, 2001, and 2024. This study will examine the effects of urban expansion and climate change on the frequency and magnitude of flooding events in the study area.

2. Study Area

Amman City is located in central Jordan and represents the largest urban center in the country (Figure 1). The city was a very small town in the beginning of the 20th century, which was confined to a strip of low land adjacent to a creek draining the nearby rugged terrains. The small town expanded from the low-lying areas to the nearby rugged mountainous terrains in a rather random manner. The downtown area, which occupies the low-lying areas and the site of vibrant commercial activities, is situated within the confluence of the water courses draining the higher parts of the city.

The city witnessed a rapid population growth due to the recurrent influx of refugees and immigration from rural areas. The population of the city increased from ~90 thousand people in 1950 to more than ~2.25 million people in 2024. In other words, the population of the city increased by about 24 folds within the past 75 years. Following this population explosion, the city size expanded by about 20 times between 1950 and 2003 (Oroud and Al-Rousan, 2004) and by more than 70% between 2003 and 2015 (Al-Kofahi et al., 2018). Figure 2 shows the population growth of the city of Amman between 1950 and 2024.

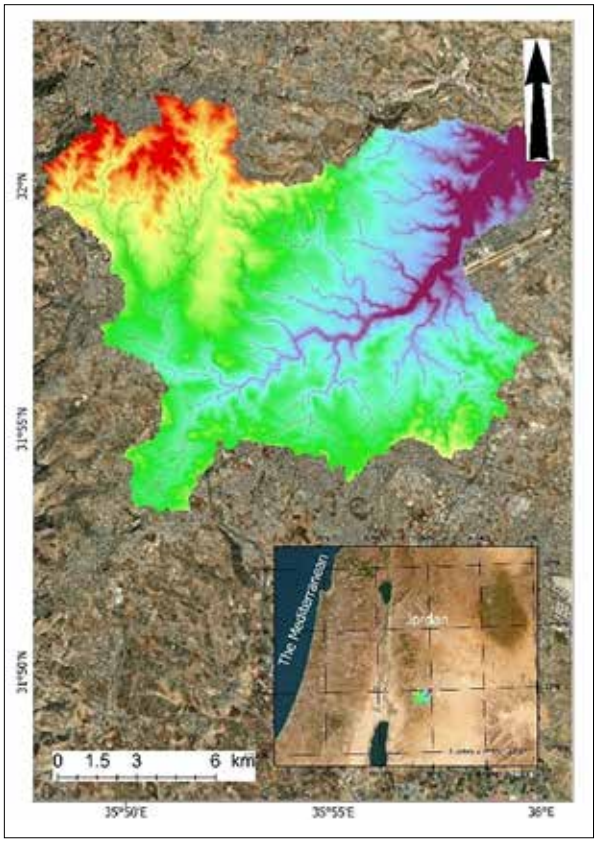

Figure 1. Location of the study area

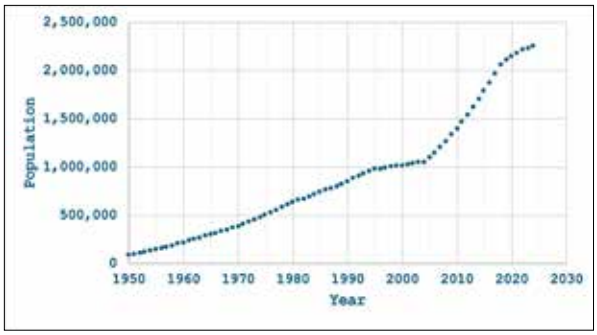

Figure 2. Population growth of Amman city during the period 1950 through 2024.

Data Source: United Nations - World Population Prospects: https://www.macrotrends.net/global-metrics/cities/21700/amman/population - Amman, Jordan.

3. Data and Method of Investigation

3.1 Meteorological Data

Daily data on the precipitation of three hydrometeorological stations was obtained from several sources including the Department of Meteorology, the Ministry of Water and Irrigation and the Ministry of Agriculture, Jordan. The daily data covers the period from 1985 through 2021. Daily data on precipitation for the three stations was cross-correlated to ensure record consistency and accuracy. Maximum and minimum air temperatures were obtained from a station within the city operated by the Department of Meteorology, Jordan.

3.2 Topography, Soil and Land Cover

The topography of the city was generated using a digital elevation model (DEM), downloaded from the Shuttle Topographic Radar Mission (STRM) from the USGS site (http://earthexplorer.usgs.gov). The DEM image, which has a spatial resolution of 30 m, was used within a GIS environment to delineate the watershed, identify the elevation of each resolution grid, and generate the various raster layers needed in the analysis of flooding and flow accumulation. The watershed, draining the city, has steep gradients with an elevation ranging from ~650 m to more than 1100 m above mean sea level. This steep topography gradient reflects the rugged nature of the city. A soil shapefile was obtained from the Ministry of Agriculture, Jordan, where each soil type was classified based on its texture (Hunting Technical Report, 1993).

The land cover for the study area was derived from Landsat images downloaded for 1986, 2001, and 2024. The three images were downloaded in April and May to identify land cover patterns correctly because arid and semiarid lands tend to give a spectral signature similar to urban landscapes during the dry season (Oroud and Balling, 2021). Landsat 5 and 7 have an 8-bit radiometric resolution, 0-255 dynamic range, while Landsat 9 has a 14-bit radiometric resolution, 0-16383 dynamic range (Table 1). This means that Landsat 9 OLI-2 has a much higher radiometric resolution, and, thus, it is capable of discerning subtle land surface tones compared to the earlier satellites images. The visible and near-infrared bands were stacked and pan-sharpened using band 8 for Landsat 7 and 9 to enhance their spatial resolution. The three images were classified using the Support Vector Machine (SVM) embedded in Arc GIS Pro (see also Oroud and Balling, 2021; Oroud, 2023).. The accuracy of the classification was checked for the image of 2024 against high-resolution Google images with a Kappa value of 92%.

Table 1. The spectral and radiometric properties of the three Landsat satellites used in this investigation.

Landsat	Date	Number of bands	Radiometric resolution	Spatial resolution
Landsat 5 TM	4-5-1986	7	8-bit	30 m
Landsat 7 ETM+	24-5-2001	8	8-bit	30 m
Landsat 9 OLI-2	05-4-2024	11	14-bit delivered to users as 16-bit	30 m

3.3. GIS tools

The GIS tools were implemented to generate watersheds and obtain the x, y coordinates and elevation values for each resolution cell. Land-cover type, soil classes and slope were overlain in a GIS environment to generate a curve number across the study area during the three land use scenarios—1986, 2001, and 2024. The curve number generated for each scenario was used in the hydrological model to calculate flooding frequency, magnitude, and its spatial distribution across the study area. The GIS tools were also used to extract the flow accumulation which can be used for operational purposes to examine flood volume for sub-watersheds.

3.4. Data Interpolation

The introduction of GIS at the end of the previous century has revolutionized data interpolation, and, thus, large spatial extents could easily be interpolated objectively and with a high degree of accuracy given the availability of a sufficient number of measuring points. The problem of direct GIS interpolation schemes can become problematic if weather-measuring stations are sparingly distributed over rugged terrains (e.g., Jeffrey et al., 2001; Apaydin et al., 2004), leading to large errors. A more rigorous procedure to interpolate meteorological data would be to take into account vertical and horizontal gradients of the specified element across the landscape (e.g., Schoener, 2010; Emmendorfer and Dimuro, 2020):

$$\delta_{i,k} = \sqrt{(x_i - x_j)^2 + (y_i - y_j)^2} \quad (1)$$

where $\delta_{i,k}$ is the Euclidean distance (m) between station I and the intended grid cell, and the x and y are the easting and northing coordinates (m). A climatological element at a grid, e.g., precipitation ($x(x_k,y_k,z_k)$ or any other climatological element like temperature, can be derived explicitly using, for example, the IDW (Emmendorfer and Dimuro, 2020; Oroud, 2022):

$$x(x_k, y_k, z_k) = \frac{\sum_{i=1}^{I}(xi+\Gamma(zi-z(k))/\delta(i,k)^2}{\sum_{i=1}^{I}\frac{1}{\delta(i,k)^2}} \quad (2)$$

where x_k is the easting (m), y_k is the northing (m) and z_k is the elevation of the grid; x_i is the meteorological element at station I, Γ is the environmental gradient/lapse rate (e.g., mm m^{-1}), z_i is the elevation of station I, z(k) is the elevation of the grid, and δ(I,K) is the Euclidean distance between station I and the intended cell. Precipitation for each grid was interpolated using the Inverse Weighing Distance using the three meteorological stations after accounting for grid elevation. The interpolation of air temperature is easier because this element depends primarily on the elevation difference between the grid and the measuring station.

3.5 The Hydrological Module

For modeling purposes, the study area was subdivided into discrete cells, each of which is 250 m side length. Each cell has its X and Y coordinates along with its unique CSN value. The Soil Conservation Service Curve Number (SCS-CN) scheme is widely implemented to characterize flooding over urban areas (e.g., Ponce and Hawkins, 1996; Dingman, 2002; Kannan et al., 2008; Jahan et al., 2021; Oroud, 2024). The SCS method implements the curve number to assess runoff response as a function of soil type, land cover, the state of landcover and topography (Borga et al., 2007; Ries et al., 2017).

The maximum potential soil moisture retention capacity (S) is derived based on the Curve Number of each resolution cell (Ponce and Hawkins, 1996):

$$S(j) = 254\left(\frac{100}{CN(j)} - 1\right) \quad (3)$$

where S(j) is the moisture potential retention capacity, and CN is the curve number of the pixel. The S(j) of soil is adjusted between the dry soil condition (CN1) and the wet conditions (CN3) as determined from the antecedent soil moisture of each resolution cell (Ponce and Hawkins, 1996),

$$CN1 = \frac{CN}{2.28-.01281CN} \quad (4)$$

$$CN3 = \frac{CN}{0.427+0.00573CN} \quad (5)$$

The CN value for a resolution cell at a given time step is as follows:

$$CN = CN1 + \frac{\mu Si^{t-1}}{S_{max}} \quad (6)$$

where S_{max} is the soil moisture retention capacity at CN1; Si^{t-1} is soil moisture retention of a resolution cell at the previous timestep (previous day), μ is determined by Ponce and Hawkins, 1996:

$$\mu = CN3 - CN1 \quad (7)$$

The curve number is adjusted for slope as suggested by Ajmal et al. (2023):

$$CN = \frac{322.79+15.63\alpha}{323.52+\alpha} \quad (8)$$

where α is the slope in percentage.

Runoff from a given grid occurs when daily precipitation exceeds its moisture potential retention (e.g., Viola et al., 2017):

$$\left\langle \begin{matrix} Ro = \frac{(P-0.2S)^2}{P+0.8S}, P > 0.2S \\ Ro = 0, P \leq 0.2S \end{matrix} \right\rangle \quad (9)$$

4. Evaporation Calculation

For the non-steady state of transient modeling, there must be tracking of surface moisture as antecedent moisture has a significant impact on actual evapotranspiration, surface runoff and groundwater recharge. The soil water change is established by using the water budget at the surface, expressed as (e.g., Viola et al., 2017; Small et al. 2018):

$$\frac{\delta S}{\delta t} = P - A_T - R_O - D_p \quad (10)$$

where the first term on the left is soil moisture change with respect to time, P, A_T, R_O, and D_p, are precipitation, actual evapotranspiration, surface runoff, and deep percolation, respectively.

Actual evapotranspiration is determined by potential evapotranspiration, soil water content, and subsurface hydraulic properties (Dingman 2002; Allen et al., 2007). Actual evaporation is calculated as a function of potential evaporation and soil moisture content within a resolution pixel. In this study, potential evapotranspiration (PE) is calculated using the following form (Hargreaves and Allen 2003):

$$PE = 0.0023R_g\left(17.8 + \bar{T}\right)\sqrt{\Delta T} \quad (11)$$

where PE is potential evapotranspiration (mm/day), R_g is daily global radiation in mm equivalent units, is the average daily temperature (OC), and ΔT is the diurnal temperature range, the maximum minus the minimum temperature.

Global radiation is parameterized by Hargreaves and Samni (1982):

$$Rg = 0.408S_{ext} \quad (12)$$

where S_{ext} is the extraterrestrial daily solar radiation as determined by latitude and declination of the sun (Iqbal, 1983):

$$S_{ext} = S_C R(\omega \sin\varphi \sin\delta + \cos\varphi \cos\delta \sin\omega) \quad (13)$$

where SC is daily solar radiation constant at the mean earth- sun distance, R, Φ, δ, and ω are the sun-earth distance ratio (-), latitude, declination of the sun, and daylength. The simulated daily extraterrestrial radiation in the study area varies from ~18 MJ m^{-2} day^{-1} at the end of December to ~ 42 MJ $m^{-2}day^{-1}$ in June. It is important to note that in the Mediterranean region precipitation and evapotranspiration are out of phase, and the major factor influencing water balance and flooding is precipitation (Unissa et al., 2023; Oroud, 2024). Furthermore, the long dry and hot summer season deletes the past memory of subsurface moisture storage, and, thus, a hydrological year can be modeled independently from previous years with very little, if any, loss of accuracy (e.g., Viola et al., 2017).

In this study, the soil profile is divided into two compartments, a top thin one with a moisture holding capacity of 15% of the total soil profile capacity, and a deep layer holding 85% of the total soil moisture. This procedure was adopted successfully by numerous researchers and gave excellent results (e.g., Palmer, 1965; Crooks and Naden, 2007). Actual evapotranspiration is assumed to be equal to the potential value (PE) when precipitation equals or exceeds P but decreases nonlinearly as soil moisture drops (e.g., Farmer et al., 2003; Liu and Smedt 2004; Enrique and Alfonso, 2010):

$$AE = PE, P \geq PE$$

$$AE = (P_E - A_{E1})\left(\frac{\theta-\theta_w}{\theta_s-\theta_w}\right)^{\sigma}, \quad AE = AE_1 + AE_2 \quad (14)$$

where A_{E2} is evapotranspiration from the second layer, AE1 is evaporation from the top layer, θ_w is soil moisture at the wilting point, and σ is an exponent larger than unity (e.g., Liu and Smedt 2004; Crooks and Naden 2007).

5. Model Verification

There are no actual measurements to establish the performance of the present model, but we used two different procedures to establish the adequacy of the model output. The present model results were tested against the simulation results of other hydrological models and the chloride mass balance in a similar environment. The present model results are commensurate with the chloride mass balance and the simulation results of other hydrological models (see Oroud, 2024). Because of the lack of direct flood observations, we resorted to archived newspapers and social media data which reported the extent of flood damage and pictured the flood magnitude. Thus, we used the archived flooding events for Amman City for the period 2010 through 2021, as reported in the local newspapers and social media. Archived flooding events were compared to those generated by the model using the 2024 land use scenario. It is well understood that flooding is closely linked to precipitation intensity—e.g.,

hourly, 3 hours, and 6 hours, which cannot be revealed by the model as it uses a daily timestep. Yet, newspaper reports would give a good indication of flooding magnitude and thus can be used to "gauge", at least qualitatively, the simulation results. Table 2 shows the dates along with precipitation and flooding magnitudes exceeding 20 mm along with the reported flooding events in the newspapers' archives for the period 2010-2021.

Table 2. The dates along with precipitation and flooding events exceeding 20 mm/day for the period 2010-2021 and flooding events as reported in the archives of newspapers.

Date	Precipitation (mm/day)	Flood magnitude (mm)	Newspapers reports
18-1-2010	51.12	28.38	No flooding reports
26-2-2010	51.92	33.18	Heavy flooding in downtown
28-2-2010	45.21	28.17	No flooding reports
4-2-2011	38.1	21.09	No flooding reports
17-2-2011	41.19	22.15	No flooding reports
29-2-2012	43.34	25.04	No flooding reports
1-3-2012	55.68	25.76	No flooding reports
7-1-2013	75.4	53.4	Heavy flooding reports
8-1-2013	54.88	37.21	Heavy flooding reports
11-12-2013	55	34.04	Heavy flooding reports
26-11-2014	37.57	20.04	No flooding reports
18-2-2015	46.55	21.19	No flooding reports
8-1-2016	37.7	21.07	No flooding reports
5-1-2018	43.74	25.16	Heavy flooding reports
18-1-2018	37.43	20.78	Heavy flooding reports
27-2-2019	42.13	24.17	Heavy flooding reports
28-2-2019	58.23	40.68	Heavy flooding reports
26-12-2019	83.32	54.03	Heavy flooding reports
8-1-2020	47.5	30.27	Heavy flooding reports

It is clear that whenever flooding exceeded 30 mm/day, massive flooding was reported. Archived results show good agreement with simulation results. The model failed to identify a major flooding event reported on 5-11-2015. This flooding event was a result of an intense localized thunderstorm that lasted for 40 minutes, and the reported precipitation across the catchment was 13 mm. The overall agreement between simulated and archived flooding events provides further support to the adequacy of the model results.

6. Results

6.1. Urban Expansion

Figure 3 shows the city size in 1986, 2001, and 2024 as obtained from Land-sat images. There has been a large urban expansion during the past four decades which reflected the rapid population growth of the city. Urban areas within the catchment area increased from ~83 km^2 in 1986 to ~137 km^2 in 2024, an increase of about 64%. On the other hand, cultivated and forest areas decreased from 68 km^2 and 28 km^2 in 1986 to ~32 km^2 and ~11 km^2 in 2024. This is a substantial land cover change during the past 40 years. The transformation of natural landscapes into highly impermeable urban fabrics is expected to heighten flood risk and reduce the concentration time of flood peaks.

This land use change reflected the very rapid population growth of the City of Amman. The number of inhabitants of the city increased from ~800 thousand in 1986 to 2.25 million people in 2024. Figure 4 shows the distribution of land use in 1986 and 2024.

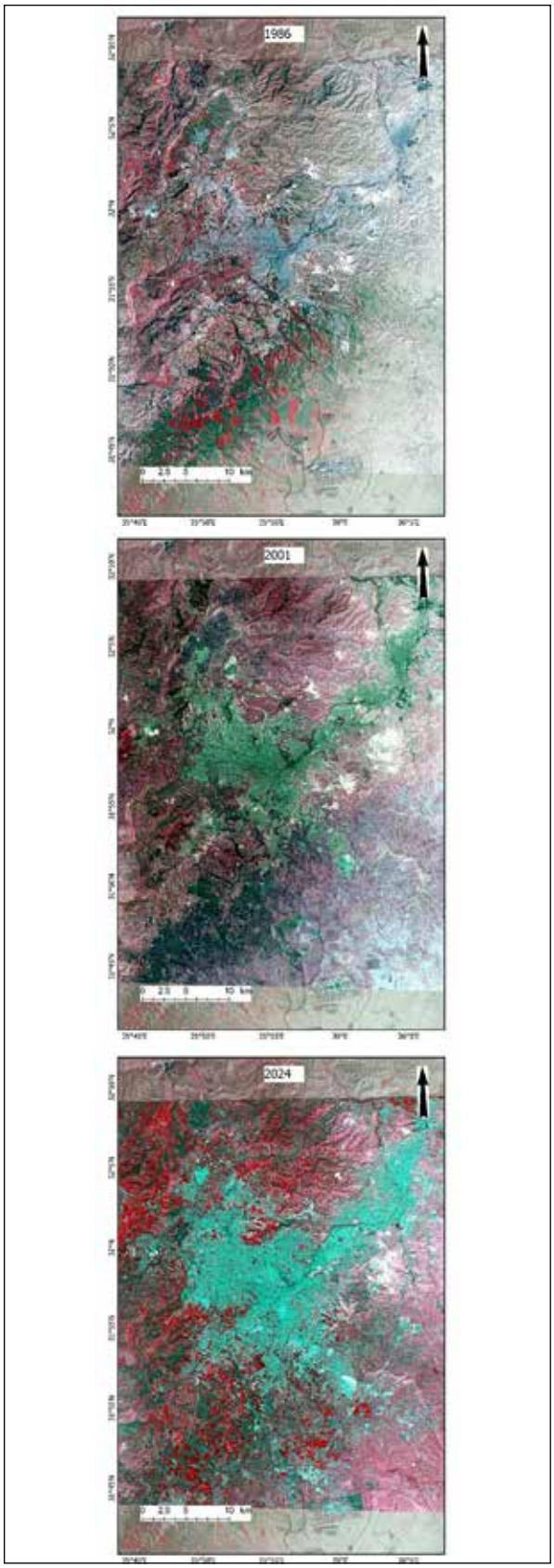

Figure 3. Urban expansion of the city of Amman as revealed by three Landsat images taken in 1986, 2001, and 2024

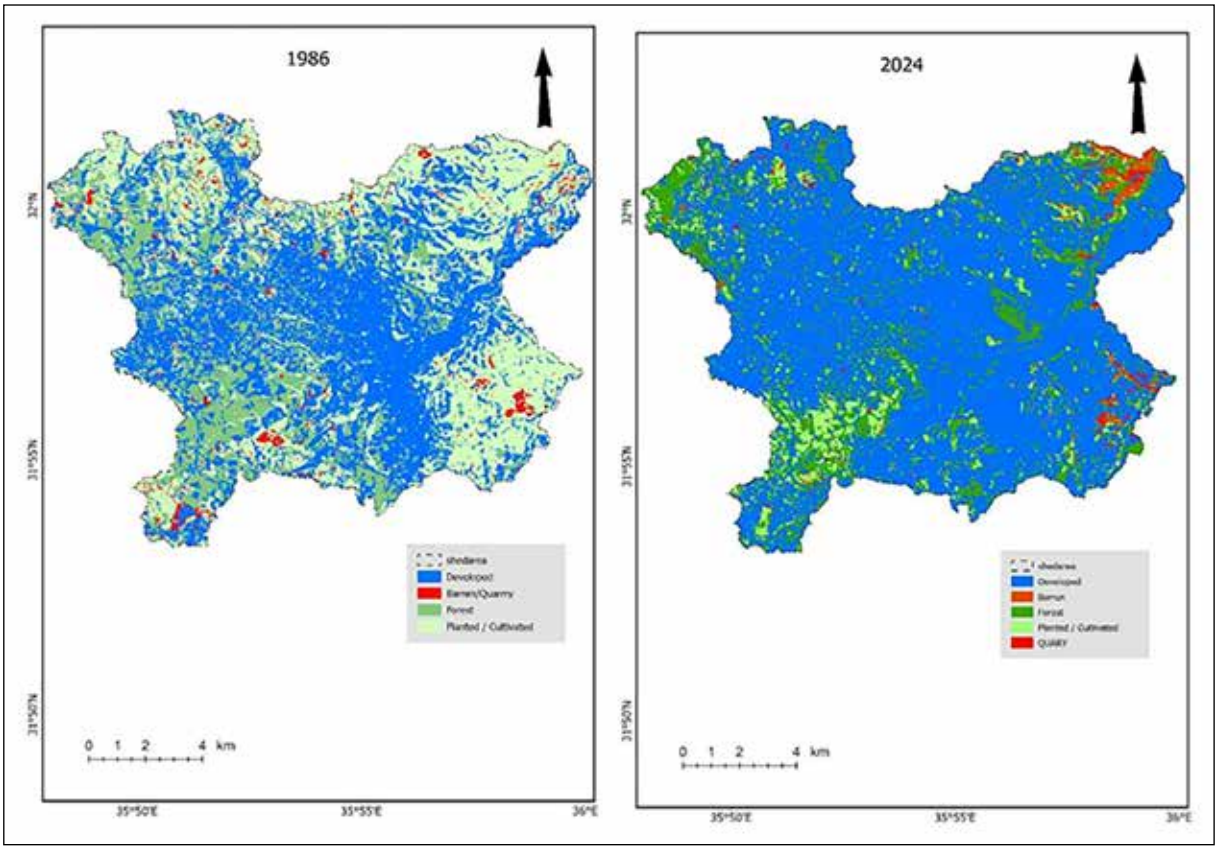

Figure 4. The extent and spatial distribution of land use in 1986 and 2024.

6.2. Spatial distribution of precipitation

There is a steep precipitation gradient across the watershed which typifies the Eastern Mediterranean environment. Precipitation follows closely the elevation contour lines. Figure 5, which is generated by the model, shows the average annual precipitation distribution across the catchment; it ranges from a minimum of ~200 mm/year in low laying areas to more than 420 mm/year in the northwestern parts of the catchment where elevation reaches 1100 m.

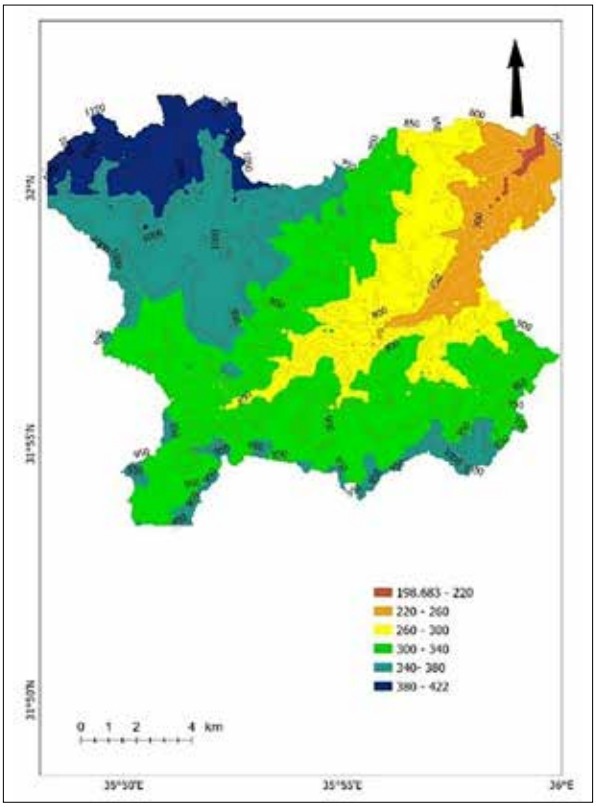

Figure 5. The spatial distribution of precipitation (mm/year) along with the elevation contour lines (meters above mean sea level)

6.3 Precipitation Events

Precipitation in the Eastern Mediterranean falls from October through May. More than 75% of precipitation occurs in the coldest months, December through February. Yet, large precipitation events also occur in the transitional seasons—Fall and Spring—mainly due to dynamic atmospheric static instability caused by upper air cold troughs advancing from the northwest, associated with low level moist warm air and penetrating along the Red Sea Trough (e.g., Oroud, 2018; Hochman et al., 2022). Figure 6 shows the frequency of precipitation categorized according to its daily amount. There were 1700 daily precipitation events (P>0 mm) during the 37-year study period, of which 273 events exceeded 10 mm, and 113 events exceeded 20 mm/day.

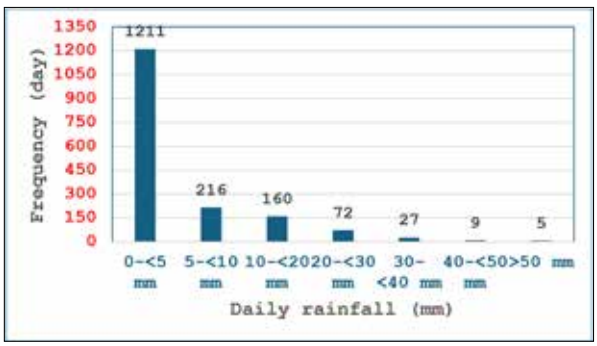

Figure 6. The frequency of precipitation as categorized according to its daily amount

Annual precipitation has decreased slightly during the past 37 years. Still, it is not statistically significant while the minimum and maximum temperatures exhibited significant increasing trends which are important at the 95% level (see Figure 7). The average maximum air temperature in the study area was 23.22 °C during 1985-2005, while its corresponding value for the second period, 2006 -2021, was 24.22 °C. Likewise, the average minimum temperature for the first period was 12.04 °C, while it was 13.14 °CC in the second period. This increasing trend is linked to global warming and urban expansion. A temperature increase is likely to reduce flooding and groundwater recharge due to the increased water loss via evaporation provided that the intensity of precipitation did not experience any change. Examination of daily precipitation data did not reveal any statistically significant changes in the intensity of precipitation during the study period. Thus, based on climate alone, there should be a reduction in runoff because of the increased air temperature.

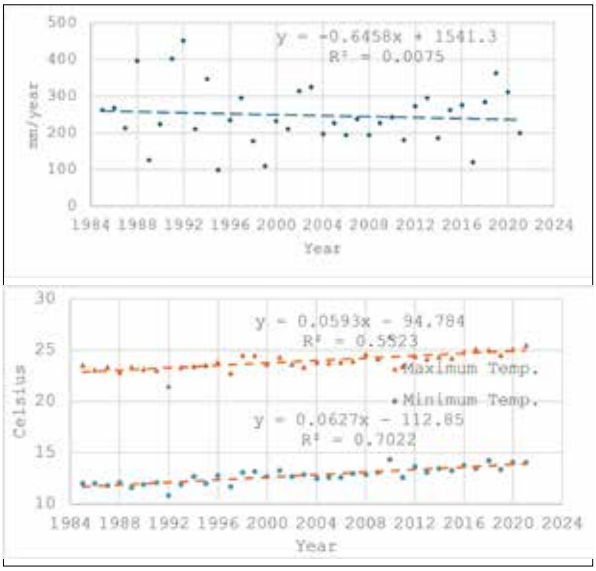

Figure 7. Annual precipitation and minimum and maximum temperature trends during the period 1985 through 2021

6.4 Runoff and Flooding Events

The significant changes in land use during the past 40 years have caused a large change in the curve number. For instance, the curve number as derived from the Landsat images was 86.0 for 1986 land use scenario, increased to 87.7 and 89.7 for land use scenarios of 2001 and 2024. Although the change in the curve number is relatively small, it is important to note that the curve number is quite high to start with, and, thus, small departures in the CN are expected to amplify runoff events significantly following urbanization expansion. Simulation results show that the average annual surface runoff for 1986 land use scenario was ~71 mm which represents ~22% of average annual precipitation while the corresponding values for 2001 and 2024 land use scenarios were 78 mm and 87 mm, respectively. The increased runoff came mainly at the expense of actual evapotranspiration. For instance, actual evapotranspiration for the 1986 scenario was 198 mm while it is 192 mm and 178 mm for 2001 and 2024 land use scenarios.

Figure 8 shows the link between daily precipitation and daily runoff for the 1986 and 2024 land use scenarios. It is clear that runoff link to precipitation exhibits a steeper response for the 2024 land use scenario as demonstrated by visual inspection and the coefficients of the regression line. Runoff tends to start, in general when precipitation exceeds 10 mm for land use scenario of 2024 but has a higher precipitation threshold for 1986 land use scenario.

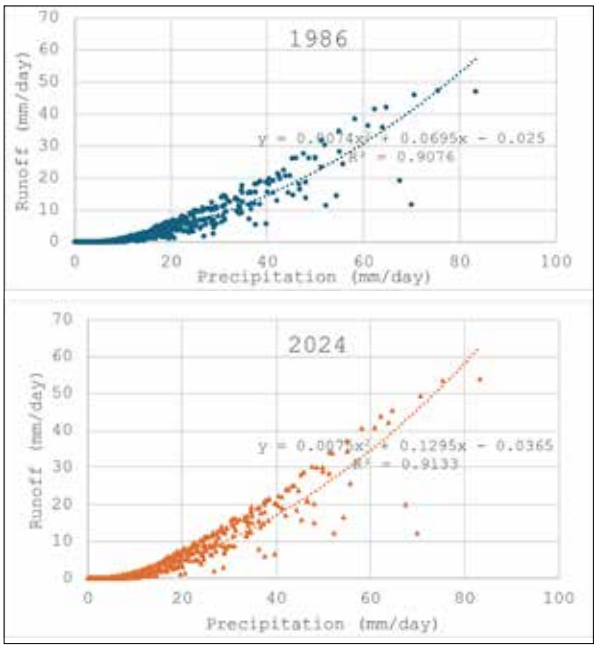

Figure 8. The link between daily precipitation and daily runoff for the 1986 and 2024 land use scenarios. Notice that the curve is steeper for land use scenario of 2024 as revealed by the regression coefficients.

A more dramatic effect of urbanization is quite distinct when examining the frequency of flooding events according to their magnitudes. Table 3 shows the runoff events categorized based on their magnitude under the three land use scenarios using the same daily precipitation and temperature records. The total number of flooding events for the three scenarios were not very different from each other, with a value ranging from 760 to 706. The picture becomes very different when comparing large flooding events among the three scenarios. For instance, the number of flooding events (runoff 10 mm) is 88 for the 1986 land use scenario, increased to 100 and 106 for 2001 and 2024 land use scenarios. The departure becomes far more distinct when comparing very large flooding events. For instance, the number of flooding events of 20 mm/day is 25 for the 1986 land use scenario while it is 39 for land use scenario of 2024, with a 56% increase. The land use scenario of 1986 did not show any flooding events in excess of 50 mm/day. Results demonstrated that the frequency of large flooding events has increased substantially following the spread of urbanization. This increase clearly demonstrates that urbanization has a significant impact on flooding in Amman despite the buffering effect brought about by precipitation reduction and air temperature rise.

Table 3. Number of runoff events categorized based on magnitude for the city of Amman as influenced by land use scenarios of 1986, 2001, and 2024. The simulation for each scenario was run from 1985 through 2021.

Runoff magnitude (mm/day)	Number of runoff events for each land use scenario			
	1986	2001	2024	% change between 2024 and 1986
>=0	759	760	766	1%
>=10	88	100	106	20%
>=20	25	30	39	56%
>=30	11	12	15	36%
>=40	5	5	8	60%
>=50	0	2	2	----

An important point is the effect of land use changes on the simulated spatial distribution of floodwater across the catchment. Figure 9 shows the average annual distribution of runoff across the catchment in 1986 and 2024. It is clear that a significant increase in runoff potential is observed for land use of 2024 compared to 1986. The alteration from agricultural and forest lands to urbanization has significantly reduced the surface capacity to absorb and retain precipitation, leading to higher runoff potential. The effect of slope on flood generation is taken into account via Eqn. 8, which implies a larger increase in the curve number as slope gradient increases. Furthermore, the combination of impermeable surfaces along with steep slopes reduces the concentration time for flood peaks.

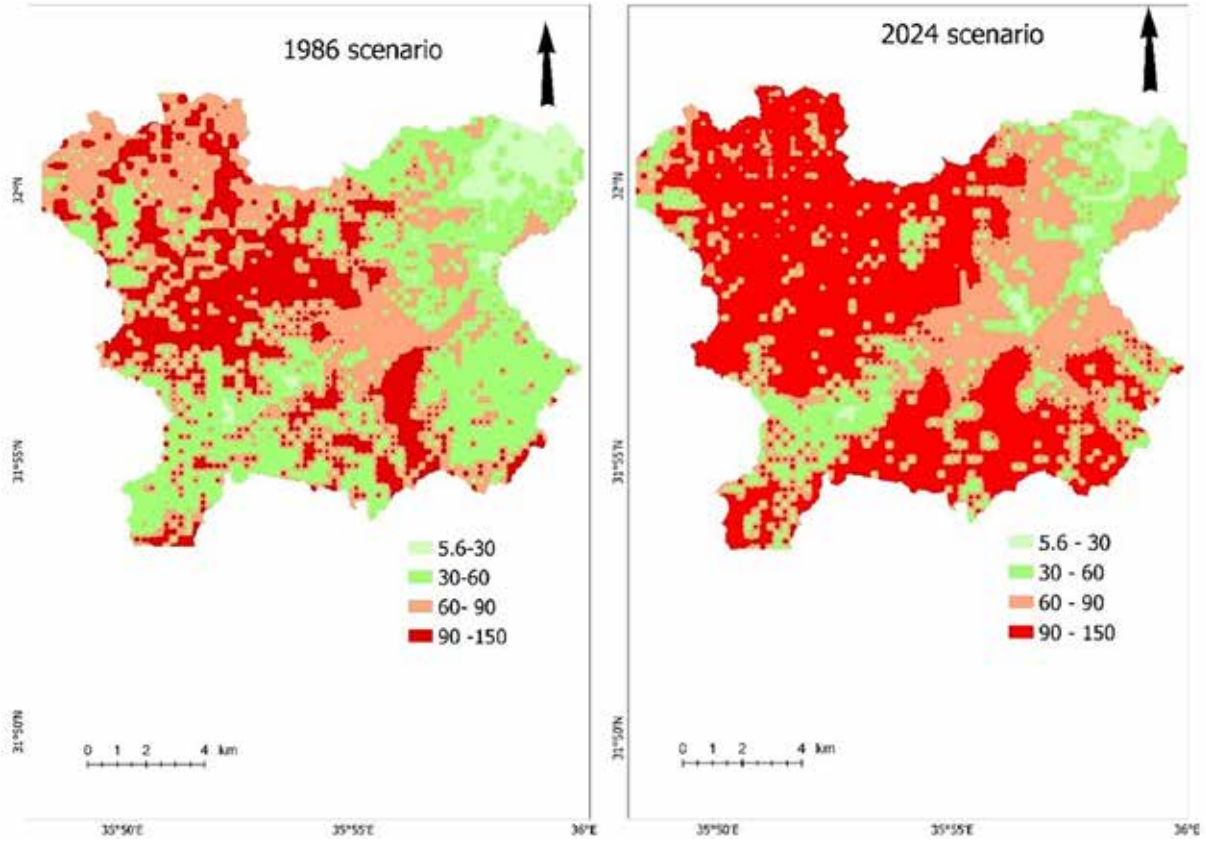

Figure 9. The average annual distribution of runoff (mm/year) across the catchment area in 1986 and 2024

6.5 Climate Change Versus Urbanization

To examine the effect of land use changes compared to climate change impacts, we subdivided the period into two parts; one extends from 1986 through 2005, and the other extends from 2006 through 2021. It is assumed that the land use in 1986 represented the first period while the second period was assumed to be represented by the land use in 2024. Calculations show that the average annual potential evapotranspiration and precipitation during the first period were 1323 mm and 340 mm while the corresponding values for the second period were 1359 mm and 323 mm, respectively. Clearly, a trend of aridification and warming is observed during the second period. Based on climate records alone, we should expect more surface runoff during the first period. Figure 10 shows that the number of flooding events 20 mm/day during the first period was 10 while in the second period, which represents land use of 2024, recorded 21 events, more than 100% increase in flooding events.

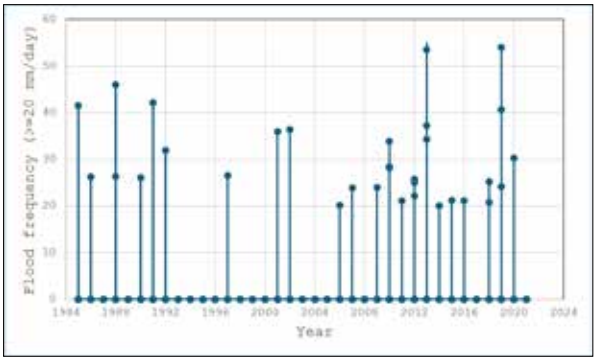

Figure 10. The number of flooding events over 20 mm/day. The land use scenario of 1986 represents the period 1986 through 2005 while the land use scenario of 2024 represents the period 2006 through 2021. Each dot in the figure represents a flooding event >= 20 mm/day.

The large increase in flooding events during the second period was only due to land use changes . The frequency of major precipitation events did not show any difference between the two periods. For instance, the number of daily precipitation events over 20 mm in the first period was 57, while it was 56 in the second period. Likewise, the number of precipitation events over 30 mm was 21 events in the first period and 20 events in the second period. This means that the significant increase in large flooding events simulated in the second period was due to land use changes. Thus, the buffering effect, brought about by aridification and warming in the second period, did not have any effect in reducing large flooding events in the study area despite the warmer and drier conditions experienced in the second period.

7. Discussion

The natural setting of Amman City, being highly urbanized and built over rugged terrain, increases the risk of flooding and poses serious threats to infrastructure and human lives, particularly in the downtown area as it represents a confluence of the various tributaries draining the upper parts of the watershed. Figure 11 can be employed for operational purposes to identify the volume of flow, peak flow and time of concentration given a specific precipitation amount. Digital elevation data can be used to identify the sub-watersheds using GIS tools, and thus the hydrological model can be implemented to estimate the volume and timing of flooding expected near the outlet of each sub-watershed.

The expected flood volume for a given tributary crossing the downtown area can be calculated using the runoff results obtained from the hydrological model along with the accumulation raster derived from the digital elevation model, using the following form:

$$QA = \sum_{i}^{n} Ri\, \Delta A \quad (15)$$

where QA is runoff volume, Ri is the runoff (mm) potential, and ΔA is the contributing area (m^2). For instance, if Ri is 20 mm and the total area contributing to the sub watershed is one km^2, then the total volume of flood is expected to be ~20 thousand m3. Because of the rugged terrains and impermeable surfaces, the time of concentration for storms is relatively short, in the order of less than one or two hours, which leaves very little time to take precautionary measures. For operational purposes, each tributary can be examined separately to identify the level of danger it poses.

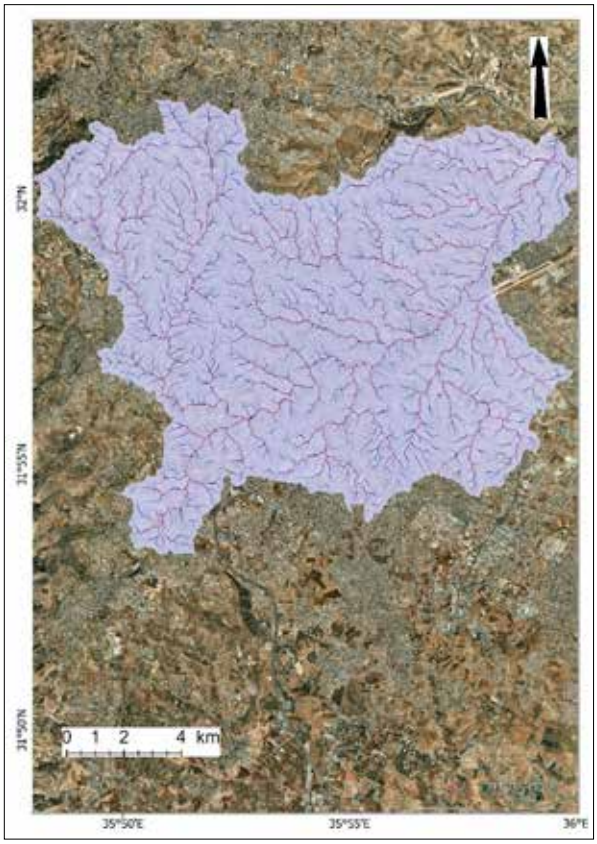

Figure 11. The sub watersheds within the study area. Note that the various drainage network confluence in the downtown area.

Flood hazards further worsen when examining the road and drainage networks. Figure 12 shows the various tributaries superimposed on the city street network. The street network in the downtown area- Al-Madina- is aligned along major tributaries draining huge, urbanized sections within the watershed. This means that large volumes of flood water would inundate the downtown area and major roads, leading to human casualties, significant monetary losses, traffic accidents and serious disruption to traffic flow (see Figure 13). Thus, increased urbanization has significantly increased the probability of large flooding events in recent years as demonstrated by the simulation results and the reported floods. The capacity of natural surface to hold moisture is much higher than those for urban landscapes. As CN increases as in the case for urban fabrics, a large portion of precipitation is converted to surface runoff. These results are commensurate with results presented by other investigators such that the hydrological changes of urbanization will increase the flood peaks and decrease the concentration times (e.g., Huong, and Pathirana,(2013, Miller and Hutchins, 2017) .

It is clear that urbanization is a significant factor in causing major flooding events in recent years. Presented results are consistent with observations obtained elsewhere. For instance, Birhanu et al. (2016) found that urbanization in Adiss Ababa in Ethiopia increase runoff by 25%. Furthermore, Bian et al. (2017) observed a 60% runoff increase in a river basin in southern China, indicating that urbanization was responsible for 59% of this increase while climate change was responsible for only 1% .

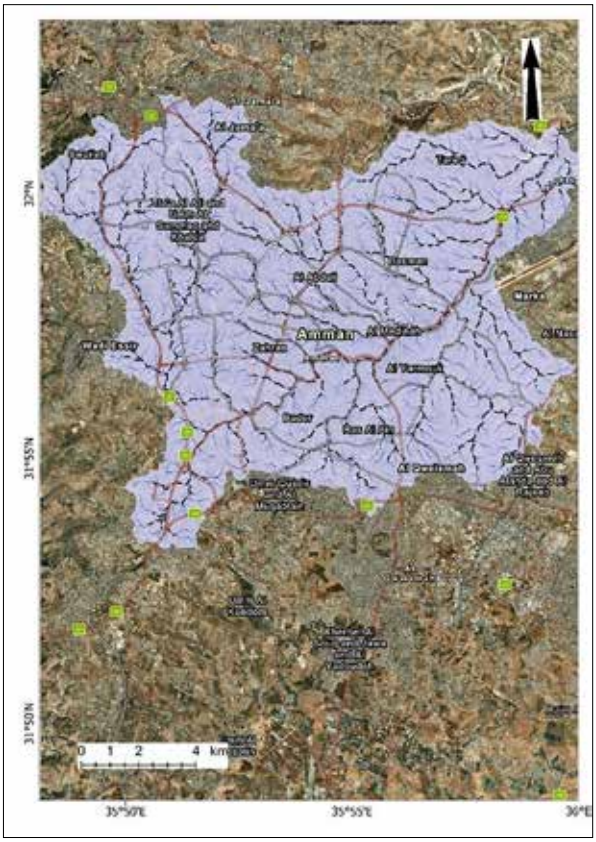

Figure 12. The various tributaries superimposed on the city road network.

Uncontrolled urbanization degrades water quality, reduces agricultural and forest lands, and increases the frequency and volume of surface runoff because of the increased imperviousness. An important urban development plan to cut down on the flooding risk, particularly for cities situated over rugged terrains, would be to study the geomorphology and watershed hydrology of the planned area prior to zoning an area for urban land use purposes. For instance, upper parts of a catchment area contributing to flooding should be zoned as agricultural/forest or parklands to eliminate, or, at least, reduce the risk of large flooding events. The effect of climate change on the frequency and magnitude of flooding does not seem to be of any importance in alleviating the flood hazard in the study area.

Figure 13. A typical flooding event inundating Downtown Amman City. This photo was taken on 28/2/2019.

8. Conclusion

Impervious surfaces and buildup land are more vulnerable to flooding than natural landscapes. The increased probability of flooding poses serious risk factors to human lives, human health, property, traffic flow and accidents. Sustainable urban planning, expansion of green infrastructure, proper zoning, and improved drainage network play pivotal roles in reducing flood vulnerabilities. The increased precipitation intensity projected by global warming will more likely exacerbate severe flooding events in the study area in the future unless more adequate engineering measures are adopted to mitigate this natural hazard. Strategies such as stormwater drainage networks play a pivotal role in mitigating the effect of flooding events in Amman. The poor zoning measures contributed significantly to the high risk of flooding because the higher areas, which were supposed to be left as agricultural land or implanted with forests, increased the probability of large flooding events. The improper and uncontrolled urban expansion on the agricultural and natural landscape such as forests has substantially increased the risk of flooding in Amman City.

Results demonstrated clearly that urban expansion surpassed the aridification and warming trend observed in the study area. The number of large flooding events has experienced a large increase in recent years despite the fact that precipitation declined, and air temperature rose substantially. There is no magic solution to the dilemma of the repeated flooding and inundations in downtown Amman City due to the limitations imposed by the topography of the city and the spatial distribution of roads and commercial properties. Although the presented model depicts flooding events very adequately, the availability of precipitation data at hourly timesteps would more likely mimic more accurately the flooding events spatially and temporally.

Measurements of precipitation and flood events using real- time data are crucial for future modeling purposes and urban planning. It is highly advisable to install a dense precipitation network across the flood- contributing areas within Amman City to monitor precipitation amount and intensity. This precipitation network should be remotely monitored through various relevant agencies such the Civil Defense Department and Amman Municipality to take precautionary measures ahead of flooding events to mitigate the adverse consequences.

Proper modeling techniques have the capability to provide adequate projection of flooding events at the watershed and sub watershed scales, thereby guiding decision-makers to take proper measures to mitigate flooding events and protect lives, infrastructure, and the economy. It is imperative to study the geomorphology and hydrology of an area prior to zoning it for urban development to avoid the consequences of costly flooding events. Findings of this study should prompt decision makers for setting environmental and urban expansion legislations to control flooding and also for managing the urban water environment and identifying knowledge gaps that limit effective management interventions.

Acknowledgment

The present investigation is funded by the Scientific Research and Innovation Support Fund, the Ministry of Higher Education and Scientific Research, Jordan, grant number: WE/1/17/2021.

References

Agonafir, C., Lakhankar, T., Khanbilvardi, R., Krakauer, N., Radell, D., Devineni, N (2023) A review of recent advances in urban flood research, Water Security, 19, https://doi.org/10.1016/j.wasec.2023.100141.

Alhasanat, H. (2014) Flash flood assessment for Wadi Mousa City-Jordan, Procedia Economics and Finance, 18, 675- 683, doi:10.1016/S2212-5671(14)00990-3

Ajmal, M., Waseem, M., Jehanzaib, M., Kim, T (2023) Development and testing of updated curve number models for efficient runoff estimation in steep-slope watersheds, Journal of Hydrology. 617, https://doi.org/10.1016/j.jhydrol.2022.129049.

Al-Kofahi, S.D., Hammouri, N., Sawalhah, M.N. (2018) Assessment of the urban sprawl on agriculture lands of two major municipalities in Jordan using supervised classification techniques. Arab Journal of Geosciences, 11, 45, https://doi.org/10.1007/s12517-018-3398-5

Allen, R.G., Tasumi, M., Morse, A., Trezza, R., Kramber, W., Lorite, I., Robinson, C.W. (2007) Satellite-based energy balance for mapping evapotranspiration with internalized calibration (METRIC) – Applications. Journal of Irrigation and Drainage Engineering, 133–395, 406.

Al Saodi, R., Al Kuisi, M., Al Salaymeh, A. (2023) Assessing the vulnerability of flash floods to climate change in arid zones: Amman–Zarqa Basin, Jordan, Journal of Water and Climate Change, 14 (12): 4376–4403. https://doi.org/10.2166/wcc.2023.237

Al Azzam, N., Al Kuisi, M. (2021) Determination of flash floods hazards and risks for Irbid governorates using hydrological and hydraulic modelling, Jordan Journal of Earth and Environmental Sciences, 9, 81-91.

Apaydin, H., Sonmez, FK., Yildirim, YE. (2004) Spatial interpolation techniques for climate data in the GAP region in Turkey. Climate Research, 28:31–40, https://doi.org/10.3354/cr028031.

Bian, G.D., Du,J.K.. Song, M.M., Xu, Y.P., Xie, S.P., Zheng, W.L., Xu C.-Y. (2017) A procedure for quantifying runoff response to spatial and temporal changes of impervious surface in Qinhuai River basin of southeastern China, CATENA, 157, 268-278, https://doi.org/10.1016/j.catena.2017.05.023.

Birhanu D, Kim,H., Jang, C., Park, S. (2016)Flood Risk and Vulnerability of Addis Ababa City Due to Climate Change and Urbanization, Procedia Engineering,154,696-702,https://doi.org/10.1016/j.proeng.2016.07.571.

Borga, M., Boscolo P, Zanon F, Sangati, M. (2007). Hydrometeorological analysis of the 29 August 2003 flash flood in the Eastern Italian Alps. American Meteorological Society, 1049–1067. https://doi.org/10.1175/JHM593.1

Chung, E., Park, K., Lee, K. S. (2011) The relative impacts of climate change and urbanization on the hydrological response of a Korean urban watershed, Hydrological Processes, 25, 4, 544-560, doi:10.1002/hyp.7781

Liu, YB., De Smedt, F. (2004). A GIS-based hydrological model for flood prediction and watershed management (Documentation and User Manual). Department Hydrology and Hydraulic Engineering, Vrije Universiteit Brussel.

Dingman, S. L. (2002). Physical hydrology (2nd ed.). Prentice Hall.

Emmendorfer, LR., Dimuro GP. (2020) A novel formulation for inverse distance weighting from weighted linear regression. In: Krzhizh anovskaya V et al (eds) Computational Science – ICCS 2020. ICCS 2020. Lecture Notes in Computer Science, 12138. Springer, Cham. https://doi.org/10.1007/978-3-030-50417-5_43

Engicon (2019) Amman Downtown Flood on 28 Feb. 2019: Preliminary Technical Report, Prime Ministry, Amman, Jordan.

Farmer, D., Sivapalan, M., & Jothityangkoon, C. (2003). Climate, soil, and vegetation controls upon the variability of water balance in temperate and semiarid landscapes: Downward approach to water balance analysis. Water Resources Research, 39, 1035–1049. https://doi.org/10. 1029/2001WR000328

Gammoh, L., A., Dawson, T, G., Katsikopoulos,, K (2023) How flood preparedness among Jordanian citizens is influenced by self-efficacy, sense of community, experience, communication, trust and training, International Journal of Disaster Risk Reduction, https://doi.or /10.1016/j.ijdrr.2023.103585.

Gharaibeh, A. A., Zu'bi, A., Esra'a, M., Abuhassan, L. B. (2019) Amman (City of Waters); Policy, land use, and character changes, Land, 8, 12, 195, doi:10.3390/land8120195

Guo, K., Guan, M., Yu, D (2021) Urban surface water flood modelling – a comprehensive review of current models and future challenges, Hydrological Earth System Science, 25 (5) (2021) 2843–2860, https://doi.org/10.5194/hess-25-2843-2021.

Hargreaves, G. H., Allen, R. G. (2003). History and evaluation of Hargreaves evapotranspiration equation. Journal of Irrigation and Drainage Engineering, ASCE, 129(1), 53–63.

Hargreaves, G. H., Samni, Z. A. (1982). Estimation of potential evapotranspiration. Journal of Irrigation and Drain age Division, Proceedings of American Society of Civil Engineering, 108, 223–230.

Hochman, A., Marra, F., Messori, G., Pinto, J. G., Raveh-Rubin, S., Yosef, Y., and Zittis, G. (2022) Extreme weather and societal impacts in the eastern Mediterranean, Earth System Dynamics, 13, 749–777, https://doi.org/10.5194/esd-13-749-2022.

Hunting Technical Services (1993) The Soils of Jordan. Ministry of Agriculture, National Soil Map and Land Use Project, Level 1: Reconnaissance Soil Survey (Scale 1: 250,000), 3 Volumes, Amman

Huong, H. T. L., Pathirana, A. (2013) Urbanization and climate change impacts on future urban flooding in Can Tho city, Vietnam, Hydrological Earth System Science, 17, 379–394, https\\w.hydrol-earth-syst-sci.net/17/379/2013/ doi:10.5194/hess-17-379-2013

Jahan, K.; Pradhanang, S.M.; Bhuiyan, M.A.E (2021) Surface Runoff Responses to Suburban Growth: An Integration of Remote Sensing, GIS, and Curve Number. Land, 10, 452. ttps://doi.org/10.3390/land10050452

Jeffrey S, Carter J, Moodie K, Beswick A (2001) Using spatial interpolation to construct a comprehensive archive of Australian climate data. Environmental Modeling Software, 16:309–330

Kannan, N., Santhi, C., Williams, J. R., and Arnold, J. G. (2008). "Development of a continuous soil moisture accounting procedure for curve number methodology and its behavior with different evapotranspiration methods." Hydrological Processes, 22(13), 2114–2121.

Liu, YB., De Smedt, F. (2004). A GIS-based hydrological model for flood prediction and watershed management (Documentation and User Manual). Department Hydrology and Hydraulic Engineering, Vrije Universiteit Brussel.

Miller, J. D., Hutchins M. (2017) The impacts of Urbanization and climate change on urban flooding and urban water quality: A review of the evidence concerning the United Kingdom, Journal of Hydrology: Regional Studies,12,2017,345-362, https://doi.org/10.1016/j.ejrh.2017.06.006., (https://www.sciencedirect.com/science/article/pii/S2214581817300435)

Odeh, T., Mohammad, A.H., Pradhanang, S.M., Ismail, M., Rödiger, T. (2022) GIS-based analytical modeling on

evaluating impacts of urbanization in Amman water resources, Jordan. Environmental Earth Sciences, 81, 160 (2022). https://doi.org/10.1007/s12665-022-10238-7

Oroud, I. M. (2015a). Water budget assessment within a typical semiarid watershed in the Eastern Mediterranean. Environmental Processes, 06/2015; 3(2):1–15. https://doi.org/10.1007/s40710-015-0072-8.

Oroud, I. M (2015b) Water balance in a typical watershed in the Karak Plateau. Jordan Journal of Earth and Environmental Sciences, 7(2): 109–117

Oroud, I. M. (2018). Global warming and its implications on meteorological and hydrological drought in the southeastern Mediterranean. Environmental Processes. https://doi.org/10.1007/s4071-018-0301-z.

Oroud, I. M., Balling, R. C (2021) The utility of combining optical and thermal images in monitoring agricultural drought in semiarid mediterranean environments, Journal of Arid Environments, 189, https://doi.org/10.1016/j.jaridenv.2021.104499.

Oroud I. M (2022) Derivation of spatially distributed thermal comfort levels using remote sensing, GIS tools and computational methods. Theoretical and Applied Climatology, 148:569–583. https://doi.org/10.1007/ s00704-022-03951-7

Oroud I. M. (2023) The future fate of the Dead Sea: Total disappearance or a dwarfed hypersaline hot lake? Journal of Hydrology, 623, https://doi.org/10.1016/j.jhydrol.2023.129816.

Oroud, I.M. (2024) The implications of climate change on freshwater resources in the arid and semiarid Mediterranean environments using hydrological modeling, GIS tools, and remote sensing. Environmental Monitoring and Assessment, 196, 979. . https://doi.org/10.1007/s10661-024-13139-3

Oroud, I. M., Al-Rousan, N. (2004) Urban Encroachment on Rain-Fed Agricultural Lands in Jordan during the Second Half of the 20th Century, The Arab World Geographer, 7 (3), 165-180, https://doi. 10.5555/arwg.7.3.p57gmvlh24287ntj

Palmer, WC. (1965). Meteorological drought. Office of Climatology Research Paper 45, Weather Bureau, Washington D.C., 58.

Ponce, V. M., & Hawkins, R. (1996). Runoff curve number: Has it reached maturity? Journal of Hydrologic Engineering. https://doi.org/10.1061/(ASCE)1084-0699(1996)1: 1(11)

Ries, F., Schmidt, S., Sauter, M., Lange, J. (2017). Controls on runoff generation along a steep climatic gradient in the Eastern Mediterranean. Journal of Hydrology: Regional Studies, 9, 18–33. https://doi.org/10.1016/j.ejrh.2016.11. 001

Schoener W (2010) Basics of climatological and meteorological observations for GIS applications. In: Carrega P (ed) Geographical Information and Climatology. Wiley-ISTE 288 PP

Small, E., Badger, A., Abolafia-Rosenzweig, R., & Livneh, B. (2018). Estimating soil evaporation using drying rates determined from satellite-based soil moisture records. Remote Sensing. https://doi.org/10.3390/rs10121945

Tabari, H, 2020 Climate change impact on flood and extreme precipitation increases with water availability, Scientific Reports, doi:10.1038/s41598-020-70816-2

Viola, F., Caracciolo, D., Forestieri, A., Pumo, D., & Noto, L. V. (2017). Annual runoff assessment in arid and semiarid Mediterranean watersheds under the Budyko's framework. Hydrological Processes, https://doi.org/10.1002/hyp.11145

المملكة الأردنية الهاشمية

صندوق دعم البحث العلمي

الجامعة الهاشمية

المجلة الأردنية
لعلوم الأرض والبيئة

JJEES

مجلة علمية عالمية محكمة

المجلد (١٦) العدد (١)

http:// jjees.hu.edu.jo/

ISSN 1995-6681

المجلة الأردنية لعلوم الأرض والبيئة

مجلة علمية عالمية محكمة

المجلة الأردنية لعلوم الأرض والبيئة: مجلة علمية عالمية محكمة ومفهرسة ومصنفة، تصدر عن عمادة البحث العلمي في الجامعة الهاشمية وبدعم من صندوق البحث العلمي - وزارة التعليم العالي والبحث العلمي، الأردن.

ترسل البحوث إلكترونيا إلى البريد الإلكتروني التالي:

رئيس تحرير المجلة الأردنية لعلوم الأرض والبيئة

jjees@hu.edu.jo

لمزيد من المعلومات والأعداد السابقة يرجى زيارة موقع المجلة على شبكة الانترنت على الرابط التالي:

www.jjees.hu.edu.jo

المملكة الأردنية الهاشمية صندوق دعم البحث العلمي الجامعة الهاشمية

JJEES

المجلة الأردنية لعلوم الأرض والبيئة

المجلد (16) العدد (1)

مجلة علمية عالمية محكمة تصدر بدعم من صندوق دعم البحث العلمي

ISSN 1995-6681 jjees.hu.edu.jo آذار 2025